Boosting the sensitivity of continuous gravitational waves all-sky searches using advanced filtering techniques

Lorenzo Pierini

Thesis directors

Cristiano Palomba, Paola Leaci

SAPIENZA
UNIVERSITÀ DI ROMA

PhD course in Physics
XXXV cycle

Department of Physics
Sapienza University of Rome

Contents

Abstract

The work presented in this PhD thesis has been done in the context of gravitational-waves searches. Since the first detection on the 14th September 2015 by the LIGO-Virgo collaboration, a growing number of gravitational-wave events has been detected, all emitted by the coalescence of binary systems involving black holes and/or neutron stars. My work is focused on the search for continuous gravitational waves, which still lack the first detection. These signals are expected to be emitted, for instance, by spinning neutron stars with an asymmetric shape with respect to the rotation axis, and are at least five orders of magnitude weaker than the typical amplitude of detected binary coalescences. In this PhD thesis I report on the work done in four different projects, with the common purpose of increasing the sensitivity of continuous-wave searches, involving both data analysis and instrumental aspects. The first project is a contribution to the commissioning of the Virgo interferometer in view of the next observing run, O4, which will start in May 2023. My contribution has been mainly devoted to the noise hunting activity, focused on the identification and mitigation of instrumental-noise sources that can degrade the sensitivity of continuous-wave searches.

The other three projects are related to data analysis. I have focused, in particular, on all-sky searches for sources without electromagnetic counterpart and long-lasting signals from rapidly evolving newly-born neutron stars. I have studied in great detail the robustness of an all-sky data analysis method in the case of overlapping signals. This is relevant for some exotic classes of continuous wave sources and, more generally, in view of third generation detectors, like Einstein Telescope. I have developed a two-dimensional filter, called triangular filter, to be applied to the search for long-lasting gravitational waves from unstable neutron stars, showing that thanks to this method an increase of the search sensitivity of about 20% is achievable. Finally, I describe the first steps of a wide work to develop a new procedure for all-sky continuous-wave searches, exploiting a statistics based on the sidereal modulation, that affects astrophysical signals, due to the Earth rotation.

Introduction

The existence of gravitational waves is among the most intriguing predictions of the theory of General Relativity, published by Albert Einstein in 1916. Gravitational waves are perturbations of the space-time metric propagating at the speed of light. The effect of a gravitational wave is to periodically change the relative separation among different pairs of test masses. Even when produced in astrophysical processes involving large masses moving at a significant speed, gravitational waves are extremely faint at the detector, and induce changes in the typical lengths of experimental apparatuses of the order of 10^{-18} m or even smaller [1]. This extremely small effect is at the origin of the experimental difficulties to directly observe gravitational waves, i.e. through the measurement of the space-time distortions they induce. The experimental effort to detect them started in the 1960s. It took up to half a century of technological progress and the construction of kilometer-scale interferometric detectors, such as LIGO and Virgo, to arrive at the first detection, on 14th September 2015, when the gravitational-wave astronomy has officially begun. Since then, various (~ 90) gravitational-wave events have been detected, all emitted by the merger of binary systems involving black holes and/or neutron stars.
The work I present here has been devoted to the search for continuous (persistent) gravitational waves, which are thought to be emitted -for instance- by deformed, spinning neutron stars. The effort to detect these sources is even more challenging with respect to binary mergers, since the expected gravitational-wave amplitude at the detector is at least five orders of magnitude weaker. However, thanks to their long duration, we can build up the signal-to-noise ratio and exploit very specific signal features, which help us to discriminate between signals and noise artefacts. My research activity is essentially focused on boosting the sensitivity of continuous gravitational wave searches, working on different aspects, involving both data analysis and instrumental aspects. Concerning the data analysis, I have focused on the so-called all-sky searches for sources without an electromagnetic counterpart, and on long-lasting waves from rapidly evolving newly-born neutron stars, whose position is known through electromagnetic observations. In both cases a huge parameter space has to be explored, so these searches are computationally bounded. The key to increase the sensitivity lies in the development of novel analysis techniques, exploiting signal features in different ways with respect to already existing methods. Another contribution is the estimation of the robustness of existing procedures with respect to new classes of potential sources and assessing the future improvements.
During my PhD I have worked on three projects covering both all-sky searches for continuous waves, including a study on new exotic sources, and long-lasting transients from young neutron stars. On the instrumental side, I have worked (for several weeks on the Virgo site)

[1] This number refers to gravitational waves with frequencies from tens to thousands of Hertz, observable by Earth-based detectors (for more details, see Chapter 1).

to identify and mitigate possible noise sources that can limit the continuous-wave search.
The work of this Thesis is organized as follows:
In **Chapter 1** I introduce the basics of gravitational-wave searches. I explain the mechanism that generates gravitational waves, showing the different kind of sources and corresponding search strategies. I introduce the basic physics of interferometric detectors and describe the fundamental noise sources that limit the search sensitivity. Finally, I describe the optical layout of LIGO-Virgo detectors, their sensitivity budget and the improvements done to achieve the first detection.
In **Chapter 2** I introduce continuous gravitational waves. I review the physics behind the possible sources, considering both neutron stars and more exotic sources, like condensates of ultra-light bosons around spinning black holes. I present the different search strategies that can be done depending on the available source knowledge. I also briefly discuss the most recent results.
In **Chapter 3** I report the experimental work done at the Virgo site as contribution to the commissioning of the interferometer. The activity on which I have mostly contributed is noise hunting, focused on the noise sources that can limit continuous-wave searches. I have focused the activity on the so-called technical noises generated by the heating, ventilation and air conditioning systems, by the vacuum system and the external environment. For each noise source I have done on-site actions to identify the noise and possibly mitigate it, followed by a data-analysis work to process the results.
In **Chapter 4** I report a study to assess the robustness of the Frequency-Hough procedure for all-sky searches of continuous waves when we are in presence of several signals, which cluster together in the same frequency band. At the moment this seems to be a remote possibility because continuous waves in standard scenarios are very weak and, with current detector sensitivity, we expect to have at most one or a few detectable signals in a given observing run. However, the possibility of signal clusters in the exotic scenario of ultra-light boson clouds has been recently considered. In such a case, the problem of resolving individual signals arises. I show that the Frequency-Hough procedure is overall robust towards the presence of signal clusters.
In **Chapter 5** I present the development and test of a two-dimensional filter to be applied to the search for long-lasting, rapidly evolving, gravitational waves, like those we expect to be emitted by new born neutron stars, as a consequence of a large inner magnetic field, or due to the excitation of unstable star oscillation modes. The so-called *triangular filter* enhances the signal-to-noise ratio, allowing to increase the search sensitivity. I define and characterize this filter, presenting specific tests to assess the achievable sensitivity gain.
In **Chapter 6** I describe the first steps of a wide work to develop a new procedure for all-sky continuous-wave searches. The basic idea is to exploit the *sidereal modulation* that astrophysical signals get entering the detector because of Earth rotation. A method to exploit such modulation has been developed within my group to search for signals from a fixed position in the sky. Here, I report the first steps I have done to extend this approach to the much more complicate case of all-sky searches.

Chapter 1

Gravitational waves and detectors

Initially fascinated by the beauty of the theory,
I was finally captured by experimental challenges.

The problem of detecting gravitational waves (GWs) has been one of the hardest challenges in the last century. Since their first prediction, there has been a growing interest on their physical meaning and on the possibility of their detection. Since the theory of General Relativity (GR) was published in 1916 by Albert Einstein, it was clear that the equations allowed for propagating wave solutions. Anyway, it took up to 20 years for Einstein to get convinced that they have a real physical meaning and they are not just spurious mathematical solutions or coordinate artifacts [1]. Twenty more years were necessary for the gravitational community to understand if they actually carry energy and what effect they have on matter. A crucial step forward was done by Felix Pirani, who showed in 1956 the effect of a GW passing through a group of particles [2]. His work laid the foundation for the development of GW detectors. The pioneer was, however, Joseph Weber, who developed Pirani's idea of detecting GWs through their action on two masses connected by a spring. In the 1960s, he developed and built the first resonant bar detector [3] and, in the subsequent four decades, resonant-mass detectors were built by various groups all over the world. However, their typical sensitivity could allow to detect only extreme events generated in our Galaxy, and no confident GW detection has never been confirmed.

The idea of GW detection through interferometers was first proposed in 1962 by M.E. Gertsenshtein and V.I. Pustovoit [4], and Rainer Weiss was the first one to study in detail, in early 1970s, the intrinsic limitations and noise sources associated to this method [5]. Since from the beginning, it was clear that the realization of such a complex instrument would have required large collaborations and large-scale science. In fact, the practical realization of the first ground-based interferometers took up to 30 years, and we have to wait until 14th of September 2015 to observe the first gravitational signal, after several instrument upgrades and 100 years after GR formulation. In this Chapter, I will introduce the basic principles that are behind the generarion of GWs and the main sources that are expected; then, I will explain the basic physics behind the interferometric detectors, introduce Virgo and LIGO detectors and their main limiting noises; finally, I will show the main discoveries that have been made during the first 3 observing runs in the Advanced detector configuration.

1.1 General Relativity and gravitational waves

GWs arise directly from GR equations. GR was formulated as a metric description of gravity that incorporates the Weak Equivalence Principle, the Local Lorentz Invariance and the Local Position Invariance. The space-time is described through the metric tensor $g_{\mu\nu}$, which allows to compute intervals between two events. In Special Relativity, space-time is flat and is described by the tensor $\eta_{\mu\nu} = \text{diag}\{-1, 1, 1, 1\}$. Instead, in GR we have to take account for curved space-time. Let $\{\vec{e}_\mu\}$ be a coordinate basis; a generic vector can be decomposed on its components with respect to that basis as[1] $\vec{V} = V^\sigma \vec{e}_{(\sigma)}$. While in a flat space-time the coordinate basis is invariant with respect to traslations, in a curved space-time they can change from point to point. Therefore, when computing derivatives we have to take account for the changing basis[2]: $\vec{V}_{,\beta} = V^\alpha_{,\beta}\vec{e}_{(\alpha)} + V^{(\alpha)}\vec{e}_{(\alpha),\beta}$. To do this, we introduce the affine connections $\Gamma^\mu_{\alpha\beta}$. Through these objects, we express the variation of the coordinate basis in terms of the basis itself, $\vec{e}_{(\alpha),\beta} = \Gamma^\mu_{\alpha\beta}\vec{e}_{(\mu)}$. They are defined as combinations of the metric tensor and its derivatives, $\Gamma^\sigma_{\alpha\beta} = \frac{1}{2}g^{\sigma\mu}\left(g_{\mu\alpha,\beta} + g_{\mu\beta,\alpha} - g_{\alpha\beta,\mu}\right)$, and are pseudo-tensors[3].

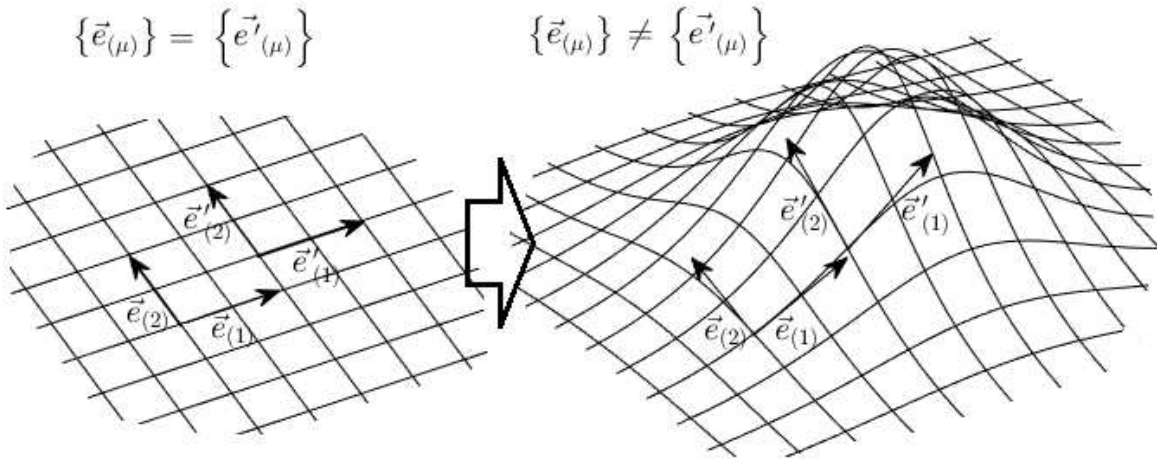

Figure 1.1: Illustration of the transition from a 2D flat space-time to a curved one. While in flat space-time a set of base vectors remains unchanged independently on the region, in curved space-time the base vectors can change region by region.

To describe properly the space-time curvature we can combine the metric tensor and its first and second derivatives in the Riemann tensor, defined as

$$\mathrm{R}^\alpha_{\mu\beta\nu} = -\left(\Gamma^\alpha_{\mu\beta,\nu} - \Gamma^\alpha_{\mu\nu,\beta} + \Gamma^\alpha_{\nu\eta}\Gamma^\eta_{\mu\beta} - \Gamma^\alpha_{\beta\eta}\Gamma^\eta_{\mu\nu}\right) \tag{1.1}$$

The components of the Riemann tensor are determined by the mass-energy distribution of the system. To do this, is more convenient to use the Ricci tensor, obtained through its 1st

[1] In this section, I will adopt the Einstein convention, where repeated indices means summation over all the 4 components, e.g. $a^\mu b_\mu = \sum_{\mu=1}^4 a^\mu b_\mu$.

[2] In this section, the use of the comma means a partial derivative: $v^\mu_{,\nu} = \frac{\partial v^\mu}{\partial x^\nu}$.

[3] A pseudo-tensor is a quantity that transforms like a tensor under coordinate transformation, but changes sign if the transformation includes a reflection

and 3rd indices contraction, $\mathrm{R}_{\mu\nu} = \mathrm{R}^{\alpha}_{\mu\alpha\nu}$, and the Ricci scalar $\mathrm{R} = g^{\mu\nu}R_{\mu\nu}$, and use it to build the Einstein tensor $G_{\mu\nu} = \mathrm{R}_{\mu\nu} - \frac{1}{2}\mathrm{R}g_{\mu\nu}$. With this notation the space-time curvature, expressed through the Einstein tensor $G_{\mu\nu}$, is determined by the mass-energy distribution through the Einstein field equations [6]

$$G_{\mu\nu} = \frac{8\pi\mathrm{G}}{c^4}\, T_{\mu\nu} \tag{1.2}$$

The $T_{\mu\nu}$ tensor on the right side is the stress-energy tensor, and describes the distribution of mass-energy. Chosen a reference frame with coordinates $\vec{\xi}$, given n non-interacting particles with locations $\vec{\xi}_i$, four-momenta p_i^{μ} and energies E_i, the stress-energy tensor is defined as

$$T^{\mu\nu} = c^2 \sum_{i=1}^{n} \frac{p_i^{\mu} p_i^{\nu}}{E_i}\, \delta^3\left[\vec{\xi} - \vec{\xi}_i\,(t)\right] \tag{1.3}$$

Equation 1.2 represents a system of 10 second-order mixed differential equations and allows to fully determine the metric $g_{\mu\nu}$. However, in practice we are not able to resolve that system except for very simple and symmetric systems. Most of the solutions are typically obtained using perturbation theory or require numerical techniques.

GW solutions are obtained expanding the Einstein equations around the flat-space metric. Therefore we introduce the perturbation $h_{\mu\nu}$ in order to write

$$g_{\mu\nu} = \eta_{\mu\nu} + h_{\mu\nu}\ , \qquad |h_{\mu\nu}| \ll 1 \tag{1.4}$$

and then, expand the 1.2 to first order in $h_{\mu\nu}$. Taking the traceless part $\bar{h}_{\mu\nu} = h_{\mu\nu} - \frac{1}{2}\eta_{\mu\nu}h$ and imposing the harmonic gauge $\partial^{\nu}\bar{h}_{\mu\nu} = 0$, we get a simple wave equation,

$$\Box\, \bar{h}_{\mu\nu} = -\frac{16\pi\mathrm{G}}{c^4}\, T_{\mu\nu} \tag{1.5}$$

Equation 1.5 is obtained under the physical assumption that the source moves in flat space-time, with motion determined by their mutual interaction. Studying the propagation of GWs outside the source, where it reduces to $\Box\bar{h}_{\mu\nu} = 0$, we see that the presence of the D'Alembert operator $\Box = -\left(1/c^2\right)\partial_t^2 + \nabla^2$ implies that GWs propagate at the speed of light in vacuum. Moreover, outside the source we can simplify the form of the metric by imposing the transverse-traceless (TT) gauge:

$$h^{0\mu} = 0, \quad h^{i}_{\ i} = 0, \quad \partial^{j} h_{ij} = 0 \tag{1.6}$$

By imposing the TT gauge, we are setting 4+3+1 constraints to the 1.5, so we have reduced from the original 10 degrees of freedom to only 2. In vacuum, 1.5 and 1.6 allow for plane wave solutions [6],

$$h^{TT}_{\mu\nu}\,(t,\vec{x}) = \begin{pmatrix} 0 & 0 & 0 & 0 \\ 0 & h_+ & h_\times & 0 \\ 0 & h_\times & -h_+ & 0 \\ 0 & 0 & 0 & 0 \end{pmatrix}_{\mu\nu} \cos\left[\omega\left(t - \frac{z}{c}\right)\right] \tag{1.7}$$

, where we have chosen the z axis as propagation direction, ω is the GW pulsation and h_+, $h_\times$ are the amplitudes of the + and × polarization of the wave. In presence of the source, we have to solve Equation 1.5 by means of the retarded Green's function. In the limit of

distant sources ($r \gg d$) and low velocity ($v \ll c$), we can expand the stress-energy tensor in flat space-time. By defining the momenta M of T^{00} and the momenta P of

$$\begin{aligned} \mathrm{M}\left(t\right) &= \tfrac{1}{c^2}\int d^3x\, T^{00}\left(t,\vec{x}\right), & P^i\left(t\right) &= \tfrac{1}{c}\int d^3x\, T^{0i}\left(t,\vec{x}\right), \\ \mathrm{M}^i\left(t\right) &= \tfrac{1}{c^2}\int d^3x\, T^{00}\left(t,\vec{x}\right)x^i, & P^{i,j}\left(t\right) &= \tfrac{1}{c}\int d^3x\, T^{0i}\left(t,\vec{x}\right)x^j, \\ \mathrm{M}^{ij}\left(t\right) &= \tfrac{1}{c^2}\int d^3x\, T^{00}\left(t,\vec{x}\right)x^ix^j & P^{i,jk}\left(t\right) &= \tfrac{1}{c}\int d^3x\, T^{0i}\left(t,\vec{x}\right)x^jx^k \end{aligned} \tag{1.8}$$

and pointing out that $\dot{\mathrm{M}} = 0$, $\dot{\mathrm{M}}^i = P^i$ and $\dot{P}^i = 0$, we can solve Equation 1.5 in term of multipoles [7]:

$$h_{ij}^{TT}\left(t,\vec{x}\right) = \frac{1}{r}\frac{4\mathrm{G}}{c^4}\Lambda_{ij,kl}\left(\hat{n}\right)\cdot\left\{\frac{1}{2}\ddot{\mathrm{M}}^{kl} + \frac{1}{c}n_m\left[\frac{1}{6}\dddot{\mathrm{M}}^{klm} + \frac{1}{3}\left(\ddot{P}^{k,lm} + \ddot{P}^{l,km} - 2\ddot{P}^{m,kl}\right)\right] + \mathcal{O}\left(\frac{1}{c^2}\right)\right\}_{t-\frac{r}{c}} \tag{1.9}$$

where $\Lambda_{ij,kl}\left(\hat{n}\right)$ is an operator that projects the tensors in the TT gauge along the propagation direction $\hat{n}$. Equation 1.9 is the basis for the multipole expansion. It is important to underline that the first non-null term, that dominates the emission, is the 2nd momentum of T^{00}. There is neither monopole nor dipole gravitational radiation. This is not surprising, given that M and P^i are conserved quantities and so their time derivatives vanish. This important fact, which is here obtained in the context of linearized theory, holds also more generally (see [7], p.112).

If we restrict to the leading term of 1.9, noting that the 0-0 component of the stress-energy tensor to the lowest order of v/c has the physical meaning of a mass-energy density, i.e. $T^{00} = \rho c^2$, we can introduce the quadrupole moment

$$Q^{ij} \equiv \mathrm{M}^{ij} - \frac{1}{3}\delta^{ij}\mathrm{M}_{kk} = \int d^3x\, \rho\left(t,\vec{x}\right)\left(x^ix^j - \frac{1}{3}r^2\delta^{ij}\right) \tag{1.10}$$

If we now apply the TT gauge projector to the quadrupole moment, the emitted GW amplitude at the leading order is given by

$$h_{ij}^{TT}\left(t,\vec{x}\right)\big|_{\mathrm{quad}} = \frac{1}{r}\frac{2\mathrm{G}}{c^4}\ddot{Q}_{ij}^{TT}\left(t - \frac{r}{c}\right) \tag{1.11}$$

The emission of gravitational radiation influences the evolution of the source system itself, since GWs carry energy and angular momentum away from it. The estimated radiated power through GWs, also known as gravitational luminosity of the source, is given at the leading order by

$$\mathcal{L}_{\mathrm{gw}}\big|_{\mathrm{quad}} = \frac{\mathrm{d}E_{\mathrm{gw}}}{\mathrm{d}t} = \frac{\mathrm{G}}{5c^5}\left\langle \dddot{Q}_{ij}\dddot{Q}_{ij}\right\rangle_{t-\frac{r}{c}} \tag{1.12}$$

and the angular momentum, considering both the spin and the orbital contribution, carried out by the GW, is at the leading order

$$\left.\frac{\mathrm{d}J^i}{\mathrm{d}t}\right|_{\mathrm{quad}} = \frac{2\mathrm{G}}{5c^5}\epsilon^{ikl}\left\langle \ddot{Q}_{ka}\dddot{Q}_{la}\right\rangle_{t-\frac{r}{c}} \tag{1.13}$$

From the above considerations, it is clear that the condition for a source to emit GWs is that its dynamics produces a quadrupole moment with non-vanishing second time derivative. In physical terms, it means that the system dynamics must violate the cylindrical symmetry. Furthermore, given the smallness of the constant term in Equation 1.9 ($4\mathrm{G}/c^4 \sim 3.3 \cdot 10^{-44} s^2/Kg \cdot m$), only astrophysical sources involving masses of the order or greater than

the solar mass ($M_\odot$) can produce GWs with detectable amplitudes. The explicit calculation of Q^{ij} and h_{ij}^{TT} depends on the particular geometry of the source.

The general solution expressed in 1.9 is an expansion in terms of v/c, but is still assuming that the background space-time is flat. The implicit assumption done is that the background space-time curvature and the velocity of the source can be treated as independent parameters, a condition that holds when the system is governed by non-gravitational forces. However, the astrophysical systems on which we are interested are typically held together by gravitational forces. In this condition the independence assumption is no longer valid as a consequence of the virial theorem. For a self-gravitating system with total mass M and typical size d, we have $(v/c)^2 \sim \mathrm{G}M/c^2d$, where the right-side term is also a measure of strength of the gravitational field near to the source. When treating a moderately-relativistic self-gravitating system, it has to be described by a post-Newtonian (PN) formalism. In PN formalism, the Einstein equations 1.2 have to be expanded in terms of a small parameter

$$x = \frac{v}{c} \sim \left(\frac{\mathrm{G}M}{c^2 d}\right)^{1/2}$$

and all the equations above have to be properly corrected. We refer to an expansion up to a x^n power as to a 'n-PN' order. A detatiled description of the PN formalism can be found in Chapter 5 of [7]. Finally, in the case of strongly relativistic system there is no possibility to use the perturbation theory. Hence, the Einstein equations have to be solved explicitly, in the non-linear regime, through computational methods called Numerical Relativity.

1.1.1 Gravitational wave sources

Gravitational signals can be roughly classified in macro-categories depending on the time they remain in the detector sensitivity band. This time does not depend only on the astrophysical process, but also on the type of detector, ad can actually change if we consider for example space-based detectors. Here we refer to Earth-based wide-band detectors. We can mark GW signals as transient, if they stay in the detector sensitivity band for a limited time, or continuous, if they last for the entire observation time of the detector. Another classification can be done for modeled and unmodeled signals, depending on the good and expected understanding of the physical mechanisms and on the capability to generate accurate waveform templates. In Table 1.1 the classification is reported, and the main emission mechanisms are then reviewed.

	Modeled	Unmodeled
Transient signals	Coalescence of compact binaries Postmerger neutron stars	Bursts Supernova explosions
Continuous signals	Periodic sources	Stochastic background

Table 1.1: Classification of GW signals between transient/continuous and modeled/unmodeled.

Coalescence of compact binaries

The gravitational radiation produced by two coalescing compact bodies, like black holes (BHs) and neutron stars (NSs), is one of the most important subjects, since in the first 3

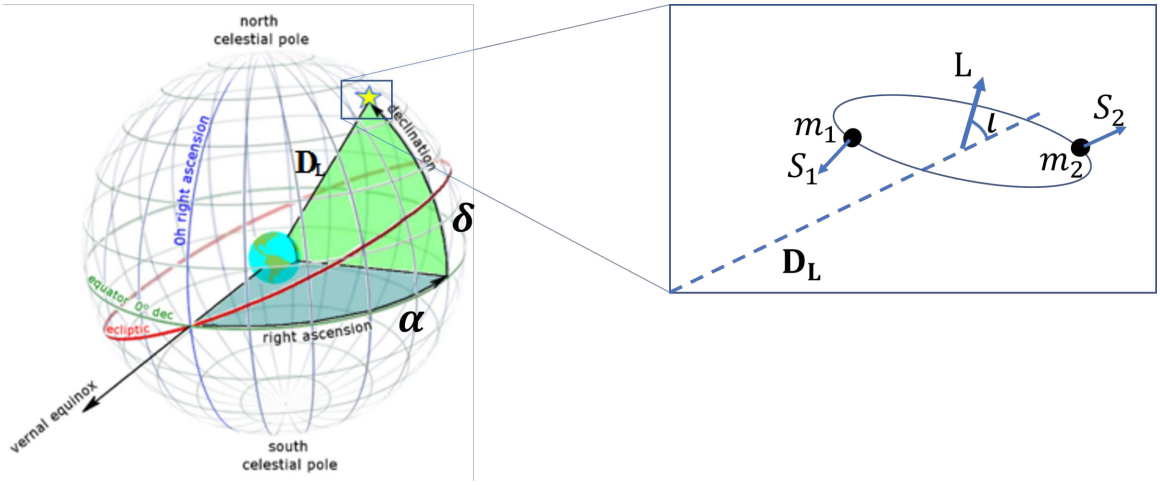

Figure 1.2: Representation of the parameters that fully describe a binary system of compact stars

LIGO/Virgo observing runs all the detected GWs belong to this category [8, 9, 10, 11]. The configuration of two (or more) mutually orbiting bodies is among the most efficient GW emitters, since it strongly violates the cylindrical symmetry. In order to fully describe a binary system we need 15 parameters:

- Localization (3): distance D (or luminosity distance D_L), right ascension α, declination δ;
- Orientation (2): angle ι between the line of sight and the orbital angolar momentum, polarization angle ψ (i.e. the direction of the projection of orbital momentum on the plane orthogonal to the line of sight)
- Intrinsic (8): couple masses (m_1, m_2) and spin[4] $\left(\vec{S}_1, \vec{S}_2\right)$
- Dynamics (2): coalescing time t_c and phase ϕ_c

The calculation of the system dynamics at the leading Newtonian order bring to a quadrupole moment that depends on the binary masses only through a symmetric combination, called chirp mass:

$$\mathcal{M} = \frac{(m_1\, m_2)^{3/5}}{(m_1 + m_2)^{1/5}} \tag{1.14}$$

At the first quadrupolar order, the emitted GW can be easily computed. The two polarization amplitudes are

$$h_+(t) = \frac{1}{D_L}\left(\frac{\mathrm{G}\mathcal{M}}{c^2}\right)^{5/4}\left[\frac{5}{c\,(t_c - t)}\right]^{1/4}\frac{1+\cos^2\iota}{2}\cos\left[\phi\,(t)\right] \tag{1.15}$$

$$h_\times(t) = \frac{1}{D_L}\left(\frac{\mathrm{G}\mathcal{M}}{c^2}\right)^{5/4}\left[\frac{5}{c\,(t_c - t)}\right]^{1/4}\cos\iota\ \sin\left[\phi\,(t)\right] \tag{1.16}$$

[4]Please note that the use of the "spin" term is intended as the rotational angular momentum of the compact object. This usage is frequent in the gravitational wave community, and will be used in the text.

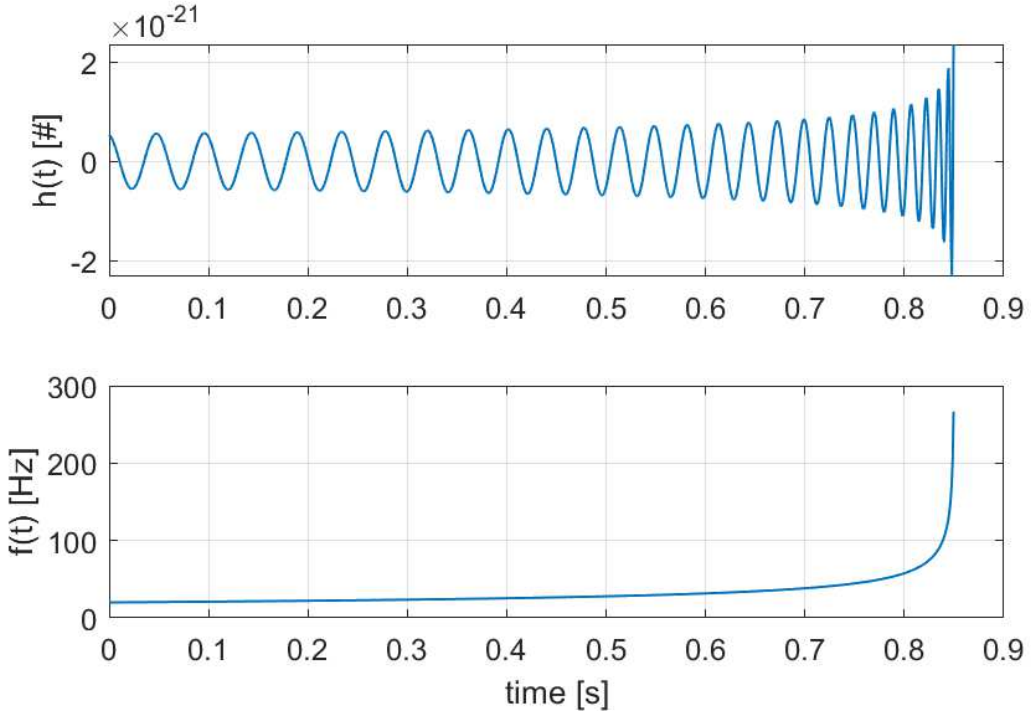

Figure 1.3: Last cycles of a simulated quadrupolar chirp signal from a binary with chirp mass $\mathcal{M} = 28M_{\odot}$ and luminosity distance $D_L = 410$Mpc, starting from 20 Hz. In the top plot, the signal h_+ strain amplitude is shown. In the bottom plot, its instantaneous frequency evolution is shown.

, where the phase evolution is obtained by integrating the frequency evolution of the signal

$$f_{\rm gw}(t) = \frac{1}{8\pi}\left(\frac{\mathrm{G}\mathcal{M}}{c^3}\right)^{-5/8}\left(\frac{5}{t_c - t}\right)^{3/8} \tag{1.17}$$

$$\phi(t) = \int 2\pi f_{\rm gw} dt = -2\left[\frac{c^3}{5\mathrm{G}\mathcal{M}}(t_c - t)\right]^{5/8} + \phi_c \tag{1.18}$$

Both the signal amplitude and frequency have a growing trend in time. For this reason, the signal produced by CBCs is typically called *chirp*. It is important to note that in these quadrupolar formula there is a degeneracy with respect to the intrinsic parameters of the binary system: individual masses are not resolved individually, and there is no dependence at all on the total and individual spin. The reason is that when computing the quadrupole moment, the orbiting bodies are treated as point-like particles interacting through Newtonian gravity. Under these assumptions, the motion is fully symmetric in the individual masses, and their intrinsic rotation is not considered. However, binary systems typically do not satisfy the flat space-time condition, at least at their final stage when they enter the Earth-based detectors sensitivity. To accurately describe the CBC dynamics we need to compute the wave-forms at least up to the 3.5-PN order, see [12, 13].

The PN formalism is valid until the moderately-relativistic condition holds. However, at the final phase of the coalescence also the weak-field condition is no more valid and the system has to be treated in the strong-field regime. The analytic solution is valid until the

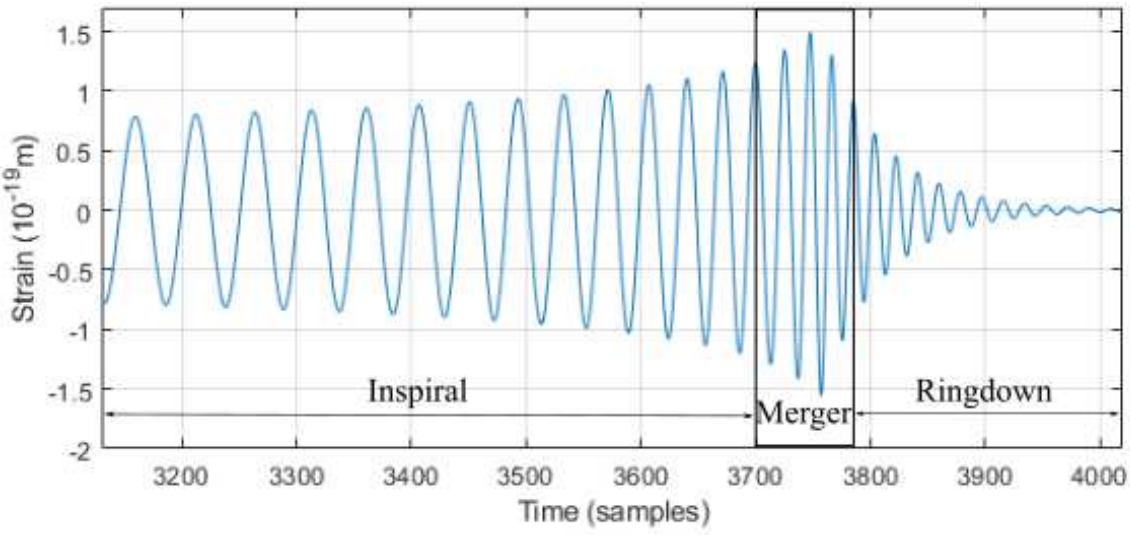

Figure 1.4: A sample waveform describing a full CBC signal from a BBH, computed with Numerical Relativity. The three distinct regimes, namely the inspiral, merger, ringdown, are highlighted.

orbital separation between the individual bodies reaches the value $r \simeq 6\mathrm{G}\left(m_1 + m_2\right)/c^2$, obtained in the quadrupole approximation, which is the inner-most stable circular orbit (ISCO). After that, if the binary components are BHs the system has to be treated with Numerical Relativity methods, which are computationally bounded. Since 2005 new numerical methods have been introduced, based on generalized harmonic coordinates, that can evolve a binary BH during the last crucial stages of a merger [14]. Before, no code has been able to simulate a nonaxisymmetric collision through coalescence and subsequent relaxation of the final BH. The numerical templates must have continuity with the analytic waveforms before the ISCO. After the merger, there is an unique event horizon, highly asymmetric and with an high rotational spin because of the conservation of orbital angular momentum. During this last phase, called ringdown, the resulting BH performs few damped oscillation cycles. Its GW emission is given by a superposition of its quasi-normal modes, with frequency and damping time depending only on the BH mass and spin [15]. An example of a complete waveform, referring to the first observed GW150914, is shown in Figure 1.4.

Despite some computational limitations for a full numerical simulation, the physics of CBCs is generally well understood. The prediction of the emitted GW signal is therefore very accurate and reliable. In this case, signals can be found using matched filter based searches [16]. The shortness of the signals when they enter the Earth-based detectors sensitivity window allows to build large template banks, which are typically used to scan the detectors data. During the first three observative runs of Advanced Virgo and LIGO, various different implementations of matched filter have been used. The main one used are PyCBC [17], GstLAL [18] and MBTA [19], which differ in the way they implement the filter, they combine results of different detectors and establish the significance of a detection. In Section 1.3 the discoveries done up to now will be presented, all of them associated to CBCs.

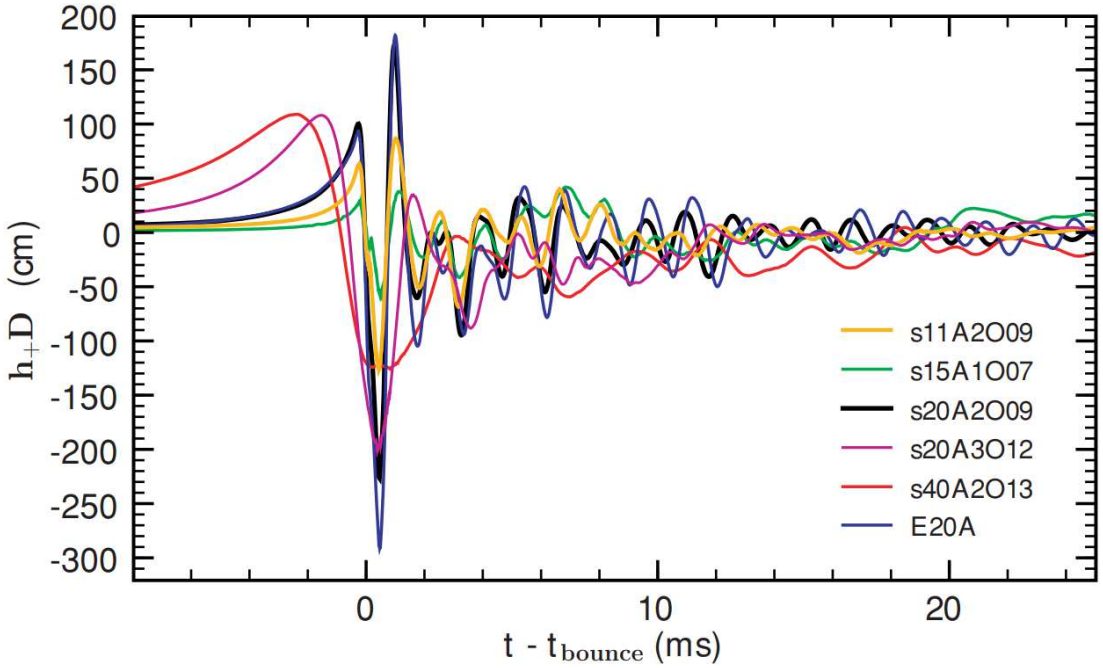

Figure 1.5: Some examples of GW templates (h_+D in units of cm, where D is the distance of the source) computed with a 2D GR model. All the waveforms exhibit one pronounced spike at core bounce and a subsequent ring down.

Short-duration bursts

There is a wide range of astrophysical sources that are expected to emit GW transients lasting from milliseconds up to seconds within the sensitivity band of Earth-based detectors. Differently from CBCs, most of these sources signals are poorly or even not modeled because of the complicated physical processes that occur.

Historically, the most famous expected source of short bursts are probably the core-collapse supernovae (CCSN). These were among the first considered sources since the beginning of GW searches, but they still miss the first detection. They are typically associated to supernovae (SN) of kind *Ib*, *Ic* and *II*, according to the current SN classification [20], but only *II* SNe are considered potential sources. Building models of stellar collapse and subsequent post-bounce evolution is an extremely complicated task, and requires highly detailed numerical modeling, as shown for instance in [21], Chapter 10. The numerical simulations should be three-dimensional and they should cover length-scales from a few meters (corresponding to typical turbulence scales) up to kilometers (corresponding to typical stellar core scales). Additionally, they must follow the system evolution for at least $1 - 2\,s$ with computational steps $\leq 10^{-6}s$, and the evolution should be studied using full GR. These requirements imply that modeling the stellar collapse in its full generality is an extremely hard task, probably still beyond the limits of present computing power. Nevertheless, in the last decade many progresses have been made and many classes of expected waveforms have been computed [22]. A general feature of the expected signals is a strong spike, corresponding to the core bounce, followed by a ring-down, like the ones shown in Figure 1.5.

The basic problem with GWs from CCSN is that only the fraction of the explosion

that violates the system axial symmetry produces a non-vanishing time-varying quadrupole moment and then GWs. Consequently, the emitted GW is weaker with respect to the one produced by CBCs and these signals are observable only for limited distances of the source. An event located in our Galaxy, at a distance of few kilo-parsecs, would be observable with present sensitivities, but SN explosions are extremely rare events, estimated to take place with a $\sim 1/100$ years rate. With the Advanced LIGO/Virgo design sensitivities, these explosions could be observed with a good Galactic coverage up to the nearby dwarf galaxies, like the Large Magellanic Cloud (which is about $\sim 50\,\mathrm{kpc}$ far away)[23].

Because of the difficulty of building a complete template bank, matched-filter-based searches are not the optimal solution. The search strategy adopted by the LIGO/Virgo collaboration is to perform agnostic searches with no assumption on the waveform. The main pipeline currently used is called Coherent Waveburst (cWB). Originally developed in [24] and strongly improved in [25], it coherently combines the data streams of all the detectors in a maximum-likelyhood statistics in the time-frequency wavelet domain. The searches performed during the first three observing runs of Advanced LIGO/Virgo did not find significant candidate signals different from CBCs, since cWB is also sensitive to them [26, 27, 23]. Thus, the null result of the search allows to set rate upper limits on the observable events. The most recent ones can be found in [23].

Periodic sources

The periodic sources are the subject of the present work. While the already discussed sources radiate a short duration signal - from a fraction of a second to several seconds at most - a periodic source emits a nearly monochromatic signal, often called continuous wave (CW). These signals typically last for periods much longer than the observing time of the detectors, so they are always present in the data. An intermediate case are the long-lasting transients, with typical duration that ranges from hours to days, even up to months. The most important source are rapidly spinning NSs, that are thought to emit GWs if they are deformed from the axial symmetry. There are also more exotic possible sources of CWs, like the boson condensates around spinning black holes. CW sources and search strategies will be treated detail in Chapter 2.

Stochastic background

The stochastic GW background has received growing interest in the last decade. As a stochastic process, a stochastic background can be seen as a superposition of plane waves, with frequencies covering a given range, which amplitudes are random variables. Therefore, this process cannot be described through an analytic waveform: instead, it is defined by its own spectral density, and the goal of the stochastic searches is to extract that spectrum from the noise. The stochastic background can originate from the superposition of many, unresolved astrophysical sources [28]. This background can reveal important information on the distribution of sources in the near and far universe and can be an-isotropic. A stochastic background can originate also from cosmological phenomena [29]. The detection of a cosmological GW background would have a strong impact on the cosmology research field. It would represent a probe on the earliest stages of the Universe at times around $t \sim 10^{-43}$s, much earlier than the decoupling of the Cosmic Microwave Background (which happened at $t \sim 3.8 \cdot 10^5$years [29]. The expected spectra of the cosmological GW background is strongly model-dependent, but generally they can be modeled as power laws $\sim f^{\alpha}$ with $\alpha \in [0, 3]$

and a cutoff at $\mathcal{O}$(GHz) frequencies. On the other side, stochastic backgrounds can also disturb the detection of other signals.

The search for stochastic background is typically based on cross-correlation between detectors data and folding over the sidereal day. A very efficient algorithm used in LIGO/Virgo searches is PyStoch [30]. As no detection have been made by now, upper limits can be put both on the astrophysical and the cosmological sources. The most recent results can be found in [31, 32, 33, 34].

1.2 Gravitational waves observation: LIGO and Virgo

In this section, I introduce the basic principles of GW detection, with particular reference on the actual implementation of the existing interferometers.

1.2.1 The effect of gravitational waves on matter

Describing the effect of a GW passing through a system of test masses is a task to be carried on carefully. The reason is that, despite GR is invariant under coordinate transformations, the way we describe the GWs and the detector depend on the reference frame chosen.

As stated in Section 1.1, GWs are typically described fixing the TT gauge, where their analytic form gets simplified. However, the reference frame that physically corresponds to the TT gauge is different from that one of an Earth-based detector frame. In a curved spacetime, the motion of a particle is governed by the geodesic equation,

$$\frac{d^2x^\alpha}{d\tau^2} + \Gamma^\alpha_{\mu\nu}(x)\frac{dx^\mu}{d\tau}\frac{dx^\nu}{d\tau} = 0 \tag{1.19}$$

and vectors evolve according to the equation of geodesic deviation,

$$\frac{D^2\xi^\alpha}{D\tau^2} = \mathrm{R}^\alpha_{\mu\nu\beta}\xi^\beta\frac{dx^\mu}{d\tau}\frac{dx^\nu}{d\tau} \tag{1.20}$$

where the symbol D denotes the covariant derivative. If we take a test mass at rest at $\tau = 0$, in the TT frame the surviving components of the affine connections are null, $\Gamma^i_{00} = 0$. So, in the TT frame, particles at rest before the GW arrival remain at rest even after its arrival (excluding $\mathcal{O}\left(h^2\right)$ contributions). This means that the coordinates of the TT frame stretch themselves in response to the arrival of the wave, in such a way that the position of free falling test masses initially at rest does not change.

As a consequence, to physically implement the TT frame we can use the free test masses themselves to mark the coordinates: these masses continue to mark the origin and the other reference points of the reference frame even when the GW is passing. This means that also the coordinate separation between the test masses remain constant and hence we cannot observe the effect of a passing GW just looking at the coordinates. However, this is not surprising since GR is invariant under coordinate transformations. In order to observe physical effects, we have to monitor proper distances or proper times, starting from the perturbed metric

$$ds^2 = -c^2dt^2 + \left(\delta_{ij} + h^{TT}_{ij}\right)dx^i dx^j \tag{1.21}$$

When a plane GW like the one described in Equation 1.7 with pulsation ω_{gw} is passing, taking the z axis coincident with propagation direction, the interval can be expressed as

$$ds^2 = -c^2dt^2 + (1 + h_+\cos\omega_{\mathrm{gw}}t)\,dx^2 + (1 - h_+\cos\omega_{\mathrm{gw}}t)\,dy^2 + (2h_\times\cos\omega_{\mathrm{gw}})\,dxdy + dz^2 \tag{1.22}$$

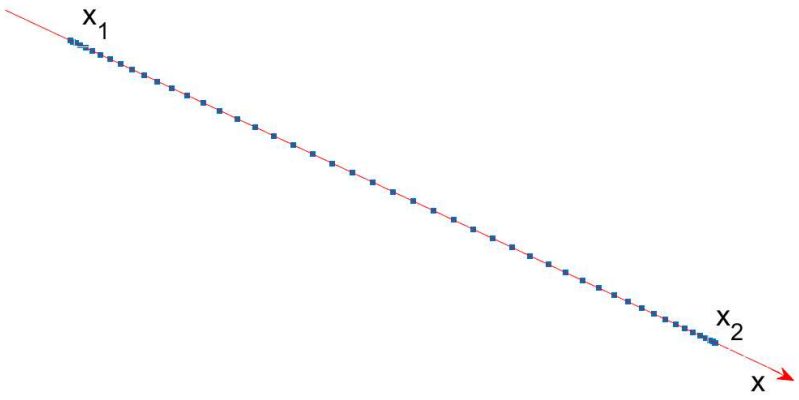

Figure 1.6: Representation of TT coordinates along one dimension when a GW is passing. The coordinates x_1, x_2 keep unchanged, but the intervals between the dots are stretched in response to the GW.

Let's take for instance a GW with just the '+' polarization and two events located on the x-axis at the same time, with coordinate separation $L = x_2 - x_1$. By integrating the 1.22 we get the proper distance

$$s = (x_2 - x_1)\sqrt{1 + h_+ \cos\omega_{\rm gw} t} = L\left(1 + \frac{1}{2}h_+ \cos\omega_{\rm gw} t\right) + \mathcal{O}\left(h^2\right) \tag{1.23}$$

Therefore in the TT gauge, even if the coordinate distance L remains constant, the proper distance between the two events oscillates as a consequence of the GW passing. More in general, if we consider a generic wave and two events with spatial separation $\vec{L}$, the proper distance is affected as

$$s = L + \frac{1}{2}h_{ij}\frac{L_i L_j}{L} + \mathcal{O}\left(h^2\right) \tag{1.24}$$

By separating the components of the proper distance, the above relation implies that, at linear order in h,

$$\ddot{s}_i \simeq \frac{1}{2}\ddot{h}_{ij} L_j \simeq \frac{1}{2}\ddot{h}_{ij} s_j \tag{1.25}$$

It is important to note that the perturbation of the proper distance between two points results to be proportional to the unperturbed distance. So, in the TT frame the effect of the GW is to perturb the proper distances between objects, making them oscillate with the same pulsation of the wave. If the test masses are two mirrors with a light beam traveling between them, the effect of a GW can be revealed measuring the round-trip time, since it is a measure of the proper distance.

Now consider the effect of the wave in the proper detector frame. This is the reference frame that is implicitly used by an experimenter to describe the apparatus. Differently from TT frame, positions are not marked by freely falling particles, but after choosing the origin, the coordinates are defined through rigid rules. The ideal configuration would be a laboratory inside a drag-free satellite, in order to have the whole apparatus in free fall in

the gravitational field of the Earth, plus that one of the GW. In a such ideal laboratory, the metric would be flat even in presence of a GW, up to the linear order in $\left|x^i\right|$:

$$ds^2 \simeq -c^2dt^2 + \delta_{ij}dx^idx^j \tag{1.26}$$

Expanding up to second order, we recover the effect of a passing GW, expressed in terms of the Riemann tensor

$$ds^2 \simeq -c^2dt^2\left[1 + \mathrm{R}_{0i0j}x^ix^j\right] - 2cdtdx^i\left(\frac{2}{3}\mathrm{R}_{0jik}x^jx^k\right) + dx^idx^j\left[\delta_{ij} - \frac{1}{3}\mathrm{R}_{ikjl}x^kx^l\right] \tag{1.27}$$

However, an Earth-based detector is not in free fall with respect to the Earth's gravitational field. It has an acceleration $\vec{a} = -\vec{g}$ with respect to a local inertial frame, and moreover it rotates wit angular velocity Ω with respect to local gyroscopes. To correctly express the metric of such frame, we need to make a coordinate transformation from the inertial frame to a accelerating and rotating frame. The result is given by [7]:

$$ds^2 \simeq -c^2dt^2\left[1 + \frac{2}{c^2}\vec{a}\cdot\vec{x} + \frac{1}{4}\left(\vec{a}\cdot\vec{x}\right)^2 - \frac{1}{c^2}\left(\vec{\Omega}\times\vec{x}\right)^2 + \mathrm{R}_{0i0j}x^ix^j\right] + \tag{1.28}$$

$$+2cdtdx^i\left[\frac{1}{c}\epsilon_{ijk}\Omega^jx^k - \frac{2}{3}\mathrm{R}_{0jik}x^jx^k\right] + dx^idx^j\left[\delta_{ij} - \frac{1}{3}\mathrm{R}_{ikjl}x^kx^l\right]$$

which is actually the metric of the *proper detector frame*. In this frame the evolution of the coordinates of test masses is described in terms of forces. The corresponding geodesic equation includes Newtonian forces like Newtonian gravity, Coriolis force, centrifugal forces, gravity gradients and so on (see [35] for the full expression). So, in principle the GW effect is overwhelmed by a large variety of effects that are many orders of magnitude stronger. However, all these Newtonian forces have typical variation time-scales larger than few seconds. This means that GWs with frequencies greater than a few Hertz see those forces as static and are not hidden. In other words, there is a frequency window where the metric can be described, as it was a freely falling, by the 1.27 rather than 1.28. By applying the equation of geodesic deviation 1.20 to the test masses coordinates, since the detector motion is non-relativistic we get

$$\frac{d^2\xi^i}{d\tau^2} = -\mathrm{R}^i_{0j0}\xi^j\left(\frac{dx^0}{d\tau}\right)^2 \tag{1.29}$$

Since the Riemann tensor is invariant, it can be computed in any frame. Therefore, it is convenient to compute it in the TT frame, where GWs get the simplest analytic form. The relevant components are

$$\mathrm{R}^i_{0j0} = -\frac{1}{2c^2}\ddot{h}^{TT}_{ij} \tag{1.30}$$

Since the Riemann tensor is $\mathcal{O}(h)$, we can limit the 1.29 to linear order in h, so that the proper time coincides with the coordinate time and the equation becomes

$$\ddot{\xi}^i = \frac{1}{2}\ddot{h}^{TT}_{ij}\xi^i \tag{1.31}$$

Equation 1.31 implies that in the proper detector frame the effect of a GW on the test masses can be described in terms of a Newtonian force

$$F_i = \frac{m}{2}\ddot{h}^{TT}_{ij}\xi^i \tag{1.32}$$

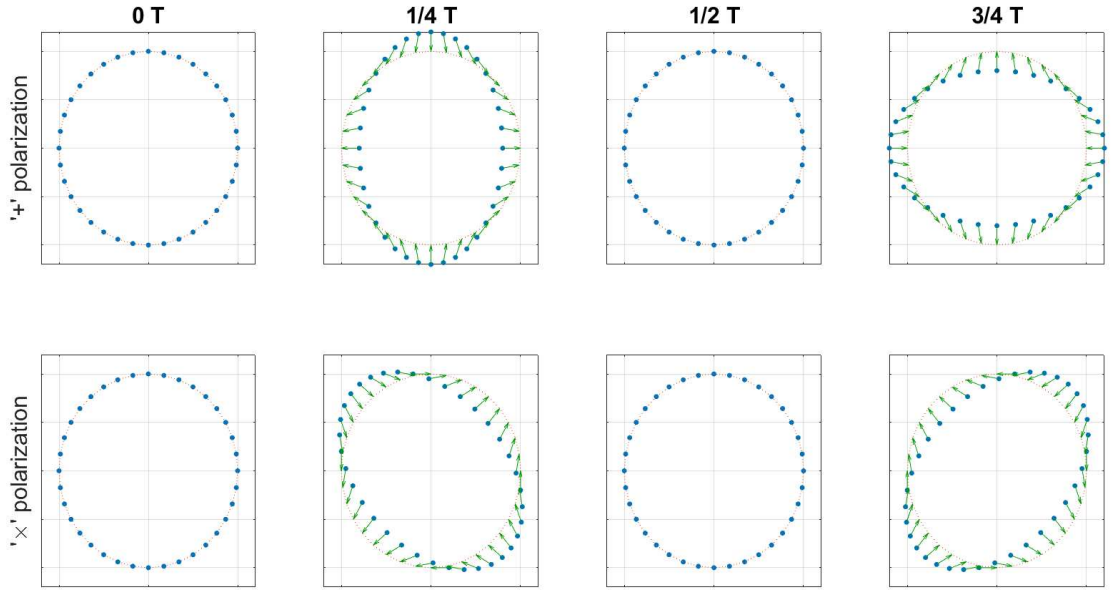

Figure 1.7: Representation of the effect of a GW on a ring of masses, seen at different fractions of the GW period. In the first row is shown the effect of a "+" polarized wave, in the second the effect of a "×" wave. The effect of the two polarizations is the same, but is rotated by 45 degrees.

Please note that in the TT frame the coordinates would remain constant, whereas the proper distences are stretched by the GW. In the proper detector frame, the metric is flat up to the linear order in $\left|x^i\right|$, so the proper distances are not affected. Instead, the coordinates of the test masses are perturbed as they experienced a sort of tidal force. The effect of the 1.31, 1.32 on a set of test masses is shown in the example in Figure 1.7, for a '+' and a '×' polarization respectively. During one single period, the GW deforms a ring of matter as an ellipse in two orthogonal directions. The effect is analogous both for the '+' and the '×' polarization, but they are rotated by 45 degrees one respect to the other.

The effects of a GW described in the TT frame by 1.25 and in the proper detector frame by 1.31 have the same mathematical form, but the equations apply on different objects. This is not surprising. In GR the physics must be invariant under coordinate transformations, but the description of both GWs and detector depends on the reference frame choice. So, it is not a problem to have different descriptions of the effect of a GW depending on the reference frame, but they must produce the same physical observable. This will be clear in the next Subsection, where the time travel of an electromagnetic wave will be used to measure the effect of the GW.

1.2.2 Broad-band interferometers: basic principles

In Section 1.2.1 it has been shown the effect of a GW on a set of test masses. If the test masses are mirrors and a light beam is traveling between them, the effect of a GW can be detected measuring variations of the round-trip time of the beam. The basic idea is to implement a Michelson interferometer. It was first used by Albert Abraham Michelson and Edward Morley to try to detect the Earth's motion through the supposed luminiferous

aether, and actually demonstrating its non-existence [36]. In its basic concept, shown in Figure 1.8, it consists in two mirrors and a 50% partially reflective mirror called beam splitter. A coherent laser source sends a laser beam at 45° on the beam splitter, so that it is divided in two beams traveling in orthogonal directions. The two mirrors are placed along the beam travel directions, orthogonal to them, at distances respectively L_x and L_y from the beam splitter. The two laser beams are reflected by the mirrors, so they come back and recombine at the beam splitter, and finally the resulting beam is read by a photo-diode.

TT frame

First, we describe the Michelson interferometer in the TT frame. The problem is that the mirrors of a ground-based detector are not freely falling, since they are suspended to compensate Earth's gravity. However, in the previous Subsection we have seen that the gravitational forces are static with respect to GWs with frequencies above few Hertz. Moreover, even if in the vertical direction the mirrors are bounded, if we restrict to the horizontal plane the masses follow the geodesics of the time-dependent part of the gravitational field, so they can be taken as freely falling. So, we can define the origin of the TT frame as the location of the beam splitter, marking it with $(0, 0)$ coordinates, and we can mark the positions of the mirrors at the end of the x and y arms respectively with coordinates $(L_x, 0)$ and $(0, L_y)$. As shown in Section 1.2.1, the metric of a flat spacetime perturbed by a GW is given by 1.21. Let's take for simplicity a GW with just the '+' polarization. Given that a light beam travels on a null geodesic, where $ds = 0$, the two laser beams exiting the beam splitter do propagate in the x and y directions with

$$\begin{cases} dx = \pm\, c\, dt \left[1 - \frac{1}{2} h_+ (t)\right] + \mathcal{O}\left(h^2\right) \\ \\ dy = \pm\, c\, dt \left[1 + \frac{1}{2} h_+ (t)\right] + \mathcal{O}\left(h^2\right) \end{cases} \tag{1.33}$$

where the plus and minus signs correspond to prograde and retrograde traveling respectively. The two laser beams travel back and forth in the cavities, getting reflected by the mirrors and then recombining at the beam splitter. Finally, the combined beams arrive at the photodiode at a measured time 't'. However, in principle the optical paths of the two beams are different because of arms with different lengths $L_x \neq L_y$ or as a consequence of a GW. So, this means that the beam observed at the photodiode at the time 't' is the result of two beams entered in the interferometer at different times $t_0^{(x)}$, $t_0^{(y)}$, given at linear order in h by:

$$\begin{cases} t_0^{(x)} = t - \frac{2L_x}{c} - \frac{L_x}{c} h_+ \left(t - \frac{L_x}{c}\right) \mathrm{sinc}\left(\frac{\omega_{\mathrm{gw}} L_x}{c}\right) \\ \\ t_0^{(y)} = t - \frac{2L_y}{c} + \frac{L_y}{c} h_+ \left(t - \frac{L_y}{c}\right) \mathrm{sinc}\left(\frac{\omega_{\mathrm{gw}} L_y}{c}\right) \end{cases} \tag{1.34}$$

It is important to note that the part involving the effect of the h_+ GW in 1.34 is scaled by a function $\mathrm{sinc}\,(x) = \sin x / x$ with argument $x = \omega_{\mathrm{gw}} L/c = 2\pi L/\lambda_{\mathrm{gw}}$. This means that the effect of the GW is maximum when $L \ll \lambda_{\mathrm{gw}}$, so the arms length must be much smaller than the GW wavelength.

The input laser beam can be expressed in the spatial component of the electric field as

$$E_0 e^{-i\omega_L t + i\vec{k}_L \cdot \vec{x}} \tag{1.35}$$

where ω_L is its pulsation and $k_L = \omega_L / c$ is its wavenumber. During the free propagation the phase is conserved, while reflections and transmissions give to the beams an overall factor

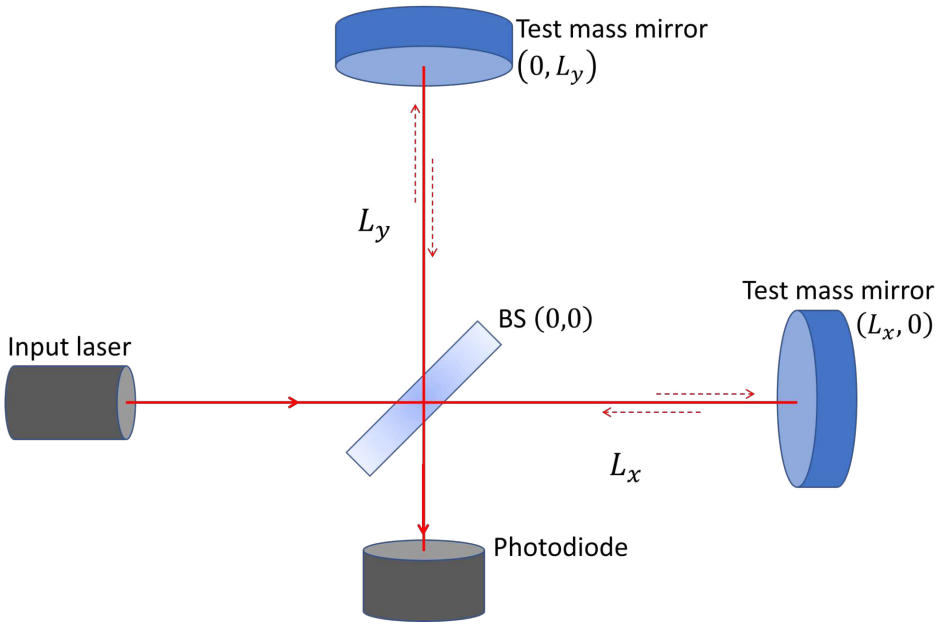

Figure 1.8: Basic scheme of a simple Michelson interferometer. The 50% beam splitter is put at 45 degrees with respect to the input laser direction. The laser beam is then divided into two orthogonal beams that travel onto a straight line until they are reflected back by the end mirrors. They finally recombine at the beam splitter and arrive at the photo-diode for the detection. In the TT frame description, the beam splitter marks the $(0, 0)$ coordinate and the two end mirrors mark the $(L_x, 0)$, $(0, L_y)$ coordinates, thus defining the x and y axes.

$\pm 1/2$. So, from the 1.34 different entering times determine a phase difference between the two beams when they recombine

$$\begin{cases} E^{(x)}(t) = -\frac{1}{2} E_0 e^{-i\omega_L t_0^{(x)}} = -\frac{1}{2} E_0 e^{-i\omega_L \left(t - \frac{2L}{c}\right) + i\phi_0 + i\Delta\phi_x(t)} \\ E^{(y)}(t) = +\frac{1}{2} E_0 e^{-i\omega_L t_0^{(y)}} = +\frac{1}{2} E_0 e^{-i\omega_L \left(t - \frac{2L}{c}\right) - i\phi_0 + i\Delta\phi_y(t)} \end{cases} \tag{1.36}$$

where L_x and L_y have been substituted with $L = (L_x + L_y)/2$ with an error $\mathcal{O}(h^2)$; the phase $\phi_0 = k_L (L_x - L_y)$ is a free parameter, tunable by adjusting the arms length; the phase shift induced by GWs in a single arm is

$$\Delta\phi_x = -\Delta\phi_y = k_L L\, h_+ \left(t - \frac{L}{c}\right) \mathrm{sinc}\left(\frac{\omega_{\mathrm{gw}} L}{c}\right) \tag{1.37}$$

So, the recombined beam is given by

$$E_{\mathrm{tot}} = E^{(x)}(t) + E^{(y)}(t) = -i\, E_0 e^{-i\omega_L \left(t - \frac{2L}{c}\right)} \sin\left[\phi_0 + \Delta\phi_x(t)\right] \tag{1.38}$$

and the power observed as output at the photodiode is

$$P_{\mathrm{out}} = \frac{P_0}{2} \left\{1 - \cos\left[2\phi_0 + \Delta\phi_{\mathrm{Mich}}(t)\right]\right\} \tag{1.39}$$

where $\Delta\phi_{\mathrm{Mich}}$ is the total phase difference on the Michelson interferometer

$$\Delta\phi_{\mathrm{Mich}} = \Delta\phi_x - \Delta\phi_y = 2\Delta\phi_x \tag{1.40}$$

By comparing the $\Delta\phi_{\text{Mich}}$ and ϕ_0 terms, in the limit $\omega_{\text{gw}}L/c \ll 1$ the effect of the GW on the phase shift is formally equivalent to a change in the arms length like

$$\frac{\Delta\left(L_x - L_y\right)}{L} \simeq h\left(t - \frac{L}{c}\right) \tag{1.41}$$

The direct effect of the GW on the laser is to generate side-bands. In fact, since $\Delta\phi_x$ is linear in h_0, the electric field in 1.36 can be expanded to linear order in h_0 as

$$E^{(x)}(t) = \frac{1}{2}E_0 e^{i\beta}\left[e^{-i\omega_L t} + \frac{i}{2}\left|\Delta\phi_x\right| e^{i\alpha}e^{-i(\omega_L-\omega_{\text{gw}})t} + \frac{i}{2}\left|\Delta\phi_x\right| e^{-i\alpha}e^{-i(\omega_L+\omega_{\text{gw}})t}\right] + \mathcal{O}\left(h^2\right) \tag{1.42}$$

where α, β are constant phases. So, while the original electromagnetic wave, called the carrier, has pulsation ω_L, the GW generates two additional waves, called side-bands, with pulsations $\omega_L \pm \omega_{\text{gw}}$ and amplitude $\mathcal{O}(h_0)$ with respect to the carrier.

Proper detector frame

In the proper detector frame, coordinates are measured by means of rigid rulers. The effet of a GW is a displacement of the masses coordinates following the 1.31, as effect of a GW force which expression is given by 1.32. The condition is that the linear dimension of the apparatus, which is the interferometer arm-length, is small compared to the GW wavelength, $L \ll \lambda_{\text{gw}}$. Until this condition is satisfied, in that region the space-time metric can be taken as flat up to linear order, with quadratic corrections given by 1.27. So, the basic assumption is that

$$\frac{\omega_{\text{gw}}L}{c} \ll 1 \tag{1.43}$$

Since the solution found in the TT frame is an exact function of $\omega_{\text{gw}}L/c$, the solution in the proper detector frame can be only an approximate one. Considering a GW with only the '+' polarization and the propagation along the 'x' arm, Equation 1.31 becomes

$$\ddot{\xi}_x = \frac{1}{2}\ddot{h}_+\xi_x \tag{1.44}$$

Therefore, the end mirror located at $(L_x, 0)$ keeps oscillating as

$$\xi_x(t) = L_x + \frac{1}{2}L_x h_0 \cos\omega_{\text{gw}}t \tag{1.45}$$

Considering at the lowest order a flat spacetime as in 1.26, a photon propagates following the trajectory $x(t) = c(t - t_0)$, so when it comes back to the beam splitter at the time 't' its entering time is given by

$$t_0^{(x)} = t - \frac{2L_x}{c} - \frac{L_x}{c}h_+\left(t - \frac{L_x}{c}\right) \tag{1.46}$$

This is the same result as the one in 1.34 except for the missing $\text{sinc}(\omega_{\text{gw}}L/c)$ function, which is substituted by its lower-order expansion $\text{sinc}(0) = 1$. Considering also the next term in the approximation, the photon propagates in a curved spacetime which metric is 1.27 and along the x direction reduces to

$$ds^2 = -c^2dt^2\left(1 + \text{R}_{0101}x^2\right) + dx^2$$

where the Riemann tensor can be computed using the the TT gauge expression

$$\mathrm{R}_{0101} = -\frac{1}{2c^2}\ddot{h}_+ = \frac{1}{2c^2}\omega_{\mathrm{gw}}^2 h_0 \cos\omega_{\mathrm{gw}} t \tag{1.47}$$

Therefore, the photon propagates on the background with motion

$$x\left(t\right) \simeq c\left(t - t_0\right) + \frac{c}{12}\omega_{\mathrm{gw}}^2 \left(t - t_0\right)^3 h_0 \cos\omega_{\mathrm{gw}} t_0 \tag{1.48}$$

and when it comes to the beam splitter, its entering time is corrected from the previous value 1.46 to the more accurate value

$$t_0^{(x)} = t - \frac{2L_x}{c} - \frac{L_x}{c} h_+ \left(t - \frac{L_x}{c}\right)\left[1 - \frac{1}{6}\left(\frac{\omega_{\mathrm{gw}} L_x}{c}\right)^2\right] \tag{1.49}$$

The expression inside the last bracket represents the first two terms of the 'sinc' function

$$\mathrm{sinc}\left(x\right) = \frac{\sin x}{x} = 1 - \frac{1}{6}x^2 + \mathcal{O}\left(x^4\right) \tag{1.50}$$

So, the calculation in the proper detector frame reproduces the results obtained within the TT frame restricting to the leading and next-to-leading terms in $\omega_{\mathrm{gw}} L/c$. We can conclude that even if the proper detector frame description is more intuitive, in the TT frame we can get the exact solution of the interaction between the GW and the detector.

Fabry-Perot cavities

Since the observed quantity is the total output power at the end of the interferometer and the information on the GW is encoded in the phase $\Delta\phi_{\mathrm{Mich}}$, we want to maximize it. From 1.40 and 1.37 we see that $\Delta\phi_{\mathrm{Mich}} \propto \left(\omega_L/\omega_{\mathrm{gw}}\right)\sin\left(\omega_{\mathrm{gw}} L/c\right)$, so the maxima is reached at $\omega_{\mathrm{gw}} L/c = \pi/2$, which implies an optimal value of the arms length

$$L \simeq 750\mathrm{km}\left(\frac{100\mathrm{Hz}}{f_{\mathrm{gw}}}\right) \tag{1.51}$$

For such values, the time shift induced by the GW on the beam maintain the same sign and sums coherently. For larger values, during the beam propagation the GW inverts its sign and then cancels the accumulated phase. This is a strong limitation, since it is impossible to build arms of hundreds of kilometers. Therefore there is the need to fold this optimal optical path of the laser several times in order to obtain the same result in a manageable size. The solution adopted in present Virgo and LIGO interferometers is to transform each arm into a Fabry-Perot cavity. A Fabry-Perot cavity consists in two parallel mirrors. The mirrors have a high-reflecting coating on the interior of the cavity, and their reflection and transmission coefficients r_i, t_i are such that $r_i^2 + t_i^2 = 1 - p_i$, being p_i the mirror losses and $i = 1, 2$ the index to mark 1st and 2nd mirror. An incoming electric field is partially reflected and transmitted by the first mirror; the transmitted field propagates to the second mirror, where it is partially reflected and transmitted, and so on. At the end the total field reflected by the cavity, as well as the interior and the transmitted fields, are given by the superposition of many beams, resulting from multiple bounces. In particular, the reflected field that goes back to the beam splitter is

$$E_{\mathrm{ref}} = E_0\, e^{-i\omega_L t_0} \frac{r_1 - r_2\left(1 - p_1\right) e^{i2k_L L}}{1 - r_1 r_2 e^{i2k_L L}} \tag{1.52}$$

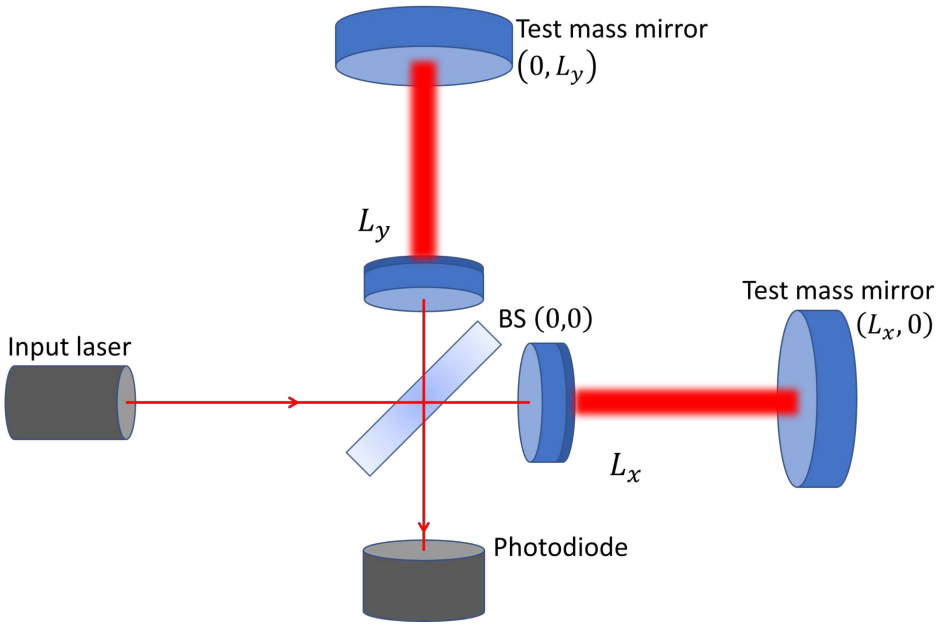

Figure 1.9: Variation of the basic scheme described in Figure 1.8. Two additional mirrors (called input mirrors) are inserted with an highly reflective substrate pointing towards the end mirrors. In this way, in each arm the input and end mirrors form a Fabry-Perot cavity.

and also the fields inside the cavity and the transmitted have the same denominator. When the condition $2k_L L = 2\pi n$ is satisfied, the various beams interfere constructively and since the denominator becomes $(1 - r_1 r_2)$ with $r_1, r_2 \sim 1$, the total field raises to very large values. In this configuration the cavity is said to be in *resonance*. The power circulating is therefore related to the cavity length as

$$P \propto |E|^2 \propto f\left(2k_L L\right) = \frac{1}{1 + \left(r_1 r_2\right)^2 - 2 r_1 r_2 \cos 2k_L L} \tag{1.53}$$

This dependence is shown in 1.10. The more the reflectivity of the mirrors is close to one, the thinner are the resonance peaks and the more difficult is to put the cavity in resonance. By defining the free spectral range $\Delta\omega_L$ as the distance between tha maxima in terms of the beam pulsation,

$$\Delta\omega_L = \frac{\pi c}{L} \tag{1.54}$$

and the peaks width at half maximum as

$$\delta\omega_L = \frac{c}{L} \frac{1 - r_1 r_2}{\sqrt{r_1 r_2}} \tag{1.55}$$

the *finesse* $\mathcal{F}$ of the cavity is defined as the ratio betweem the free spectral range and the peaks width at half maximum

$$\mathcal{F} = \frac{\Delta\omega_L}{\delta\omega_L} = \frac{\pi\sqrt{r_1 r_2}}{1 - r_1 r_2} \tag{1.56}$$

The finesse of the cavity has a strong impact since it directly influences the storage time of the cavity τ_s, which is defined as the average time spent inside by a single photon and in

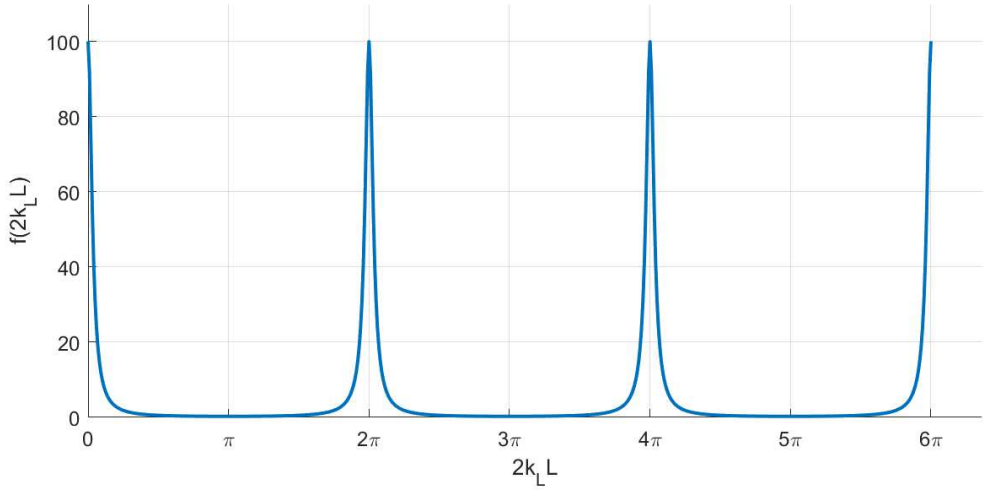

Figure 1.10: Plot of the function $f\left(2k_L L\right)$ defined in the 1.53, which shapes the circulating power, as function of $2k_L L$. In the plot the value $r_1 r_2 = 0.9$ has been used.

the high-finesse limit, is given by

$$\tau_s \simeq \frac{2L}{c}\frac{\mathcal{F}}{2\pi} \tag{1.57}$$

So, the average time spent by a photon inside the cavity is enhanced by a factor $\mathcal{F}/2\pi$ with respect to the time spent in a simple Michelson arm , which is $2L/c$. By looking at the electrical field, the reflected field in 1.52 can be written in the form $E_{\text{ref}} = |E_{\text{ref}}|\, e^{-i\omega_L t + i\phi}$ where the phase is given by

$$\phi = \pi + \arctan\left[-\frac{r_2\left(1-p_1\right)\sin\left(2k_L L\right)}{r_1 - r_2\left(1-p_1\right)\cos\left(2k_L L\right)}\right] - \arctan\left[-\frac{r_1 r_2 \sin\left(2k_L L\right)}{1 - r_1 r_2 \cos\left(2k_L L\right)}\right] \tag{1.58}$$

A plot of the phase ϕ as function of $2k_L L$ is shown in Figure 1.11. It is important to note that when the cavity is far from resonance the phase of the electrical field is insensitive to changes in L. On the other side, when the cavity is locked to resonance the phase is strongly sensitive to a length change. Defining the phase distance from a resonance $\varepsilon = 2k_L L - 2\pi n$, in the limit $\varepsilon \ll 1$ the phase sensitivity to a length change is

$$\frac{\partial\phi}{\partial\varepsilon} \simeq \frac{2\mathcal{F}}{\pi} \tag{1.59}$$

Since for a simple Michelson arm $\phi = \varepsilon$, by comparison we find that the sensitivity of a Fabry-Perot cavity to changes in $2k_L L$ is enhanced by a factor $2\mathcal{F}/\pi$. A similar result can be obtained for the full interferometer. By repeating the calculations done for the simple Michelson scheme, we can express the total phase shift in a Michelson + Fabry-Perot interferometer in the form $\Delta\phi_{\text{FP}}\left(t\right) = |\Delta\phi_{\text{FP}}|\cos\omega_{\text{gw}} t$, with

$$|\Delta\phi_{\text{FP}}| \simeq h_0 \frac{4\mathcal{F}}{\pi} k_L L \frac{1}{\sqrt{1 + \left(f_{\text{gw}}/f_p\right)^2}} \tag{1.60}$$

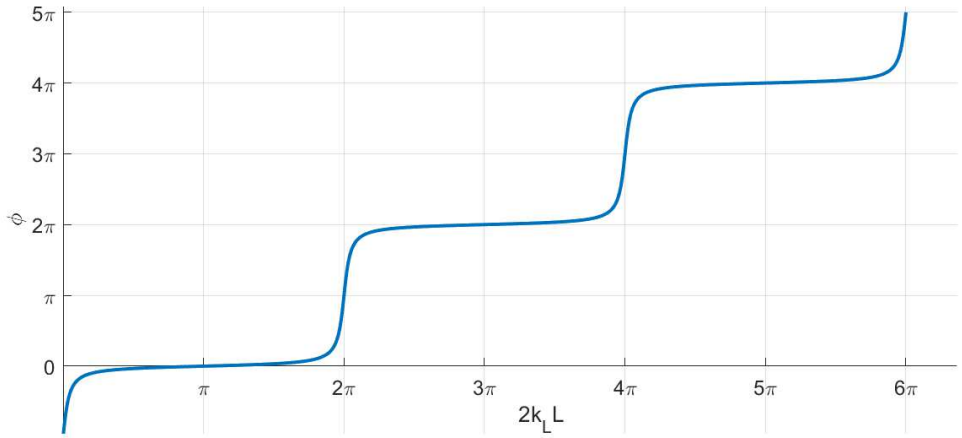

Figure 1.11: Plot of the phase ϕ of the reflected field defined in 1.58 as function of $2k_L L$. For this plot the values $r_1 = 0.9$, $r_2 = 0$ and $p_1 = 0$ have been used. The arctan function output has been unwrapped to better show the behavior. It is important to note that the derivative of ϕ is significantly non-vanishing only around the $2n\pi$ resonances. Away from them, the phase is insensitive to changes in the arms length.

having defined the *pole frequency* as $f_p = 1/(4\pi\tau_s)$ and in the limit where $\omega_{\rm gw} L/c \ll 1$. Within this limit, the ratio between the phase shifts in magnitude is

$$\frac{|\Delta\phi_{\rm FP}|}{|\Delta\phi_{\rm Mich}|} \simeq \frac{2\mathcal{F}}{\pi} \frac{1}{\sqrt{1+(f_{\rm gw}/f_p)^2}} \tag{1.61}$$

Thanks to the implementation of Fabry-Perot cavities, it is possible to achieve the optimal sensitivity required by 1.51, but with an actual arm length of $3-4$ km.

Detector pattern functions

The whole calculation done in this Section can be generalized to GWs with both the polarization components and coming from an arbitrary direction. Since the motion of the mirrors is governed in a more general way, in the limit $\omega_{\rm gw} L/c \ll 1$ by the geodesic equation

$$\begin{aligned} \ddot{\xi}_x &= \tfrac{1}{2}\ddot{h}_{xx} L \\ \ddot{\xi}_y &= \tfrac{1}{2}\ddot{h}_{yy} L \end{aligned} \tag{1.62}$$

This means that the relative phase shift between the two arms is driven by the factor $\frac{1}{2}(\ddot{h}_{xx} - \ddot{h}_{yy})$, so the h_+ used in this Section should be replaced by $\frac{1}{2}(h_{xx} - h_{yy})$. The reference frame of the GW is marked with (x', y', z') so that the z' axis coincides with the propagation direction. On the other side, the proper detector frame is (x, y, z) with x, y coincident with the detector arms and the z axis orthogonal ti the detector plane, oriented outside the Earth's surface. The GW propagates with direction $\hat{n} = (\theta, \varphi)$ with respect to

the z axis in the detector frame, so the GW tensor h'_{ij} in the TT frame

$$h'_{ij} = \begin{pmatrix} h_+ & h_\times & 0 \\ h_\times & -h_+ & 0 \\ 0 & 0 & 0 \end{pmatrix}_{ij} \tag{1.63}$$

must be rotated to get the tensor expression in the detector frame, $h_{ij} = \mathcal{R}_{ik}\mathcal{R}_{jl}h'_{kl}$, with the rotation matrix $\mathcal{R}$ given by the composition

$$\mathcal{R} = \begin{pmatrix} \cos\phi & \sin\phi & 0 \\ -\sin\phi & \cos\phi & 0 \\ 0 & 0 & 1 \end{pmatrix} \begin{pmatrix} \cos\theta & 0 & \sin\theta \\ 0 & 1 & 0 \\ -\sin\theta & 0 & \cos\theta \end{pmatrix} \tag{1.64}$$

As a result, the GW enters the detector through a combination of the + and × polarizations

$$h(t) = F_+(\theta,\varphi)\, h_+(t) + F_\times(\theta,\varphi)\, h_\times(t) \tag{1.65}$$

where the components are weighted by the *detector pattern functions* $F_+, F_\times$ defined as

$$\begin{aligned} F_+(\theta,\varphi) &= \tfrac{1}{2}\left(1+\cos^2\theta\right)\cos 2\varphi \\ F_\times(\theta,\varphi) &= \cos\theta \sin 2\varphi \end{aligned} \tag{1.66}$$

It is clear therefore that an interferometer has some optimal observing directions and, above all, some blind directions. It is insensitive to '+' polarized GWs propagating in the plane defined by $\varphi = \pi/4; 3\pi/4$, while it is insensitive to '×' GWs from $\theta = \pm\pi/2$ or $\varphi = 0; \pi/2; \pi; 3\pi/2$. This also means that there are four directions where the detector is completely blind. The result found in 1.65 and 1.66 can be taken as general, since the travel time is negligibly affected by the GW direction.

1.2.3 Real interferometers: LIGO and Virgo

In Section 1.2.2 the GW detection theory has been introduced. However, the practical realization of the descibed interferometers introduces a huge number of practical issues. Here, I discuss some important modifications and additions that are needed in order to get a real working interferometer, introducing the Virgo [37] and LIGO [38] detectors. The Virgo detector is located near the city of Pisa, Italy. Its construction started in 1996 after project approval by the French National Centre for Scientific Research (CNRS) and the Italian Istituto Nazionale di Fisica Nucleare (INFN). Its construction was completed in June 2003 and it have been recording data from 2007 to 2011 during four scientific runs. LIGO have two detectors in the United States, located in Hanford, Washington and in Livingston, Louisiana. Their construction started in 1994 and 1995 respectively, and they have been recording data from 2002 to 2010, in five scientific runs. Both the experiments implement the basic setup described in Section 1.2.2. The two LIGO detectors have Fabry-Perot cavities 4 km long, whereas the Virgo detector cavities are 3 km long. In addition to the basic outline, there are several modifications to apply as well as extra components to add:

- **Diffraction and spherical mirrors.** When considering the transverse extension of the beam and the finite-size of the mirrors, there is the problem of the diffraction.

For interferometers like Virgo and LIGO, with typical laser wavelength $\lambda_L \simeq 1\mu m$, arm length $L = 3 - 4$km and a beam transverse width of few centimeters, the beam is in the regime of Fraunhofer diffraction. A beam with initial width $1 - 2$cm would broaden strongly even after the first one-way trip in the cavity. Therefore Fabry-perot cavities, where the beam perform $\mathcal{O}(100)$ bounces, cannot be done with flat mirrors. From the laser side, the optimal choice consists in generating beams with a Gaussian profile, since they saturate the uncertainty principle and so have the minimum possible spreading. Since the wavefronts of a Gaussian beam can be considered spherical with great approximation, the mirrors are spherically shaped so that their surfaces match the constant-phase surfaces of the beam. In this way, once reflected, the beam is focused back, converges and re-expands going towards the other mirror, and so on. The typical dimensions of Virgo and LIGO mirrors are about $\mathcal{O}(10)$ cm.

- **Mode-cleaner.** As stated above, there is the need to have a laser beam with Gaussian profile. However, in general a laser beam can get higher order modes from the emission and propagation, that are typically called *Hermite-Gauss modes* and are denoted as TEM_{mn}. The Gaussian profile is the fundamental mode, denoted as TEM_{00}. The laser emits a beam that is predominantly Gaussian, but with a contamination $< 10\%$ from higher modes, mostly TEM_{01} and TEM_{10}. These modes are not resonant, resulting in just additional noise, so they have to be ruled out before the laser enters the beam splitter. In order to eliminate these modes, the input laser is sent into a *mode-cleaner*. This consists in a triangular shaped Fabry-Perot cavity with very high finesse, operated in transmission. Its length is tuned so that only the $(0, 0)$ is resonant, so it is the only mode that is efficiently transmitted. In the same way, during the propagation inside the interferometer the beam can get further higher modes because of mirrors imperfections or misalignments, so an *output mode-cleaner* is placed after the beam splitter and before the detection system.

- **Phase modulation for dark fringe detection.** The final step consists in the extraction of the GW phase shift from the output. From 1.39 we see that the output is given by the total power $P(\phi) = P_0 \sin^2 \phi$, where the phase $\phi = \phi_0 + \Delta\phi_{\text{gw}}(t)$ is the sum of the phase shift $\Delta\phi_{\text{gw}}$ induced by the GW and of a phase ϕ_0 that can by adjusted by the experimenter changing the position of the mirrors. It is clear that the maximum derivative $\partial P/\partial\phi$, where the power should be more sensitive to a phase shift due to a GW, is reached at $\phi_0 = \pi/4$. However, at this configuration the power of the laser is $P_0/2$ and therefore is subject to fluctuations that are many orders of magnitude bigger than the searched $\Delta\phi_{\text{gw}}$. Given the small effect, there is the need to have a *null instrument*, with output zero when the signal is absent, so that it is not overwhelmed by calibration uncertainties. Such configuration, called *dark fringe*, is reached at $\phi_0 = 0$. However, in this configuration we have $P = 0$ but also $\partial P/\partial\phi = 0$, and since $\Delta\phi_{\text{gw}} = \mathcal{O}(h)$, the effect of a GW on the output power would be $\Delta P = \mathcal{O}\left(h^2\right)$, so practically undetectable since typical GW amplitude is $h < 10^{-21}$. The solution consists in the application of a time-varying phase modulation to the input beam. In practice, the beam passes through a Pockels cell before entering the beam-splitter. The Pockels cell is a crystal with an index of refraction that depends on an applied electric field. The external field oscillates with a pulsation Ω_{mod}, so the index of refraction oscillates with the same pulsation, and the beam itself acquires a time-vaying phase. The effect at first order is to generate sidebands with pulsation

$\omega_\pm = \omega_L \pm \Omega_{\rm mod}$. When the arms have the same length, $\Delta L = 0$, both the carrier and the sidebands are in dark fringe. However, the arms can be set to differ for a multiple of the laser wavelength, $\Delta L = n\lambda_L$, which is called *Schnupp asymmetry*. The difference in length is on the distance between the beam splitter and the first mirrors of the two Fabry-Perot cavities, while the cavities themselves have the same length. With this choice, the carrier is still on dark fringe, while the sidebands are no longer in dark fringe. Moreover, $\Omega_{\rm mod}$ is chosen so that inside the cavity only the carrier is resonant, while the sidebands are not. When a GW arrives, the field of the carrier is shifted from the value $(E_{out})_c = 0$ to a value $(E_{out})_c \propto (2\mathcal{F}/\pi)\, Lh\,(t)$. The sidebands, instead, are shifted from their $\prime\,(1)$ value, proportional to $\cos(\Omega_{\rm mod}t - \alpha)$, into two terms $\mathcal{O}(1) + \mathcal{O}(h)$. Looking at the output power, which is proportional to $|(E_{out})_{tot}|^2$, the components of the carrier and the sidebands interfere together. The squared fields give an irrelevant $\mathcal{O}\left(h^2\right)$ for the carrier and a DC term that oscillates at $2\Omega_{\rm mod}$ for the sidebands. The mixed term, i.e. the beatings between the carrier and the sidebands, is

$$\propto P_0 \frac{2\mathcal{F}}{\pi} h\,(t) \cos(\Omega_{\rm mod}t - \alpha)$$

So, finally at the output we have a term linear in $h\,(t)$ even if the carrier is on dark fringe, that can be extracted using a mixer, and is insensitive to the power fluctuations of the carrier.

- **Power recycling mirror.** Since the detector working point is the dark fringe of the carrier, when no GW is passing no light goes out from the beam splitter at the carrier frequency. In this situation, the full interferometer acts like a mirror, so all the light finally goes back to the laser and is wasted. Since to minimize high-frequency read-out quantum noise there is the need to keep the circulating power as high as possible (see Section 1.2.4), the attempt is to recycle the power that comes back from the beam splitter towards the laser source. The solution is to place a mirror between the beam splitter and the laser, called *power recycling mirror*, that reflects back the light. This mirror, together with the interferometer seen as an "equivalent mirror", forms a new Fabry-Perot cavity. By tuning it in order to be resonant for the input laser light, a gain of $\mathcal{O}(100)$ can be obtained on the circulating power. Since continuous laser is produced at $\mathcal{O}(10 - 100)$ W, in initial Virgo/LIGO configuration the power circulating between the power recycling and the beam splitter raises to $\sim$ 1kW, and up to $\sim$ 15kW in the interferometer cavities.

Considering all the introduced elements, the optical layout of the detector is represented in Figure 1.12. In initial Virgo, the laser is emitted with $\lambda_L = 1.064\mu$m as a continuous Nd:Yag, with power $\leq$ 20W. Then, it passes through the Pockels cell where it gets sidebands at $\Omega_{\rm mod}/2\pi = 6.2$MHz. Both the carrier and the sidebands enter the input mode-cleaner, coming out as a nearly pure TEM_{00} mode. It is transmitted through the power-recycling mirror, which has the high-reflective substrate ($\simeq 0.95$) on the interferometer side, and is divided by the beam splitter. The interferometer arms realize the Schnupp asymmetry with the input mirrors of the cavities respectively at $l_x \simeq 6.4$m and $l_y \simeq 5.5$m from the beam splitter, whereas the cavities are 3 km long and with a finesse $\mathcal{F} = 50$. The input mirrors are plane, with $r \simeq 0.88$, and the end mirrors have a radius of curvature $R_c = 3500\,$m and $r = 0.99995$. Since the working point is in dark fringe, the carrier is finally reflected back to the power-recycling mirror and then sent back to the interferometer. When a GW displaces the carrier from the dark fringe, the beating between the carrier and the sidebands

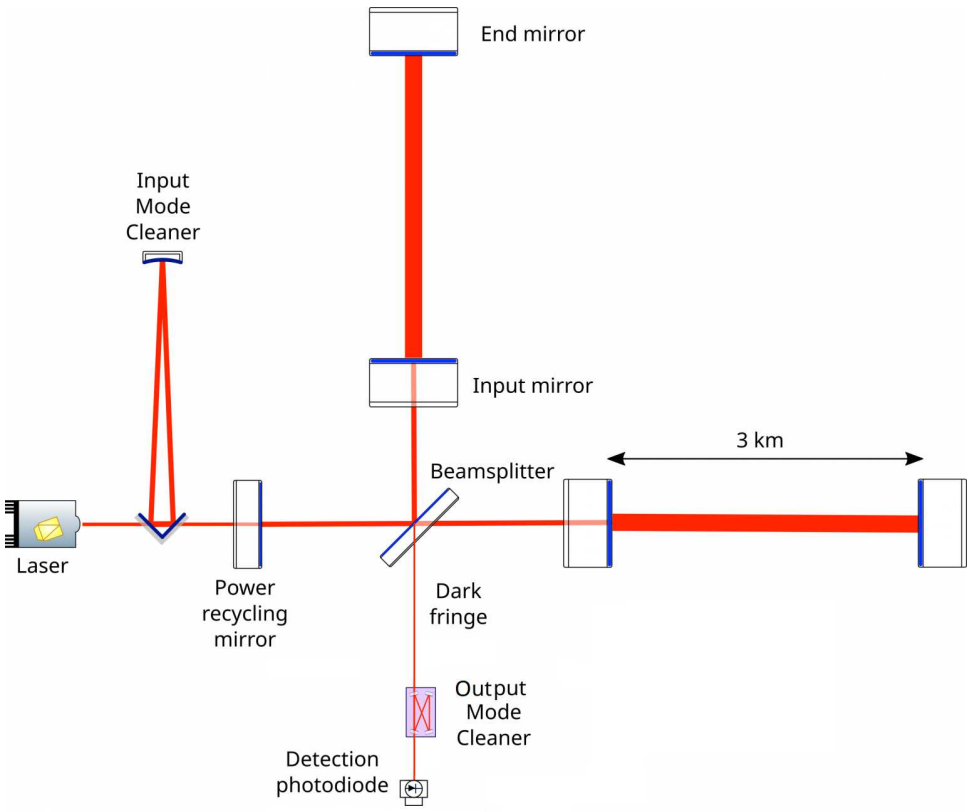

Figure 1.12: Basic optical layout of initial Virgo. The input laser passes in the input mode-cleaner (a triangular-shaped Fabry-Perot cavity) and then then enters the interferometer passing through the low-reflective side of the power-recycling mirror, which creates a further cavity with the interferometer. The beam at the output of the beam-splitter passes through the output mode-cleaner before arriving at the photodetectors.

is transmitted through the output mode-cleaner and finally to the detection system, where it is demodulated and recorded. The two LIGO detectors have a very similar scheme, with some differences. For instance, the cavities are 4 km long, with the input mirrors that are spherical and an overall finesse $\mathcal{F} = 200$.

The raw output of the detector is dominated by the control loops used to control the interferometer. In order to keep the Fabry-Perot cavities in resonance as well as the power-recycling mirror and to be on dark fringe within a small fraction of wavelength, the relative position of the mirrors must be kept fixed within a precision

$$\delta L \sim \left(10^{-12} - 10^{-10}\right) \mathrm{m} \tag{1.67}$$

Such a precision is achievable because of the transverse size of the laser beam, which is of few centimeters. Even if the length scale of the atoms is 10^{-10}m, the laser senses the position of the mirrors averaged over a macroscopic scale, which actually cancels the individual atomic fluctuations. Moreover, there is no need to know in which of the $2k_L L = 2\pi n$ resonances the cavity is, but only if it is on a resonance: we only need to keep the cavity resonant within $\delta L \sim 10^{-4}\lambda_L$. To lock the cavity on one of its resonances the strategy is to use control loop systems. These systems are composed by a sensor, which measures the desired quantity and produces an error signal, and an actuator, which provides a feedback based

on the error signal in order to keep the measured quantity closer to the chosen one. So, the detector output is dominated by the control loops noise in the range $10\text{Hz} - 100\text{Hz}$. In order to reconstruct the calibrated $h(t)$ series, there is need to account for the readout electronics, subtract the control noises and calibrate the optical gain of each mirror, as it is explained in [40].

1.2.4 Noise budget and sensitivity curves

With the described structure of the detector, it is possible to estimate the noises affecting the instrument and consequently the sensitivity that is possible to achieve. As a typical reference, the detector should be sensitive to GWs produced by a burst occurring in the Virgo cluster, or by a CBC at $\mathcal{O}(\text{Mpc})$ distances, with typical amplitude $h_0 \sim 10^{-21}$. When the wave arrives to interferometers like Virgo or LIGO, with arms length $L = 3 - 4\text{km}$, produces a coherent displacement of the mirrors by

$$\Delta L \sim (1-2)\, 10^{-18}\text{m} \tag{1.68}$$

Considering a laser with wavelength $\lambda_L \sim 1\mu\text{m}$ and Fabry-Perot cavities with finesse $\mathcal{F} = \mathcal{O}(100)$, the mirrors displacement corresponds to a phase shift on the output beam

$$\Delta\phi_{FP} \sim 10^{-8}\text{rad} \tag{1.69}$$

So, this effect has to compete with other effects produced by different noise sources that superpose. The noises affecting an interferometer can be classified in two categories: the optical read-out noise and the displacement noise.

Optical read-out noise

The optical read-out noise is related to the quantum nature of the light. Quantum mechanics places limits on the accuracy of any measurement of the position of a free mass. If the position of the mirror is measured with high precision, its momentum is perturbed and subsequently it produces uncertainties in position. Even if this effect is typically relevant on microscopic scales, given the required sensitivity it affects also the determination of the position of a macroscopic-scale object like a mirror. The electromagnetic field inside the interferometer is perturbed by vacuum zero-point fluctuations in phase and amplitude that enter from the output port. These fluctuations produce two opposite effects that intrinsically limit the sensitivity of an interferometer at high and low frequencies: the shot noise and the radiation pressure [41].

- Shot noise. The shot noise, also known as granular noise, originates from the fact that light is made by discrete quanta, the photons. Since the observed quantity is the output power at the photodiode, if the number of photons that arrive in an observing time T_{obs} is N_γ, the average power measured is

$$P = \frac{N_\gamma}{T_{\text{obs}}}\hbar\omega_L \tag{1.70}$$

Measuring the average power is actually a counting operation. Therefore, the outcome follows the Poisson distribution and for large N_γ the fluctuation in the number of photons is given by

$$\Delta N_\gamma = \sqrt{N_\gamma} \tag{1.71}$$

The direct effect is a fluctuation in the observed power, which is due to the discrete nature of light, given by

$$\Delta P|_{\text{shot}} = \sqrt{\frac{\hbar\omega_L}{T_{\text{obs}}}P} \tag{1.72}$$

This effect competes against the power variation due to a GW, which is given by

$$\Delta P|_{\text{gw}} = \frac{P_0}{2}\left|\sin 2\phi_0\right|\left|\Delta\phi_{\text{FP}}\right| \tag{1.73}$$

By evaluating the signal-to-noise ratio of the power variation due to a GW with respect to the one due to the shot noise, we get the strain sensitivity $S_n^{1/2}(f)$ due to the shot noise

$$S_n^{1/2}(f)\Big|_{\text{shot}} = \frac{1}{8\mathcal{F}L}\sqrt{\frac{4\pi\hbar\lambda_L c}{\eta P_{\text{bs}}}}\sqrt{1+(f/f_p)^2} \tag{1.74}$$

where $P_{\text{bs}} = CP_0$ is the power on the beam splitter after recycling (with $C \sim 50-100$) and η is the efficiency of the photodetector, which reduces the power used to extract electrons. It is worth to note that typically the shot noise is flat, independent on the frequency. In our case instead the strain is flat up to the pole frequency f_p, and then increases linearly with the frequency. This is because the transfer function of a Fabry-Perot interferometer degrades linearly with the frequency when it is greater than f_p.

- Radiation pressure. The radiation pressure arises from the fact that a photon, once reflected by a mirror, exerts a pressure on the mirror itself. Given a photon with energy E_γ and momentum $|\vec{p}| = E_\gamma c$, at reflection it transfers a momentum $2|\vec{p}|$. So, a beam of power P exerts on the mirror a mean force $F = 2P/c$. Using the 1.72, the root mean square fluctuations of that force during T_{obs} is given by

$$\Delta F = \frac{2\Delta P}{c} = 2\sqrt{\frac{\hbar\omega_L P}{c^2 T_{\text{obs}}}} \tag{1.75}$$

This acts like a stochastic force with spectral density flat with respect to the frequency. The effect on a single mirror is a displacement with spectral density

$$S_x^{1/2}(f) = \frac{2}{M(2\pi f)^2}\sqrt{\frac{2\hbar\omega_L P}{c^2}} \tag{1.76}$$

Inside an interferometer, the beam splitter scatters randomly and independently each photon into one of the two arms. As a result, the number of photons in each arm follow the Poisson distribution, and these distributions are *anti-correlated*, producing a "$\sqrt{N}$" force. This effect is an intrinsic property of an interferometer and has nothing to do with fluctuations in input laser power [42]. When the cavities are resonant, the power circulating inside is

$$P_{\text{cav}} \simeq P_{\text{bs}}\frac{2\mathcal{F}}{\pi} \tag{1.77}$$

and therefore the fluctuations in ΔP_{bs} are magnified by a factor $2\mathcal{F}/\pi$. As consequence of the mirrors vibration, the cavity is displaced from the resonance, with a reduction in the

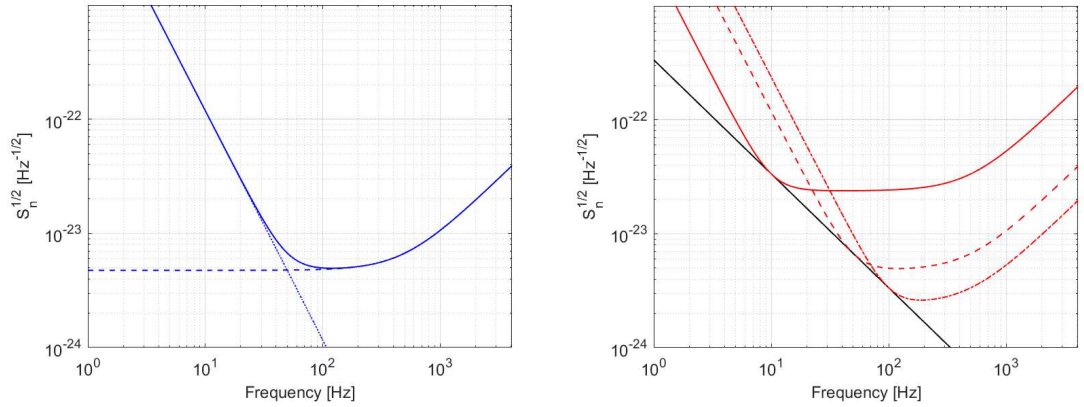

Figure 1.13: Left plot: the strain sensitivity due to shot noise (dashed blue line) and radiation pressure (dotted blue line) and the total optical read-out quantum noise (solid blue line). Right plot: different curves (solid, dashed and dotted red lines) of the strain sensitivity due to the optical read-out quantum noise, obtained varying the laser power in order to have at the beam splitter a power of 0.5kW, 10 kW and 50 kW respectively. The parameters used are those of initial Virgo. The curves are compared to the standard quantum limit (solid black line).

circulating power by a factor $[1 + (f/f_p)^2]$. Putting all together, the strain sensitivity due to the radiation pressure is given by

$$S_n^{1/2}(f)\Big|_{\text{rad}} = \frac{16\sqrt{2}\mathcal{F}}{ML(2\pi f)^2}\sqrt{\frac{\hbar}{2\pi}\frac{P_{\text{bs}}}{\lambda_L c}}\frac{1}{\sqrt{1+(f/f_p)^2}} \tag{1.78}$$

Far from the pole frequency, the radiation pressure results to be proportional to f^{-2}, so it limits mostly the low frequencies, which is the opposite effect with respect to the shot noise.

- The standard quantum limit. Looking at 1.74 the indication would be that in order to beat the shot noise we need to increase the power P_{bs}. However, by doing this we are increasing the radiation pressure: in fact, the former is proportional to $P_{\text{sb}}^{-1/2}$, whereas the latter is proportional to $P_{\text{bs}}^{1/2}$. A gain in sensitivity at high frequencies in this way would result in a sensitivity loss at low frequencies, and vice-versa. Is it the uncertainty principle in action. We refer to the combination of these two noise sources as optical read-out noise, defined as the sum of the two power spectral densities

$$S_n(f)|_{\text{opt}} = S_n(f)|_{\text{shot}} + S_n(f)|_{\text{rad}} \tag{1.79}$$

A plot of the shot noise and of radiation pressure as function of the frequency, together with their sum defined in 1.79, is shown in the left plot of Figure 1.13. It turns out that for each value of the frequency there is an optimal value P_{bs} that minimizes $S_n^{1/2}(f)|_{\text{opt}}$. The corresponding optimal value of $S_n^{1/2}(f)|_{\text{opt}}$ defines the *standard quantum limit* and is given by

$$S_{\text{SQL}}^{1/2}(f) = \frac{1}{2\pi f L}\sqrt{\frac{8\hbar}{M}} \tag{1.80}$$

Equation 1.80 represents the minimum value of the amplitude spectral density that can be obtained at a given frequency. Physically, it originates directly from the minimum possible error in the determination of the mirror position [42]. The optical read-out noise then can be expressed directly as function of the standard quantum limit

$$S_n(f)|_{\text{opt}} = \frac{1}{2} S_{\text{SQL}}(f) \left[\frac{1}{\mathcal{K}(f)} + \mathcal{K}(f) \right] \tag{1.81}$$

where the dimensionless function $\mathcal{K}(f)$ is defined as

$$\mathcal{K}(f) = \frac{8\omega_L P_{\text{bs}}}{ML^2} \frac{1}{(2\pi f)^4 \left[1 + (f_p/f)^2 \right]} \tag{1.82}$$

A plot of the $S_{\text{SQL}}^{1/2}(f)$, together with different $S_n(f)|_{\text{opt}}$ curves corresponding to different P_{bs} values, is shown in the right plot of Figure 1.13. From the plot it is also clear that the 1.80 represents the envelope of the minima of the $S_n(f)|_{\text{opt}}$ functions.

Displacement noise

The discussed read-out noise is intrinsic to the way that has been chosen to measure GWs. However, the mirrors can also move because of other effects that can mimic a GW. As well as a GW changes the length of a Fabry-Perot cavity by a $\Delta L = hL$, a change Δx in the cavity length is equivalent to a GW with amplitude $\Delta x/L$. These effects are denoted as *displacement noises*, and their computation depends on many technical details like properties of materials, isolation mechanisms, environment. Here, the main noise sources will be taken in account.

- Seismic noise. In general, the Earth's ground is in continual motion. Earthquakes are only one extreme manifestation of the Earth's crust motion, but they occur randomly and with a limited time duration. Their typical frequency range is between $[\,0.03\,,\,0.1\,]$ Hz and their strength can be high enough to cause the unlock of the interferometer even with the best screening strategies. Atmospheric cyclonic systems over oceans generate micro-seismic waves, which transfer energy from the atmosphere to the ocean and then to the ocean floor. Then, the vibrations propagate over $\sim 10^3$km in the crust in the form of surface waves, guided in near-surface layers and through multiple reflections in deeper layers, with amplitudes of the order of micrometers. These micro-seismic waves shake directly the suspension mechanisms with amplitudes of few microns and, finally, the test masses. This activity is relevant to the lock of the interferometer (also because it is often linked to the wind activity), and is typically limited to the frequency range $[\,0.1\,,\,1\,]$ Hz. An example of the impact of earthquakes and sea activity on the seismic noise is shown in the spectrogram in Figure 1.14, taken on a day where both an earthquake and an increased sea activity occurred. In general the ground motion covers the full spectrum and its displacement spectrum, at least for frequencies above $1\,Hz$, can be described with a power law

$$S_x^{1/2}(f)\Big|_{\text{seis}} \simeq A_{\text{seis}} \left(\frac{1\text{Hz}}{f} \right)^2 \frac{\text{m}}{\sqrt{\text{Hz}}} \tag{1.83}$$

where the typical amplitude for quiet locations can be $A_{\text{seis}} \simeq 10^{-7}$. More details can be found in [43],[44]. Starting from Equation 1.83, the corresponding strain sensitivity should

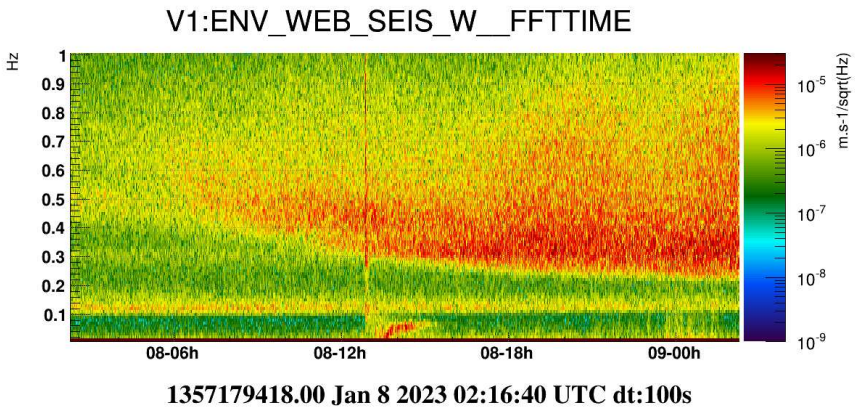

Figure 1.14: Seismic spectrogram recorded at 08/01/2023 covering 24 hours. The data are collected by a seismometer placed on the ground of the Virgo West-End Building (see Section 3.2). From $\sim$ 06 : 00 : 00 UTC the sea activity, recognisable in the $[\,0.1\,,\,1\,]$ Hz band, starts increasing its intensity. At $\sim$ 13 : 30 : 00 UTC an earthquake generated in Vanuatu Islands hits the Virgo site, with a typical banana-shaped increasing frequency in the $[\,0.03\,,\,0.1\,]$ Hz band.

be obtained by dividing the displacement spectrum by the arm length, which is $3 - 4$ km. However, the obtained strain sensitivity results more than 10 orders of magnitude larger than the typical $h \sim 10^{-21}$ that we are looking for. Therefore, there is the need to attenuate seismic vibrations by a huge factor. The typical solution consists in suspending the mirrors to a set of pendulums in cascade. The basic principle is simple: a single pendulum with resonance frequency f_0 transmits the vibrations with frequencies $f \gg f_0$ attenuated by a factor $(f_0/f)^2$. A composite pendulum made by N single-pendulum stages provides an attenuation factor $(f_0/f)^{2N}$.

The solution adopted in initial Virgo, called *Superattenuator*, results to be particularly efficient. It is described in detail in [45] and it is an 8 m long pendulum chain, with all the resonance frequencies confined below 2 Hz. In this way the seismic vibrations are reduced by more than 10 orders of magnitude starting from a few Hertz. Its full transfer function, extrapolated by a stage by stage measurement, is shown in the left plot of Figure 1.15. To obtain the residual mirror displacement, the input seismic noise has to be multiplied by that transfer function. In the right plot of Figure 1.15 a spot measurement of the attenuation factor is shown. The vibrations at the top stage are measured with an accelerometer, whereas the mirror displacement is measured by the interferometer.

- Thermal noise. Thermal noise is due to the thermal kinetic energy of the atoms and molecules of the various detector parts. The mirrors and the suspensions have a definite temperature T, so the thermal noise produces a stochastic force that induce vibrations. For a displacement $x\,(t)$ describing a linear system subject to an external force $F\,(t)$, we can express the equation of motion in the Fourier space in the form

$$\tilde{F}\,(f) = -i\,2\pi f Z\,(f)\,\tilde{x}\,(f) \tag{1.84}$$

This relation defines the impedance $Z\,(f)$ of the system. The *fluctuation-dissipation* theorem links the power spectrum of the stochastic force responsible for thermal noise with the

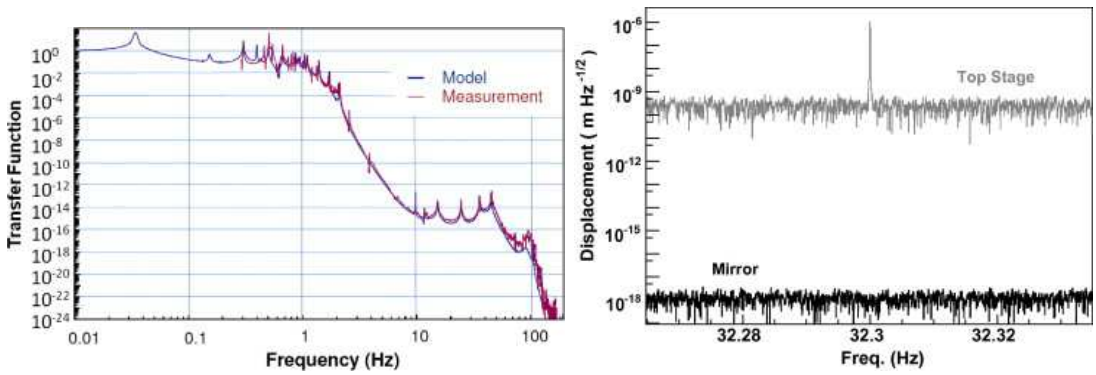

Figure 1.15: Left plot: the transfer function of the superattenuator in initial Virgo, as it has been modeled (blue curve) and as it was measured (red curve). Since the individual pendulum resonance frequencies are $f_0 \leq 2\,\mathrm{Hz}$, at frequencies above a few Hertz an attenuation by a factor $\sim 10^{-14} - 10^{-12}$ is achieved. Right plot: one example of the attenuation of the vibrations around 32.3 Hz in initial Virgo. The vibration on the top stage of the superattenuator is measured by an accelerometer, while the mirror displacement is measured by the interferometer itself.

temperature and the impedance of the system, as

$$S_F(f) = 4k_B T\,\mathrm{Re}\,(Z(f)) \tag{1.85}$$

Using both the 1.84 and 1.85, the corresponding displacement spectral density can be written as

$$S_x(f)|_{\mathrm{thermal}} = \frac{1}{2\pi f\,|Z(f)|}\sqrt{4k_B T\,\mathrm{Re}\,Z(f)} \tag{1.86}$$

In [46],[47] this result, originally proven in the statistical mechanics domain, has been extended to macroscopic thermodynamic domain and generalized for multiple extensive parameters. Consequently, we are able to predict the spectral displacement of a system due to thermal noise if we have knowledge of its impedance $Z(f)$ and its temperature. For a complex extended object the impedance associated to a normal mode with frequency f_0 can be expressed in a general form as

$$Z(f) = -2\pi i\,\frac{m}{f}\left[f^2 - f_0^2 + if^2\phi(f)\right] \tag{1.87}$$

where the dimensionless function $\phi(f)$ is called loss angle, and accounts for the internal friction in the materials [48]. The most important noise sources can be grouped into two families: the thermal noise of the suspensions and the thermal noise of the test-masses.

The suspensions thermal noise is due mainly to the thermal fluctuations that induce an horizontal motion of the mirrors. There is also a vertical-horizontal coupling that propagates the vertical fluctuations in horizontal motion, but the coupling is of order $\simeq 10^{-4}$. This noise follows a power law and is dominant at the low frequencies, for $f < 50$Hz. In addition, there are the violin modes. These are the excitation of the normal modes of the wires, and produce a set of narrow-band spikes at the multiples of the resonance frequency.

The test-masses thermal noise regards the thermal fluctuations on the mirrors themselves. The atoms of the mirrors are subject to a Brownian motion due to their kinetic energy, exciting the normal modes of the mirror. Another important contribution is due

to the thermal noise of the coating of the mirrors. Other contributions come from thermo-elastic and thermo-refractive fluctuations. The test mass noise is the dominant one between few tens and few hundred Hertz.

In general, the thermal noise depends on the dissipation in the system, and consequently on the material used. Therefore, one important strategy for its mitigation consists in the search for materials with optimal properties.

- Newtonian noise. In Sections 1.2.1,1.2.2 it turned out that the detector test masses can be considered as freely-falling only for the motion that concerns the horizontal plane, and for GW frequencies above few Hertz. When we approach to that frequency region, the forces originated by mass density fluctuations can no more be considered as static. The main source are the micro-seismic waves generated by cyclonic and oceanic activity already described within the seismic noise. These micro-seismic waves produce mass density fluctuations, inducing a stochastic gravitational field that couples directly with the test masses. This results in a *Newtonian noise*, also known as gravity gradient noise [49]. The estimated strain sensitivity has the general form of a power law

$$S_n^{1/2}(f)\Big|_{\text{newt}} \simeq A_{\text{newt}} \left(\frac{1\text{Hz}}{f}\right)^4 \text{Hz}^{-1/2} \tag{1.88}$$

where for instance for the Virgo site the amplitude has been estimated to be $A_{\text{newt}} \simeq 3 \cdot 10^{-17}$. A detailed study on Newtonian noise can be found in [50]. In present GW detectors, low frequencies are dominated by seismic noise and suspensions thermal noise and the Newtonian noise is not an issue. However, these noises can be in principle reduced arbitrarily working on attenuation and on the materials. Instead, it is impossible to screen the gravitational forces that act on the mirrors. So, even if in the future we will be able to push down the seismic and thermal wall, the Newtonian noise will continue to limit any ground-based detector. The only way to mitigate it consists in monitoring it with an extended array of seismometers or accelerometers with a low sampling rate, and then subtracting it from the data.

The sensitivity curve

The presented noise sources act simultaneously and shape the overall sensitivity of the detector to a GW, each one at its typical frequency range. In Figure 1.16 the contributions of the noise sources to the strain sensitivity are plotted together as function of the frequency, as well as the total noise. At low frequencies ($f < 60\,\text{Hz}$), the sensitivity is limited by the seismic noise, the thermal noise of the suspensions and by the radiation pressure. The Newtonian noise is less strong, but will become significant in future detectors when the already mentioned noise sources will be mitigated. At intermediate frequencies ($70\text{Hz} < f < 400\text{Hz}$), the main limiting noise comes from the thermal noise of the coating, and then there is the optical quantum noise. At high frequencies ($f > 400\,\text{Hz}$), the sensitivity is mostly limited by the shot noise.

There are also many other noise sources to be considered. One source comes from the residual gas and organic molecules that remain inside the interferometer after the vacuum is made: the residual pressure was $< 10^{-7}$mbar in initial detectors and progressively reduced to $< 10^{-9}$mbar in the advanced detectors. The residual gas particles interfere with the laser beam, inducing scattering on photons. The residual organic molecules can condense and accumulate on the optical elements, so their partial pressure must be kept below 10^{-13}mbar

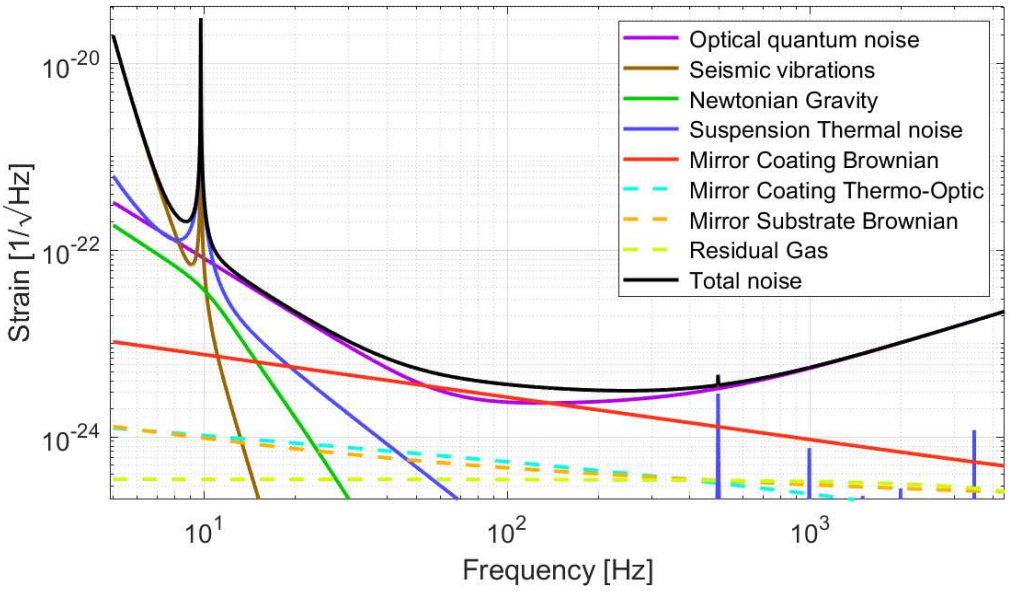

Figure 1.16: An example of theoretically calculated noise budget in LIGO Hanford interferometer. The most dominant noise sources are plotted as solid lines, while the less dominant are dashed. The result of the whole contributions, the total noise, is the solid black line.

to avoid this effect for a few years. Another noise source, as already pointed in Section 1.2.2, is the fluctuation in the input laser power, which has to be kept under control with great accuracy. Then, there is a big family on noises that are generated by the interferometer infrastructure itself, comprehensive of all the control noises, both longitudinal and angular, the light that is scattered during the interaction with all the optical elements, all the noises generated by the vacuum system, the conditioning system, and so on. The more the fundamental noise sources are mitigated, the more these other noise sources become progressively important. The hunt and mitigation of technical noises will be treated in Chapter 3.

In Figure 1.17 the best sensitivity curves recorded by the LIGO and Virgo detectors in their initial configuration, just before the long shutdown, are reported. The arms length of 4km in LIGO produce a better sensitivity at frequencies above 100Hz with respect to Virgo. On the other side, at low frequencies is well visible the effect of the better seismic mitigation system in Virgo with respect to initial LIGO. While in LIGO the seismic wall is at about 40Hz, in Virgo it is between $10 - 20$Hz. This gap disappeared after the upgrades that brought to the advanced detectors. It is worth to remember that even the best sensitivities obtained by initial LIGO and Virgo have not been enough to observe any GW signal during their observing runs. The noise floor at the lower-intermediate frequencies was still too high to cover an universe volume big enough to have strong events like CBCs with high enough rates, compatible with observing periods of few months.

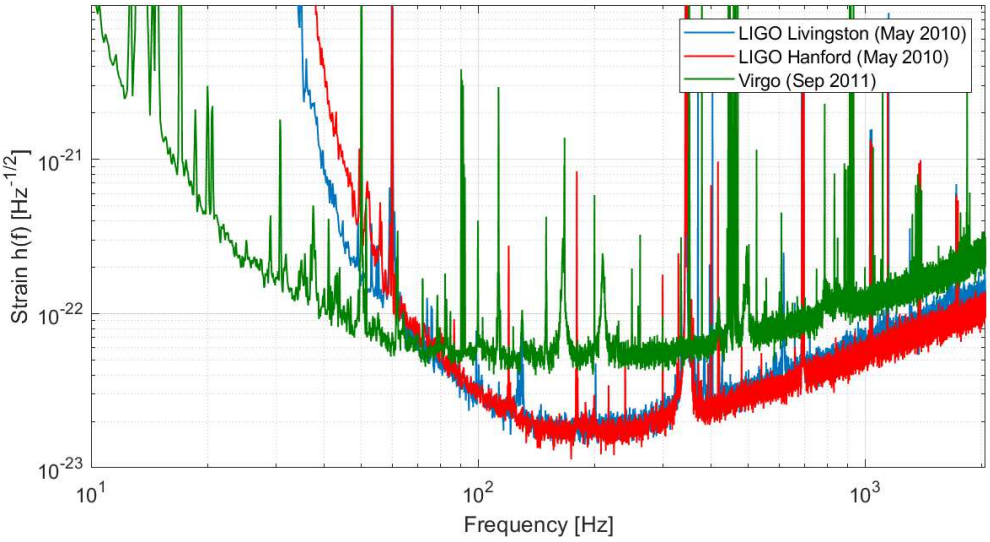

Figure 1.17: Plot of the latest sensitivity curves achieved by initial Virgo and LIGO interferometers before the long shutdown for upgrading to AdV and ALIGO. The two LIGO sensitivity curves (Livingston in blue, Hanford in red) belong to the LIGO scientific run named S6, which lasted until May 2010. The Virgo sensitivity curve (in green) is referred to the Virgo scientific run named VSR4, ended in September 2011. Virgo results way more sensitive at low frequencies thanks to the superattenuator, while at intermediate and high frequencies LIGO achieves the best sensitivities thanks to its 4-km-long cavities (Virgo has 3-km arms).

1.3 Advanced detectors and the discoveries during their first 3 observing runs

As already stated, the initial Virgo and LIGO detectors remained in their initial configuration until 2010-2011, even if progressively enhancing their sensitivity. After that, they were turned off and undergone to a few-years-long upgrade period. The changes were so invasive, and resulted de-facto in new detectors. The new interferometers are labeled as *Advanced Virgo* (AdV) and *Advanced LIGO* (ALIGO), and are considered as second-generation (2G) detectors. The full modifications that have been made are described in detail respectively in [51] and [52]. Here there are some of the major improvements:

- A progressive increase of the input laser power. While in the initial configuration the injected power was $\mathcal{O}(10\text{W})$, in the 2G detectors this power is gradually, step-by-step increased up to $\mathcal{O}(100\text{W})$. The direct effect is a direct reduction of the shot noise, since $S_n|_{\text{shot}} \propto P^{-1}$, thus improving the sensitivity at high frequencies. The circulating power in the cavities would raise up to $\mathcal{O}(1\text{MW})$ and some adjustments are necessary to compensate the thermal lensing of the mirrors.

- Since $S_n|_{\text{rad}} \propto P$, the increased power raises the radiation pressure, worsening the sensitivity at low frequencies. However, the radiation pressure is also inversely proportional to the end mirror masses, $S_n|_{\text{rad}} \propto M^{-1}$. Therefore, in order to contrast the radiation pressure the initial mirrors with $M \simeq 20\text{kg}$ are substituted by newer ones

with $M \simeq 40$kg.

- ALIGO introduces better seismic isolation, improving the sensitivity at low frequencies, whereas in Virgo the superattenuator has still the needed performances.
- The test-mass suspensions, which in initial detectors were made of steel wires, are replaced by silica, directly fused to the mirrors in order to obtain a monolithic object. The effect is a strong reduction of the suspension thermal noise, which become lower than the radiation pressure and comparable with Newtonian noise.
- Investigation to find better coatings for the mirrors, with lower thermal noises.
- Addition of a new mirror, the *signal-recycling mirror*, at the output of the interferometer before the photodetectors. With this addition a new cavity, the signal-recycling cavity, is created. This technique was first implemented in GEO600, even if without Fabry-Perot cavities [53]. The signal-recycling cavity can be tuned to be resonant with a given $\omega_L \pm \omega_{\rm gw}$ sideband, in order to increase the sensitivity of the interferometer in a given frequency range at the cost of the bandwidth. Alternatively, the cavity can be tuned to be anti-resonant, in order to increase the bandwidth of the detector with respect to the case when no signal-recycling cavity is present. Interferometers with both power-recycling and signal-recycling cavities are called dual-recycled.
- Implementation of quantum non-demolition techniques, like the frequency-independent or frequency-dependent squeezing. These techniques have been first theorized in [41], while the application to modern dual-recycled interferometers is considered in [54].

Some of the presented improvements have been implemented gradually, with different timelines between LIGO and Virgo. At the present, three observing runs have been completed, called "O1", "O2" and "O3", with progressively increased sensitivity. In Figure 1.18 the typical sensitivity curves of the three detectors are reported and are compared with their last sensitivities before the upgrade to the advanced stage. Now, at the low frequencies the LIGO detectors have no gap with respect to Virgo thanks to new-concept suspensions. At intermediate and high frequencies, Virgo pays the one-kilometer lower length of its cavities with respect to the LIGO ones. Moreover, Virgo started the upgrade to AdV with a two-years delay with respect to LIGO and joined the observing run just during the last month of O2. Consequently, also some upgrades were delayed with respect to LIGO.

Thanks to the great improvement in sensitivity at low and intermediate frequencies, the Advanced detectors are able to observe an universe volume sufficiently big to make the first detection likely. On 14th of September 2015, during the engineering run that preceded the scientific run O1, the two LIGO interferometers observed in coincidence the first GW [55]. The signal, observed with a ~ 7 ms delay between the detectors, is produced by the coalescence of two black holes with masses $m_1 \simeq 36 M_\odot$ and $m_2 \simeq 29 M_\odot$ at a luminosity distance $D_L \simeq 410$ Mpc. During the whole duration of O1, a total of three GWs have been observed by the LIGO detectors[5] [56].

Advanced Virgo joined Advanced LIGO during the last month of O2, in August 2017. Its first GW detection, which was also the first three-detector observation, happened on 14th of August 2017 [57]. The event, labeled as GW170814, was generated by two colliding black

[5] At the time of the publication one of the three events, labeled as LVT151012, had too low significance to be confidently claimed as a detection. Further reprocessing have subsequently reconsidered this statement, and that event was confirmed as a detection, labeled as GW151012.

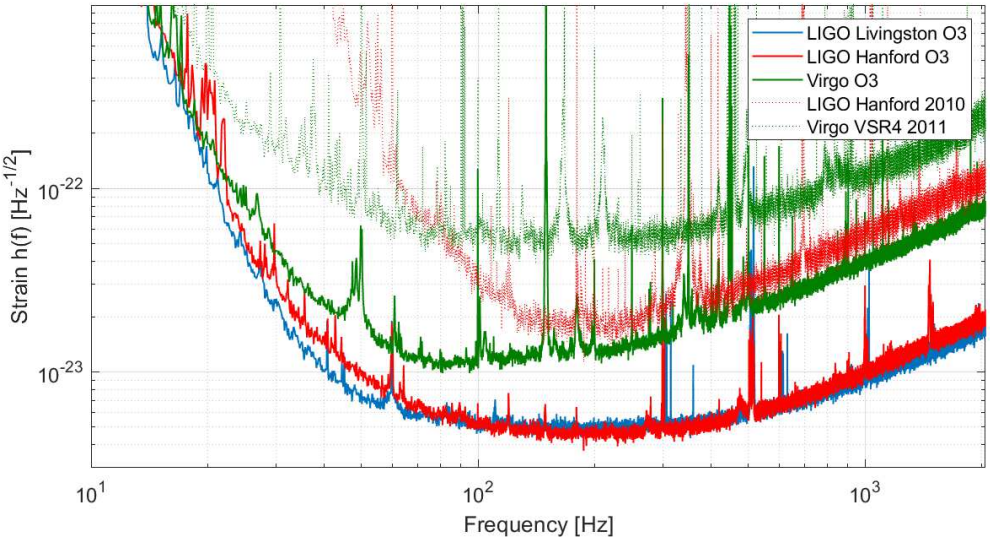

Figure 1.18: Plot of the most recent sensitivity curves recorded by Advanced Virgo and LIGO interferometers during O3 (2020), with a comparison with the best sensitivities before the upgrade as they are shown in Figure 1.17. The LIGO Livingston O3 curve is shown in solid blue. LIGO Hanford is plotted in red: the solid line represents O3 data while the dotted one is the initial S6 (2010). The Virgo sensitivity curve is plotted in green: the solid line represents O3 data while the dotted one is the initial VSR4 (2011). LIGO detectors have removed the gap with respect to Virgo at low frequencies thanks to a new suspension system. In general, the combined effect of lower thermal noise from suspensions and coating, higher power and larger beam results in a wide-band better sensitivity.

holes with masses $m_1 \simeq 30M_\odot$ and $m_2 \simeq 25M_\odot$ at a luminosity distance $D_L \simeq 540\,\mathrm{Mpc}$. Thanks to the contribution of Virgo, the localization of the event have greatly improved: for GW170814 the area of the 90% credible region passed from the $1160\,\mathrm{deg}^2$ that would have been obtained with only two detectors to the actual $60\,\mathrm{deg}^2$ with three-detector observation. This improvement makes more feasible the search for an electromagnetic (EM) counterpart of the GW event, sending the localization area coordinates to traditional telescopes. The first big achievement in this sense arrived just three days after, in 17th of August 2017. The online triggers revealed a GW from the first-ever coalescence of a binary neutron star at a luminosity distance $D_L \simeq 40\,\mathrm{Mpc}$, labeled as GW170817 [58]. The event was localized within a sky region of $28\,\mathrm{deg}^2$. Independently, the Fermi Gamma-ray Burst Monitor detected a gamma-ray burst (GRB 170817A) with a delay of $\sim 1.7\,\mathrm{s}$ with respect to the merging time, and with a sky localization compatible with the one inferred through GWs. After the trigger, an extensive observing campaign has been carried on during the following hours an days. A bright optical transient was observed 11 hours after by independent telescopes, with a red-ward evolution over $\sim 10\,\mathrm{days}$. Moreover, X-ray and radio emission were observed respectively ~ 9 and $\sim 16\,\mathrm{days}$ after the merger [59]. Thanks to these observations it has been possible to confirm the hypotheses that put BNS merger as possible explanation for gamma-ray bursts. this event officially opened the era of multi-messenger astronomy. Globally, during O1 and O2 have been observed 11 CBC events, divided in 10 BBH and 1 BNS [8]. A strong jump has been done in O3, which has been divided in two parts called

O3a and O3b. The reason is that to a sensitivity enhancement corresponds a proportional increase of the distance at which it is possible to detect signals, and the observable volume of universe goes as the cube. During O3a and O3b respectively 44 [9, 10] and 35 CBCs detection have been confirmed [11], bringing the total count of GWs detection in the 2G detectors era to 90. The trend is shown in Figure 1.19.

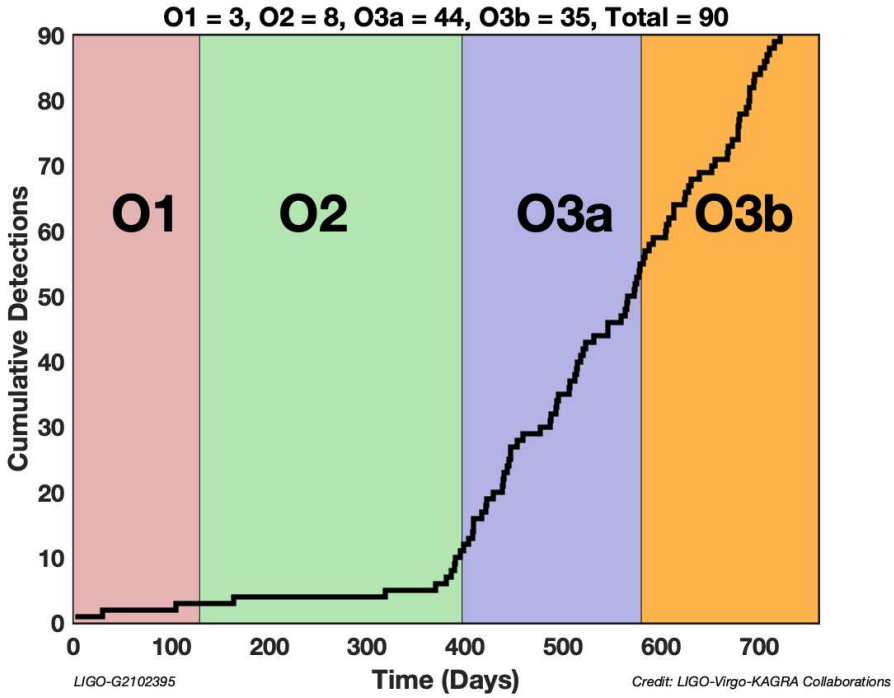

Figure 1.19: Plot of the cumulative detections made by the LIGO, Virgo and network during the first three observing runs in the Advanced configuration, as function of the consecutive observing days. From public LIGO DCC G2102395

.

The 79 observations in O3 include some exceptional events. There are the second detection of a putative BNS [60], without EM counterpart because of the distance and a poor sky localization; the detection of two BBHs with highly asymmetric masses [61, 62]; the detection of the coalescence of the two heaviest observed BHs that led to the formation of an intermediate BH with $M \simeq 142\,M_{\odot}$ [63]; the detection of the first-ever coalescences from NS-BH systems [64]. Moreover, thanks to the consistent number of detections, several tests of GR have been made, like putting more severe constraints to post-Newtonian and Lorentz-violating coefficients, bounding the mass of the graviton, searching for deviations from Kerr solution in the BBH remnant quasi-normal modes [65, 66].

Chapter 2

Continuous gravitational waves

Have you ever tried to hear someone whispering
from the opposite side of a crowded room?

Continuous waves are among the gravitational signals that still lack a first detection. They are expected to be emitted by rotating NSs or other more exotic sources, and their expected amplitude is not greater than $\sim 10^{-26} - 10^{-25}$. This amplitude is at least five orders of magnitude weaker than the GWs that arrive on Earth by BBH CBCs, but thanks to the greater duration (~ 1 year versus $\sim 1\,\mathrm{s}$) the integration time can, in principle, compensate this gap. Their search was carried on since the resonant-bar detectors were operating. However, they were not enough sensitive to search for CWs with amplitude weaker than $\sim 10^{-24}$. Moreover, the search was strongly limited by the narrow frequency window at which the detectors were sensitive: just a few tens of Hertz around their resonance frequency, which was typically $\mathcal{O}(\mathrm{kHz})$. Some of the latest CW searches made with resonant-bar detectors are reported in [67, 68]. As will be shown in Section 2.1, at these search frequencies the majority of the known NSs is out-of-window. Interferometric wide-band detector are optimal for these kind of searches, since CWs are expected to be emitted at a wide range of frequencies, from few Hertz to thousands of Hertz. So, potentially they could be found in the whole sensitivity band of the interferometers.

The chapter is structured as follows: in Section 2.1 the NSs are described in their origin and structure, introducing the pulsars and presenting the full population of known NSs. Then, the main physical mechanisms expected to lead to the emission of CWs are shown. These include the continuous emission due to the presence of permanent deformations in the NS body, as well as long-lasting transients generated by instabilities mostly in young NSs. In Section 2.2 a new potential source of CWs is introduced, represented by ultra-light boson clouds that could condensate around spinning BHs and then produce CWs through annihilation. In Section 2.3 the main CW search strategies are presented. These differ one with respect to the other depending on the available information on the sources. They can be roughly divided in three families: targeted, directed and all-sky searches. The most recent results of these searches are also reported.

2.1 Spinning neutron stars

The possibility of the existence of degenerate stars was firs introduced by Lev Landau in 1932, when he mentioned the possible existence of "dense stars that look like one giant

nucleus", even if without the concept of the neutron and violating quantum mechanics rules [69]. However, the first realistic proposal that a NS would be the remnant of a supernova explosion is from Baade and Zwicky in 1934 [70], after the neutron discovery, and basic properties and equilibrium solutions for NSs were first worked by Oppenheimer and Volkoff in 1939 [71]. Their existence was definitively proved in 1967, with the discovery of a pulsating radio source, named PSR B1919+21 and localized in the Galaxy [72]. The physical mechanism behind the emission of the pulses by rotating NSs was promptly explained as a theoretical follow-up of the discovery [73].

At the present state of knowledge, NSs are the outcome of supernova explosions of stars that are too massive to form white dwarfs after fuel consumption and too light to form a black hole after the explosion. The estimated progenitor star masses range between $\sim 6\,M_\odot$ and $\sim 20-30\,M_\odot$, with many different possibilities depending on the star composition [74]. The observed NSs at the equilibrium have masses of $\sim 1-2\,M_\odot$ and a radius between $\sim 10-15\,\mathrm{km}$ and are prevented from collapse by neutron degeneracy pressure. The structure of the NS have different phases: there is the crust, with typical thickness of $\sim 0.8-1\,\mathrm{km}$, and the core. The crust have an external layer of $\sim 0.3\,\mathrm{km}$ thickness, constituted by neutron-rich heavy nuclei organized in a rigid lattice. The internal crust, with a thickness of $\sim 0.5\,\mathrm{km}$, is made by a proton rich matter permeated by a neutron fluid. Going deeper, the nuclei may become distorted and elongated, forming a "nuclear pasta" of ordered nuclei and gaps. Still deeper we reach the core, where the density is greater than the nuclear saturation density: the nuclear pasta gives way to an hyper-dense neutron fluid, composed by a $\sim 90\%$ of neutron and a $\sim 10\%$ of protons plus a number of electrons similar to the protons. The fluid is in equilibrium between the beta decay and the inverse beta process [6, 75]. In the inner core the mass-energy density reaches values many times larger than the nuclear saturation density. In that situation the hadronic interaction must be treated within the quantum chromodynamics framework, but at this energy scale the physics is not well understood and different models are possible. There would be different phase transitions involving hyperons, perhaps to a quark-gluon plasma, or even perhaps to a solid strange-quark core [76].

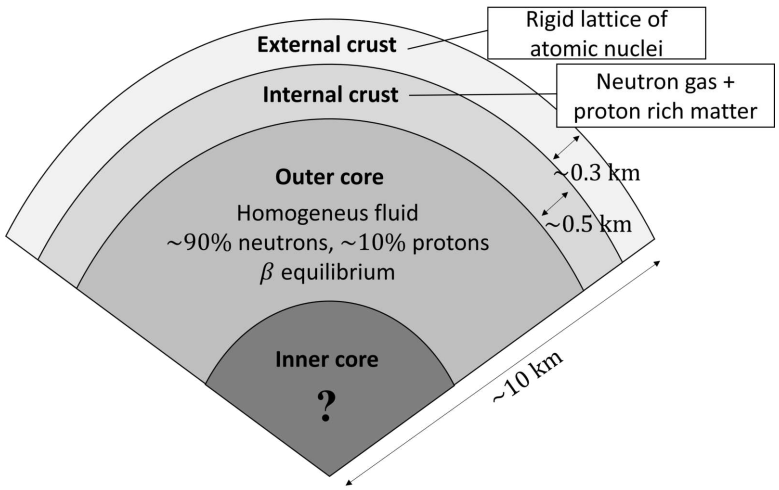

Figure 2.1: Out of scale representation of the internal structure of a NS.

All the different physical models determine the NS composition and consequently their

equation of state (EoS) that models the pressure-density relation. There is therefore a high number of possible EoS, each one of them leading to a maximum mass and radius of a NS [76]. While the mass of a NS in a binary system can be measured from orbital parameters, NS radii are especially challenging to measure directly. The most recent measurements, where mass and radius are determined simultaneously from individual stars, are from the NICER X-ray satellite and they are constraining more tightly the allowed equations of state than in the past [77, 78, 79].

At the moment, there are about $\sim$ 3300 known NSs in the Galaxy. Most of them are pulsars, observed through electromagnetic emission, primarily in the radio band, but also in X-rays, γ-rays and optical band. In pulsars a beam of radiation is generated by highly-energetic particles emitted from the magnetic poles, through the curvature radiation mechanism [80]. This beam is misaligned with respect to the rotation axis, so it rotates with the NS. If the beam hits the Earth, it is observed as a pulse as it sweeps across the Earth once per rotation. Thus, the pulses from NS are typically observed at the rotation frequency of the star itself.

The majority of the known NSs are shown in the $P - \dot{P}$ diagram in Figure 2.2, where $\dot{P}$ is the 1st-order derivative of the observed rotation period P. In fact, all the NSs are slowly losing energy mainly through electromagnetic emission and are therefore slowing down their rotation. In Figure 2.2, NSs in binary systems are marked with blue circles while isolated NSs are marked with red triangles. The dashed black lines represent the inferred surface magnetic fields of the NSs, ranging from 10^8G to 10^{15}G. Such high values are a natural result of the collapse that leads to the NS formation. If the magnetic flux is approximately conserved during the collapse, the reduction of the outer surface of the star to the typical $\sim 10 - 15$ km radius produces surface fields with such high magnitude. The highest values are reached by the *magnetars*, highly-magnetized young NSs with $\sim 1 - 10$ s period and strong spin-down (top-right corner in Figure 2.2) which are believed to get the highest magnetic field through a dynamo process [83]. The dashed blue lines represent the different inferred nominal ages of the NSs, assuming that the rotational energy is lost entirely through magnetic dipole emission, in the $P_{\rm obs} \gg P_{\rm birth}$ limit [6, 7]

$$\tau_{\rm mag} = \frac{P}{2\dot{P}} \tag{2.1}$$

From Figure 2.2 two distinct populations can be distinguished. The top right group of pulsars, with periods above 10^{-1}s, have the highest spin-down values and are for the most part isolated pulsars. They have the highest magnetic fields, with typical values $B > 10^{11}$G, and are typically younger, with ages $\tau < 10^8$ years for the most part. The bottom left group of pulsars is characterized by shorter periods and smaller period derivatives. These objects, called *millisecond pulsars* (MSPs), are for the majority bound in binary systems. They are considerably older, with $\tau > 10^9$ years for the most part, and have weaker magnetic fields, typically $B < 10^9$G. They are thought to get immense rotational energies from the accretion of matter from a binary companion. The observed pulsars represent only a small fraction of the existing NSs. The actual number of NSs in the Galaxy is estimated to be $\sim 10^8 - 10^9$. Aside from all the stars that disappear as they evolve toward the death line and cease pulsations, there are various selection effects that reduce the fraction of observable population. A pulsar is visible to us only if its radiation beam crosses the Earth; moreover, its radiation must be bright enough to be seen in the observing band, and must be not absorbed or scattered at the level to become undetectable with current radio telescopes [84]. Given the huge pressure on the nuclear matter and the typical rotational periods, one

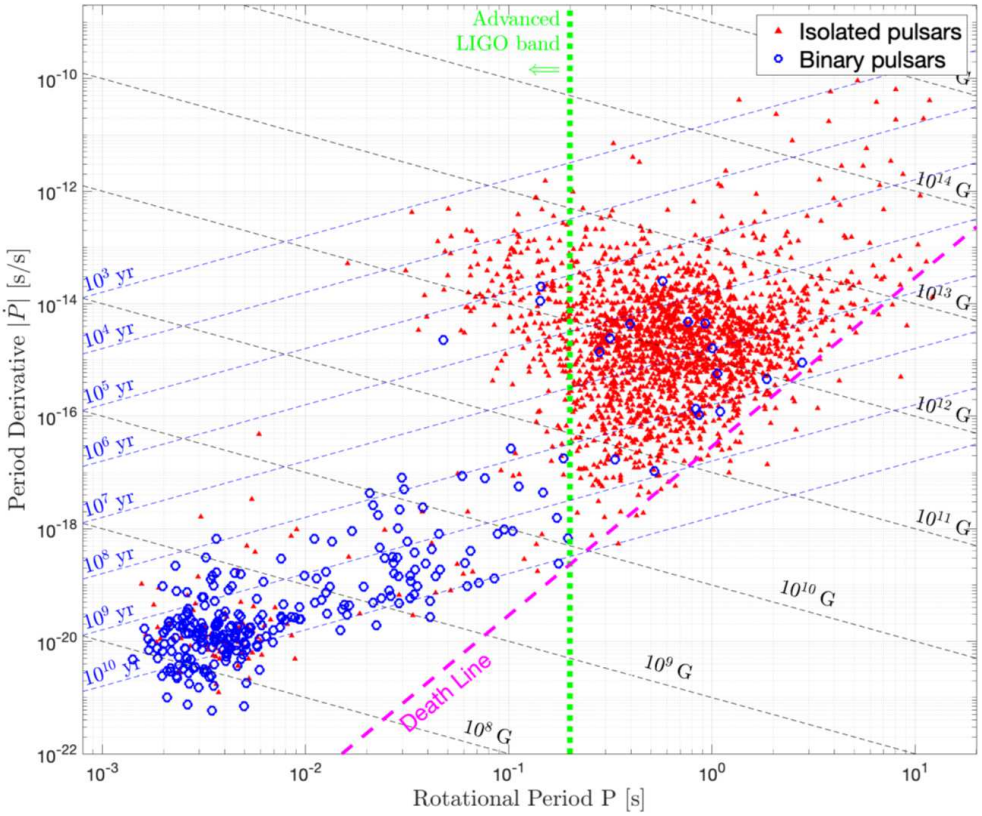

Figure 2.2: The population of known NSs, with their measured rotational period P and period first derivative $\dot{P}$. The dashed purple line represents the death line, beyond which the radio pulsar mechanism is believed to turn off. The dotted green line represents the frequency wall that limits the sensitivity to frequencies above 10 Hz for Advanced LIGO and Virgo design, assuming that the pulsars emit CWs at twice their rotational frequency (see Section 2.1.1). The plot is an elaboration by [81] of the ATNF Pulsar Catalogue [82].

expects a NS to be shaped as an axisymmetric ellipsoid or as a sphere in the non-rotating limit. In that case, we would not expect any quadrupolar GW emission due to rotation. All the CW searches assume a small but detectable mass or mass-current that violates the axisymmetry. In the following, both the possibilities will be examined.

2.1.1 Permanent deformations

A rotating NS that is symmetric with respect to its rotation axis do not emit GWs according to 1.11, since it has a constant quadrupole moment. If there is a deviation from axisymmetry, it produces a non-vanishing time-varying quadrupole moment. A common way to model an oblate NS is to consider it as an ellipsoid with semi-axes $a \neq b \neq c$ and momentum of

inertia, referred to the semi-axes, given by

$$I_{ij} = \begin{pmatrix} I_{xx} & & \\ & I_{yy} & \\ & & I_{zz} \end{pmatrix} = \frac{M}{5} \begin{pmatrix} b^2+c^2 & & \\ & a^2+c^2 & \\ & & a^2+b^2 \end{pmatrix} \tag{2.2}$$

Assuming the z axis as the rotation axis, the NS acquires a non-vanishing quadrupole $Q_{ij}(t)$ if $I_{xx} \neq I_{yy}$, that is, if $a \neq b$. A common way to express the deformation is through the ellipticity ε, which is defined as

$$\varepsilon \equiv \frac{I_{yy} - I_{xx}}{I_{zz}} \simeq 2\frac{a-b}{a+b} \tag{2.3}$$

The magnitude of the quadrupole is then given by [85]

$$|Q_{ij}| = \sqrt{\frac{8\pi}{15}} I_{zz}\varepsilon \tag{2.4}$$

There are different mechanisms that can cause a deformation of NSs from the axisymmetry. One possibility, valid only for NSs in accreting systems, is that temperature gradients in the crust, created by asymmetries in the accreting matter, induce a local deformation sustained by the elastic strain [86]. One other possibility, first pointed out by Chandrasekar and Fermi [87] and valid for all NSs, is that the huge magnetic field of the NS induce quadrupolar deformations on spherically symmetric stars, with ellipticities ε proportional to the ratio between magnetic energy and gravitational energy. A detailed study on the possible mechanisms can be found in [88]. As a general feature, poloidal fields have the effect to distort the star making it oblate, while toroidal fields deform the star in the opposite way, giving it a prolate shape. A purely poloidal magnetic field induces an oblateness depending on its mean value $\bar{B}_{\rm pol}$ as

$$\varepsilon_{\rm obl} \simeq 10^{-12} \left(\frac{\bar{B}_{\rm pol}}{10^{12}{\rm G}}\right)^2 \tag{2.5}$$

while a purely toroidal magnetic field induces a prolateness depending on its mean value $\bar{B}_{\rm tor}$ as

$$\varepsilon_{\rm pro} \simeq 10^{-11} \left(\frac{\bar{B}_{\rm tor}}{10^{12}{\rm G}}\right)^2 \tag{2.6}$$

It is clear that poloidal and toroidal fields induce opposite deformation effects on the NS. In a more realistic description, the magnetic field of a NS has a *twisted-torus* configuration where both the poloidal and toroidal components contribute. In this case the magnitude of the induced ellipticity depends on the ratio between the toroidal and the poloidal components, see [89] for a detailed discussion. Another constrain comes from the maximum sustainable ellipticity for elastic stresses, which depends on the crustal breaking strain $u_{\rm break}$ as [90]

$$\varepsilon < 2 \cdot 10^{-5} \left(\frac{u_{\rm break}}{0.1}\right) \tag{2.7}$$

where the strain has an extimated value $u_{\rm break} \simeq 0.1$. However, the actual constraints strongly depend on the EoS [89]. If the NS gets a deformation from axisymmetry, acquires a non-vanishing quadrupole and then emits GWs with frequency twice their rotational frequency

$$f_{\rm gw} = 2\, f_{\rm rot} \tag{2.8}$$

The observed signal at Earth detector depends on the detector pattern functions as in Equation 1.65, where the polarization amplitudes, according to the quadrupole formula 1.11, are given by

$$\begin{aligned} h_+ &= h_0 \tfrac{1+\cos^2\iota}{2} \cos\left(2\pi f_{\rm gw} t\right) \\ h_\times &= h_0 \cos\iota \sin\left(2\pi f_{\rm gw} t\right) \end{aligned} \tag{2.9}$$

where the amplitude h_0 depends on the NS quadrupole moment, on the GW frequency $f_{\rm gw}$ and on its distance r as

$$h_0 = \frac{4\pi^2 \mathrm{G}}{c^4} \frac{I_{\rm zz}\varepsilon}{r} f_{\rm gw}^2 \tag{2.10}$$

Equation 2.10 can be parameterized using a nominal moment of inertia for typical NS mass and size, an ellipticity compatible with recent upper limits, a distance of $\sim 1\,\mathrm{kpc}$ and considering a GW frequency in the LIGO/Virgo best-sensitivity region, so that

$$h_0 = 1.1 \cdot 10^{-26} \left(\frac{I_{zz}}{10^{38}\mathrm{kg\,m^3}}\right) \left(\frac{\varepsilon}{10^{-6}}\right) \left(\frac{1\,\mathrm{kpc}}{r}\right) \left(\frac{f_{\rm gw}}{100\,\mathrm{Hz}}\right)^2 \tag{2.11}$$

The expected GW amplitude results to be about five orders of magnitude weaker than the signals emitted by stellar-mass CBCs. The reason relies on the amount of mass that contributes to the quadrupole, which is $\mathcal{O}(M_\odot)$ for CBCs and $\mathcal{O}(\varepsilon M_\odot)$ for deformed NSs. However, the signal duration is way longer than the typical observed CBCs and covers the whole duration of the detectors observing runs. As it will be shown in Section 2.3, integrating on such long observation times gives CWs some detection chances. The GW carries out from the NS an amount of power given by

$$\mathcal{L}_{\rm gw} = \frac{32\mathrm{G}}{5c^5} I_{zz}^2 \varepsilon^2 \omega_{\rm rot}^6 \tag{2.12}$$

By equating the energy loss from GW emission and the rotational energy of the star, we get the spin-down evolution of the NS and the GW

$$\dot{f}_{\rm gw} = -\frac{32\pi^4 \mathrm{G}}{5c^5} I_{zz}\varepsilon^2 f_{\rm gw}^5 \simeq -1.7 \cdot 10^{-14}\mathrm{Hz/s} \left(\frac{\varepsilon}{10^{-6}}\right)^2 \left(\frac{f_{\rm gw}}{100\,\mathrm{Hz}}\right)^5 \tag{2.13}$$

It is worth to note that the typical spin-down values observed in known pulsars produce little relative variations in the star's rotational frequency during a nominal observing time of 1 year. Thus, the emitted CW can be treated as a nearly-monochromatic, considering the frequency evolution with the perturbation theory, as will be shown in Section 2.3. It is possible to use the measured P and $\dot{P}$ for known pulsars in Figure 2.2 to infer the maximum expected amplitude of the CW emitted by each one of them. Equating the power loss in 2.12 and the time-derivative of the Newtonian rotational kinetic energy, we can define the *spin-down limit* $h_{\rm sd}$ as

$$h_{\rm sd} = \frac{1}{r}\sqrt{-\frac{5\mathrm{G}}{2c^3} I_{zz} \frac{\dot{f}_{\rm gw}}{f_{\rm gw}}} \simeq 8.2 \cdot 10^{-25} \left(\frac{1\,\mathrm{kpc}}{r}\right) \sqrt{\left(\frac{I_{zz}}{10^{38}\mathrm{kg\,m^3}}\right) \left(\frac{100\,\mathrm{Hz}}{f_{\rm gw}}\right) \left(\frac{-\dot{f}_{\rm gw}}{10^{-10}\mathrm{Hz/s}}\right)} \tag{2.14}$$

The spin-down limit represents the expected amplitude of the emitted GW if the observed spin-down in a pulsar was due entirely to GW emission. In the same way, the 2.13 would

represent the the actual spin-down evolution if the NS loses energy only through GW emission. However, rotating NSs loose their rotational energy mainly through electromagnetic emission. This is straightforward, since even a rotating perfect sphere has a permanent magnetic dipole and thus radiates in the electromagnetic spectrum. A magnetic momentum $\vec{M}$ with inclination α with respect to the NS rotation axis emits radiation with luminosity $\mathcal{L}_{\rm em}$ given by [81]

$$\mathcal{L}_{\rm em} = \frac{\mu_0}{6\pi c^3} M^2 \sin^2(\alpha)\, \omega_{\rm rot}^4 \tag{2.15}$$

As done previously, equating this energy loss to the rotational energy loss, assuming a purely magnetic dipole $M = (2\pi/\mu_0) B\, R^3$ we get the spin evolution

$$\dot{\omega} = -\frac{\mu_0 R^6}{6\pi c^3 I_{zz}} B^2 \sin^2(\alpha)\, \omega^3 \tag{2.16}$$

The Equations 2.13, 2.16 represent two distinct contributions to the star rotational dynamics and they likely act together, with weights that depend on the particular phase of the NS evolution. More in general, the NS spin is expected to evolve following a power law of the kind

$$\dot{\omega} = -k\, \omega^n \tag{2.17}$$

where n is called the braking index and can be computed from the measurements of the rotational frequency ω and its first two derivatives, $\dot{\omega}$ and $\ddot{\omega}$, as

$$n = \frac{\omega\, \ddot{\omega}}{\dot{\omega}^2} \tag{2.18}$$

Performing the calculation for the small subset of known pulsars for which the second derivative $\ddot{\omega}$ has been measured, it has been found that they evolve with a braking index $n \sim 2 - 3$. This means that, at least in that subset, the electromagnetic emission is the dominant one, and that GW emission represents a little fraction of the energy loss. The spin-down limit is actually an upper limit for the amplitudes of CWs emitted by known NSs, because they emit electromagnetic radiation. A non-detection leads to bound the maximum contribution of GW emission on the observed NS dynamics.

In Figure 2.3 the measured $P - \dot{P}$ parameters of known NSs reported in Figure 2.2 have been translated in the expected GW frequency $f_{\rm gw}$, assuming that the 2.8 holds, and in the strain spin-down limit $h_{\rm sd}$ using the 2.14. Clearly the NSs with the strain $h_{\rm sd}$ above the sensitivity curve represent the an interesting subset of the whole population, even if we don't know how much the actual GW amplitude is . On that population it is worth to make dedicated CW searches. The kind of search that can be carried on on this sources, where the intrinsic parameters are mostly known, will be shown in Section 2.3.1.

2.1.2 Long transients from neutron star instabilities

Differently from the previous case, quadrupole perturbations can be generated also by non-permanent mechanisms, with time-scales that can vary from seconds to days, up to months in some cases. The ones that are considered here have typical duration of hours up to days, and are expected to occur in newly-born or young NSs.

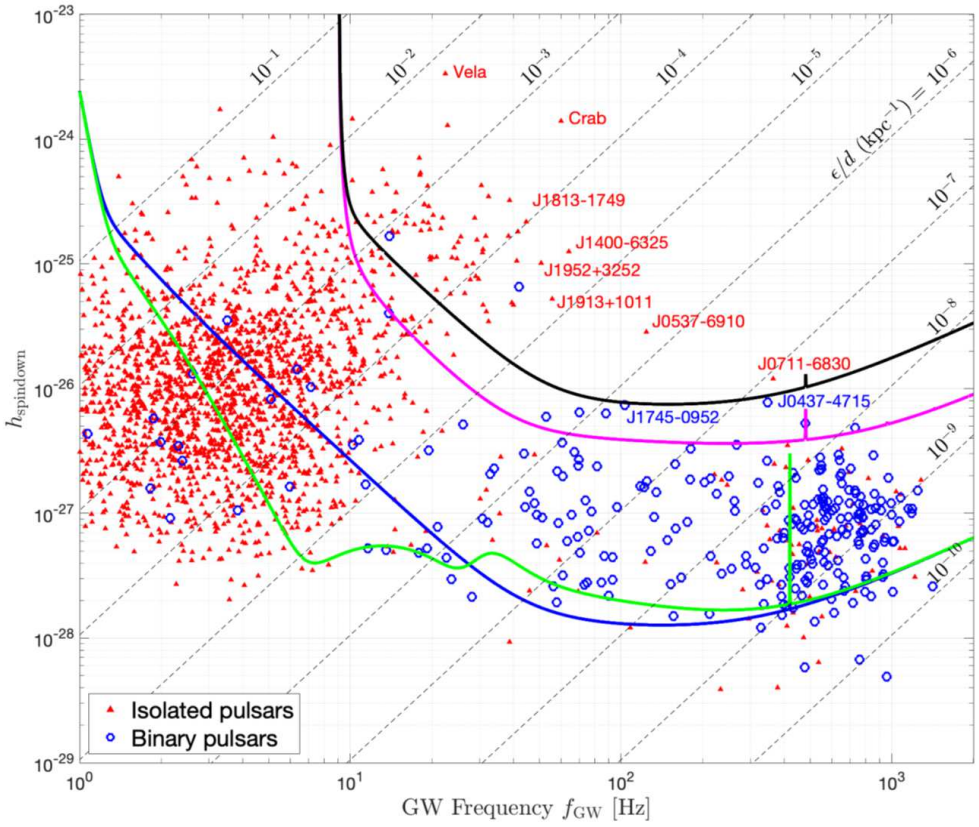

Figure 2.3: Expected GW frequencies and strain spin-down limits for the known NSs shown in Figure 2.2. Red triangles indicate isolated stars, blue circles indicate binary NSs. The solid black curve is the reference sensitivity for O3, while the solid magenta one assumes a 2-years observing run at Advanced LIGO design sensitivity. The blue and green solid curves represent a 5-year Einstein Telescope data run for two different designs (ETB and ETC respectively) In both cases an optimal, coherent analysis method has been assumed, see Section 2.3.1. Source: [81].

R-mode instability in young neutron stars

Any extended object has its own resonant normal modes, depending on its composition and geometry. Normal modes can be spheroidal or toroidal if the oscillation affects respectively the radial or the angular coordinates of the star. For non-rotating stars, spheroidal and toroidal modes are decoupled. In that case, the NS fundamental modes (f-modes) can be excited, as well as pressure and gravity modes (p-modes and g-modes), and they can be classified in terms of the spherical harmonic numbers (l, m) [91]. For rotating stars, the Coriolis force provides a weak restoring force that favours toroidal modes and leads to the so-called r-modes. R-mode oscillation is a toroidal mode, due to fluid motion of neutrons (or protons) in the crust or core of the star, that may be excited in rapidly rotating NSs. They are expected to take place typically on the result of the coalescence of a NS binary, on a supernova remnant or in accreting NSs. Their non-relativistic equivalent associations are

the well known Rossby waves that take place in Earth atmosphere. Perturbations of the NS angular velocity field grow rapidly thanks to the Chandrasekhar–Friedman–Schutz instability until they reach a saturation amplitude and then stops [92]. That saturation amplitude characterizes the emitted wave and is quantified by the dimensionless parameter α. Being a toroidal mode, the r-mode does not produce a significant effect on the quadrupole moment of the NS. Instead, in this case the leading GW emission mechanism is the higher-order current quadrupole. GWs produced by current quadrupole have a different polarization with respect to mass quadrupole. As demonstrated in [93], since the difference between mass and current multipoles is parity, the '+' and '×' signal amplitudes transform as

$$(h_+ \, , \, h_\times) \rightarrow (-h_\times \, , \, h_+) \tag{2.19}$$

So, the detector response to a passing current-quadrupole GW is equivalent to the response to a mass-quadrupole GW with polarization angle rotated by $\pi/4$. Considering a source located at a distance r, its r-mode GW strain amplitude $h_0\,(t)$ is given by [94]:

$$h_0\,(t) = \sqrt{\frac{2^9\pi^7}{5}}\frac{G}{c^5}\tilde{J}MR^3\frac{\alpha f_{\rm gw}^3\,(t)}{r} \tag{2.20}$$

where $\tilde{J}$ is the dimensionless angular momentum of the NS valid for politropic models, M and R are respectively its mass and radius. The GW frequency f_{gw} is related to the NS rotational frequency $f_{\rm rot}$ as

$$f_{gw} \sim \frac{4}{3} f_{\rm rot} \tag{2.21}$$

If we consider also relativistic corrections and rotational effects, Equation 2.21 must be corrected as shown in [94]. Using nominal values of the parameters, the typical expected signal amplitude can be expressed as

$$h_0 \simeq \left(3.6 \cdot 10^{-26}\right)\left(\frac{R}{11.7\,\mathrm{km}}\right)^3\left(\frac{1\,\mathrm{kpc}}{r}\right)\left(\frac{\alpha}{10^{-3}}\right)\left(\frac{f_{\rm gw}}{100\,\mathrm{Hz}}\right)^3 \tag{2.22}$$

where for the dimensionless angular momentum the value corresponding to a Newtonian polytrope with index 1, $\tilde{J} \sim 0.0164$, has been assumed [93]. As in the case of permanent deformations the ellipticity ε played a crucial role on the signal amplitude, here the detectability of the r-mode signal depends strongly on the saturation amplitude α. The GW extracts energy and angular momentum from the mode and the NS itself, so that its slows down its rotation following a power law [93]

$$\dot{\omega}_{\rm rot} = -\left(\frac{4096\pi^7 \mathrm{G}}{225\,c^7}\frac{M^2R^6\tilde{J}^2}{I_{zz}}\right)\alpha^2\omega_{\rm rot}^7 \tag{2.23}$$

Here, the frequency is expected to vary significantly with respect to its initial value, so the signal amplitude itself decreases following the frequency as shown in Equation 2.20. However, as shown in Section 2.1.1, it is clear that r-mode emission would not likely be the unique acting mechanism, as the electromagnetic emission is dominant. As consequence, the NS spin evolution is not expected to follow precisely the 2.23. A recent targeted r-mode search on the "big glitcher" PSR J0537–6910 can be found in [95]. In the same way of the permanent deformations, also with r-modes a non-detection can be useful to put upper limits on the GW amplitude and consequently on the value of the saturation amplitude α.

Newborn millisecond magnetars

Magnetars have been already introduced in Section 2.1 as a sub-population in the $P-\dot{P}$ diagram. They are NSs whose emission is powered by the release of energy from their extremely strong magnetic fields, with magnitude $\sim 10^{15} - 10^{16}$G. They are generally associated to Soft Gamma Repeaters [96] and Anomalous X-ray Pulsars [97], and are typically observed with rotational periods $\sim 1 - 10$ s. However, they are believed to form with millisecond rotational period and then to rapidly loose a big amount of their rotational energy. They would represent a non-negligible fraction of the whole population of young NSs. There are many possible formation channels for millisecond magnetars. The main one is believed to be the collapse of massive stars, associated to core-collapse supernovae and long gamma-ray bursts (GRBs), but there is the possibility to have this outcome as a result of a binary NS merger, thanks to the conservation of the large orbital angular momentum of the two NSs at the time of coalescence [98]. Anyway, this last possibility depends sensitively on the not well constrained maximum mass of a NS. The same outcome could arise from binary white dwarf mergers or neutron star - white dwarf mergers [99]. Recent studies favour the millisecond magnetar model to explain long GRB observations, showing a rapid energy loss compatible with the X-ray and dipole emission [100, 101].

There is a great expectation on newly born NSs to have large internal toroidal fields and correspondingly large ellipticities. Strong differential rotation combined with turbulent convection in the newly-born NS drives an efficient dynamo, which winds up a toroidal field as strong as 10^{16}G. Even if the symmetry axis of the wound-up field is aligned to the rotation axis of the star, the ellipsoidal star will evolve on a viscous dissipation timescale to become an orthogonal rotator through free-body precession, and therefore an optimal GW emitter [102]. By using the same notation than in Section 2.1.1 we can quantify the induced distortion through the ellipticity ε. As stated in [103], internal magnetic fields with magnitude $\geq 10^{16}$G would produce strong ellipticities

$$\varepsilon \sim 10^{-4} \tag{2.24}$$

that in magnetars distant up to few Mpc would produce GWs detectable by Earth-based detectors. The expected wave strain amplitude for a source is formally the same described in Equation 2.10, the GW frequency f_{gw} is twice the NS rotational frequency the same way. Theoretically, also the NS rotation should slow down following the power law in Equation 2.13, but as in Section 2.1.1, we know that the real dynamics is complicated by the most efficient electromagnetic emission. As stated in [103], magnetars are expected to form at a rate of $\geq 1\text{yr}^{-1}$ within the Virgo cluster. Given the Virgo cluster nearness, if a fraction of these has sufficiently high inner magnetic fields, they would be a promising source of observable GWs.

2.2 Boson clouds around spinning black holes

Beside the most traditional sources of GW, a new intriguing potential source has been proposed in the last decade [104]. Among the various dark-matter candidates that have been proposed, the most interesting one for GW searches is that the dark matter is composed of ultralight, electromagnetically invisible bosons. There are various possible ultralight bosons, such as dark photons, the QCD axion or the axion-like particles that arise from the string theory [104, 105, 106], with masses in the range $10^{-20}\text{eV} - 10^{-9}\text{eV}$. These fields interact

very weekly with other standard model particles, but they couple with gravitational fields as the equivalence principle imposes. If such ultra-light bosons exist and they permeate the space, they would clump around spinning BHs through the superradiance process [107]. Superradiance for rotating BHs was first demonstrated by Roger Penrose for particles as a way to extract energy from BHs [108]. The same process can apply to bosonic waves, which can be amplified at the expense of the rotational energy of the BH. The effect is maximized when the bosonic field, with mass m_b, has a Compton wavelength comparable to the Schwarzschild radius of the BH

$$\frac{\hbar}{m_b c} \sim \frac{2\mathrm{G}M_{\mathrm{BH}}}{c^2} \tag{2.25}$$

Under this condition, the bosonic field can clump around the BH, growing and forming a Bose condensate which is analogue to an hydrogen atom, also called *gravitational atom* cloud. This gravitational atom, in analogy with the electromagnetic case, can be characterized by the *gravitational fine-structure constant* α, defined as

$$\alpha = \frac{\mathrm{G}M_{\mathrm{BH}}}{c^3}\frac{m_b}{\hbar} \simeq 0.075 \left(\frac{M_{\mathrm{BH}}}{10\,M_\odot}\right)\left(\frac{m_b}{10^{-12}\mathrm{eV}}\right) \tag{2.26}$$

The superradiant instability has a typical duration of the order of days, depending on the BH mass and spin. As long as the BH dimensionless spin χ_i is above the critical value $\chi_c \sim 4\alpha/(1+4\alpha^2)$, the cloud grows and subtracts energy from the BH. At the equilibrium, the cloud could have reached a mass as big as $\sim 10\%\, M_{\mathrm{BH}}$. Then it starts dissipating, emitting quadrupole GWs through boson annihilation into gravitons. Here, we focus only on GWs from scalar bosons. The timescale of the dissipation is way longer than the superradiant instability one, depending on the BH mass and spin and on the fine-structure constant as

$$\tau_{\mathrm{gw}} \simeq \left(6.5 \cdot 10^4 \mathrm{years}\right)\left(\frac{M_{\mathrm{BH}}}{10\,M_\odot}\right)\left(\frac{1}{\chi_i}\right)\left(\frac{\alpha}{0.1}\right)^{-15} \tag{2.27}$$

Given the very different timescales, if there is a bosonic field forming a gravitational atom cloud, it is likely to be already dissipating. Moreover, the huge duration of the dissipation makes the gravitational signal a CW with respect to typical Earth-based detectors observing times. The emitted wave has proper frequency depending mainly on the boson mass m_b with a second-order correction depening on both the boson and the BH masses, as [109, 110]

$$f_{\mathrm{gw}} \simeq 483\,\mathrm{Hz}\left(\frac{m_b}{10^{-12}\mathrm{eV}}\right)\left[1 - 7\cdot 10^{-4}\left(\frac{M_{\mathrm{BH}}}{10\,M_\odot}\frac{m_b}{10^{-12}\mathrm{eV}}\right)^2\right] \tag{2.28}$$

The GW amplitude slowly decreases over the dissipation time. For values $\alpha \ll 0.1$, the GW emission can be computed with the perturbation theory. Within this limit, the amplitude depends on the fine-structure constant and on the BH mass (both explicitly and indirectly through α) and spin as

$$h_0 \simeq 3\cdot 10^{-24}\left(\frac{\alpha}{0.1}\right)^7\left(\frac{\chi_i - \chi_c}{0.5}\right)\left(\frac{M_{\mathrm{BH}}}{10\,M_\odot}\right)\left(\frac{1\,\mathrm{kpc}}{r}\right)\left(1 + \frac{t}{\tau_{\mathrm{gw}}}\right)^{-1} \tag{2.29}$$

The signal frequency then evolves slowly, with a spin-up due to annihilation and to self-interacting terms. These self-interactions come from the bosons energy level transition and

from the change in the self-interaction energy as the cloud dissipates [111]. In the case of negligible self-interactions, the spin-up is driven by annihilation and is given by

$$\dot{f}_{\rm gw} \simeq + \left(7 \cdot 10^{-15}{\rm Hz/s}\right) \left(\frac{m_b}{10^{-12}{\rm eV}}\right)^2 \left(\frac{\alpha}{0.1}\right)^{17} \tag{2.30}$$

Equation 2.29 shows that also CWs from boson clouds have extremely weak amplitude, if they exist. For this reason, as for NSs we limit the searches to BHs within few kpc at most, which means inside our Galaxy. Inverting Equation 2.28, it turns out that with the sensitivity window between $\sim 10\,$Hz and few kHz of Earth-based detectors we can probe only bosons with masses in the range $(10^{-13} - 10^{-11})\,$eV [110, 109]. Searches for CWs from scalar boson clouds can be directed towards known galactic BHs, or towards directions where they are thought to be present, e.g. the galactic center or globular clusters. Also blind all-sky searches can be performed, assuming that there are lots of unknown nearby BHs that could be potential sources. However, their search hide some difficulties and subtleties that will be addressed in Chapter 4. From a non-detection, we can set upper limits on the GW strain amplitude h_0. These can be translated in upper limits on the boson mass when BH mass and spin are known, or in exclusion regions in the $M_{\rm BH} - m_b$ plane for unknown BHs. Last results from a dedicated all-sky search for boson clouds can be found in [112].

2.3 Search strategies

The methods that can be used for CW searches are so different with respect to the ones used for transient GW searches. The reason is that, while to search for a short transient we have to analyze independently short data chunks searching for signals that have a starting time and a duration, a CW is present in the whole data set. Considering a generic CW source, located at right ascension α and declination δ, with amplitude h_0 and a slow frequency evolution, the strain amplitude at the detector is given by

$$h\left(t\right) = h_0 \left[F_+\left(t, \alpha, \delta, \psi\right) \frac{1 + \cos^2 \iota}{2} \cos\Phi\left(t\right) + F_\times\left(t, \alpha, \delta, \psi\right) \cos\iota \, \sin\Phi\left(t\right)\right] \tag{2.31}$$

Here, ι is the inclination of the source with respect to the line of sight, ψ is the polarization angle of the wave and $\Phi\left(t\right)$ is the phase evolution of the signal. The phase takes into account both the intrinsic GW frequency evolution in the source frame and the frequency modulation that affect the observed signal because of the Doppler effect. Since for all CW sources the frequency evolution is extremely slow (see Equations 2.13 and 2.30) and that all known pulsars have rotational frequency derivatives generally lower, in modulus, than 10^{-9}Hz/s, the source-frame GW frequency $f_0(t)$ can be described by the Taylor expansion

$$f_0\left(t\right) = f_0 + \dot{f}_0\left(t - t_0\right) + \mathcal{O}\left(t^2\right) \tag{2.32}$$

However, the time of arrival of a signal at the detector, t, is shifted with respect to the time of arrival at the Solar System Barycenter (SSB), $\tau(t)$. The latter can be written in terms of the signal time of arrival t at the detector as

$$\tau\left(t\right) = t + \delta t = t - \frac{\vec{p}\left(t\right) \cdot \hat{n}}{c} + \Delta_{E\odot} + \Delta_{S\odot} \tag{2.33}$$

where $\vec{p}(t)$ is the position of the detector with respect to the SSB, $\hat{n}$ is the unit vector pointing to the source direction, and $\Delta_{E\odot}$ and $\Delta_{S\odot}$ are respectively the solar system Einstein

and Shapiro time delays [113]. Their impact on the observed frequency is not negligible in targeted searches, where the frequency resolution is of the order of 1/year. Due to the Doppler effect, the observed GW frequency at the detector is spread with respect to the emitted frequency as

$$f_{\mathrm{gw}}(t) = \frac{1}{2\pi}\frac{d\Phi(t)}{dt} = f_0(t)\left(1 + \frac{\vec{v}(t)\cdot\hat{n}}{c}\right) \tag{2.34}$$

where $\vec{v}(t)$ is the velocity vector of the detector with respect to the SSB reference frame. As a consequence, the signal at the detector is no more monochromatic. Instead, the frequency experiences a drift due to the presence of spin-down/up and eventual subsequent terms $\{\dot{f}_0, \ddot{f}_0, ...\}$, and a double oscillation due to the annual and daily motion of the Earth. In fact, the velocity of Earth in the SSB can be decomposed in the orbital and rotational ones, $\vec{v} = \vec{v}_{\mathrm{orb}} + \vec{v}_{\mathrm{rot}}$. The orbital velocity has annual periodicity and has a mean magnitude $v_{\mathrm{orb}} \simeq 10^{-4}c$. The rotational velocity has daily periodicity and a mean magnitude $v_{\mathrm{rot}} \simeq 10^{-6}c$. The two contributions have act on very different scales, and their amplitude and phase depend on the sky position of the source. In Figure 2.4 I show an example of Doppler modulation on the time evolution of the frequency of the expected GW from the known pulsar PSR J0835-4510, also known as Vela. The blue plot is obtained using the observed position of Vela, while the red one is obtained using a wrong sky position. The modulation induced by the rotational motion of the Earth results in daily oscillations of the frequency, 2 orders of magnitude weaker than the yearly oscillation induced by orbital motion. The

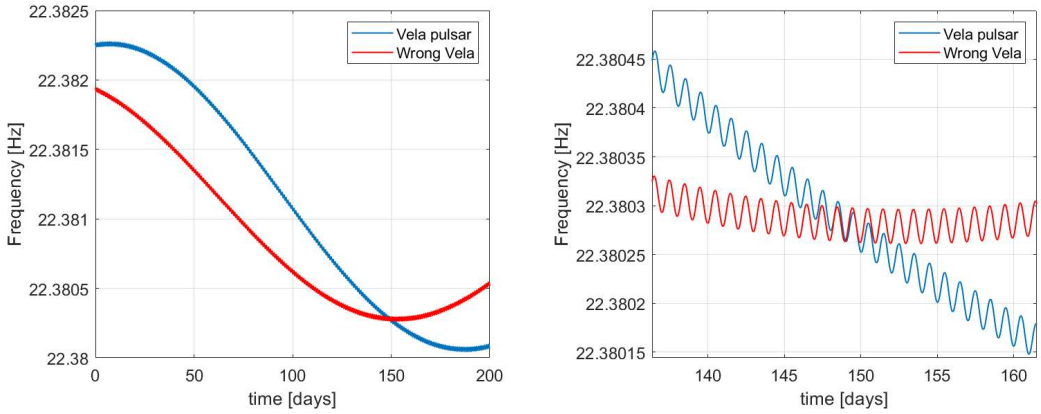

Figure 2.4: Expected evolution in time of the GW frequency from the Vela pulsar, in its actually observed sky position (blue line) and considering a different sky position (red line). The left plot shows the whole evolution, where the annual modulation is dominant. The right plot shows a zoom on day-scale, at which the daily modulation becomes visible.

detector pattern functions $F_{+/\times}$ encode the varying angle between the wavefront and the detector arms, because of the Earth rotation with angular velocity Ω_r. The formulation given in Equation 1.66 have some practical limitations for CW searches, since it is computed in the reference frame of a steady detector. They can be more conveniently written in the equatorial coordinate system as

$$\begin{aligned} F_+(t) &= \sin(\zeta)\left[a(t)\cos(2\psi) + b(t)\sin(2\psi)\right] \\ F_\times(t) &= \sin(\zeta)\left[b(t)\cos(2\psi) - a(t)\sin(2\psi)\right] \end{aligned} \tag{2.35}$$

where ζ is the angle between the two arms, which is typically $\pi/2$ for Virgo and LIGO detectors, and ψ defines the polarization angle of the source wave frame. The pattern functions $a(t)$, $b(t)$ depend both on the orientation of the detector and the source as

$$\begin{aligned}
a\left(t\right) =& \frac{1}{16}\sin 2\gamma\left(3-\cos 2\lambda\right)\left(3-\cos 2\delta\right)\cos\left[2\left(\alpha-\phi_r-\Omega_r t\right)\right]+\\
&-\frac{1}{4}\cos 2\gamma\sin\lambda\left(3-\cos 2\delta\right)\sin\left[2\left(\alpha-\phi_r-\Omega_r t\right)\right]+\\
&+\frac{1}{4}\sin 2\gamma\sin 2\lambda\sin 2\delta\cos\left[\alpha-\phi_r-\Omega_r t\right]+\\
&-\frac{1}{2}\cos 2\gamma\cos\lambda\sin 2\delta\sin\left[\alpha-\phi_r-\Omega_r t\right]+\frac{3}{4}\sin 2\gamma\cos^2\lambda\cos^2\delta
\end{aligned}$$

$$\begin{aligned}
b\left(t\right) =& \cos 2\gamma\sin\lambda\sin\delta\cos\left[2\left(\alpha-\phi_r-\Omega_r t\right)\right]+\\
&+\frac{1}{4}\sin 2\gamma\left(3-\cos 2\lambda\right)\sin\delta\sin\left[2\left(\alpha-\phi_r-\Omega_r t\right)\right]+\\
&+\cos 2\gamma\cos\lambda\cos\delta\cos\left[\alpha-\phi_r-\Omega_r t\right]+\\
&+\frac{1}{2}\sin 2\gamma\sin 2\lambda\cos\delta\sin\left[\alpha-\phi_r-\Omega_r t\right]
\end{aligned}$$

where (α, δ) are the equatorial coordinates of the source, λ is the detector latitude, γ is the counterclockwise angle between the bisector of its arms and the eastward direction and ϕ_r is a phase defined implicitly by the interferometer's longitude. The effect of the angular pattern functions is an amplitude modulation of the GW signal with periodicity of 1/2 and 1 sidereal day. Therefore, the interferometer's response to a monochromatic source in the Earth center's reference frame is splitted in up to five distinct frequency components, corresponding to the "carrier" frequency and two pairs of positive and negative sidebands, respectively at $f_{\rm gw}$, $f_{\rm gw} \pm f_\oplus$ and $f_{\rm gw} \pm 2f_\oplus$, with the sidereal frequency $f_\oplus = 1.16 \cdot 10^{-5} Hz$. The way the signal power is splitted in the five peaks depend on the sky localization of the source. In Figure 2.5 a simulated CW signal from an hypothetical source emitting at $f_0 \simeq 108.86\,\mathrm{Hz}$ from a given sky position is shown. The sidereal modulation depends on the sky coordinates of the source. Algorithms that search for CWs have to take into account for all the presented features. From one point of view, frequency and amplitude modulations strongly complicate the signal pattern, which otherwise would be nearly monochromatic. Search algorithms should have under control the resolution of the parameter space, since any error on the signal parameters rapidly propagates on the expected phase and over long observing times. On the other side, these modulations are a powerful tool to distinguish between CWs, with astrophysical origin, and narrow-band spectral artifacts that are present in the detectors data.

Depending on the available information on the sources, different search strategies can be used. A general review on all the existing search methods for CWs can be found in [81]. We can classify them in three families:

- Targeted searches, when all the parameters are known and the timing data are available (as for known pulsars).
- Directed searches, when the source position is known to a good accuracy, while rotational parameters are unknown (e.g. SN remnants, globular clusters, galactic center).
- All-sky searches, looking for unknown sources from any possible sky direction.

In the following I briefly describe the main features of the different kinds of searches.

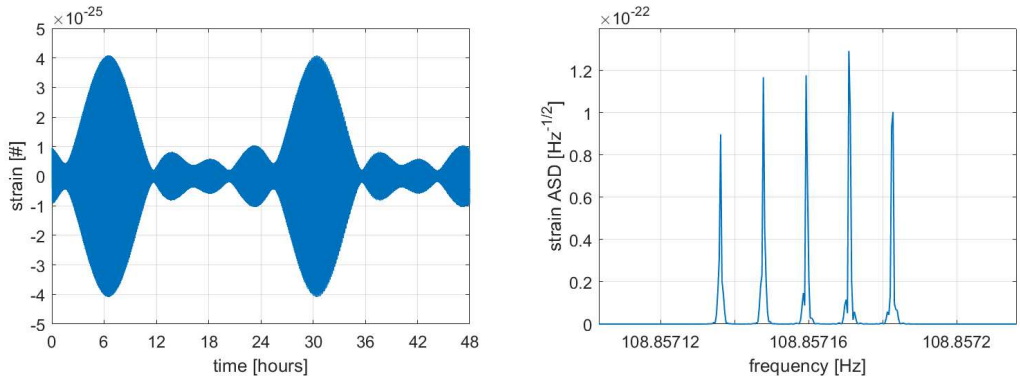

Figure 2.5: An example of the amplitude modulation that characterizes a CW. Left plot shows a two-day time series of a simulated CW, without noise, with carrier frequency $f_0 \sim 108.86\,\mathrm{Hz}$ from a fixed sky position. The signal amplitude shows a pattern with periodicity of a sidereal day. Right plot shown the amplitude spectral density of the signal, after the removal of the Doppler modulation. The spacing between the peaks corresponds to the sidereal frequency $f_\oplus \simeq 1.16 \cdot 10^{-5}\mathrm{Hz}$.

2.3.1 Targeted searches

Targeted searches assume a complete knowledge of the source parameters which determine the CW signal. Since the hypothetical waveform is known, fully coherent methods based on matched filter provide the best sensitivity. The phase of the CWs is assumed to be locked to the rotational phase of the star. This part is crucial, since for each target we need to get very precise timing data from electromagnetic observatories. The observations are typically made in radio and X-ray wavelengths, and are provided by the the CHIME, Hobart, Jodrell Bank, MeerKAT, Nancay, NICER, and UTMOST observatories [115]. As an ideal case, we can compute the theoretical SNR of a monochromatic signal with amplitude h_0 and frequency f_0 with respect to the detector strain sensitivity $S_n(f)$ as [7]

$$\frac{S}{N} = \sqrt{\langle F_+^2 \rangle} \left(\frac{T_{\mathrm{obs}}}{S_n\left(f_0\right)} \right)^{1/2} h_0 \tag{2.36}$$

where the detector pattern function F_+ has been averaged over the solid angle and over the polarization angle. Thus, the SNR of a CW scales as the square root of the observing time. Sufficiently long observing times can compensate for the extremely weak amplitudes, which are at least five orders of magnitude weaker than the ones of coalescing binaries. However, several factors limit the sensitivity. The matched filter is optimal on stationary and Gaussian noise, but detector noise is non-stationary over the observing run. As a further complication, some pulsars randomly exhibit glitches, i.e. jumps on the pulses frequency. After the glitch, the pulses jump to an higher frequency and progressively slow down to their previous trend, but they are not in phase with the pre-glitch timing. The presence of glitches limits the maximum coherent observing time: we can apply the matched filter on shorter data chunks, cut in correspondence with the glitches, and then combine the statistics. However, the result is intrinsically sub-optimal with respect to an uninterrupted analysis.

The general approach for targeted searches consists in demodulating the detector data, through hetherodyne or resampling methods, in order to correct for Doppler modulation

and signal spin-down and to get back with a monochromatic signal at the proper frequency f_0. The resampling exploits the fact that the observed modulations are the effect of a time-dependent delay of the received signal. The time of each sample is re-defined taking into account the various contributions [116]. This technique has the advantage of being independent from the frequency (at least the Doppler), but is typically computationally expensive, since according to the Nyquist theorem the sampling time needed to properly reconstruct the signal is inversely proportional to the frequency. In heterodyne correction the data are multiplied by a complex exponential function that removes the phase modulation [117]. This operation is much cheaper than the resampling, but is referred to a specific frequency and is limited to it. Given the length of typical observing times, the huge amount of corresponding data and the narrow-band localization of the signal in frequency, the analysis are typically carried on sets of sub-sampled data. The main methods currently used are the Time-domain Bayesian method [117], the $\mathcal{F}$-/$\mathcal{G}$-statistics method [114, 120] and the 5-vector method [118, 119]. The first two implement the matched filter in time-domain, the latter implements a matched filter in the Fourier space. The search is typically focused on the pulsars with highest spin-down limit. A particularly interesting subset, the so-called high-value pulsars, is composed by those pulsars with spin-down limit greater than the search sensitivity.

The most recent results for targeted searches are obtained from the O3 run [115]. Since no significant candidates are found, for each pulsar a 95% credible upper limit on the amplitude $h_0^{95\%}$ is placed. The results are shown in Figure 2.6. Among 236 searched pulsars, for 23 of them have upper limits lower than their spin-down limit. In particular, the Crab and Vela pulsars have the highest h_0^{sd}. The Crab pulsar rotates at $f_{\mathrm{rot}} \sim 29.7\,\mathrm{Hz}$ with a period derivative $\dot{P} \sim 4.2 \cdot 10^{-13}$, which gives a spin-down limit $h_0^{\mathrm{sd}} = 1.4 \cdot 10^{-24}$. The upper limit for its amplitude is $h_0^{95\%} = 1.3 \cdot 10^{-26}$, meaning that its ellipticity is not grater than $\varepsilon^{95\%} = 7.2 \cdot 10^{-6}$, and that GWs contribute to less than 0.009% to the observed rotational energy loss. The Vela pulsar rotates at $f_{\mathrm{rot}} \sim 11.2\,\mathrm{Hz}$ with a period derivative $\dot{P} = 1.2 \cdot 10^{-13}$ and so has a spin-down limit $h_0^{\mathrm{sd}} = 3.4 \cdot 10^{-24}$. Its upper limit is $h_0^{95\%} = 1.8 \cdot 10^{-25}$, which implies an ellipticity not greater than $\varepsilon^{95\%} = 9.3 \cdot 10^{-5}$ and that GWs are responsible for less than 0.05% of the observed energy loss.

2.3.2 All-sky searches

On the opposite side, all-sky searches look for CWs from unknown NS from any possible direction in the sky. Targeted searches achieve the best sensitivities, but they are limited to search only for known pulsars, which are a little fraction of the total estimated in the Galaxy. As far as we know, there may be NSs that are nearest than the known population, or that exhibit stronger spin-down and have larger ellipticities. This motivates the need to perform blind searches covering the whole sky directions, frequencies and frequency derivatives. Unfortunately, such search cannot be performed through the fully-coherent techniques used for targeted searches. Given the length of the observing times, $T_{\mathrm{obs}} \sim 1$ year, since the resolution of each parameter scales with T_{obs}, there would be an huge parameter space to be explored to demodulate the data for each possible combination of sky position, frequency and frequency derivative. The full broad-band search would be computationally unfeasible, therefore coherent all-sky searches are practically impossible [121]. Hence, for those searches the so-called *semi-coherent* algorithms are typically used.

The basic idea behind the semi-coherent searches consists in splitting the whole data series in N_s segments of length T_{coh} eventually interlaced by a relative factor $1/\alpha$, so that

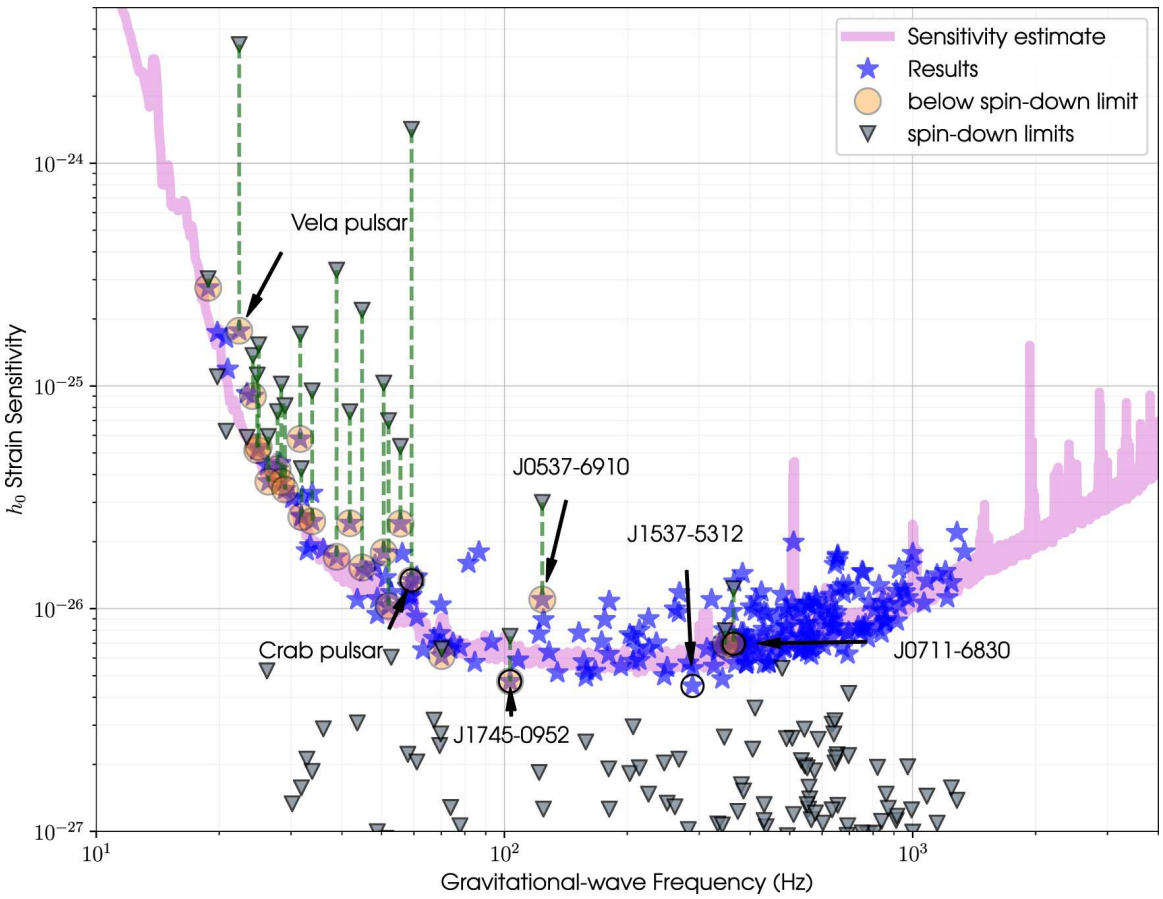

Figure 2.6: Upper limits for h_0 from the O2-O3 targeted search, taken from [115]. Gray triangles represent the spin-down limits for each targeted pulsar. Blue stars show 95% credible upper limits on their corresponding amplitudes of h_0. The pink curve gives an estimate of the expected strain sensitivity of all three detectors combined during O3. Green dashed lines connect h_0 upper limits with the spin-down limits for pulsars that have surpassed it.

$T_{\rm obs} = \alpha N_s T_{\rm coh}$. The segments are individually coherently analyzed and then combined together incoherently, so the phase information across different block is lost. The segment length is chosen in such a way that CWs inside it would be monochromatic within the frequency resolution $\delta f = 1/T_{\rm coh}$. The segments have typical duration $T_{\rm coh} \sim 10^3{\rm s} - 10^4{\rm s}$, so for 1 year of data their number is typically $N_s \sim 10^3 - 10^4$, assuming a typical interlacement by a factor 1/2. In this way the computational costs are strongly reduced and the search becomes feasible [121]. On the other side, the lost information on the signal phase implies a sensitivity loss with respect to a coherent search. In a single stack, the optimal SNR of a signal is given by substituting $T_{\rm coh}$ to $T_{\rm obs}$ in Equation 2.36. When the N_s stack spectra are summed, the variance is reduced by a factor $1/\sqrt{N_s}$, so at the end the global SNR is given by [7]

$$\frac{S}{N} = \frac{\sqrt{\langle F_+^2 \rangle}}{N_s^{1/4}} \left(\frac{T_{\rm obs}}{S_n\left(f_0\right)} \right)^{1/2} h_0 \tag{2.37}$$

This means that semi-coherent searches theoretically achieve a sensitivity lower than the coherent searches by a factor $N_s^{1/4}$, which corresponds roughly to one order of magnitude.

In practice, the outputs of the analysis have different statistical distributions and one has to put a maximum threshold on the number of candidates to be selected. This implies different thresholds for the selection of signal candidates, and results in a reduced sensitivity loss with respect to coherent searches (see [122] for an example). In any way, the sensitivity distance is reduced with respect to coherent searches.

There are many different search algorithms that perform all-sky searches. These are the Frequency-Hough [122], the Sky-Hough [123], the Time-domain F-statistics [124], the SOAP [125] and Einstein@home [126]. They implement different strategies and often cover a different parameter space. A comparison of these methods can be found in [127]. The last LIGO-Virgo all-sky search during the O3 run did not produce significant candidates, so 95% credible upper limits $h_0^{95\%}$ have been placed over the whole frequency space by each search pipeline. The results are shown in Figure 2.7. Since the search has no targets, the $h_0^{95\%}$ upper limits cannot be translated automatically in upper limits on the NSs ellipticities [128].

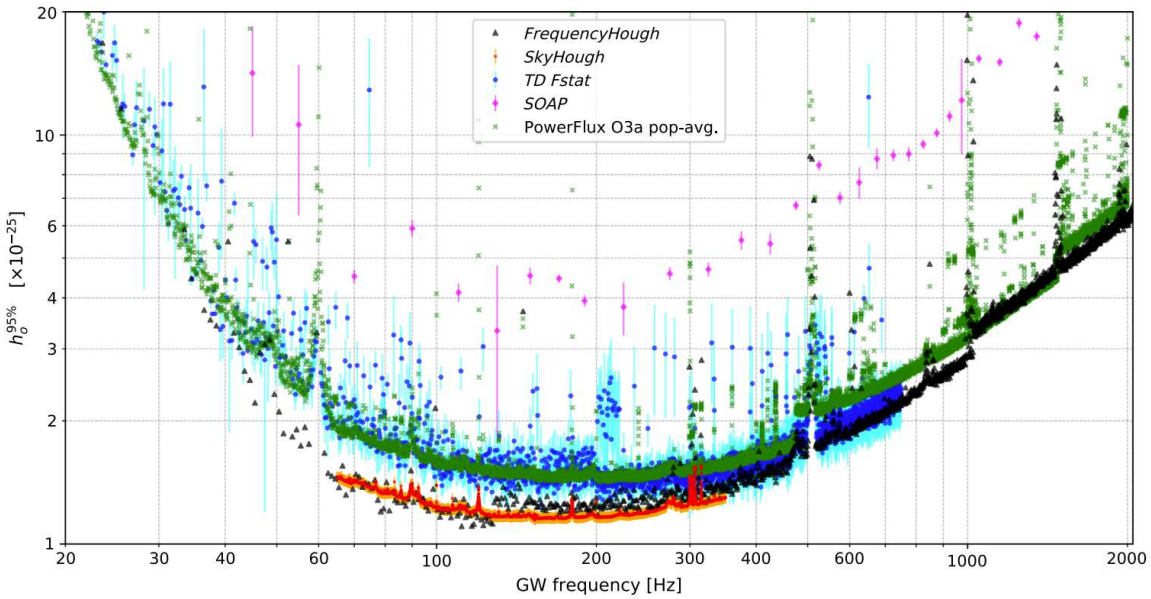

Figure 2.7: Comparison of broadband search sensitivities obtained during the O3 run, taken fron [128]. The results shown are obtained by the FrequencyHough pipeline (black triangles), the SkyHough pipeline (red squares), the Time-Domain F-statistic pipeline (blue circles), the SOAP pipeline (magenta diamonds) and PowerFlux (only on O3a data, green crosses). Vertical bars mark errors of $h_0^{95\%}$.

2.3.3 Directed searches

Directed searches constitute an intermediate situation between targeted and all-sky searches. In targeted searches, all the sources parameters are known. In all-sky searches, no parameter is known. However, there is a variety of cases in which the sky position of a presumed source is known, but no timing data is available, so the source rotational frequency and its derivatives are unknown. An example can be given by a non-pulsating X-ray source at the center of a supernova remnant, or by the Milky Way center, which is thought to host a large population of NSs. The methods used for directed searches are semi-coherent too,

but they take advantage from the knowledge of the sky position. The data are typically demodulated through hetherodyne or resampling methods in order to compensate for the Doppler effect only. Then, data are split in stacks as in all-sky searches, but in this case one can take advantage from the corrected Doppler enlarging the length of the stacks. The directed search in this can achieve better sensitivities with respect to the all-sky. The most recent searches pursued on the Galactic Center and on the low-mass x-ray binary Scorpius X-1 are reported in [129] and [130] respectively. Also in these cases no detection has been made, so upper limits on the CW amplitude are set for the explored frequency range. In particular, the most stringent limit for the Galactic Center is $7.6 \cdot 10^{-26}$ at 142 Hz, while the best upper limit for Scorpius X-1 is $6.16 \cdot 10^{-26}$ at 256 Hz.

Chapter 3

Noise Hunting for continuous waves at Virgo

A good wave hunter
is first of all a good noise hunter.

In any experiment where the searched signals are extremely weak with respect to the noise floor, the experimenter has to master the possible noises that can degrade the sensitivity or produce spurious artifacts that can mimic some signal features. In this sense, the chances to detect rare or weak events are increased as the experimenter gets a deep knowledge of the typical artifacts that affects its search. A good knowledge of those features would allow them to build search algorithms that are able to distinguish between real signals and spurious artifacts. In GW searches with Earth-based detectors, the study of noise artifacts can become also an independent activity that goes in parallel with the dedicated searches. *The work to improve the sensitivity of CW searches can be done not only on the side of software development, but can also start directly from the mitigation of noise sources that disturb the search algorithms.* This work can be done from two different points of view. One is the *Detector Characterization* (DetChar), which is basically a data-analysis activity, focused on the detector side [131, 132]. Its aim is to identify noises of various origin inside the detector data and to look for correspondences with the auxiliary channels, i.e., sensors that are placed all over the detector infrastructure, in order to identify their origin. More in general, the DetChar activity evaluates the quality of the data taken during the observing time and permits to assess if candidate signals are more likely due to noise artifacts or to astrophysical sources. On the other side *Noise Hunting* is more an instrumental-side activity. The aim is to characterize the noise sources and the way in which the noise propagates and couples with the interferometer main channel. The subsequent step, if possible, is the mitigation of that noise acting directly on the source or on the propagation mechanism and, finally, to assess the effectiveness of the mitigation action. Clearly, DetChar and Noise Hunting are complementary activities that constitute a fundamental part of the commissioning and operation of the interferometer.

In this chapter I present the contribution that I am giving to the commissioning of the Virgo interferometer, on the noise hunting activity. The work is not yet concluded, since the commissioning of the interferometer has been delayed for issues on the instrument sensing and control and other external factors. In fact, from one side the noise hunting activity can be started independently from other activities, just characterizing the potential noise sources and possibly mitigating them. On the other side, it needs stable and reproducible

interferometer locks in order to look at its sensitivity curve, to assess the actual impact of the noise sources and of the mitigation actions. For this activity I have focused on the typical noise sources that can limit CW searches.

3.1 Noises affecting continuous waves searches

The kind of noises that impact CW - and also stochastic background - searches are different from those that disturb short-duration GW searches, like those for CBCs and bursts. While the latter are degraded mainly by the presence of short-duration glitches [133], CW searches are mainly affected by long-lived narrow peaks in frequency spectra, typically referred to as lines [134]. Since CW signals are intrinsically narrow-band, the presence of lines in the same frequency region can degrade the sensitivity up to the point of makin the search blind at that frequency. In the Solar System barycenter frame, a CW is nearly monochromatic, while in the detector frame it is shifted into many frequency bins by the Doppler effect. Instead, a narrow stationary spectral artifact is nearly monochromatic in the detector frame, and is spread in many frequency bins when it is projected in the Solar System barycenter. These opposite characteristics can be used to discriminate the candidate signals. This can be done more efficiently in targeted searches, where the knowledge of the timing from ephemerides can be used to demodulate the signal at the expenses of noise lines. Conversely, all-sky searches are more impacted by the presence of spectral lines, that could make them blind in the parameter space region interested by the line. The time-frequency plot in Figure 3.1 gives an idea of the problem: in Virgo O3 data, at $\sim 18.6\,\mathrm{Hz}$ there is a $\sim 0.02\,\mathrm{Hz}$ wide wandering line, which has been identified as generated by the air handling unit that served the clean rooms in the central building. I have generated a simulated CW signal with frequency overlapping the noise line, and then added it to the Virgo O3 data. The aim was to show that if a CW is present in that frequency range, it would be probably overwhelmed by the noise, since typically all-sky algorithms search for excess-of-power from a CW inside each FFT. In fact, very often the frequency regions containing spectral noises are vetoed and excluded from the search.

The output data from an interferometer is generally non-stationary and non-Gaussian if considered over the whole observing run. However, if we restrict to shorter time periods, they can be considered approximately as stationary within that periods, with the exception of wandering lines, i.e. spectral narrow noises that change frequency in time. Moreover, the data can be considered as mainly Gaussian, with the addition of non-Gaussian artifacts given by short-duration glitches and long-duration lines. Spectral lines can be characterized through the Q-factor, which is the ratio between the frequency at the maximum and the line width at half maximum. They can be roughly classified as:

- **Stationary lines**, whose frequency remains unchanged during the whole observing time. They are typically associated to resonant modes in mechanical systems, e.g. the violin modes of the mirrors suspensions or the power mains (typically 50 Hz in Europe, 60 Hz in USA).
- **Wandering lines**, whose frequency slowly varies in time, both regularly and randomly. They are typically characterized by lower Q-factors with respect to resonant modes, and are often generated by the detector infrastructure, like motors, fans, belts and pumps in the air conditioning system.

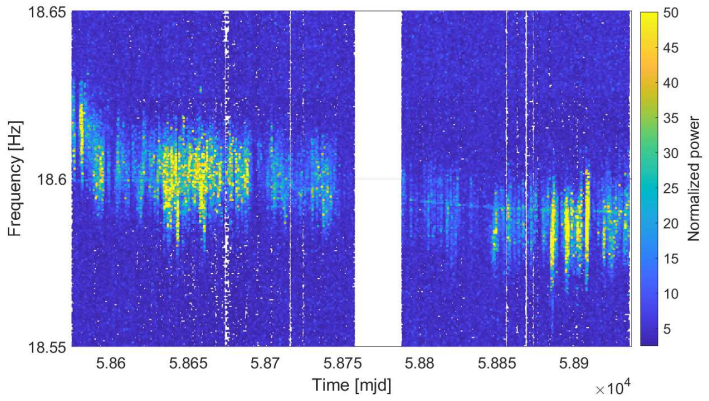

Figure 3.1: Time-frequency PM of Virgo O3 data for the whole run duration in the 18 - 19 Hz band. The plot is zoomed on a wandering line $\sim 0.02\,\mathrm{Hz}$ wide at a $\sim 18.6\,\mathrm{Hz}$ frequency, originated from an air handling unit in the central building of Virgo. In the data has been added a simulated CW signal with parameters $f_0 \simeq 18.6\,\mathrm{Hz}$ and $\dot{f}_0 = -3.0 \cdot 10^{-10}\mathrm{Hz/s}$, an unrealistically strong amplitude $h_0 = 2 \cdot 10^{-23}$ (in order to make it visible by eye) and sky localization $\alpha \simeq 37.4\,\mathrm{deg}$, $\delta \simeq -29.5\,\mathrm{deg}$.

- **Comb**, sets of lines occurring in distinct pattern with even spacing. Their frequencies at a given time can be expressed as $f_n(t) = f_0(t) + n\Delta f$, where Δf is the spacing and n is an integer indicating the n-th line. They can be either stationary and time-varying. Some possible sources are errors in timing systems, modulations induced in power supplies, too coarse digitization used in digital-to-analog conversions and so on.

Indicatively, the instrumental lines that degrade CW searches have typical Q-factors $\sim 10^3$ or greater. For comparison, CWs from astrophysical sources are broadened by a factor $\sim f_0 \cdot 10^{-4}$ because of Earth's orbital Doppler. There are many different ways the noise disturbances can couple to the GW channel [134]. One of the most common is the coupling through shared power or ground: if an electronic component drags current with periodic voltage drops, it will propagate these drops with all the components that share the supply with it. If there are optical or magnetic actuators that share the current, they will be affected by the same drop. Another typical noise comes from the scattered light inside the interferometer. Scattered light noise occurs for example when a tiny stray light beam hits an interferometer part, the scattering source, that is ground connected (e.g. a wall of the vacuum chamber) and vibrate. Scattering back into the main beam path this light carries a phase noise with the signature of the vibration of the scattering source. Coil-magnet actuators on the Virgo test masses and along the suspension chain can also couple directly with magnetic or electrostatic fields present in the experimental buildings [135]. Some noise sources can enter the interferometer directly through mechanic coupling, e.g. through the thermally excited resonances of the suspension wires of the optics. Finally, noise lines can be generated directly by data acquisition artifacts and non-linear couplings.

Aside spectral lines, CW searches obviously also benefit from broad-band noise reduction. Recalling Figure 2.3, a not negligible number of known pulsars have their spin-down limit just above the Advanced LIGO design sensitivity curve. Most isolated pulsars has expected GW frequency $< 100\,\mathrm{Hz}$, while the majority of pulsars in binary systems has GW frequency $> 100\,\mathrm{Hz}$. If we assume that the subset of known pulsars is representative of the

whole NS galactic population, this means that, generally speaking, searches for isolated pulsars benefit from low-frequency noise reduction and searches for pulsars in binary systems mainly benefit from high-frequency noise reduction. While lowering the noise floor at high frequencies is currently mainly a matter of circulating power, quantum noise and coating thermal noise, the low-frequency noise wall (i.e. below 100 Hz), after lowering quantum and thermal noise, is limited by seismic noise. Since my focus is on isolated pulsars, in my work I have focused mainly on low-frequency noise. In particular, my activity has regarded the hunt for noise lines associated to the vacuum system, the air conditioning infrastructure and to the external environment.

3.2 Technical and environmental noises

In Section 1.2.4, the main fundamental noise sources that determine the sensitivity curve of an interferometric detector have been introduced. Beside them, there are the so-called *technical noises* and *environmental noises*. The impact of the environment on Virgo observing runs is discussed in great detail in [136, 137]. Technical noises include all the disturbances generated by the interferometer components, from the laser injection to the final detection passing through all the intermediate stages. From the beginning, the generated laser is not perfectly stable: it introduces some noise on its intensity, frequency and polarization, and moreover the beam pointing mechanism is affected by uncertainties. The injection system uses multiple modulation oscillators (the EOM introduced in 1.2.3) which are affected by intrinsic phase and amplitude noise. The control loops used for beam pointing and more generally in the input benches produce a noise associated to the sensors and the actuators. The injection system introduces also scattered light noise, due to low frequency motions of suspended benches or to environment-driven vibrations for in-air benches and not suspended benches. More in general, the scattered light issue involves also the detection system and all the suspended baffles associated to the optics. The detection system includes the output mode cleaner and the suspended benches that host the array of photo-detectors. The output mode cleaner introduces noises in terms of length noise and fluctuations in the mode polarization. The photo-detectors have their own electronic noise, and in general all the controls associated to the suspended benches that host them are affected by sensor and actuator noise. The thermal compensation system, which adjusts the radius of curvature of the optics to compensate for the curvature induced by the circulating laser, introduces magnetic, electrostatic and thermal noise associated to the ring heaters, which are placed in correspondence of each optic. The superattenuator and the payload, i.e. the last stage of the pendulum to which the optics are connected, are affected by the control noises, and moreover the presence of residual charges on the mirrors induce electrostatic noise on the actuators. The longitudinal and angular controls used to keep the interferometer locked are affected by sensing noise due to the interface with injection and detection systems, by the actuation noise due to the interface with superattenuators and payloads and by numerical noise due to the interface with the data acquisition system. The data acquisition itself introduces phase and amplitude noise on the demodulation of the output signal. Also the calibration process is affected by noise through the photon calibrator and the Newtonian calibrator.

The technical noises on which I have worked are associated to the infrastructure and vacuum systems. The former includes all the noises generated by Heating, Ventilation and Air Conditioning (HVAC) devices: air handling units (AHU), hot and cold water pumps,

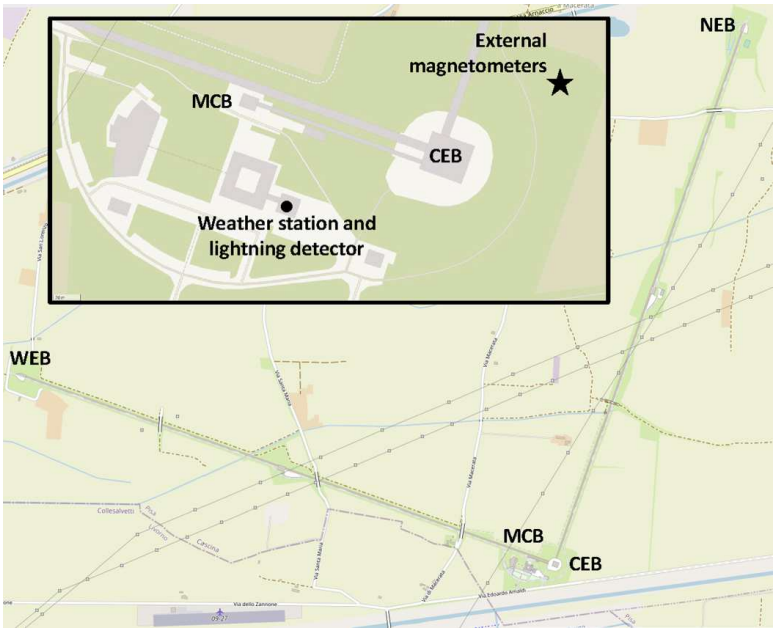

Figure 3.2: Map of the EGO site, taken from [138, 136]. The Virgo detector is shown, with the location of the main buildings identified in the text. The central insert shows a zoom around the interferometer vertex, with the Central Building (CEB) and Mode-Cleaner Building (MCB) highlighted.

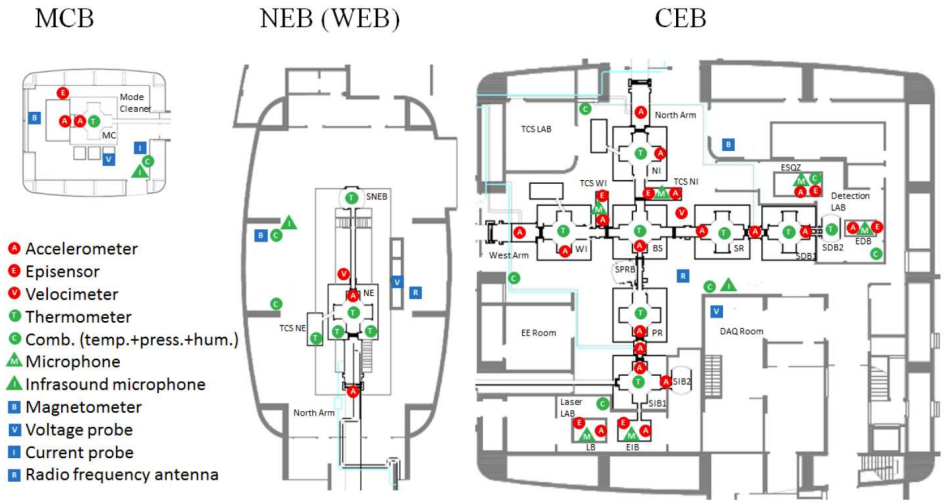

Figure 3.3: Virgo environmental probes, taken from [139, 136]. Top left: mode cleaner building (MCB). Middle: North end building (NEB). West end building (WEB) is identical. Right: central building (CEB).

air compressors, heaters and chillers. The latter includes the noise generated by turbo-molecular pumps, dry pumps and cryogenic traps. All these units are displaced along all the experimental buildings of Virgo, shown in Figure 3.2. The Central Building (CEB) hosts the majority of the optics, which are put under vacuum towers: the beam splitter tower (BS), the West and North input towers (WI, NI) that host the West and North input

mirrors, and the power-recycling and signal-recycling towers (PR, SR) hosting the power-recycling and signal-recycling mirrors. Then, there are the input tower (IT) bringing to the input benches, which include an under-vacuum part and in-air parts like laser, external injection benches and the pre-stabilized laser, and the detection tower (DT) which brings to the detection laboratory. The North-End and West-End Buildings (NEB, WEB) host the North-End and West-End towers respectively, each one containing the corresponding end mirror and the suspended benches with the photo-detectors to control the locking of the Fabry-Perot cavities. With respect to the scheme described in Sections 1.2.2,1.2.3, the North and West arms correspond to the 'x' and 'y' arms respectively. Finally, the Mode Cleaner Building (MCB) hosts the end mirror of the input mode cleaner.

To monitor the conditions of the surrounding environment, a distributed network of probes is used all over the experimental buildings, as shown in Figure 3.3 [140]. There are accelerometers, episensors and velocimeters placed on the ground and on towers and benches to measure seismic vibrations, microphones and infra-sound microphones to detect acoustic vibrations, magnetometers to monitor magnetic fields in each structure, voltage and current probes and thermometers. In particular, accelerometers, episensors and velocimeters are sensitive to local seismic noise. However, there is a superposition of vibrations associated to human activity on the site and in the nearing and vibrations produced by the infrastructure and vacuum devices mentioned above. The effect is the raising of the seismic floor with respect to purely seismic vibrations. With the progressive improvement of the detectors sensitivity, we expect the interferometer to become more and more sensitive to technical noises.

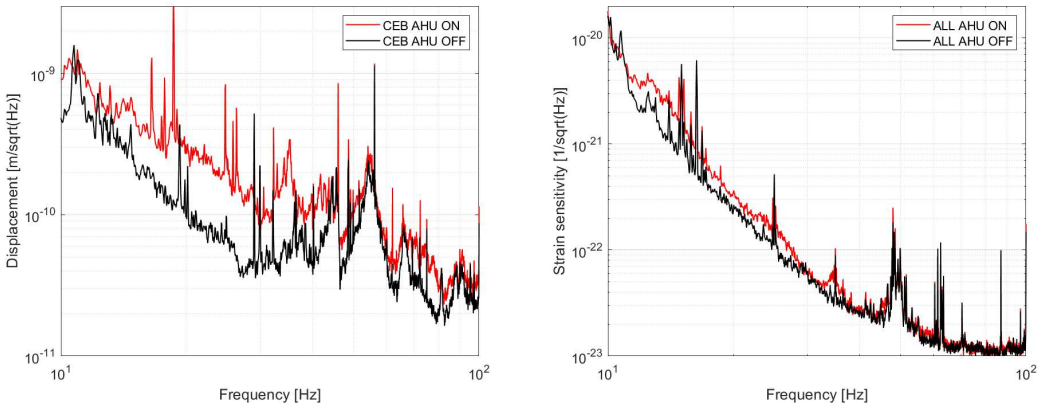

Figure 3.4: Effect of turning off the conditioning systems at the beginning of the O3 run [140, 141]. The left plot shows the impact of the switch-off on the floor displacement in CEB, while the right plot shows the impact on the detector strain sensitivity. The red curves represent the situation in which all the devices are properly working, while the black curves when all the devices are turned off.

In the plots in Figure 3.4 a test done in 19th of April 2019, at the beginning of the O3 run, is shown when all the conditioning systems of Virgo have been switched off for half an hour. The test is explained more in detail in [140, 141]. Here, it is useful to note how the seismic noise floor reduces when the units are switched off, as well as many noise lines associated to AHU fans and motors. The positive effect on the detector strain sensitivity is well visible, with a broad-band noise reduction in the 10 - 60 Hz region. For broad-band

GW searches like CBCs, it has been estimated that the impact of this reduction corresponds in an increase of ~ 3 Mpc in the distance at which a binary NS coalescence can be detected, a $\sim +6\%$ relatively to the sensitivity reached at the time [140].

Obviously, it is not possible to keep all the conditioning units switched off, as they play a central role in maintaining the stability of the physical parameters, like temperature, humidity and cleanliness, in the experimental buildings. However, this measure motivates an increasing effort in insulating or at least mitigating the potential noise sources, since their impact will be stronger as the detector sensitivity improve.

There are various methods used for noise hunting [140]. The first step is typically the data mining. From the reconstructed strain of the detector, noise features are identified and analyzed to track their evolution and eventually link a change in their trend to actions made or events occurred at the same time. Then, a dedicated software searches for coherence between the strain output and the thousands of auxiliary sensors displaced over all the Virgo site. The searches are done looking for linear coupling but also for more challenging non-linear coupling, like beatings or scattered light. With the help coming from data mining, several experimental actions are done to find the source of a noise. One method is the so-called *sniffing*, which consists in inspecting the experimental area with portable sensors looking for the specific noise. Another method, the *switch-off test*, consists in switching off the various devices one at a time. The right source is identified when the noise disappears as it is turned off. Another method consists in doing *noise injections*, causing localized enhancements of the ambient noise up to produce a measurable effect in the detector strain: in this way it is possible to compute the noise coupling function. Once the source is identified, several mitigation actions can be performed. All these actions can be made also in a preliminary way, in absence of a fully locked detector, in order to characterize the noise emitted by the present devices.

A very interesting example of how CW searches can directly benefit from noise hunting comes from the second scientific run of initial Virgo, VSR2, in 2009. In that occasion, during off-line data analysis the *NoEMi* pipeline (Noise frequency Event Miner) found a double wandering line [142]. This noise partially was superposing the frequency band of the expected GW from the Vela pulsar, which at that time was emitting at ~ 22.38 Hz, causing a sensitivity loss by about 20%. Its pattern is shown in Figure 3.5(a,b). NoEMi found a coincidence between that noise and an accelerometer put on the thermal compensating system optical bench (Figure 3.5(c)). Further searches identified the source in the two chillers, which refrigerate and circulate water to cool down the lasers used by the system. In particular, the source was in a mechanical component with nominal rotational frequency at 22.4 Hz, which transmitted its noise to the optical bench through the cooling pipes. To solve the problem, in order to move the disturbance away from the Vela region, it was installed a variable frequency driver. Its task was to move the rotation frequency of the chillers sufficiently away from the Vela frequency. The effect of this installation, done from the subsequent scientific run VSR3, is shown in Figure 3.5(d).
In the next sections I present the contributions that I have done to the noise hunting activity.

3.3 Noise from water pumps at terminal buildings

In this section I report the first activity in which I have been involved joining the noise hunting group. The noise sources to investigate are the hot and cold water pumps that serve the AHUs. These pumps are placed, in couple, in the technical rooms located behind

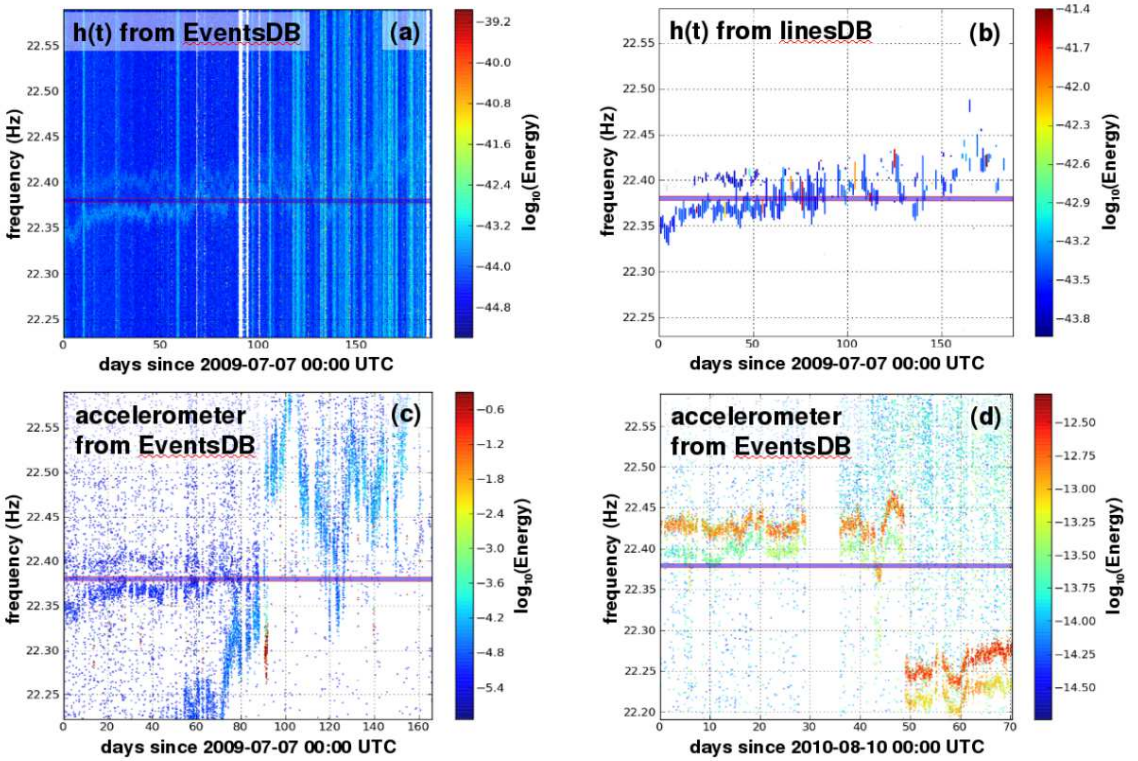

Figure 3.5: The disturbance produced during VSR2 by the chillers of the thermal compensating system at the Vela pulsar frequency seen in the NoEMi Events DB (a), in the Lines DB (b) and in the Events DB of an accelerometer (c). Plot d) shows the effect (on the accelerometer data) of the shift away from the Vela region of the frequency of the chiller engine causing the disturbance, on the 49th day of VSR3. The purple band show the Doppler band of the Vela pulsar frequency. Plots taken from [142].

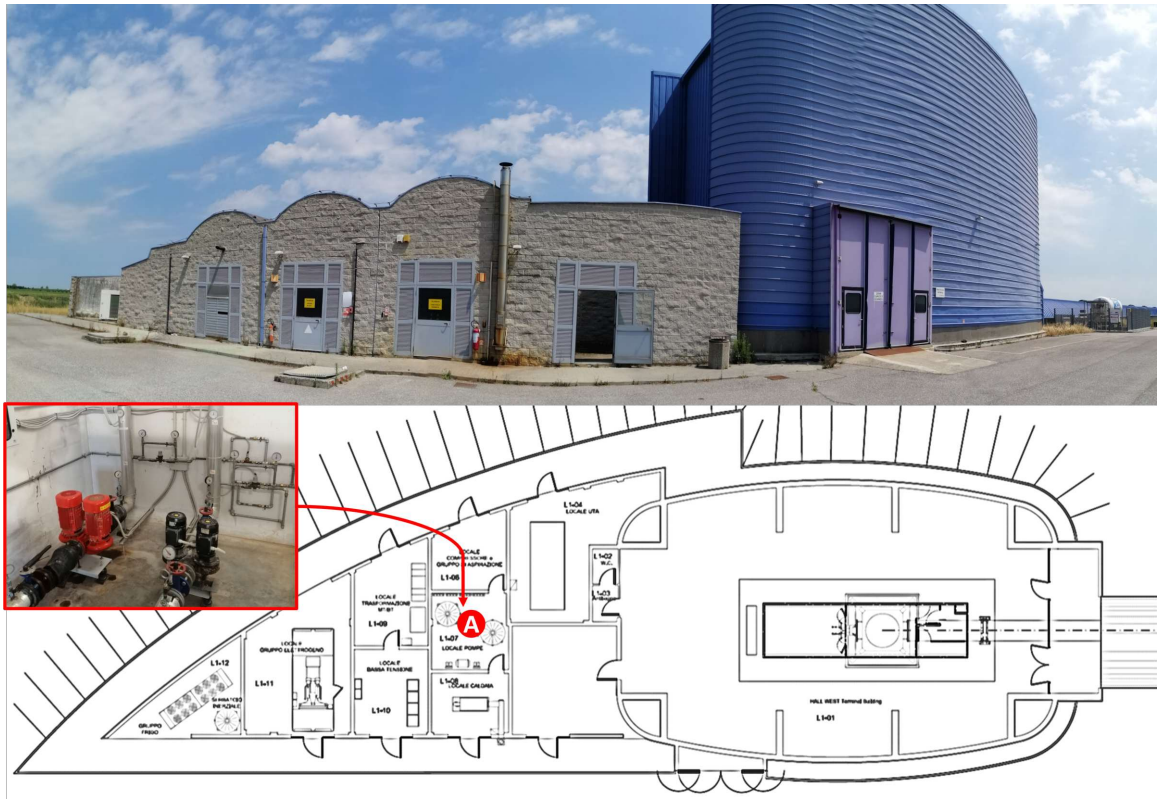

Figure 3.6: Top: wide angle picture of the WEB (blue building on the right) and the technical buildings (on the left) that host AHU, hot and cold water pumps, heater, chillers, air compressors and the electric groups. Bottom: planimetry of the same buildings, with the red-bounded picture showing the hot and cold water pumps. The "A" red bullet indicate approximately the location of the temporary accelerometers placed in the pumps room.

the NEB and WEB. They take hot and cold water from heaters and chillers and then pump it to the AHU through water pipes. In Figure 3.6 the organization of the WEB is shown, together with a picture taken in the pumps room. In the MCB, instead, there is only the cold water pump. The pumps are expected to generate a noise line at a frequency corresponding to their rotation frequency. That noise line is expected to be wandering, since the rpm rates depend first on the supply frequency, which is not perfectly stable, and is influenced by pressure and temperature of the circulating water and of the environment. Moreover, they can contribute to the wide-band increase of the seismic floor. Differently from the past, the pumps now are no more placed directly on ground but there is a spring mitigation that reduces the vibrations transmitted to the ground. In fact, their noise can propagate through the buildings up to the towers in many different ways. The most obvious one is through seismic waves in the underground. The path followed by the seismic waves is not necessarily straightforward, since it depends on the stratification in the underground. In addition, the pumps vibrations can also propagate through the water pipes. These vibrations can propagate beyond the AHU following the air ducts and arrive directly on the experimental building floor. However, they can also propagate from the pipes to the building walls and then go through floor and pipes as a secondary way of propagation. Moreover, the vibration noise propagates also through the fluid itself, in the form of pressure noise.

The understanding of the main propagating channels is essential in order to establish the right mitigation actions.

At the first step, there is the need to correctly identify the noise lines associated to the pumps in order to monitor them. On 21th of November 2020, a series of selective switch-off tests of HVAC devices have been done at different times in all the experimental buildings [143]. At different times, the devices linked to the AHUs, water pumps included, have been turned off. In this way the devises can be associated to the noise lines that interrupt at their turn-off time. I have analyzed the data of these switch-off tests, looking at the most representative environmental sensors. On the magnetic side, I have found no hints of noise line from the water pumps in the magnetometers. More precisely, I have searched for lines at the frequency of the pumps rpm rates and for sidebands of the power mains (50 Hz) and its second harmonics. In fact the friction of the pump, together with its natural imbalance, can create ripples in its power supply, which propagate back through the electric cables and thus create sidebands in the current and in the associated magnetic field. In practice, if $f_{\rm rpm}$ is the pumps frequency, I have searched in the magnetometers for interrupting lines at frequencies $f_{\rm rpm}$, $\sim 50\,{\rm Hz} \pm f_{\rm rpm}$ and $\sim 100\,{\rm Hz} \pm f_{\rm rpm}$. No magnetic lines have disappeared in coincidence with the time the pumps are turned off. Instead, I have found that the pumps noise propagate mainly as seismic and acoustic waves at the pumps rpm frequency and harmonics. The inspected sensors are microphones, placed inside the experimental buildings, and velocimeters/accelerometers placed on the ground near to the towers and directly on the vacuum chambers. The noise lines are visible in the left side spectrograms in Figure 3.7. Even in the short time considered ($\sim$ 1 hour window), their frequency trend results quite irregular. When taking the averaged amplitude spectral densities (ASDs), shown in the right side of Figure 3.7, this results in typical Q-factors about $\sim 0.3 - 0.4 \cdot 10^3$. These lines have typical frequencies around 47 - 48 Hz, with the cold water pumps lines stronger than the hot pump ones because they are more powerful by a ~ 2 factor. Their frequencies are summarized in Table 3.1, together with their amplitudes.

Building	Device	Line frequency	Line amplitude
NEB	Cold water pump	48.00 Hz	$5.18 \cdot 10^{-11}{\rm m}/\sqrt{\rm Hz}$
NEB	Hot water pump	47.50 Hz	$2.14 \cdot 10^{-11}{\rm m}/\sqrt{\rm Hz}$
WEB	Cold water pump	47.95 Hz	$3.93 \cdot 10^{-11}{\rm m}/\sqrt{\rm Hz}$
WEB	Hot water pump	46.70 Hz	$2.37 \cdot 10^{-11}{\rm m}/\sqrt{\rm Hz}$
MCB	Cold water pump	48.55 Hz	$3.90 \cdot 10^{-10}{\rm m}/\sqrt{\rm Hz}$

Table 3.1: Summary of the noise lines associated to water pumps as measured in the test on 21th November 2020 [143] and shown in Figure 3.7. The frequency resolution used for the analysis is $\delta f = 0.05\,{\rm Hz}$.

Once the link between sources and noises has been established, various mitigation strategies can be pursued. The first intervention has involved the vibrations generated by the pumps themselves. The aim was to assess if the amplitude of the vibrations can be reduced slowing the rotation frequency of the pumps. So, together with the noise hunting crew, I have performed a slow-down test on the hot water pump in WEB [144]. The hot pump have been connected to a variable frequency driver (inverter) in order to change its mains frequency, since the pumps rpm rates are expected to scale proportionally. The first test was done in 16th of June 2021. Both cold and hot pumps are mounted together with a spare one which is usually inactive and is used in case of malfunctioning of the main pump.

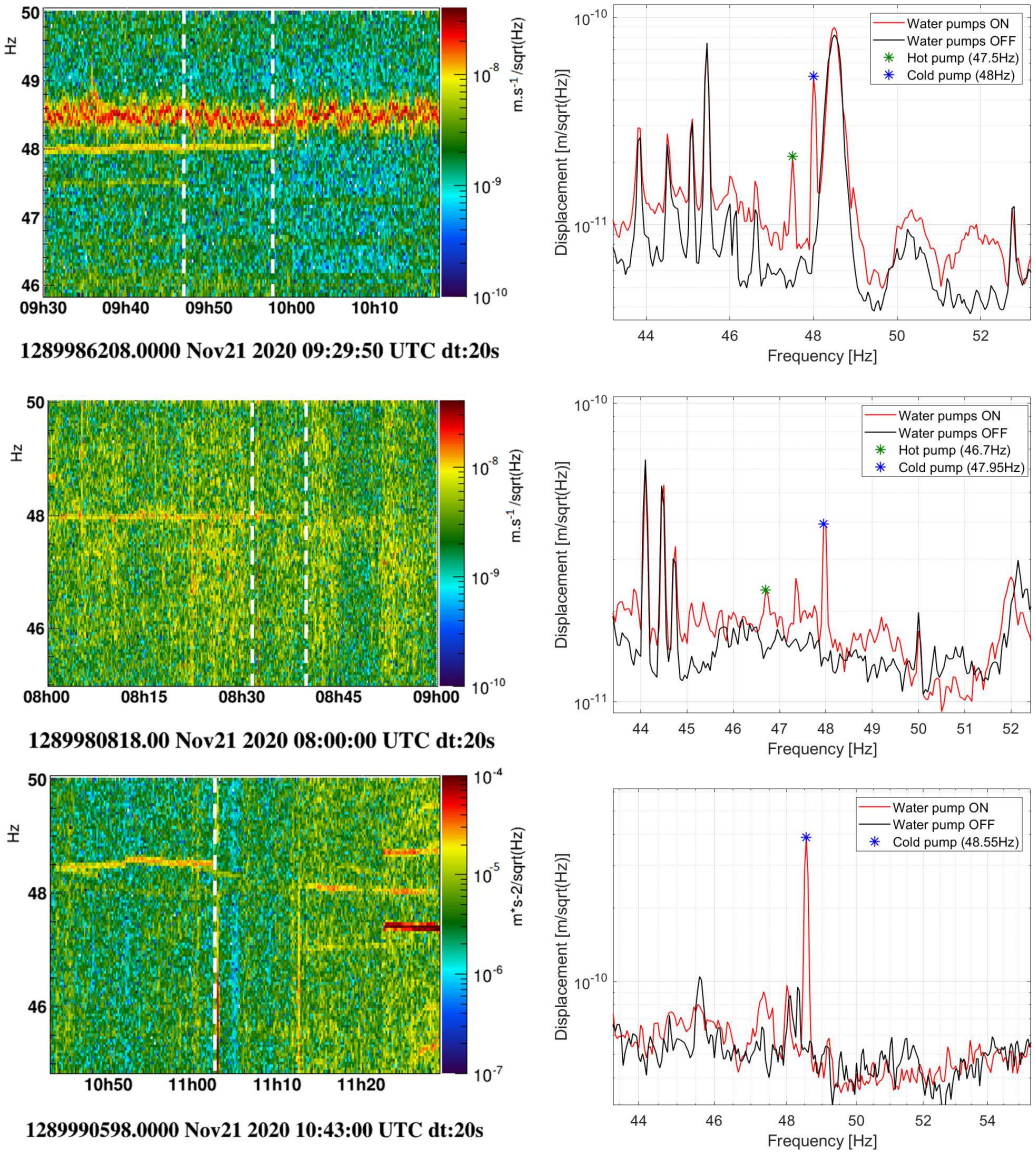

Figure 3.7: Most representative plots of the switch-off test done in [143]. The plots on the left side are amplitude spectrograms of the data recorded from the seismic sensors, zoomed on the switch-off times and on the expected noise frequencies. The vertical, dashed white lines indicate when the water pumps are turned off and coincide with a noise line stopping. The plots on the right side are the averaged ASDs extracted at a time when both the pumps are working (red curves) and at a time when both the pumps are turned off (black curves). The stars indicate the frequency lines associated with the sources. Top and middle plots: displacement in the north direction recorded from the velocimeter in WEB and NEB, respectively. Note that in NEB the hot pump line is very weak, so in the spectrogram it is not well visible. Bottom plots: displacement in the north direction recorded in MCB from the accelerometer. All the plots are done with a frequency resolution of $\delta f = 0.05\,\mathrm{Hz}$.

During the test, the supply was switched alternatively on both the main and the spare pump, and the input frequency was progressively reduced starting from the nominal 50 Hz down to 35 Hz, at steps of 5 Hz, through the inverter, as described in [144]. We have found that the minimum sustainable frequency is 40 Hz, since at this value after few minutes the water pressure in the circuit becomes too low and the security system shut down the boiler. To end the test we then increased gradually the inverter frequency up to 50 Hz with steps of 1 Hz. To analyze the effects of the test, we have installed four extra sensors in the pumps room: two of them have been put onto the hot and cold water pumps, one on the ground floor between them and one on the hot water pipe. In addition, two water pressure probes have been installed on the inlet and outlet water pipes. The spectrogram in Figure 3.8 shows the evolution of the vibration line associated to the hot pumps, as sensed by the accelerometer mounted on it. From the original frequency of 46.70 Hz, the noise line of the main hot pump drops correspondingly to each 5-Hz-jump of the inverter. The measured frequency lines, together with the inverter frequency, are shown in Table 3.2.

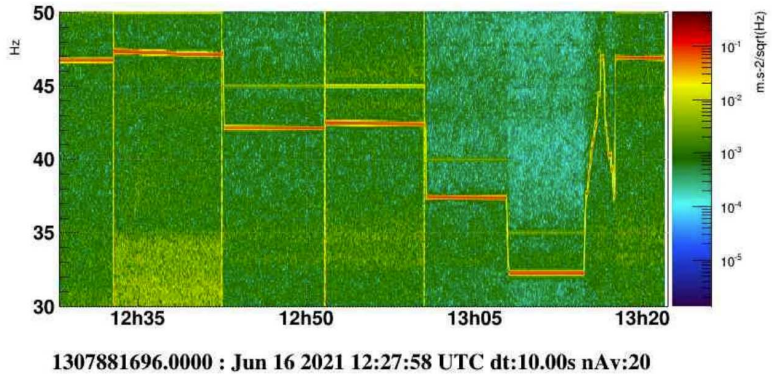

Figure 3.8: Spectrogram of data from the accelerometer mounted on the hot water pump during the slow-down test described in [144]. The noise line associated to the pump rate moves from the usual 46.70 Hz down to 42.10 Hz, 37.40 Hz and 32.25 Hz as the inverter frequency decreases, from 50 Hz to 35 Hz, at steps of 5 Hz. The frequency resolution is $\delta f = 0.05\,\mathrm{Hz}$.

Inverter frequency	Pump rotation frequency
50 Hz	46.70 Hz
45 Hz	42.10 Hz
40 Hz	37.40 Hz
35 Hz	32.25 Hz

Table 3.2: Summary of the changes in the WEB hot water pump rotation frequency (second column) as function of the inverter frequency (first column).

I have made a subsequent analysis on the four different configurations obtained looking at the ASDs of all the sensors. The most relevant results are shown in Figure 3.9. Looking at the lines directly on the hot pump, their amplitude does not seem to be affected by the changing rotation frequency. Looking at the same lines on the ground sensors (the first two from the top in Figure 3.9) still there is no hint of reduction in the amplitude, rather in some cases they result to be slightly stronger. However, the most significant change is a broadband noise reduction observed when jumping from 50 Hz to 45 Hz.

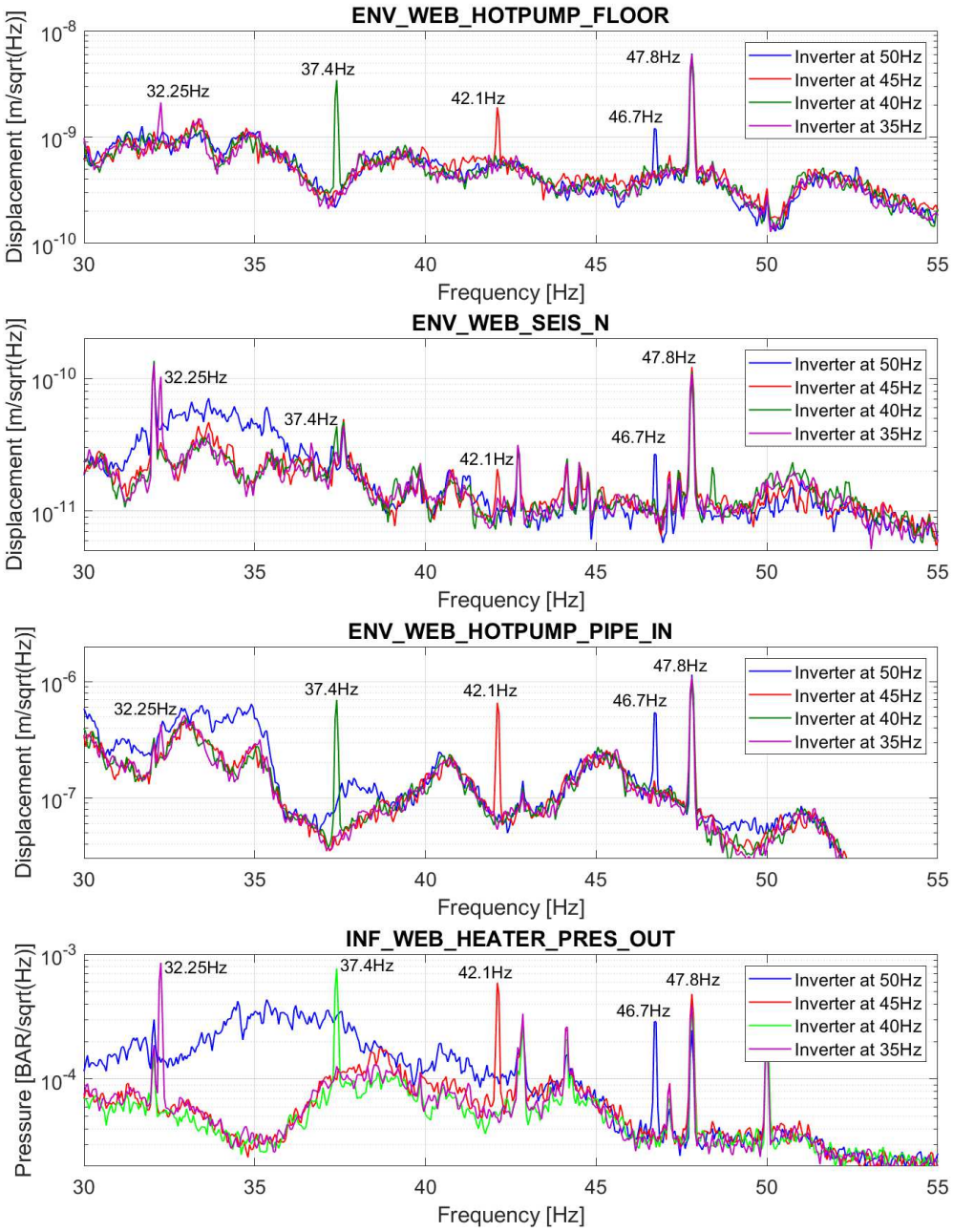

Figure 3.9: Averaged ASDs from most representative sensors during the slow-down test [144]. Blue, red, green and purple curves represent data taken with the pump inverter set respectively to 50, 45, 40 and 35 Hz. From the top to the bottom, the plots show data from: the acclerometer put on the ground floor in the pumps room; the velocimeter on the ground floor in WEB near to the tower; the accelerometer put on the hot water pipe; the water pressure probe installed on the outlet water pipe.

Looking at the accelerometer on the pipe and at the water pressure probe (the last two from the top in figure 3.9) it is clear that the pumps vibrations propagate efficiently through the water circuit: the noise is carried both inside the pipes by the fluid, as pressure noise, and on the pipes surface as vibrations. Except for the accelerometers put on the pumps and on the ground in the pumps room, which are dominated by the engines vibrations, the sensors on the pipes and in the experimental building sense a broad-band noise that spreads from 30 Hz up to 35 - 40 Hz. This noise is present only when the inverter is set to the nominal value of 50 Hz and then for all the lower levels tried the sensors sense the same, lower, noise floor. However, we have noticed that the noise bump has not come back promptly when we have restored the pump at the nominal speed. Instead, it have taken the whole day to come back. The day after, on 17th of June 2021, we have performed a second, longer slow-down test which lasted 7.5 hours during which the inverter was set to 45 Hz [145]. This time the noise bump did not disappear promptly as in the previous test, even if some reduction is observed in the water pressure, as can be seen in Figure 3.10. In 2nd of July 2021 a further slow-down test has been done, while having both the AHU and the cold water pump turned off. In that occasion, there has been observed some broad-band noise reduction in different regions between 10 Hz and 25 Hz, not strictly coincident with the performed actions. It seems to be the result of a slow reassessment occurring in the following hours. The hints collected in these tests suggest that the presence of varying noise bumps in different frequency regions are linked with some changing turbulence regime of the water flowing in the pipes. These changes seem to be triggered by many components of the water circuit, including the water pumps. The investigation on this noise have been then object of dedicated tests.

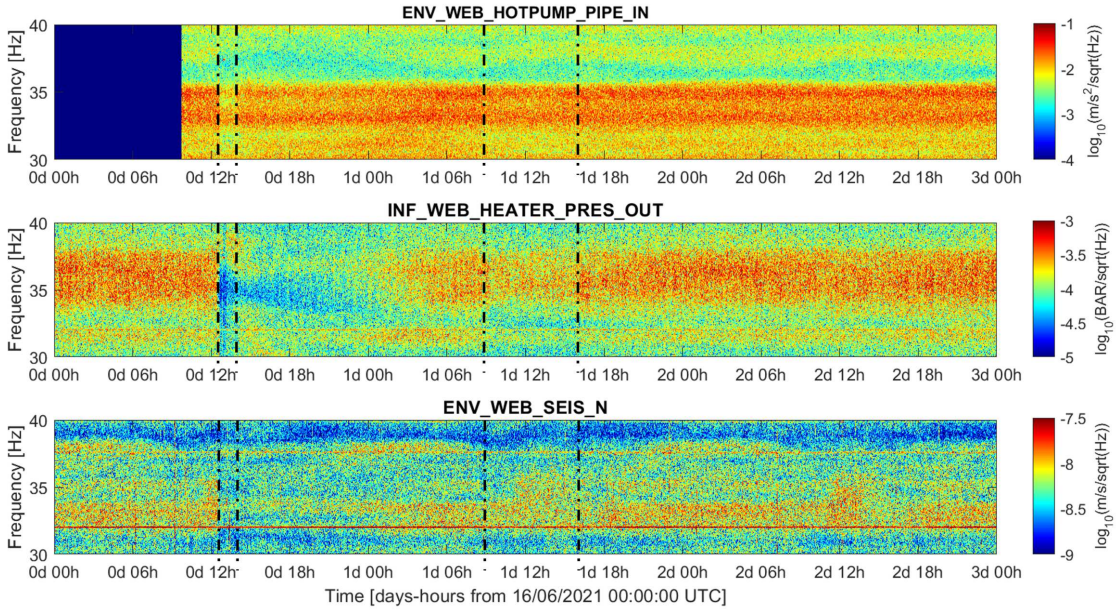

Figure 3.10: Spectrograms of the long slow-down test done in [145]. Top plot: data from the accelerometer put on the hot water pipe. Middle plot: data from the water pressure probe on the outlet water pipe. Bottom plot: data from the velocimeter on the ground floor near to the tower. The vertical dashed black lines indicate the starting and ending times of the first and second slow-down tests.

I have analyzed the data of the first slow-down test looking at the spatial distribution of the pumps noise lines. After the end of the O3 run, an array of Newtonian seismic sensors has been installed in both CEB, NEB and WEB with the purpose of studying the Newtonian noise on Virgo site and implement a subtraction from the detector data. The same array can be used to monitor the amplitude of a noise line in different locations in the buildings. I have developed a tool in Matlab to plot the measured amplitudes at a given frequency (or in an extended band) and at a given time, placing them in the right locations of the Newtonian sensors in the building map and representing the amplitude with a color scale. The tool can plot also further elaborations of the data, as SNR, root-mean-square values or coherence with a witness channel.

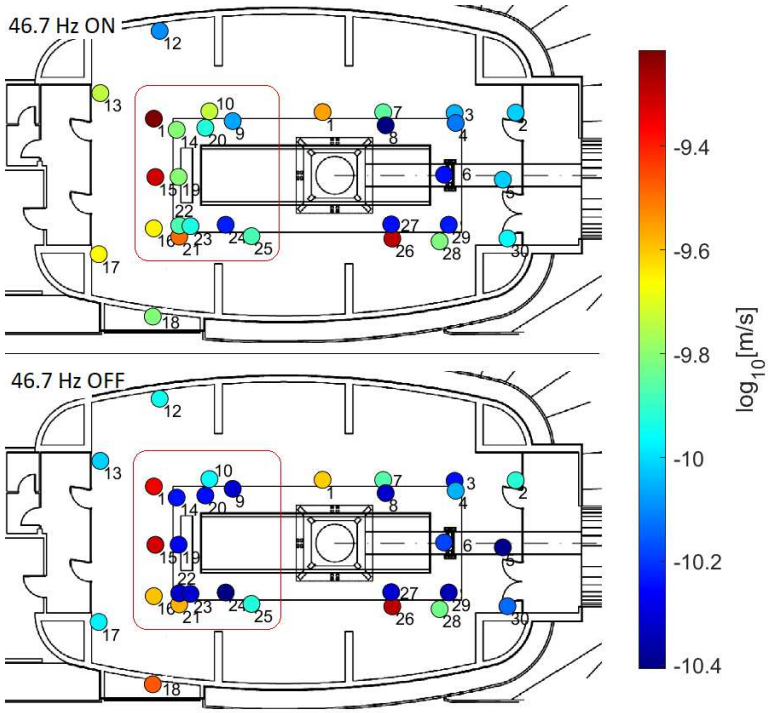

Figure 3.11: Plots of the root-mean-square displacement measured by the Newtonian array in WEB at the frequency 46.7 Hz corresponding to the hot pump noise line. The displacements are represented logarithmic on a color scale. The top plot shows the measured displacements before the slow-down test. The bottom plot shows the same quantities, at 46.7 Hz, when the hot water pump inverter was set at 45 Hz and the noise line moved in frequency. The most impacted area is in the left side, nearest to the pump (out of map on the left) and to the walls.

In Figure 3.11 I show the ASD measured by each Newtonian sensor in logarithmic color scale. By comparing the noise sensed by the array before and after the switch-down, it turns out that the impact of the 46.7 Hz noise line is stronger on the area near to the entrance (on the left side in the plots). This is not surprising, since the water pumps and generally all the technical buildings are behind the WEB, on the entrance side (see the map in Figure 3.6). A straight-line propagation of the underground seismic waves obviously hit the nearest sensors when the vibrations are stronger. However, this path partially superposes with the one followed by the vibrations that propagate through the pipes and are transmitted to the

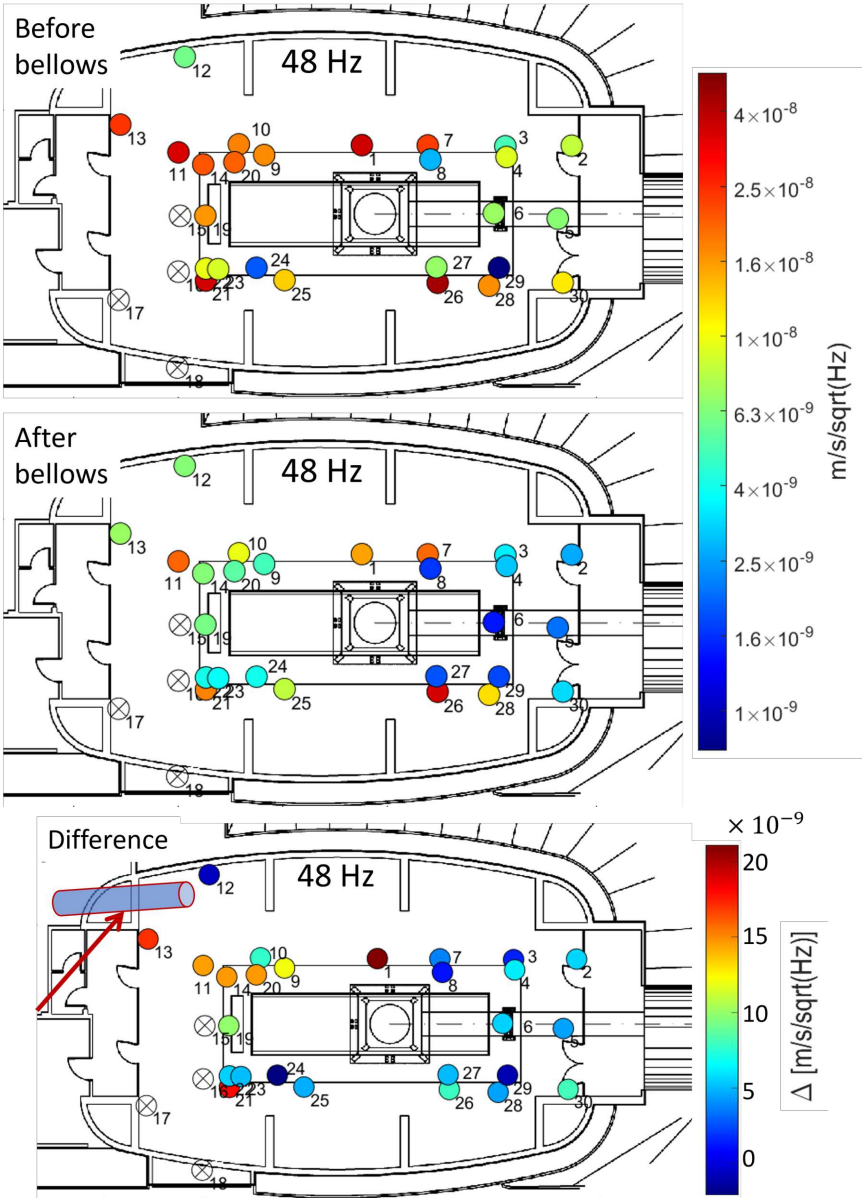

Figure 3.12: First two plots from top: ASDs measured by Newtonian array in WEB at the cold water pump frequency 48 Hz, before the installation done in [147] (first plot) and after that installation (second plot), in logarithmic color scale. The bottom plot reports the difference between the two measures per each sensor, in linear color scale. The highest impact of the interventions is on the North-West area of the building, where the pipes connecting the AHU with the clean room cross the wall and their vibrations spread down to the ground. The crossed sensors were out of order.

walls at their intersection. It is worth also to note that the black rectangular area including the WE indicates a more stable floor, called "tower platform", since it lays on a deeper foundation. In fact, the sensors inside that platform sense a less intense noise line.

Further tests at NEB demonstrated that the water pipes feeding cold water to the AHU of the tower clean rooms act as a seismic short circuit (see [146] and comments therein). Thanks to the experience gained at NEB, on 05/10/2021 a valve and an anti-vibration joint have been installed on clean-air AHU cold water pipe, inside the pumps room [147]. The subsequent tests and results are reported in [148]. The effect is the reduction of the cold pump noise line at the environmental sensors, by an average factor 2. This noise reduction seems associated to the insertion of the bellows, while other actions like opening and closing the valve have no relevant systematic effects on the residual noise. This can be the hint that the actual residual 48Hz noise sensed at the tower platform is following different paths. For this reason I have done an analysis on the Newtonian array before and after the installation in WEB. The results are shown in Figure 3.12. From the top plot it is clear that the impact of the cold water pump noise line is stronger in the North-West side of the building, where the pump room is located. The most interesting information comes from the bottom plot, which shows the difference between the measures taken before and after the installation. From that plot, we can see that the noise reduction due to the insertion of the bellows is stronger on the path between the tower platform and the North-West corner. It is important to underline that the pipes that connect the AHU with the tower clean room cross the West-side wall of the building just at that corner. Thus, the hypothesis that the pipes vibrations spread down to the ground through the wall is strongly supported by this result. This seems to confirm that the obtained mitigation is due to the partial interruption of the short circuit of vibrations coming through the water pipes that connect the AHU with the tower clean rooms. The impact of the installation is a reduction of the 48 Hz noise line by an average factor of ~ 2.4 over all the building, with maxima of $\sim 4-5$ in the North-West corner. Unfortunately, at the time of these works the interferometer was not working, so there is no information of the impact that the noise lines generated by water pumps would have on the detector outcome with the O4 run sensitivity. Future tests with a stably working interferometer would give more information.

3.4 Seismic noise lines at Central Building

From the beginning of 2022 I have started a work to identify the sources of some noise lines observed in CEB seismic spectrum and still not well understood at that moment. The lines on which I have worked are shown in the zoomed ASD in Figure 3.13.

The structure of CEB is way more complicated than WEB and NEB, since it hosts the laser laboratory, the input benches, the detection laboratory, the thermal compensation system room and many other structures, and obviously all the towers that host the mirrors. It is organized in four levels, which are shown in Figure 3.14. Level 1 is placed at second underground floor. It is limited in the area under the towers and hosts the clean rooms to enter into the towers. Level 2 is the first underground floor, and is the main level, where the towers are leaning and where are the laser laboratory, the injection benches, the detection laboratory and so on. Level 3 is at ground floor. There are the main entrance, the data acquisition room, vacuum and electronics laboratories. Level 4 is at first floor. There are mainly storage rooms and terraces. The majority of electronic and mechanic devices is at level 2, but there are also some vacuum devices in level 3, besides an AHU

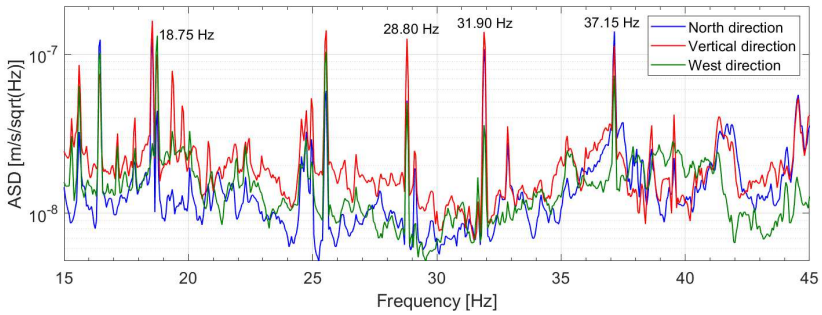

Figure 3.13: Plot of the ASD of the seismometer data in CEB at 23/02/2022, 00:00 UTC. The blue, red and green curves show the vibrations in the north, vertical and west directions respectively. The labeled lines are unknown in their origin.

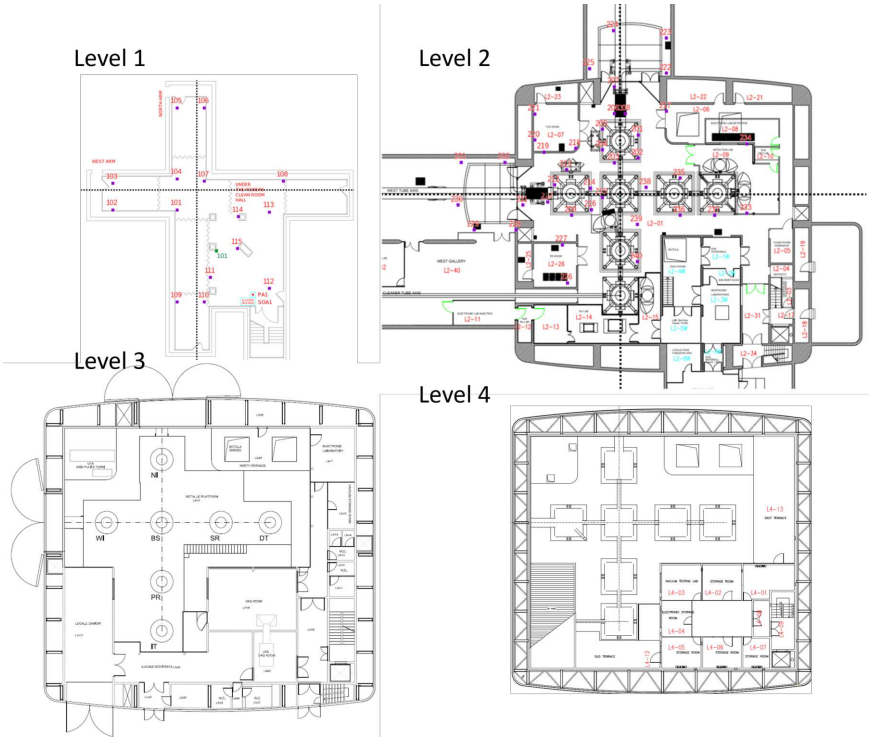

Figure 3.14: Map of the four levels of CEB. Top left plot is level 1, at second underground floor. Top right plot is level 2, at first underground floor. Bottom left plot is level 3, at the ground floor. Bottom right plot is level 4, at first floor.

serving the data acquisition room. The possible sources for unidentified noise lines should be searched between level 2 and level 3. There are many ways the vibrations can enter the interferometer.

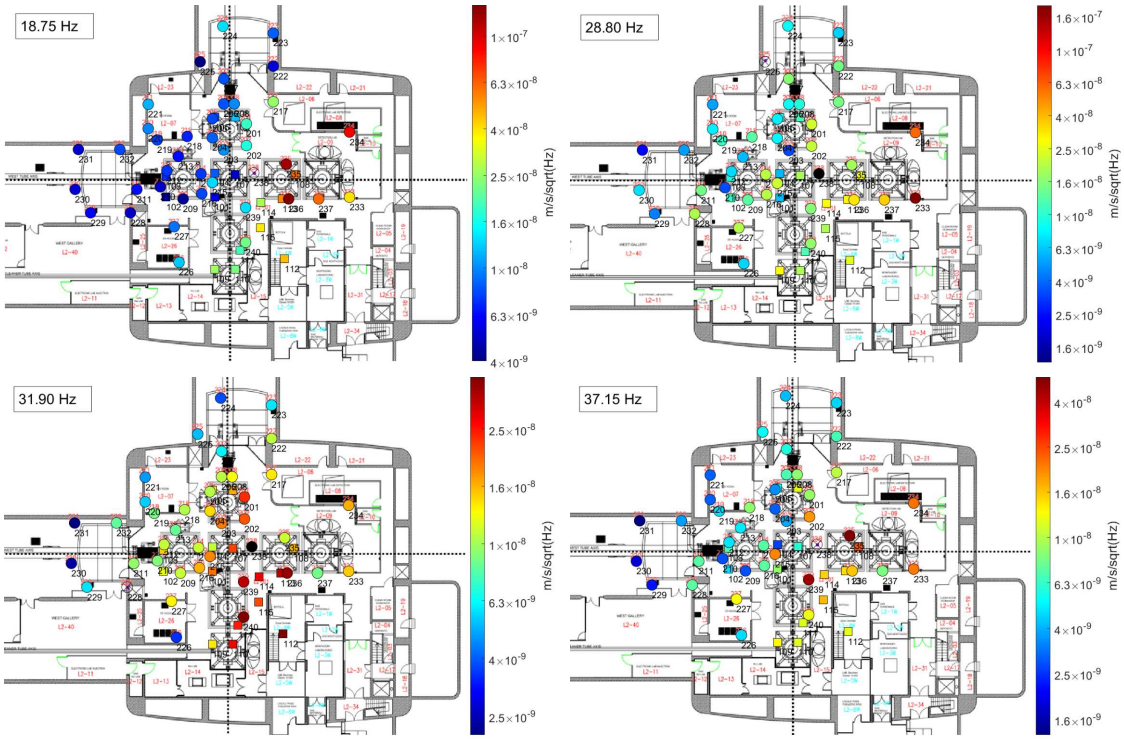

Figure 3.15: Maps of the level 2 of CEB with the ASDs measured at 23th of February 2022, 00:00 UTC, by the Newtonian array and plotted in color scale, with a resolution of $\delta f = 0.05\,\mathrm{Hz}$. Circles indicate the locations of sensors in level 2. Squares indicate the locations of sensors in level 1. Top left: ASDs measured at 18.75 Hz, indicating the area with maximum noise around the detection tower. Top right: ASDs measured at 28.80 Hz, that maximize towards the wall after the detection tower. Bottom left: ASDs measured at 31.90 Hz, showing the injection, power-recycling and signal-recycling towers as most impacted area, indicating the direction of the AHU serving the clean rooms. Bottom right: ASDs measured at 37.15 Hz, maximum between the beam splitter and signal-recycling towers.

In order to get hints on the origin of noise lines I have used the tool that I have developed, and introduced in Section 3.3, to make 2D maps of the noise sensed by the Newtonian array. It has the great advantage to give a rapid estimate of localization coinciding with the area where the noise sensed is maximum. Once the most impacted area is individuated, one can search for the nearest possible noise sources compatible with the noise frequency and features. I have generated a map of CEB level 2 for each one of the four selected lines, superposing the Newtonian sensors placed at level 1 to the sensors placed at level 2. In each map I plot the ASD of the peak measured by the sensors at the searched frequency at 23/02/2022, 00:00 UTC. The results for the four noise lines are shown in Figure 3.15. Looking at the maps, they give useful -and very different- information on the lines origin. The lines at 18.75 Hz and 37.15 Hz are strongly localized and decay rapidly in amplitude when going farther. The lines at 28.80 Hz and 31.90 Hz, instead, spread along the whole building affecting almost all the sensors. Each one of these lines has been addressed

separately.

3.4.1 Noise line at 18.75 Hz

Looking at the top-left plot in Figure 3.15, it indicates that the most impacted area is mainly around the detection tower and secondarily in the injection area. The interest on this noise is due to the fact that its frequency is very near to the one of the 18.55 Hz noise line, generated by the clean room AHU and seen in the detector data during O3 (see Figure 3.1), and with a comparable intensity. Differently from the 18.55 Hz line, which has a slightly wandering frequency, the 18.75 line is extremely sharp and constant in frequency. This suggests that it does not originate from active mechanical devices like pumps, motors, fans. Another argument against the devices is that there is no acoustic noise at that frequency in the microphones, neither the ones near to the detection chamber, and there is no a magnetic noise associated. Triggered by the localization given by the Newtonian array, we have made a further search on the sensors present on the detection tower and in the detection laboratory.

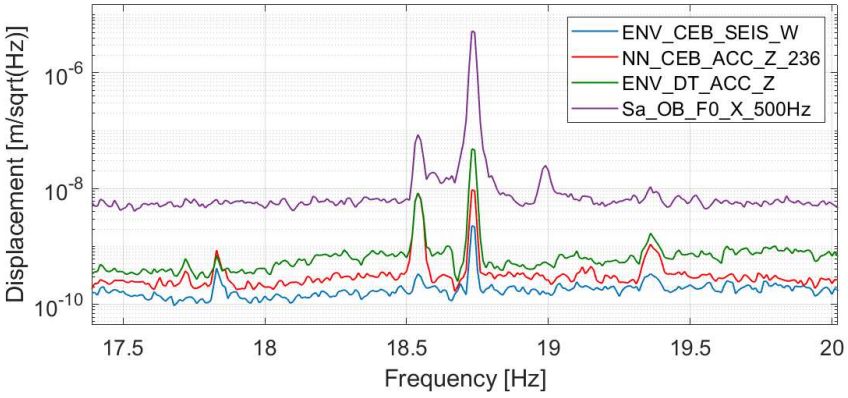

Figure 3.16: Displacement spectra measured by the most representative sensors at the frequency 18.75 Hz at 23/02/2022, 00:00 UTC. The blue curve shows the West-direction vibrations measured by the seismometer placed on ground near to the beam splitter tower. The red curve shows the most affected Newtonian sensor, on ground. The green curve is the accelerometer placed on the detection tower. The purple curve shows the sensor on the first stage of the superattenuator in the detection tower.

The results have supported this indication, measuring a signal ~ 10 times stronger with respect to ground sensors. The maximum is reached on the accelerometer located on the East flange of the detection tower. We have made a sniffing test in 24/05/2022 with a portable accelerometer and a portable digital analyzer [149]. Looking at the output in real-time we have taken several measurements all over the building, founding the strongest signal on North side of the detection tower. We have made then other measurements, excluding possible noise propagation through the pipe. We have detected on the rack that serves the detection laboratory, located on level 3, a noise signal 10 times stronger with respect to the tower. However, after further tests we get convinced that the line is not produced by the cooling fan of the vacuum module present in the rack, neither is associated to a mechanical resonant mode of the rack itself. In fact, tapping and pushing the rack we have measured some resonances around 5 Hz and 25 Hz, but no changes around 18.75 Hz ([150]

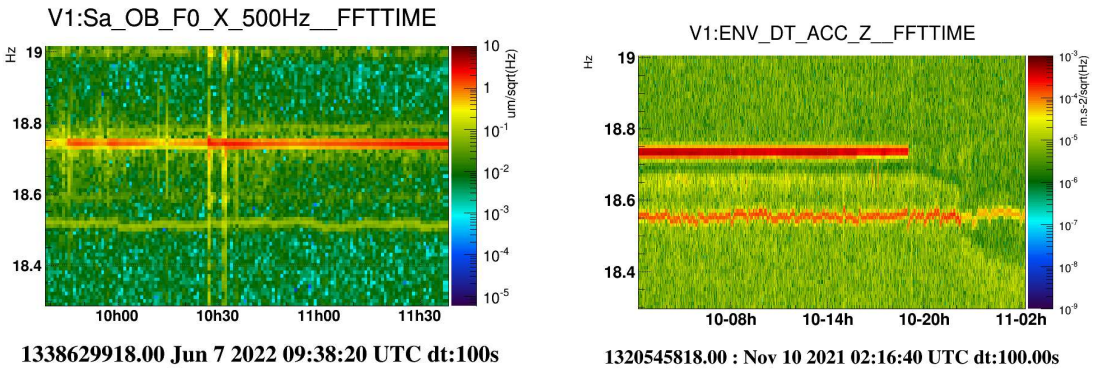

Figure 3.17: Spectograms of the data around the 18.75 Hz line taken at different times. Left plot shows the data from the displacement sensor placed on the top stage of the superattenuator during the test described in the report in [150]. Right plot shows the data from the accelerometr placed on the detection tower corresponding to the venting done in November 2021.

and attached report). Instead, the same noise is well visible with vibrations stronger by more than one order of magnitude on the first stage of the superattenuator, by the sensors that monitor its displacement from the safety structure. This suggests that the noise line could be generated from the tower itself of from internal components. The most significant measures are reported in Figure 3.16, where is evident the increasing amplitude of the noise line as the sensors are nearest to the source. Then, with the portable sensor placed on the top shell of the detection chamber, about one meter above the tower platform, we have tapped the shell from the opposite side of the tower and then pushed from the bottom. In this occasion, we have observed an amplification of the noise line, which gets excited in correspondence with the time of the actions. This is clearly visible in the spectrogram plotted on the left side of Figure 3.17. This fact strongly favours the hypothesis for the line to be associated to a resonance mode of the detection tower or something inside it. In particular, the 18.75 Hz might be a resonance mode of the safety structure which is located inside the vacuum chamber of the detection tower and mechanically coupled to it. Looking in the past data, we have found that in November 2021 this line completely disappeared during a venting that was done on the tower. This is clearly visible in the right plot of Figure 3.17. This is probably the most evident clue that the noise line originates from the mentioned resonance mode. However, the dynamics of this disturbance remain still mysterious. We have no explanation of why in some periods the line amplitude grows and in some others it decreases, neither we know if there is a way to mitigate the resonance. Thus, at the moment this noise line remains unidentified.

3.4.2 Noise line at 28.80 Hz

Among all the checked noise lines, the one at 28.8 Hz is the one localized most precisely in the CEB map. Looking at the top-right plot in Figure 3.15, we can note that the noise line is sensed by almost all the sensors in the map and that the measured amplitude grows gradually towards the direction of the sensor number 233, where it reaches its maximum. There are not many engines in that direction that can produce that noise line. We have soon individuated a vacuum dry pump at level 3 as a possible source. The pump, an Edwards

nXDS15 model, is part of a large set of vacuum dry pumps that are distributed over all the interferometer and maintain stably its vacuum state. It is placed in a soundproof room in level3, in front of the data acquisition room, as shown in Figure 3.18, and serves as a first-level pumping to all CEB towers. Its nominal working rate is at 29 Hz, well compatible with the observed noise line, which is slowly wandering in frequency and has a Q-factor of $\sim 1.4 \cdot 10^3$.

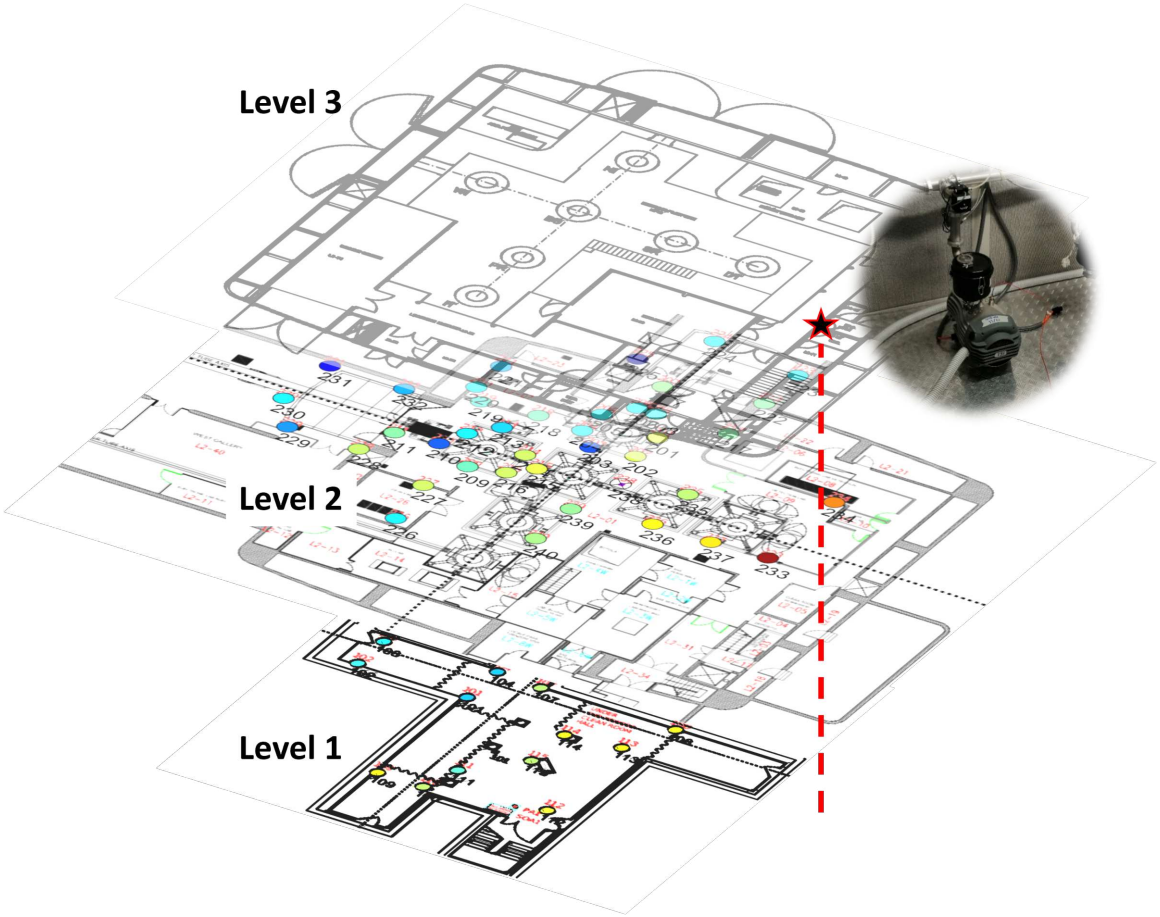

Figure 3.18: Perspective map of the first three levels of CEB, with the coloured circles showing the ASDs measured by the Newtonian array, with the same color scale of Figure 3.15 (top-right plot). The red-contour star a level 3 indicates the location of the vacuum dry pump shown in the picture next to it. Following the red dashed vertical line, the floor, the walls and the pipes act as a shortcut for the vibration to spread in the lower floors.

Looking at Figure 3.18, the vertical projection of the pump location intersects the lower levels at a point very near to the sensor that actually senses the stronger noise. Since the pump is not leaning on the ground floor, its vibrations can spread both through walls, level 3 floor and pipes which act as a shortcut to the lower floors. In order to confirm this hypothesis, in 21/03/2022 we have installed a temporary accelerometer directly on the dry vacuum pump [151]. During the night time, which is seismically quieter than day time, I have checked the coherence[1] between that probe and the Newtonian array on the 28.8 Hz

[1]The coherence between two processes $x(t)$, $y(t)$ is defined as the squared absolute value of the cross-spectrum divided by the product of their power spectra: $C_{xy}(f) = |S_{xy}(f)|^2/[S_x(f)S_y(f)] \in [0,1]$

line. Then, I have used my tool to represent the computed coherences on the CEB map localized on the Newtonian sensors. The results are incredibly clean: most of the Newtonian sensors show a ~ 1 coherence with the accelerometer over all the building, at both first and second level, as can be seen in the left plot of Figure 3.19. As a further prove, during a switch-off test in 25/05/2022 the pump has been stopped, disconnected and then resumed [152]. The noise line, well visible in the right plot of Figure 3.19 in the accelerometer put on the dry pump (top spectrogram) and in the CEB seismometer (bottom spectrogram), moves, gets interrupted and resumed in the same way in the two sensors corresponding with the operations times. *These results taken together confirm without any doubt that the vacuum dry pump in level 3 is the source of the 28.8 Hz line.*

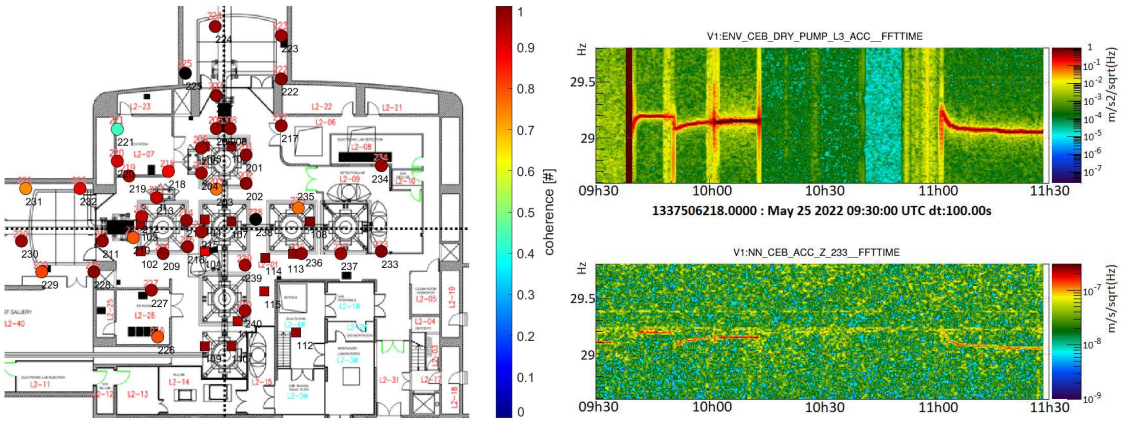

Figure 3.19: Left plot: Coherence between the Newtonian sensors and the accelerometer installed on the vacuum dry pump in CEB, measured at 22/03/2022, 00:00 UTC at the 28.80 Hz frequency. The measures are plotted in color scale, localized in correspondence with the actual positions of the sensors. Right plot: spectrograms of the accelerometer placed on the dry pump and of the most impacted Newtonian sensor during the operations described in [152]. The line associated to the dry pump moves and disappears corresponding to the pump switch-off.

Since the dry vacuum pump has been confirmed as source, we have implemented a series of mitigating actions in order to reduce the impact of its noise line over the building. First of all, the pump has been sent to maintenance and substituted with a spare one. This action is periodically done, since it is known that worn out pumps result to be more noisy. The spare pump, differently from the previous, has a built-in inverter that adapts the rpm rate according to local temperature and pressure. This means that the frequency of the noise line changes during the day, but always within the range 28.8 Hz - 29.1 Hz. Then, the pump has been insulated from the floor by adding a double layer of sorbothane rubber interspersed with a steel plate. It was also added a softer section of corrugated pipe between the pump and the pipe, in order to mitigate the propagation through pipes. I have then analyzed the data of the sensors comparing the noise line before and after the actions, both on the environmental sensors in CEB, in praticular those on the detection tower, and on the Newtonian array, through my analysis tool.

In Figure 3.20 I have reported the CEB map with the ASDs of the Newtonian sensors. The positive impact of the operations is evident, with the number of sensors measuring an ASD greater than the nominal value of $10^{-8}\mathrm{m/s}/\sqrt{\mathrm{Hz}}$ dropping from the 60.4% to the 4.4%. The results of the analysis are synthesized in Table 3.3, where I have reported both

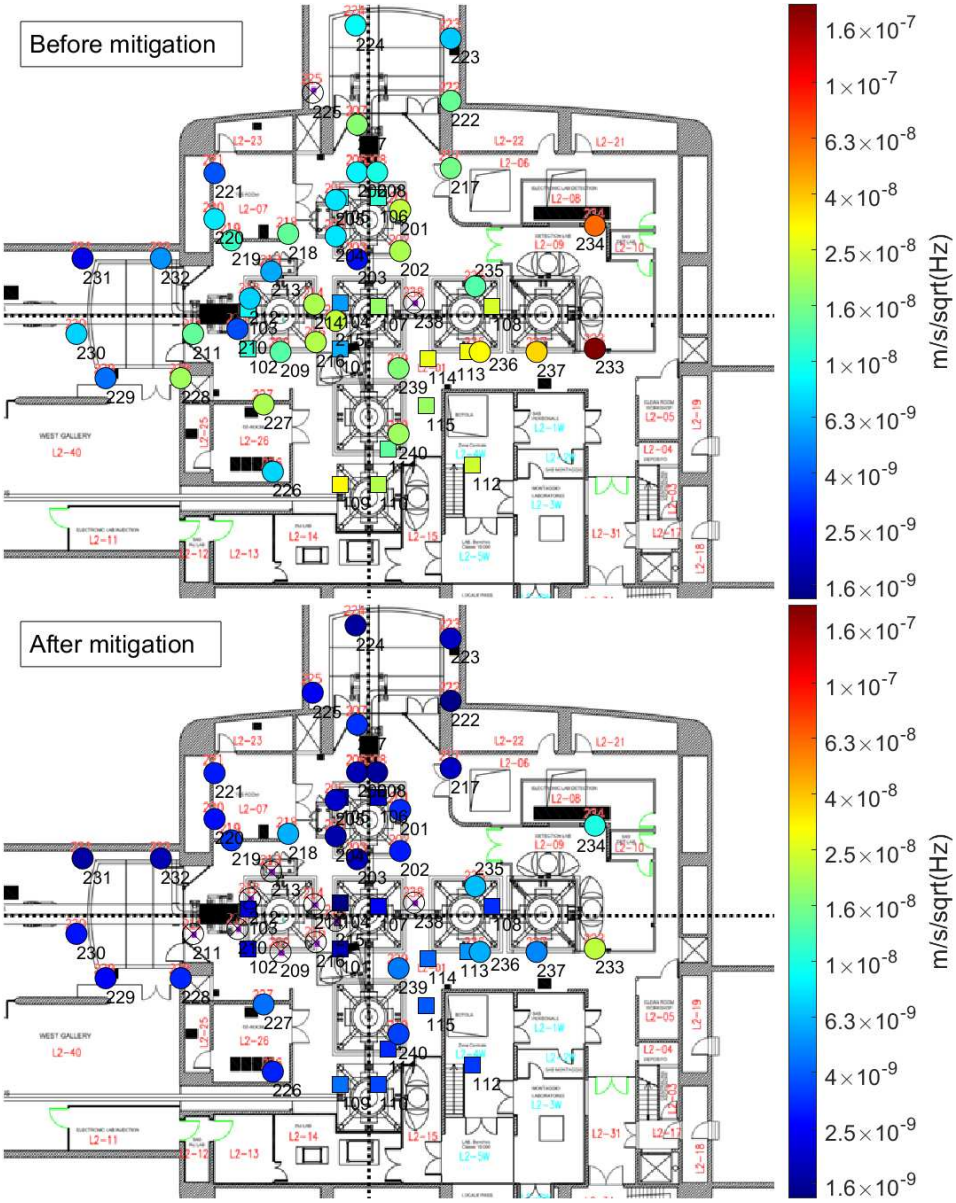

Figure 3.20: Direct comparison of the ASDs measured by the Newtonian array in CEB on the 28.8 Hz noise line, before (left plot) and after (right plot) the mitigation actions on the vacuum dry pump at level 3. The line almost disappeared from a big part of the building.

the average and maximum ASDs and the SNR of the peak against the noise floor, comparing the situation before and after the mitigation.

28.80 Hz line	ASD $\left[\frac{\mathrm{m/s}}{\sqrt{\mathrm{Hz}}}\right]$	SNR
Before mitigation	Mean = $(1.85 \pm 0.36) \cdot 10^{-8}$ Max = $1.91 \cdot 10^{-7}$	Mean = 9.1 ± 3.1 Max = 16.9
After mitigaiton	Mean = $(3.56 \pm 0.48) \cdot 10^{-9}$ Max = $2.19 \cdot 10^{-8}$	Mean = 1.9 ± 0.6 Max = 4.5
Mitigation factor	Average ratio: 5.2 Max ratio: 10.0	Average ratio: 4.8 Max ratio: 10.1

Table 3.3: Synthesis of the mitigation achieved on the vacuum dry pump in CEB level 3, measured from the Newtonian array and shown in Figure 3.20. The first column reports the average ASD and the maximum measured value, before and after the mitigation, and the corresponding ratios. The second column shows the SNRs, calculated between the ASD at the peak and the average ASD of the local floor.

We have achieved an average attenuation over all the CEB by a factor ~ 5, with peaks up to a factor 10 on the sensors nearest to the pump. Moreover, in order to disentangle the effect of the various actions, we have done a switch-off test where we have temporarily removed the insulation to the new pump [152]. It turns out that the application of the insulation layers and the soft corrugate pipe are responsible for the $\sim$ 68% of the total attenuation observed, while the remaining 32% is due to the changed pump. This proves the effectiveness of the mitigation strategy adopted.

3.4.3 Noise lines at 31.90 Hz and 37.15 Hz

The remaining two noise lines have not received the same attention of the previous ones. As I will show, in one case the source was an already known one, while in the other it was not possible to proceed with the search.

Noise line at 31.90 Hz

Looking at the map of the 31.90 Hz line in CEB in the bottom left plot of Figure 3.15,it is evident that it impacts most of the CEB, at level 1 and 2. The line has a Q-factor about $0.6 \cdot 10^3$, because of its wandering frequency. There is a wide group of Newtonian sensors that measures this line with the maximum ASD value, and they form a L-shaped pattern pointing the South-East corner of CEB. The most noisy device that is located in that direction is the AHU that serves the clean rooms of level 1, and is on level 2. This AHU is the source of a well-known noise line at 18.55 Hz, already mentioned because near to the 18.75 Hz line and visible in Virgo O3 data in Figure 3.1. Specifically, the 18.55 Hz line is associated to the fan speed of the supply machine. The amplitude pattern described by the Newtonian sensors measuring that line is almost identical to the one that we see for the 31.90 Hz line. Following this hint, on 2nd of May 2022 a temporary accelerometer has been installed on the supply AHU of the CEB clean room to verify the hypothesis that it is the source of the 31.90 Hz line too. A simple comparison between the ASD of the data recorded by that probe and the data from the seismometer in CEB, together with the coherence between the two sensors, has confirmed that hypothesis without doubts. Figure 3.21 shows

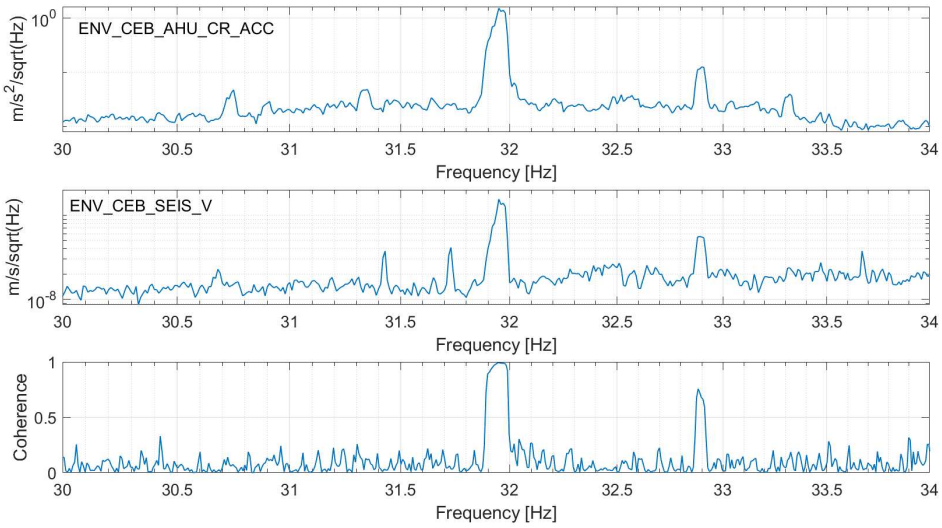

Figure 3.21: Detail of the data around the 37.15 Hz noise line, to confirm the supply CEB AHU as the source. Top plot: ASD measured from the accelerometer installed on the supply AHU. Middle plot: ASD measured from the seismometer in CEB in the vertical direction. Bottom plot: coherence between the data of the two sensors.

a detail of the data from the two sensors and their coherence, where it is possible to see that at the frequency of the noise line there is a ~ 1 coherence. A further classification work on the noise lines generated by the device revealed that the 31.90 Hz line is the 5^{th} harmonic of the belts driving the AHU supply fan, which works at a rate of 6.38 Hz. In particular, both the harmonics of the supply belt spread over the building. The fact that these lines are associated to the AHU makes the mitigation difficult, since it should regard the entire machine. Various strategies have already been tried to mitigate the 18.55 Hz line since O3, but none of them turned out to be successful. We are considering whether to keep the clean rooms AHU turned off during the O4 run. At the moment, some tests are carried on to evaluate how this would impact the clean rooms environmental parameters like temperature, humidity and cleanliness. Anyway, differently from the 18.55 Hz line, the 31.90 Hz was not sensed by the interferometer during O3.

Noise line at 37.15 Hz

Looking at the map of the 37.15 Hz noise line in the bottom right plot of Figure 3.15, it seems much more localized in the map with very little spread in the surroundings. The Q-factor of the line is quite high, $4 \cdot 10^3$. These characteristics suggest that also this line, like the 18.75 Hz, could be associated to some resonant mode in some mechanical structure in the nearing of signal-recycling or the beam splitter towers. However, the line myteriously disappeared on April 2022, so it was not possible to make any investigation on it.

3.5 Identification of an external magnetic noise

During the 13th of July 2021 an unknown magnetic disturbance appeared in the whole Virgo site. However, we did not notice it since the 17th of November 2021, when the exter-

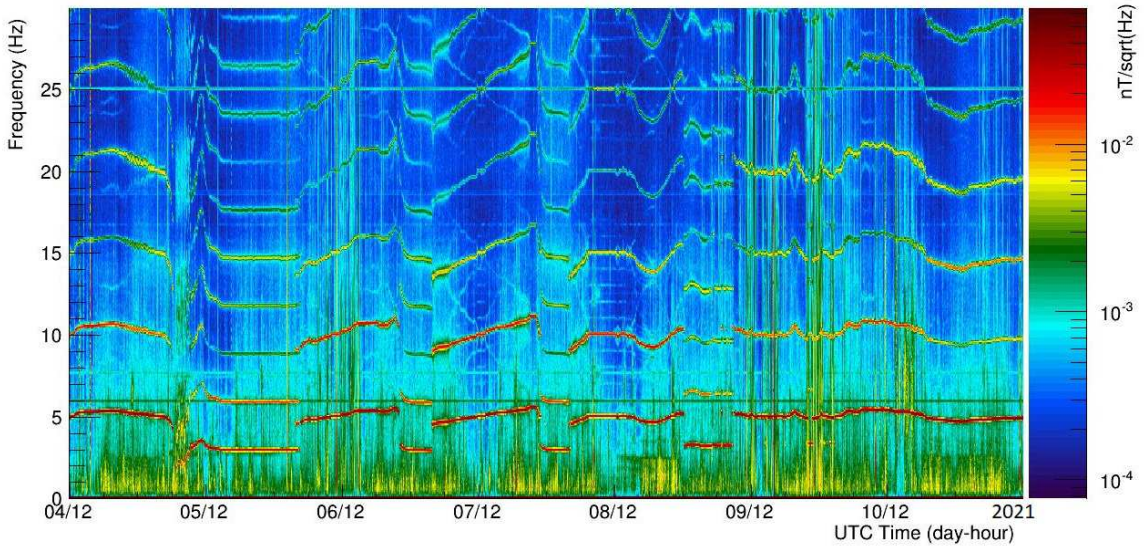

Figure 3.22: Spectrogram of one week of data, from 04/12/2021 to 11/12/2021, from the external magnetometer measuring along the West direction. A magnetic noise is visible as a set of moving harmonics polluting the whole spectrum.

nal magnetometers were restored after they were damaged by a lighting in June 2020 [153]. In fact, even if this new disturbance is seen by the magnetometers in all the experimental buildings, they are so polluted by local magnetic noises that partially hide it. The external magnetometers, instead, are free from almost all the noises related to the interferometer. It is basically a noise line with odd and even harmonics. When it appeared, it had a constant frequency of $\sim 3\,\mathrm{Hz}$ and multiples. Then, from August 2021 its frequency started varying and jumping, mainly between 3 Hz and 5 Hz, with all the harmonics following the variations. In Figure 3.22 the spectrogram of a week of data from the external magnetometer along the West direction is shown. The external magnetometers monitor the external environment and are used, together with analogue sensors placed outside the LIGO detectors, to measure the correlated magnetic noise that affects the global network of GW detectors. The problem of correlated noise is relevant for stochastic GW searches. Analysis algorithms for stochastic background are typically based on cross-correlation between data from different detectors. The implicit assumption is that the noise in different detectors is uncorrelated. However there are some disturbances, like Schumann resonances, that introduce some global correlation. Schumann resonances are resonance modes of the waveguide formed by Earth surface and ionosphere, that gets excited by lighting phenomena over all the globe [154]. These resonances couple with GW detectors data on long timescales, producing non-GW correlations between different detectors. Whereas the O3 run was free of an impact from correlated magnetic field fluctuations, future runs could be affected [155]. Monitoring this correlated noise with external magnetometers would allow to subtract these effects. However, it is evident that the newly appeared magnetic noise strongly dominates the external magnetometers, making them almost blind to Schumann resonances and thus useless for their purpose.

The investigation on this noise has taken various months of work. This noise is only visible in the magnetometers. There is no coherence with any other sensor in Virgo, with the only exception of a probe that measures the voltage difference between the CEB safety

ground and the vacuum chambers of the interferometer. However, the fact that this probe senses the disturbance does not imply any causal relation, since this voltage difference could be caused by external magnetic lines intersecting the Virgo infrastructure. The key point is that neither the sensors monitoring the Interruptible Power Supply (IPS, the experiment power supply grid) nor the ones on the Uninterruptible Power Supply (UPS, the backup power supply grid) sense this noise.

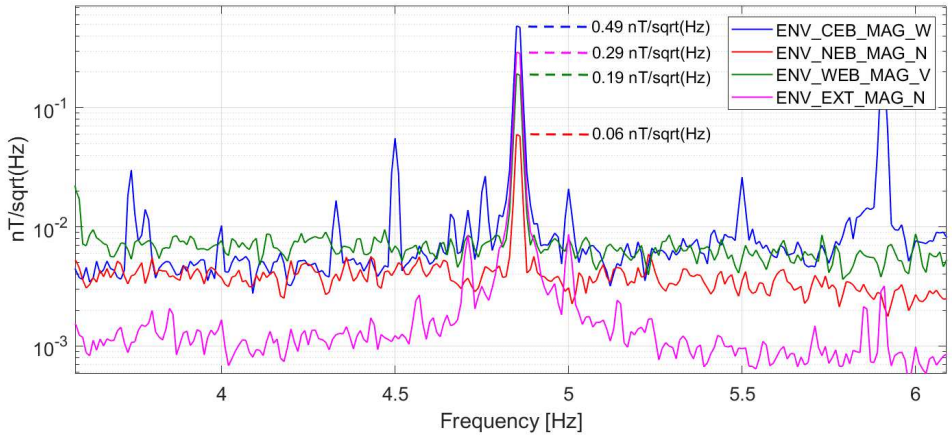

Figure 3.23: Plots of the ASD measured by the environmental magnetometers at 06/03/2022 at 00:00 UTC, zoomed around the first harmonic of the magnetic noise that at that time was at 4.85 Hz. The blue, red, green and purple curves represent the data from the magnetometers respectively in CEB, NEB, WEB and the external. The horizontal dashed lines with the texts indicate the peak ASD measured from each sensor.

Moreover, it does not disappear even when mains supply interruptions occur from the ENEL electric company. All these facts lead us to hypothesize that the noise source was external from Virgo. Another argument in favour of this hypothesis was that the jumps in frequency seem to be correlated with variations in the external temperature [156]. The signal has the features of Direct Current (DC) side-bands, that typical for pulse-width modulation systems. So, I have started an extended sniffing campaign with a portable three-axial magnetic sensor and a portable analyzer. The first hints come from the ASD measured by the environmental magnetometers: as can be seen in Figure 3.23, the noise is sensed as stronger in CEB above all. Then, in decreasing order of amplitude, it is sensed by the external magnetometers, then by the WEB ones and finally by the NEB ones. From those measures we have understood that the source should be located somewhere in South direction with respect to Virgo. However, it was not clear if the source was point-like or linearly-extended.

The first measurement campaign has been done in the Virgo area. We have checked the signal amplitude below the mains medium-voltage aerial lines crossing Virgo, but no sudden local increase has been found. We have found generally stronger amplitudes near to extended metallic objects, including the interferometer arms vacuum pipe themselves, but it is not surprising that magnetic field lines become more dense in proximity of ferromagnetic materials. In general, the signal was maximum approaching to the entrance. The next measurements have been done outside the Virgo site, probing all possible magnetic sources. We have taken measurements under the "Ferrovie dello Stato" commercial railway, which passes at Vicarello, approximately 2 km from Virgo WEB, heading South, but nothing

significant was found. We have taken measurements under the electric line poles, belonging to the Terna company, without observing any local change on the signal or even without observing it at all. We have gone to the wind farms, that are about 6 km East from the NEB, but we have found nothing. We have visited all the photovoltaic systems that are distributed in 1 km range from Virgo, but none of them has revealed local changes in the magnetic noise. Finally we have started to map the area outside Virgo in order to find local variations that could give us some clues about the direction to explore. We have taken three-axial measurements in the roads near Virgo, even entering in the accessible areas in cultivated fields. Finally, we have found fruitful information on the roads that brings to the

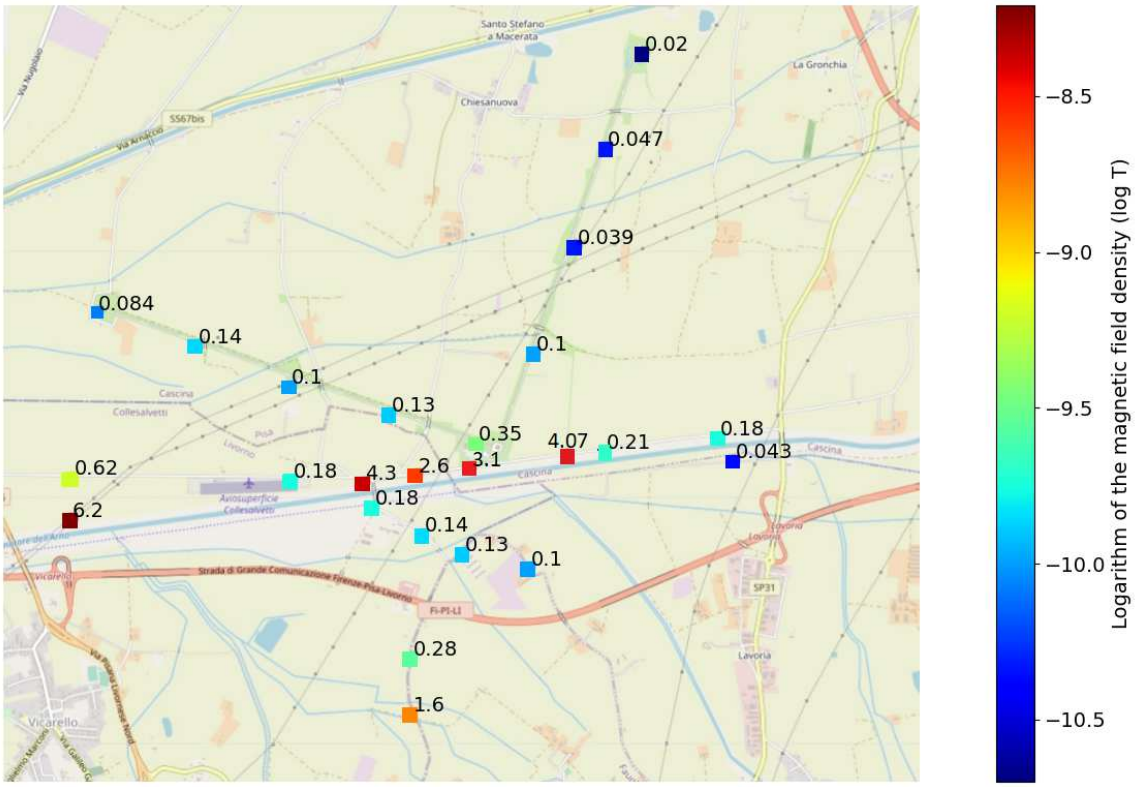

Figure 3.24: Map of the Virgo site with some of the most relevant measures taken during the sniffing campaign, reported in logarithmic color scale. There is a line collecting the measures with highest value, and coincides with the underground path of the gas ducts belonging to the SNAM company which pass under the Virgo entrance. There is another strong measurement out of the line, in the South of the map, that coincides with another ramification of the duct.

entrance (e.g. Via dello Zannone, Via Macerata, Via Edoardo Amaldi). The measurements reach local maxima over the poles that indicate the presence of the gas duct belonging to the SNAM company. Following the path of the ducts (i.e. following the straight line collecting two adjacent poles) we have found results compatible with a linear source coinciding with the gas ducts. A selection of the most indicative measurements is shown in Figure 3.24. The orange-red measurements are taken almost above the gas ducts that run parallel to the Arno spillway just on South of Virgo. Different measured values are due to different depth of the ducts with respect to the ground, as well as morphology of the places. When going

far from the ducts, towards the south direction, the magnetic noise amplitude has decreased as it is expected from longitudinal sources. However, going farther towards South the noise amplitude stopped decreasing and keep growing.

Figure 3.25: Two details of the measurement campaign done near Virgo. The top picture shows the location of two selected measurement spots (red squares) with respect to the Virgo CEB. Bottom left and right pictures show the measurements done in that spots, respectively in front of the Virgo entrance and on the East side after Virgo. The measured rms values are reported both in color scale and in the labels. I also report the inclination of the field with respect to the horizontal plane towards the North, inferred from the measured components. In the case of the right plot, also the ratio between the components and the total field is reported. The dashed orange lines indicate the path of the gas duct.

After a while, we have encountered a branch of an oil duct that belongs to the same company, and there the measures reached another maximum. It is the last orange square in the bottom of the map. Then, I have done a detailed analysis on the measurements taken in this campaign, focusing on the measurements taken near to the gas ducts.

In Figure 3.25 I have reported the most representative measure spots, plotting the rms computed on the first harmonics of the noise. As shown in the top picture, these sets of

measures have been taken in front of the Virgo entrance (bottom left picture) and on a more isolated area on the East, adjacent to farms (bottom right picture). Other similar measures have been acquired all along the ducts path. The first thing worth to note is that the intensity of the field is maximum when the measure is taken exactly over the tube, and then decreases proportionally to the inverse of the distance. This is in accordance with the expected magnetic field generated by a linearly-distributed current, $B \propto 1/d$. The second important observation is on the field direction. The magnetic field generated by a current is directed as tangent to the circumferences centered on the current. In both the measurements reported in Figure 3.25, I indicate the inclination of the magnetic field with respect to the horizontal plane, North direction, computed through the measured components. It can be seen that the inclination obtained above the gas duct is mostly in the North, with a small inclination, 13 deg −21 deg in front of the entrance and 4 deg in the cultivated fields. The measures taken at the Virgo entrance can be slightly more disturbed because of the near metallic structures like the gate. The inclination grows rapidly when the distance increases, passing to $\sim$ 50 deg and becoming mostly vertical at $\sim$ 5 m or more, with inclinations of 70 deg −75 deg. So, also the magnetic field orientation is consistent with the model of a linear current distribution, identified with the gas duct.

Once we have convinced that the source of the magnetic noise are the gas ducts, we have tried to understand how and why there was that emission. Another important thing to understand was if that phenomena was generalized to the whole duct system or if it was a local disturbance. So, we performed another measurement campaign following the gas duct beyond the last measure taken on it (the leftmost measure in Figure 3.24, 6.2 nT), towards the West direction. We have gone farther following the path of the pipe and taking magnetic measures. The results are shown in Figure 3.26. Surprisingly, we have found that the magnetic field on the duct drops as we go farther from Virgo. This measurement campaign has proved that the magnetic disturb on the gas duct is local and does not affect the whole pipe network. So, the source of the noise must be on the gas ducts around the Virgo site. In the subsequent days we have followed the Snam pipes

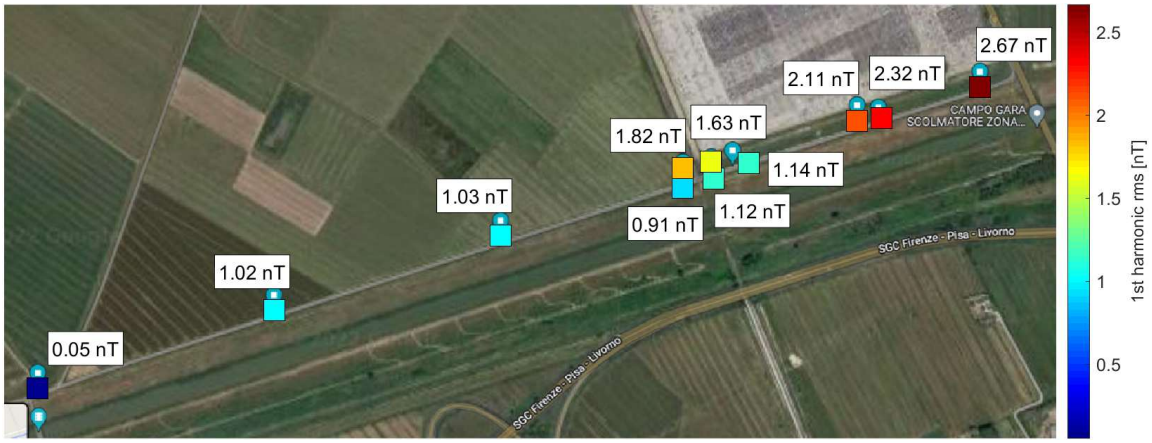

Figure 3.26: Rms measurements of the magnetic noise taken going West from Virgo, following the path of the gas duct. The magnetic field amplitude drops when going farther from Virgo.

towards other directions. Finally, we have found the signal becoming much more intense in correspondence with a 1-volt, 2-ampere DC power supply placed 4 km far from Virgo. This

is a system used to maintain an underground gas pipeline at a given voltage level relative to the ground, in order to avoid the so-called Galvanic corrosion [157]. The pipeline starts from the SNAM Mortaiolo center station, towards Cenaia - Palaia, as shown in the top picture in Figure 3.27. However, the disturbance does not come from the induced current in the pipeline itself, since a constant current or voltage it would not produce that noise. The problem was in the power supply, used by the company to regulate current or voltage by means of the pulse-width modulation. The pulse-width modulation consists in regulating the current or voltage to the requested values through alternately turning on and off at 5Hz rate. Consequently the generated current gets a typical saw-tooth waveform, which contains all the odd and even harmonics of the fundamental one, which corresponds to what we were actually observing. Once contacted the SNAM company, it has become aware of the problem and has started collaborating to solve it. Finally, on 20th of April 2022 at 14:31 UTC the SNAM staff has set the galvanic power supply to "constant current" mode, and the magnetic disturbance instantaneously disappeared, as can be seen in the spectrogram in the bottom of Figure 3.27.

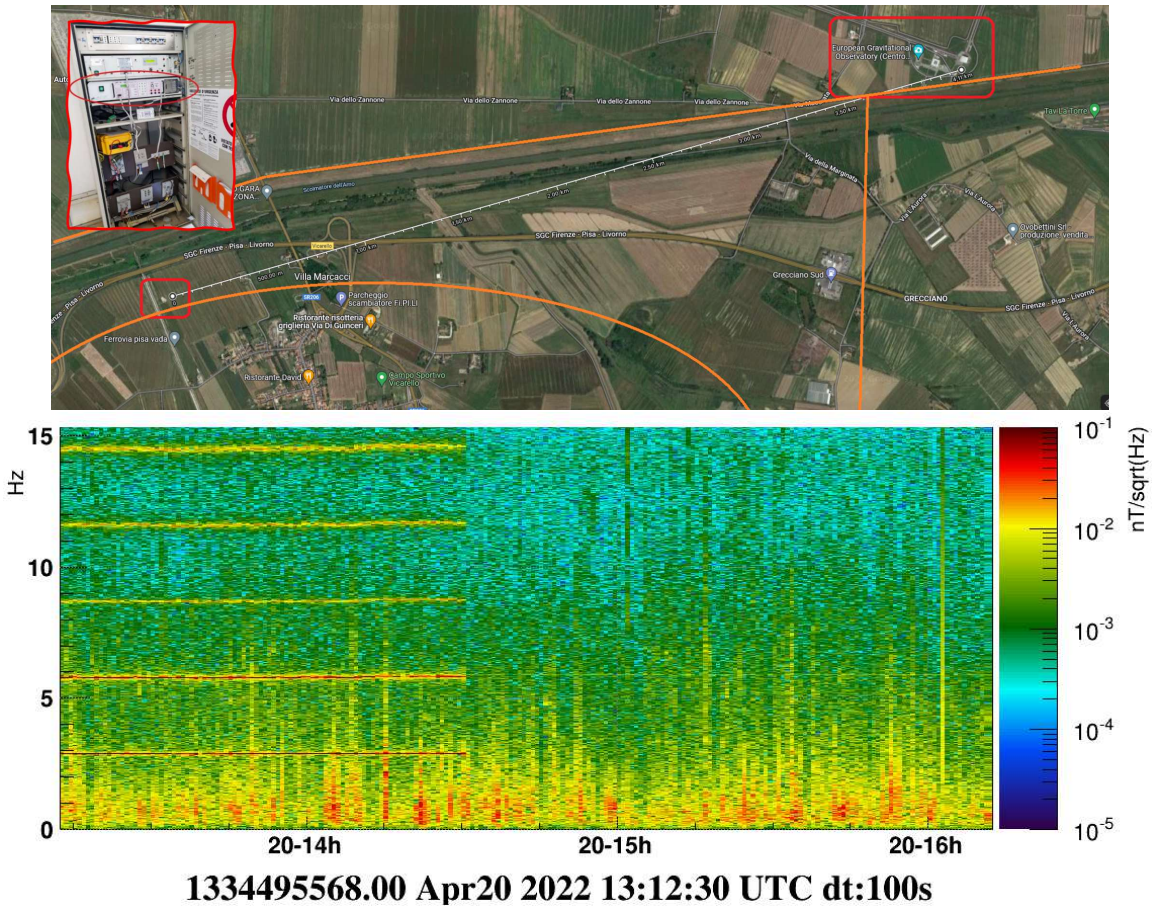

Figure 3.27: On the top: map of the area in the South of Virgo, indicated by the top right red square. The orange lines describe roughly the SNAM gas pipeline. The bottom left square indicates the position of the galvanic power supply that originates the magnetic disturbance, which can be seen in the red-bounded picture. On the bottom: spectrogram of the external magnetometer at the time when the SNAM company has set the power supply to constant current mode. The magnetic noise has stopped correspondingly.

Chapter 4

All-sky searches with clustering continuous waves

In this chapter I present a study of some relevant steps of the hierarchical Frequency-Hough (FH) pipeline. I have briefly introduced it in Section 2.3.2 as a semi-coherent method, used within the LIGO and Virgo Collaborations for all-sky CW searches. These steps, namely the spectral estimation, the *peakmap* construction and the procedure to select candidates in the parameter space, will be explained in Section 4.2. As I will show, they are critical as they contribute to determine the final search sensitivity. The FH procedure has been developed to search for signals emitted by spinning isolated NSs. In this section I investigate the performance of the FH to handle several CW signals, which cluster together in the same frequency band. From now on, a set of CW signals, which are emitted by several and strong CW sources, which are clustered in a frequency range smaller than 1 Hz is referred to as *CW clusters*. Such type of CW clusters could be also detectable by next generation detectors, like LISA, Einstein Telescope and Cosmic Explorer. Moreover, this possibility has been recently raised even for current Earth-based detectors, in the scenario presented in Section 2.2 of CW emission from ultralight boson clouds around stellar-mass BHs. I quantitatively evaluate the robustness of the FH analysis procedure, designed to minimize the loss of single CW signals, under the unusual situation of signal clusters.

The chapter is organized as follows. In Section 4.1, I introduce the possibility that some steps of the FH analysis are negatively affected by the presence of several concurrent large CW signals confined in a very small frequency range. In Section 4.2 I briefly remind the main steps of the FH pipeline, describing in detail (Subsection 4.2.1) two relevant analysis steps, i.e., spectral estimation and construction of the time-frequency peakmap. In fact, these are the steps which could be affected by the presence of dense clusters of signals. Section 4.3 shows qualitatively the behavior of these steps when multiple overlapping signals are present. In Section 4.4 an observable - the *detection efficiency* - is introduced to study the impact of the signal clusters and a first simulation of *low-density* clusters is done. Finally, in Section 4.5 a full simulation of *high-density* CW clusters is done, exploring different regimes. A brief discussion on the results in Section 4.6 closes the chapter. The results discussed in this chapter have been published in [159].

4.1 The problem of CW clusters

Starting from the O2 run [158], the LIGO-Virgo collaboration has begun to search for CW emitted from boson clouds. In particular, the results obtained for the O2 all-sky CW search have also been used to derive constraints for clouds of ultralight bosons around BHs [160]. Even if more specific methods have been developed to search for this kind of signals, see for example [161, 112], it is possible to map the results of a standard all-sky CW search into exclusions limits in a plane defined by the mass m_b of the scalar boson field and the mass $M_{\rm BH}$ of the BH, as discussed in [160]. From an analytic point of view, the expected waveform from boson clouds is well compatible with the ones expected from NSs, except for the frequency derivative which is weakly positive (see Equation 2.30). The basic assumption is that all the steps of the hierarchical FH procedure, especially designed and tested for the weak and rare CW signals emitted by isolated NSs, are compatible with the characteristics of the boson cloud population. In particular, it is important to verify if the sensitivity is degraded when the emitted signals are clustered in frequency. Such scenario could arise under optimistic assumptions on the number of stellar mass BHs present in our Galaxy [105, 162]: if we assume that the boson clouds formation mechanism affects a significant fraction of galactic BHs, we could have a large number of concurrent CW emitters. According to Equation 2.28, these signals would have proper frequency centered at a value corresponding to the boson mass (which reasonably takes just one universal value), with a second-order spread due to the BH mass distribution. If many signals are concentrated in a small frequency range and the signals are significant enough[1](see Section 4.2), it might happen that stronger signals hide weaker ones and/or that there is a consequent degradation of sensitivity due to the mix of signals, thus making difficult their identification. Such possible complication might happen especially in future GW detectors, like Cosmic Explorer [163] and Einstein Telescope [164], which will be the first pan-European ground-based GW antenna [165]. Their expected improved sensitivity with respect to current detectors, especially in the band 3-20 Hz, could make the issue of signal ensembles important. In particular, it could play a role not only for the case of emission from boson clouds around Kerr BHs, but especially for the early inspiral of NS binary systems, that would produce long duration signals and could be searched adapting techniques derived from standard CW searches. On the other side, the space-based detector LISA [166] will give us access to the mHz frequency band. In that case, the detector data are expected to be polluted by the early inspiral GWs emitted by galactic compact binaries, which may form a stochastic background.

In a recent publication [167], the impact of signal clusters on the spectral estimation used in the FH approach has been very *qualitatively* discussed. Specifically, plots suggesting the estimation procedure cancels signal peaks have been shown, when the signals are concentrated in such a way to produce bumps in the detector noise, thus reducing the search sensitivity. In this chapter I will demonstrate these conclusions are wrong in most cases. I quantify these qualitative predictions, studying how the first steps of FH behave in this situation. In fact, these are the steps of the procedure that might suffer from problems related to the presence of many strong signals. I inject simulated CW signals into O2 data to mimic this effect and to see if, and at which level of density and strength of the signals, ther would be the need to apply modifications to the procedure. For simplicity, this study is done using one week of data, which is enough to evaluate possible problems and sensitivity losses. In fact, by analyzing a longer data set the discriminatory power of the

[1]There are presently estimations which give quite different results, depending on the basic assumptions. See for example [105, 162].

Doppler modulation, that will be shown in Section 4.3, would be even stronger making our robustness tests conservative.

4.2 The Frequency-Hough procedure

One of the standard search methods for all-sky searches is the FH pipeline, described in detail in [122]. The FH pipeline is a hierarchical procedure that aims at identifying the most significant CW candidates in a wide parameter space. A follow-up procedure, described in [168], is then applied to these candidates, in order to confirm or reject them. Recently, a GPU implementation of the FH was run to analyze the highest, and computationally demanding, part of the O3 all-sky search, showing a computational gain of more than one order of magnitude [169]. As stated in Section 2.3.2, the FH hierarchical procedure strongly reduces the computational cost with respect to a fully coherent search, but at the price of a sensitivity loss. In particular, some thresholds and selection criteria are applied at various stages of the analysis. Any possible signal lost during one of these steps will not be recoverable by later steps. For this reason, each step of the procedure is designed to reduce as much as possible the loss of possible CW signals, which could be hidden by the presence of strong disturbances or even by other superposing signals. Here, I review the procedures for spectral estimation, *peakmap* (PM) construction and candidate selection applied on O2 LIGO-Virgo data, with the aim of testing their effectiveness when clusters of signals are present. All these steps play a relevant role in determining the signal detectability and may bring to unwanted sensitivity losses if not properly addressed. A scheme of the FH pipeline is given in figure 4.1 and is briefly described in the following.

- [**A**] Creation of the short fast Fourier transform (FFT) database (SFDB).

  Detector calibrated data are split into chunks of duration $T_{\mathrm{FFT}} = 8192$, 4096, 2048 and 1024 seconds, interlaced by half their duration. Each chunk is then windowed with flat-cosine window and then Fourier transformed, using the FFT algorithm. With the different chunk duration we obtain four different sets of frequency domain data covering, respectively, the frequency range [0-128] Hz, [128-512] Hz, [512-1024] Hz, and [1024-2048] Hz. The chunk duration for each frequency band is chosen in order to maintain the frequency variation of a signal because of Doppler effect within the resolution $\delta f = 1/T_{\mathrm{FFT}}$. In this way, if a CW is present in the data it will be monochromatic within the single data chunk, transforming in a delta-peak in the periodogram. A scheme of the SFDB construction is shown in Figure 4.2. At each FFT chunk are also associated additional data, such as position and velocity of the detector at the chosen reference time. There is a work in progress to make this step in a more flexible way, making use of the band-sampled data (BSD) [170] framework.

- [**B**] Autoregressive spectral estimation.

  An autoregressive (AR) algorithm, described in [171], is used produce a smoothed noise spectral density of each data segment with the scope of whitening the data. It is designed in such a way to preserve possible CW signals, which in a single FFT would be confined within one single frequency bin, and at the same time to be able to follow slower spectral variations. The filtering is usually done backwards through the frequency bins, that is from higher to smaller frequencies, to better adapt recursion to the noise behavior of the detectors, which shows much higher and rapidly varying

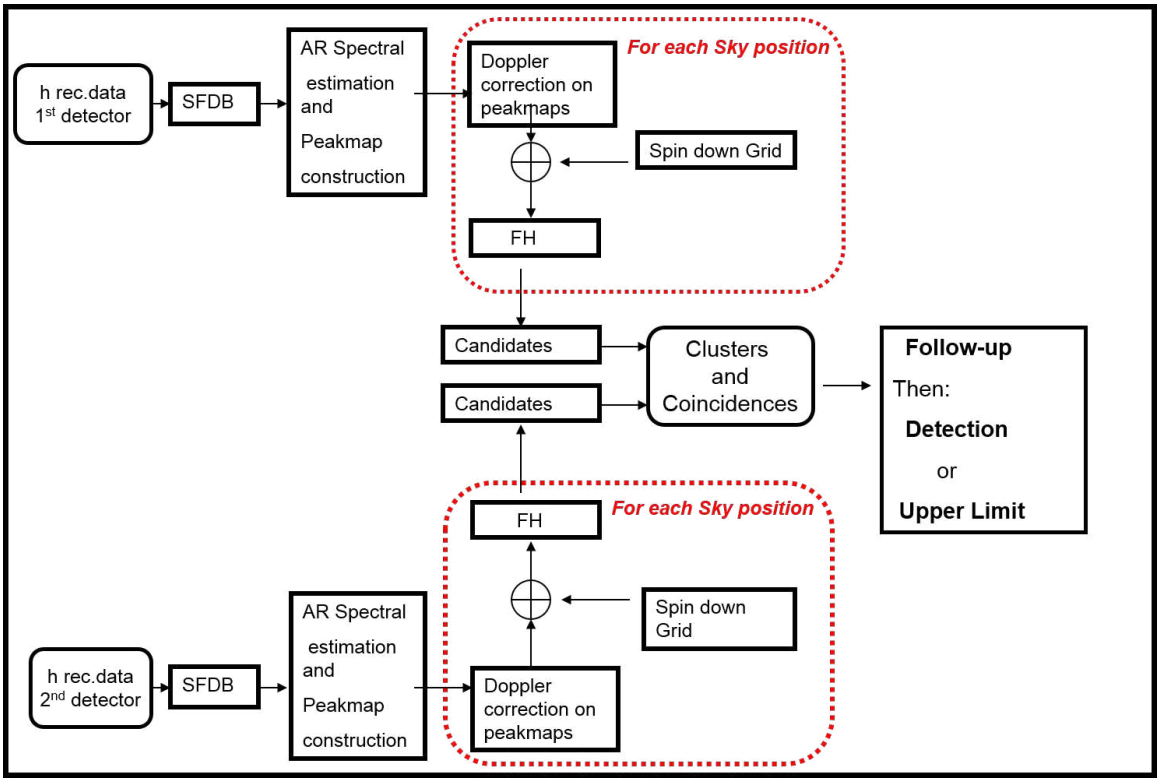

Figure 4.1: Scheme of the hierarchical FH procedure, in the case of data from 2 detectors, as described in Section 4.2.

values in the low frequency band, i.e., below $\sim 30\,\mathrm{Hz}$. The AR algorithm will be reviewed more in detail in Section 4.2.1.

- [**C**] Peakmap creation.

  For each FFT, labeled with the integer index j, the ratio $\mathcal{R}_j(f)$ among the periodogram $S_{P;j}(f)$ (square modulus of the FFT) and the AR spectrum estimation $S_{AR;j}(f)$ is computed in order to whiten the spectrum. From the ratio vector $\mathcal{R}_j(f)$, local maxima above a given threshold, called peaks, are selected. The peakmap (PM) is the collection of all the peaks, each one identified by a value of the frequency and a time (the middle time of the corresponding FFT), both measured at the detector. AR spectral estimation and PM construction have been used since many years for these analyses and their mathematics (and statistics) is described in [171, 122].

- [**D**] FH transform.

  For each sky position, the peaks in the PM are shifted in frequency to remove the Doppler effect for that position at the peak time. Figure 4.3 shows an example of a PM zoomed around a simulated signal from a pulsar, before and after the Doppler correction (top left and top right plots, respectively). When the annual and daily modulations are removed, the signal results nearly-monochromatic, with a linear spin-down at most. The shifted peaks are fed to the Hough transform, which maps the time-frequency peaks to the source frequency and spin-down plane. The Hough map is basically a 2-dimensional histogram of the PM in the $(f_0, \dot{f}_0)$ plane. This procedure

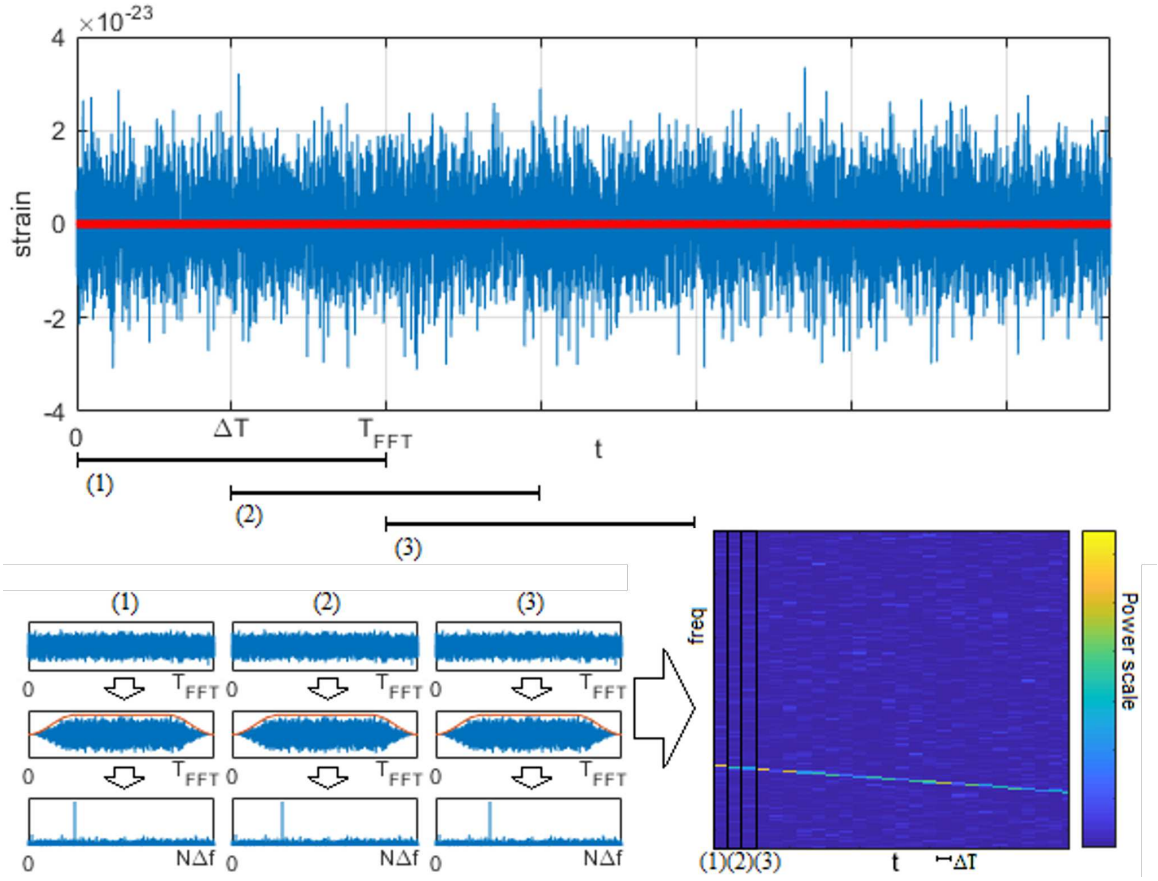

Figure 4.2: Schematic representation of how the SFDB is built. The full data series is splitted in chunks of length T_{FFT}, interlaced by $\Delta T = T_{FFT}/2$. Each data chunk is windowed and then its FFT is stored in the SFDB, together with additional data. In the example, a simulated CW is present in the data.

is repeated for each different sky position, having constructed a discrete grid in the sky optimized to the search resolution.

- [**E**] Candidate selection and coincidence analysis.

  Candidates are selected in the FH plane by finding, for each sky position, the points with highest number count in each frequency and spin-down sub-interval. Candidates from the analysis of a given data set are cross-checked against candidates found in the analysis of another data set (of the same detector or of a different detector) by means of coincidences in the signal parameter space.

- [**F**] Candidates follow-up and verification.

  A deeper analysis is done on those candidates which survive the coincidence step, in order to confirm their astrophysical origin or demonstrate they are compatible with noise or due to detector artifacts. The standard follow-up approach consists in rerunning the search starting from longer duration FFTs, in a limited portion of the parameter space around each candidate. In case of no detection, upper limits (UL) on the signal strain amplitude are computed as a function of the frequency.

The first 3 points - SFDB creation, AR estimation and PM construction - are typically performed during the observing run, as the calibrated data are recorded. Contextually, also a cleaning procedure is applied to remove all transient features that disturb CW searches. The point D - the loop to correct the PM for the Doppler effect from all sky positions and the Hough transform - must be done at the end of the run, when all the data have been collected, and is the most computationally demanding part.

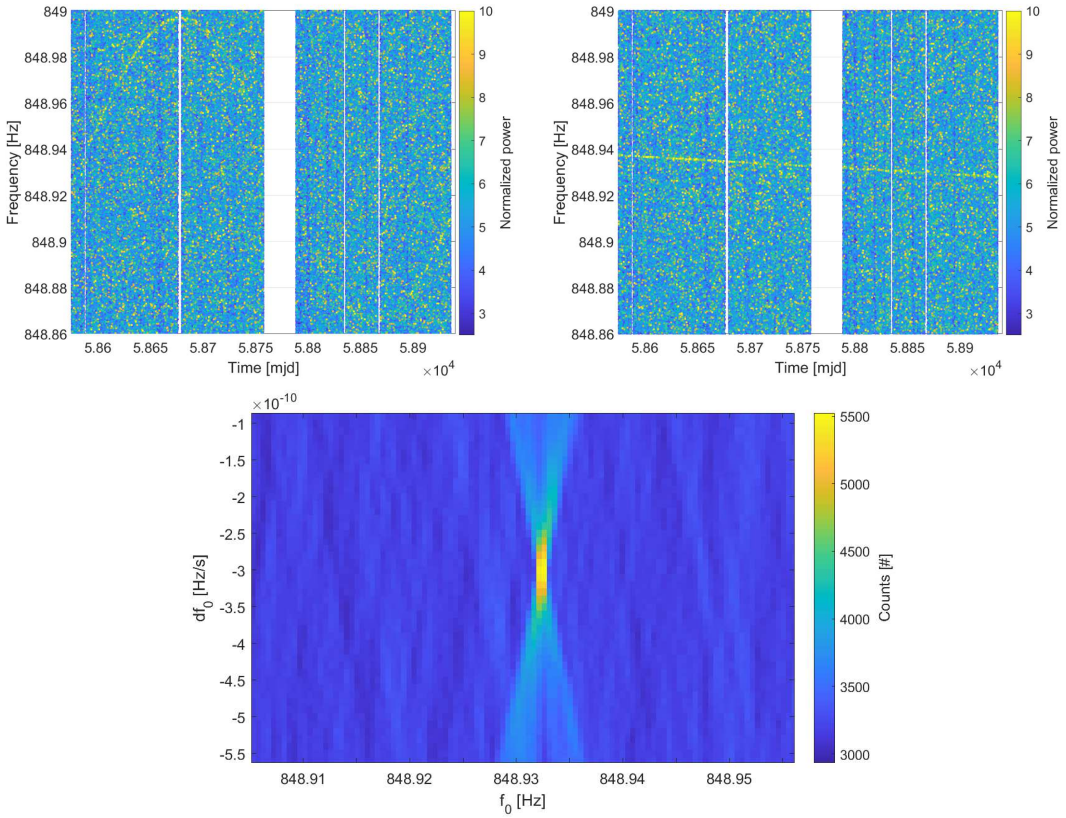

Figure 4.3: Example of the transformation on a simulated signal with $f_0 \sim 848.93\,\text{Hz}$, $\dot{f}_0 \sim -3 \cdot 10^{-10}\text{Hz/s}$, $\alpha \sim 37.4\,\text{deg}$ and $\delta \sim -29.5\,\text{deg}$. The top-left plot shows the PM containing the signal, with the annual Doppler modulation well visible. The plot shows also the peaks normalized power even if they are not used by the Hough transform. In the top-right plot, the PM has been corrected for the Doppler effect and the signal has become a straight line with parameters f_0, $\dot{f}_0$. In the bottom plot, the Hough map is shown. The $(f_0, \dot{f}_0)$ coordinates show an excess of pixel counts with respect to the foreground in correspondence with the signal parameters.

4.2.1 Spectral estimation and peakmap construction

After the construction of the SFDB, an important step with an impact on the sensitivity of the FH procedure is the estimation of the average power spectral density (point [B] in previous section). The procedure is described in details in [171] and here its basic aspects are reviewed, showing some examples using O2 data [158]. A nearly monochromatic wave with enough high amplitude will produce a delta spike above the noise floor in the periodogram.

When performing the whitening (point [C] in previous section), the periodogram is divided by the AR estimate. The whitened spectrum has exponential distribution with unit mean value, except where a narrow peak is present in the periodogram. That peak will be selected into the PM only if its whitened power, i.e. after the division, is greater than a fixed threshold θ_{thr}. If the AR estimator follow that peak, its whitened power results decreased and its chances to be selected in the PM decrease. So, a good spectral estimator for CW searches should have the following properties:

- If narrow peaks in the frequency domain are present, the estimator should not be affected by that peaks. This should be as much as possible independent on the SNR of the peak.
- If the noise level varies, either slowly or rapidly, the estimator should be able to follow the noise variations.

Let x_i be the data samples of the FFT, with the integer i ranging from 1 to the number of samples in the FFT. The amplitude spectral density is estimated from an AR estimation, as shown in the equations below:

$$y_1 = x_1$$

$$y_i = x_i + w \cdot y_{i-1}$$

$$w = e^{-\delta f/\tau_f}$$

where y_i are the samples of the not normalized AR mean, obtained using w as weight, with δf being the FFT resolution and τ_f the memory of the AR mean (with dimensions of a frequency). The values of the normalized AR estimations are given by

$$\mu_i = \frac{y_i}{Z_i},$$

where the normalization constant is $Z_i = 1 + w \cdot Z_{i-1}$, initialized as $Z_0 = 0$. Besides this, in order to have a "clean" estimator, that is not affected by spectral peaks, a threshold V_{max} and an age A_{max} are defined. While $r = \frac{x_i}{\mu_{i-1}}$ is lower than (or equal to) the threshold, the new datum x_i is used to evaluate the actual mean and the age of the estimator is set to zero (expressed in number of samples).
When $r = \frac{x_i}{\mu_{i-1}}$ is larger than the threshold V_{max}, the new datum is not used to evaluate the actual mean and the age of the estimator is incremented by 1 bin (that is, by a frequency equal to the resolution). This eliminates or at least reduces the effect of peaks from the estimation.
If the estimator becomes too old, i.e., if the age becomes greater than the maximum age we have set, we deduce that we are not in presence of a peak (and thus of a possible signal), but only that the noise characteristics have changed. The estimator thus goes back by a number of samples $n = A$, and begin a new evaluation of the mean, restarting from zero at the sample $i - A$. This is needed to deal with all those situations when the noise is highly non-stationary.

Figure 4.4 shows an example, where the AR estimation is plotted together with the absolute value of the corresponding FFT. From the plots on the left and from the zoom on the right it is possible to note how, when narrow peaks are present in the FFT, they do not appear, or appear significantly reduced, in the AR estimation, and so are not (or only slightly) suppressed in the PM. More examples are given in Section 4.3, where we show the results after adding fake CW signals to the O2 data.

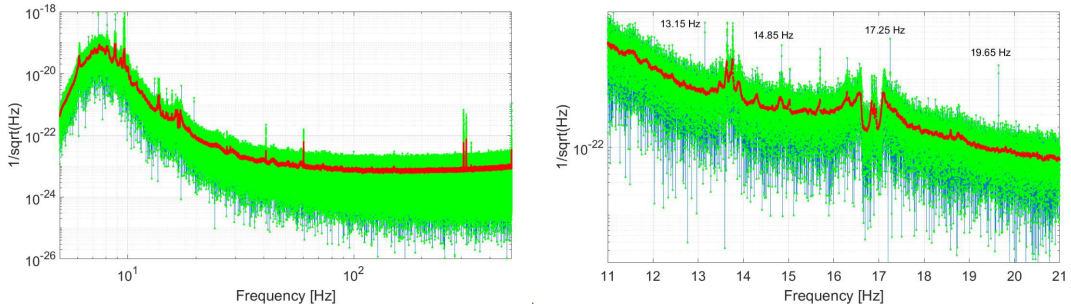

Figure 4.4: An example of one FFT (green dots, blue lines), of duration 8192 s, done using LIGO Livingston O2 data [158], and the corresponding AR amplitude spectral density estimation (red). Here, for comparison, the FFT has been normalized to represent the amplitude spectral density and its absolute value is plotted. The left plot covers the band [5-512] Hz and the second plot is a zoom in the frequency region from 11 Hz up to 21 Hz. It is possible to appreciate that the AR estimation follows sharp changes on noise floor, like those around 14 Hz and 17 Hz. On the other side, narrow peaks like those labeled in right plot do not appear in the AR estimation, as required.

After the ratio bib-by-bin is computed, the peaks are saved in the PM if they are local maxima with normalized power above a threshold θ_{thr}. A signal $h(t)$ in a single chunk would have normalized power

$$\lambda = \frac{4\left|\tilde{h}\left(f\right)\right|^2}{T_{FFT}S_n\left(f\right)} \tag{4.1}$$

Then, the probability p_0 of selecting a noise peak above θ in absence of signals is [122]

$$p_0 = p\left(\theta;0\right) = e^{-\theta} - e^{-2\theta} + \frac{1}{3}e^{-3\theta} \tag{4.2}$$

while, if a signal with normalized power λ is present, the probability p_λ to select it in the PM in the limit of small signals is [122]

$$p_\lambda = p\left(\theta;\lambda\right) = p_0 + \frac{\lambda}{2}\theta\left(e^{-\theta} - 2e^{-2\theta} + e^{-3\theta}\right) + \mathcal{O}\left(\lambda^2\right) \tag{4.3}$$

Thus, the choice of the threshold influences the search sensitivity. Its value is set to $\theta_{\text{thr}} = 2.5$ as an optimal trade-off between sensitivity loss and the expected number of selected peaks (which influences the computational costs). With this choise, the probability to select a noise peak is $p_0 \simeq 0.0755$.

4.3 Qualitative impact of multiple signals

Since the goal is to study the robustness of the FH method, it has to be tested relaxing the assumption that there are no superposing signals. In the following, the focus will be set on the AR spectral estimation and PM characterization steps, showing how they behave in presence of many CW signals spread in a narrow frequency interval.

4.3.1 Qualitative effect on autoregressive estimation

Following the steps described in Section 4.2, I have simulated a number of signals from 10 to 50 and I have added them to 4096 seconds of data from LIGO Livingston during the O2 run [158]. Then, I have generated the SFDB, with resolution $\delta f = 1/4096\,\mathrm{s} \simeq 2.44 \cdot 10^{-4}$Hz, and the AR estimate using the procedure described in 4.2.1, and I have checked the different impact of different configurations of signals. The signals have random sky localization, random source frequencies within few frequency bins around 338.5 Hz and, for simplicity, without spin-down. Their amplitude is in the range $2 \cdot 10^{-25} - 10^{-24}$, which is above the ULs found in O2 [160] around their frequencies. Details of the used configurations are given in Table 4.1.

label	n.sig	f_0 range [Hz]	h_0
1	10	$[338.5,\ 338.5 + \delta f]$	1×10^{-24}
2	20	$[338.5,\ 338.5 + 2\delta f]$	1×10^{-24}
3	50	$[338.5,\ 338.5 + 5\delta f]$	1×10^{-24}
4	50	$[338.5,\ 338.5 + 5\delta f]$	6×10^{-25}

Table 4.1: Parameters used to simulate CWs in different density configurations, labeled from 1 to 4 in the first column. The second column reports the number of simulated signals, the third column the frequency range used to randomly generate the source frequencies and the fourth column the signal amplitudes.

Figure 4.5 shows what happens to the AR estimation inside a single FFT, in the four different injection configurations. Note that all added signals have their proper frequencies f_0 within few frequency bins, but because of their randomly distributed sky position they are further spread by Doppler modulation. By looking at the trend of the AR estimation (red curve in Figure 4.5), it is clear that generally it is not strongly affected by the presence of an ensemble of signals: it gets non-negligibly higher values around 338.5 Hz only in case 3, when I have added 50 strong signals with f_0 within 5 bins, i.e. within 1.23 mHz. In this case, the whitened power that will be obtained around 338.5 Hz will be reduced by $\sim 30\%$. This fact obviously motivates a further investigation.

4.3.2 Peakmaps with multiple signals

In the previous subsection I have shown that a concentration of signals in a narrow frequency band can influence the AR estimation and consequently cause a loss in the whitened power. However, this does not imply automatically that the signal peaks in that frequency region are lost. It is important not to lose possible signal peaks at this level, as they cannot be recovered after. After the periodogram (square modulus of the FFT) and the AR spectrum estimation are computed and divided bin-by-bin, local maxima with whitened power above the fixed threshold θ_{thr} are selected. It is worth to note that the actual value of the whitened power is not used in the analysis. In fact, the Hough map is just 2-dimensional histogram in the signal parameter space: each bin counts the number of peaks corresponding to the signal described by the bin coordinates. This choice has the positive effect to reduce the impact of large noise spectral disturbances. This also implies that the reduction of whitened power influences only the probability of selecting the peaks, and does not influence the next steps.

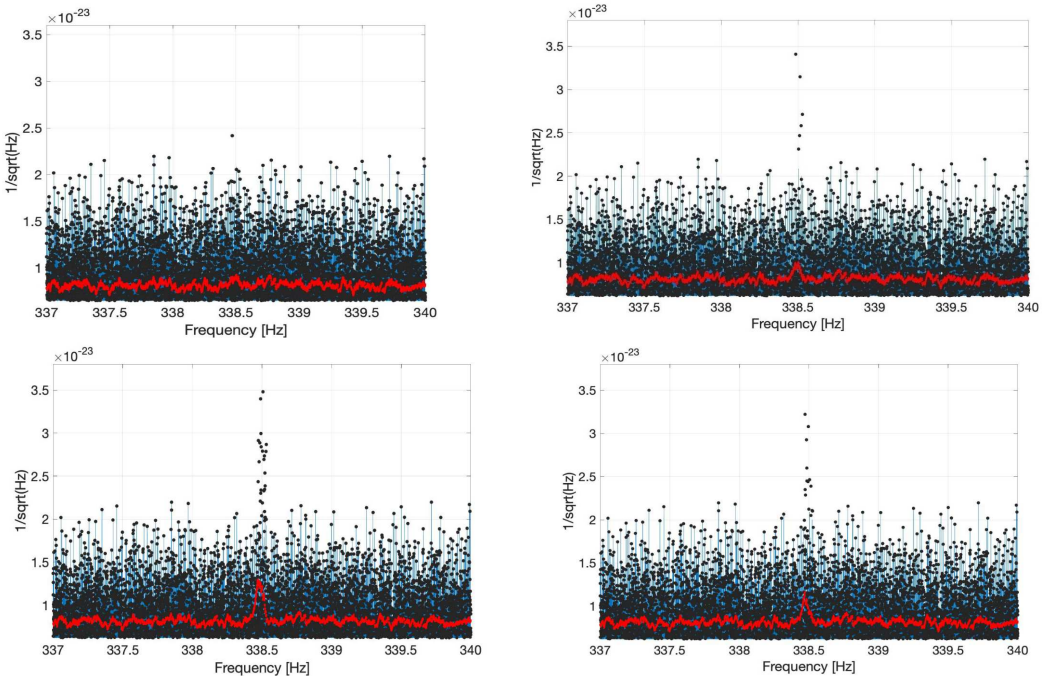

Figure 4.5: Plots of the 4 different injections listed in Table 4.1 made on one FFT calculated using 4096 s of LIGO Livingston O2 data [158]. Top left, top right, bottom left, bottom right show the configurations respectively of label 1, 2, 3 and 4.Blue lines and black dots represent the absolute value of one normalized FFT, in a 3 Hz band, around 338.5 Hz. The red line is the corresponding AR amplitude spectral density estimation. The effect of the signal peaks in the AR estimation is negligible in the first two cases, very small in the last case, while it reduces the contribution of some of the strongest peaks in the third case (50 strong signals, with source frequency f_0 within 5 bins).

When peaks from different FFTs are put together in the PM, the peaks of an astrophysical signal follow a time-dependent pattern determined by the Doppler effect. This effect has to be corrected before running the Hough transform. The Doppler correction plays a crucial role also when more signals are present. The correction is done by properly shifting the peaks frequency in the input PM, for each sky position for which the search is running. As shown in Figure 4.6, even in the case of multiple signals belonging to the same frequency bin at a given time, the Doppler correction, which is different for each sky position, permits to clearly distinguish the various signals. This is a very powerful feature as, moreover, it enhances the SNR of CW signals with respect to noise lines. The first plot in Figure 4.6 shows a zoom of a PM with 10 injected signals. The signals have been generated with the same intrinsic frequency f_0, that is within the same frequency bin, but with randomly chosen sky positions, so that their frequencies at the detector appear separated, due to the Doppler effect which introduces a maximum frequency shift of

$$\Delta f_{dop} \simeq 2f_0 \left| \frac{\vec{v} \cdot \hat{n}}{c} \right| \simeq 2f_0 \times 10^{-4}, \tag{4.4}$$

where, according with Section 2.1.1, $\vec{v}$ is the detector velocity vector and $\hat{n}$ is the unit vector identifying the source position in the sky. When the Doppler effect is removed correctly for each of these signals, we can see the injected signal as a sequence of peaks along a straight

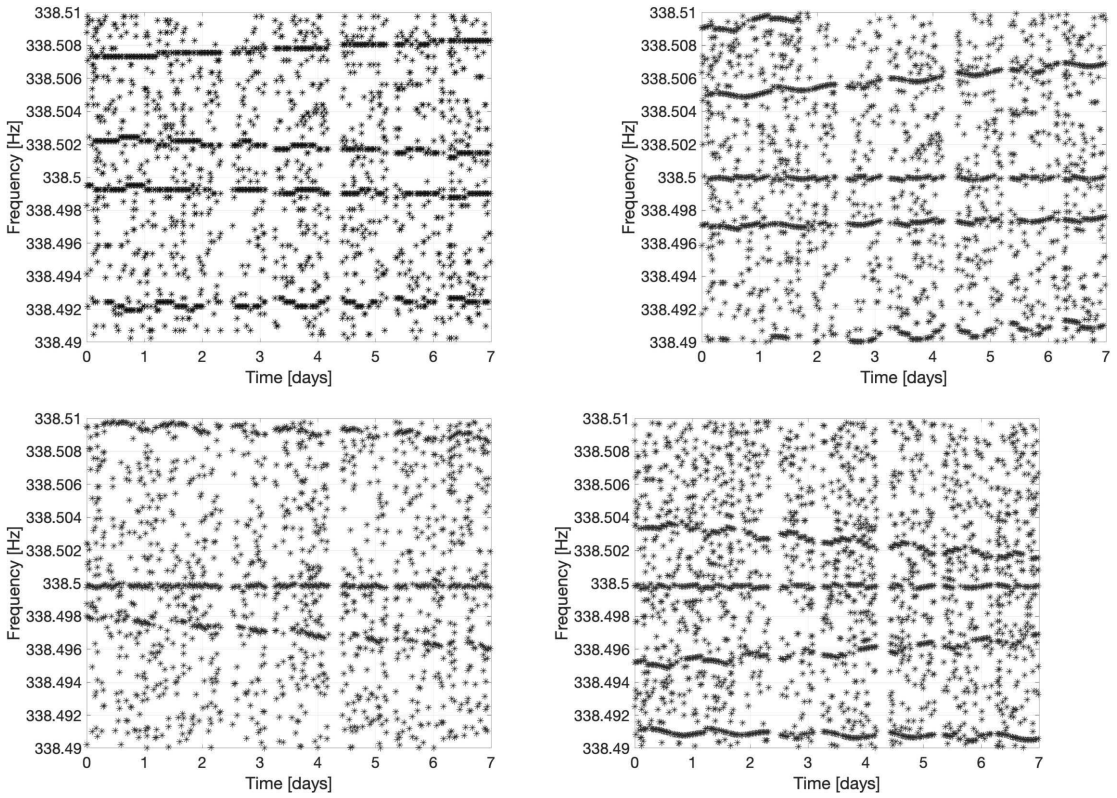

Figure 4.6: The top left plot shows a zoom on a PM of LIGO Livingston O2 data [158], where different fake CW signals are added. Those signals have all the same proper frequency, $f_0 = 338.5$ Hz, but different sky positions. They are strong enough to produce patterns visible by eye: each one follows a different time-frequency trajectory, having different Doppler modulations. In the other plots (top right, bottom left and bottom right) the Doppler correction is applied respectively for one of the signals sky direction. When the Doppler correction matches the sky localization of a signal source, its corresponding trajectory becomes a straight line confined on f_0. On the other side, the other signals trajectories get further distortion.

line at the right f_0 frequency. This is shown from the second to the fourth plots of Figure 4.6. It is possible to note here that there is only one straight line, which corresponds to the properly Doppler corrected peaks.

In conclusion, these plots show that, even if signals are clustered in frequency, the presence of the Doppler modulation gives a powerful tool to distinguish them. Thus, in all analyses where candidates are selected separately for each sky position, as in the case of the FH pipeline, the presence of signal clusters does not blind the search. Clearly, the resolving power is limited by the resolution of the sky grid used, which depends on the frequency resolution [122]. The candidate separation effect is clearly stronger as the observing time improves, and it is maximum for one year of data, when the Doppler annual modulation completes one cycle.

4.4 Study on the detection efficiency

In the previous sections we have qualitatively discussed the possible negative effects due to the presence of signal clusters. This section is devoted to properly quantify the effect of multiple signals and their impact on the pipeline performances. In order to do this, we need to define an observable. The simulated signals have negligible spin-up with respect to the analysis resolution so that after the Doppler correction they are monochromatic, meaning they are represented in the PM by a straight line at the constant emission frequency f_0. After the Doppler correction, the next step is to construct an histogram counting the number of peaks as a function of the frequency, using the same frequency resolution of the search. The expectation is to find an excess of counts in the histogram bin associated to the source frequency f_0. Let we define the *detection efficiency* as

$$\eta = \frac{n_{sig} - \bar{n}_{noise}}{n_{FFT}}, \tag{4.5}$$

where n_{sig} is the histogram number count at the frequency f_0, $\bar{n}_{noise}$ is the average number of counts at all the other frequencies except for f_0, and n_{FFT} is the number of FFTs used to construct the PM. Figure 4.7 shows an example of an histogram built on the frequency grid, having injected a signal at $f_0 = 338.5$ Hz, constructed the PM and removed the Doppler effect. It is important to underline that the detection efficiency η defined here does not determine the full sensitivity of the FH procedure, even if the two concepts are strictly related. The expected value of η is the difference between the probability p_λ of selecting a peak when a signal with normalized spectral amplitude λ is present and the probability p_0 of selecting a peak when only Gaussian noise is present,

$$E[\eta] = p_\lambda - p_0. \tag{4.6}$$

In the following, there will be computed estimates of η in different situations. In order to limit the computational cost of the study, the simulations are done using one week of data, as the goal of the work is a comparison of different situations on the same data set. The data set is extracted from the LIGO Livingston O2 run [158], starting from GPS=1186606177. The efficiency is computed as a function of the density of signals injected in given frequency intervals and compared to the case when no signal cluster is present. Let we call Δf_0 the interval in which the source-frame frequencies are randomly generated. Because of the random sky localization of the sources, the detector-frame observed frequency will be unevenly distributed into a frequency range given by

$$\Delta f = \Delta f_0 \pm \Delta f_{dop}. \tag{4.7}$$

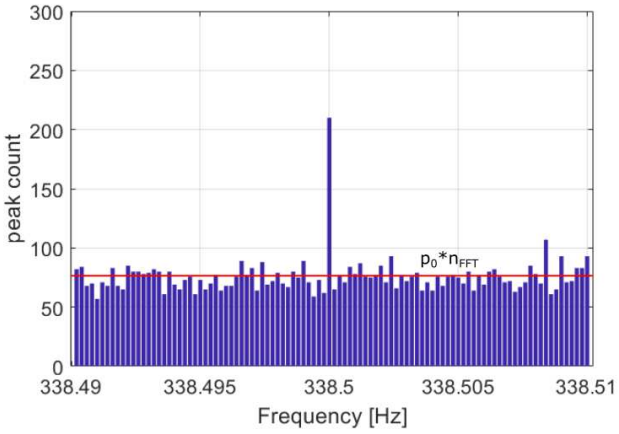

Figure 4.7: Example of an histogram of a PM, built using the frequency resolution as bin width. Here an excess of counts is clearly visible at the frequency 338.5 Hz, where a signal has been injected into $n_{FFT} = 1000$ discrete FFTs. The red line represents the theoretically calculated expected noise counts, $E[\bar{n}_{noise}] = p_0 \cdot n_{FFT}$.

where Δf_{dop} is the spread of the signal frequency at the detector frame due to the Doppler effect, given by Equation 4.4. In this way we can establish how many signals to inject in a given frequency interval by tuning f_0 and Δf_0. The number of frequency bins covered by the signals is

$$n_{\text{bin}} = \frac{\Delta f}{\delta \nu} \tag{4.8}$$

and we can refer to the resulting mean density of signals-per-frequency-bin as

$$\rho_{sig} = \frac{N_{\text{sig}}}{n_{\text{bin}}}. \tag{4.9}$$

The detection efficiency will be used in the following sections to quantify the results of Monte Carlo simulations, using different distributions for the signal amplitudes.

As a first example of how the efficiency can be used, let we consider a rather extreme scenario. In what follows 50 signals, all with the same amplitude, are simulated with proper frequency in two bands covering, respectively, a $5\delta f$ and 10 Hz width. This last one corresponds practically to a situation with non-clustered signals. The injection parameters are listed in Table 4.2. Figure 4.8 shows all the obtained efficiencies in both cases, together with mean values, median and standard deviation of the results. Estimations of the overall efficiency, also with the signal-per-bin densities, are reported in Table 4.2.

label	Δf_0	h_0	ρ_{sig}	$E[\eta] \pm \sigma_\eta$
$5\delta f$	$[338.5, 338.5 + 5\delta\nu]$	1×10^{-24}	~ 0.15	0.58 ± 0.09
10Hz	$[333.5, 343.5]$	1×10^{-24}	$\sim 10^{-3}$	0.72 ± 0.09

Table 4.2: Parameters used to simulate CWs in two different density configurations, labeled as $5\delta f$ and 10Hz, the obtained signal densities ρ_{sig} and efficiency estimations.

Looking at the outcome, we observe a loss in efficiency of $\sim 19\%$ between the clustered signals configuration and the one with non-clustered signals. In other words, in presence

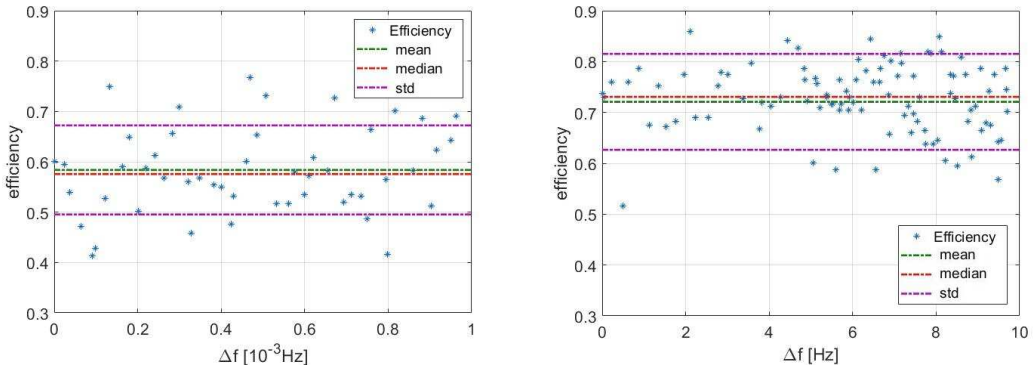

Figure 4.8: Efficiency η in the two cases of: 50 injected signals with $h_0 = 10^{-24}$ distributed in $\Delta f_0 = 5\delta f \sim 1.2$ mHz - left plot - and widely spaced (over 10 Hz) - right plot. Mean, median and standard deviation of the efficiency are also shown.

of the cluster we recover in average the 81% of signal pixels with respect to non-clustered signals. Obviously the presence of only strong signals, all with the same amplitude, is an unrealistic limit-case, since in general the signals are distributed in amplitude.

4.4.1 Varying amplitude signals with low densities

In this subsection I present the results of multiple injections in a more realistic regime in which signal amplitudes are not constant, as in the previous case, but uniformly distributed. In order to get a complete understanding, the whole frequency region where the detectors have the best sensitivity, [70 - 512] Hz, is covered. The signals have been simulated with source frequencies around 12 different values in that interval and with source positions randomly chosen. For each one of that 12 central frequencies, 10 signals have been injected with proper frequencies distributed in six different ranges Δf_0. The choice is done to search for evidence of a decreasing efficiency when the signals are concentrated in a smaller range. All the chosen parameters are reported below:

$h_0 \in [2 \cdot 10^{-25}, 1 \cdot 10^{-24}]$
$f_0 \in \{70.5;\ 105.5;\ 120.5;\ 170.5;\ 205.5;\ 220.5;\ 270.5;\ 330.5;\ 380.5;\ 420.5;\ 442.5;\ 492.5\}$ Hz
$\Delta f_0 \in \{\delta f;\ 10\delta f;\ 20\delta f;\ 50\delta f;\ 100\delta f;\ 10$ Hz$\}$

Thus, the signal densities ρ_{sig} explored in this section are in the range [0.001 - 0.1]. We can refer to this test as a "low density" regime.

Figure 4.9 shows bar plots of median values of the obtained efficiencies. They are grouped according to the different Δf_0 (represented by different colors), for the different injection frequencies. The efficiency values do not show any systematic decrease when going toward the smaller Δf_0. In Figure 4.10 the bar plots are combined together and the average efficiencies (with respect to the injection frequency), together with standard deviations, are shown as a function of Δf_0. The highest standard deviation in the case of signals injected in 10 Hz is due to the fact that within such a large band it is more likely to find strong narrow disturbances that worsen the detection efficiency in that band. Also in this plot, there is no clear effect on efficiencies due to the clustering of source frequencies. We can

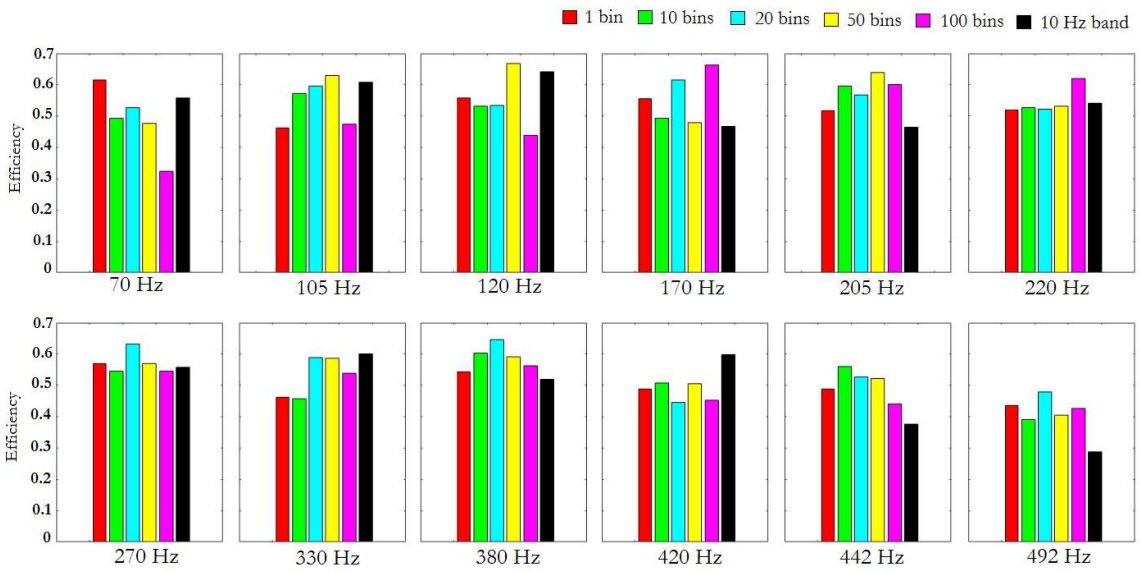

Figure 4.9: Bar plots of the simulation done in Section 4.4.1. The bars show the median efficiency computed for 10 signals with source frequency within respectively 1, 10, 20, 50, 100 frequency bins δf and 10 Hz (equivalent to $40960 \cdot \delta f$ bins). The color code is: 10 signals in 1 (red) 10 (green) 20 (cyan) 50 (yellow) 100 (magenta) bins and 10 Hz (black). On the bottom of each box the central source frequency of the injected signals is shown. Signal amplitudes have been generated from a uniform distribution in the range $h_0 = 2 \cdot 10^{-25} - 1 \cdot 10^{-24}$. Those plots show that there is not an evident efficiency loss when signals are concentrated in smaller Δf_0.

conclude that in the low density regime, that is $\rho_{\rm sig} < 0.1$, there is not efficiency reduction and the procedure is able to recover all the signals.

4.5 Simulation of signal clusters from boson clouds

In this section, I simulate situations that are expected in the most extreme cases of CWs emitted by boson clouds around galactic BHs. In the study proposed in [167], it has been suggested that an high number of galactic BHs could potentially produce up to thousands of signals with amplitude above the O2 ULs at the detectors. Depending on galactic BH population and the boson mass, those signals could cluster into a frequency region having a width that spans from ~ 0.01 Hz to ~ 1 Hz. Based on these indications, I have reproduced two scenarios, namely one with signals clustered into a [0.04 - 0.06] Hz band and another with signals in a 0.8 Hz band, one order of magnitude larger. Also in these cases I have repeated the simulations injecting signals in ranges of different width around different central frequencies, in the range [70 , 512] Hz. Over 4,000 signals were generated with random parameters and amplitude in the range $[1 - 20] \cdot 10^{-25}$, following a power law distribution $\sim h^3$ such to mimic the ratio of detectable signals below and above the O2 UL as found in [167]. These signals are added in one week of data from LIGO Livingston during O2. Then, I have constructed the FFTs and the PM and I have repeatedly corrected for the Doppler for all the signals. After each Doppler correction, I have constructed the histogram on the frequencies and evaluated the detection efficiency for that signal. Then, I have repeated the

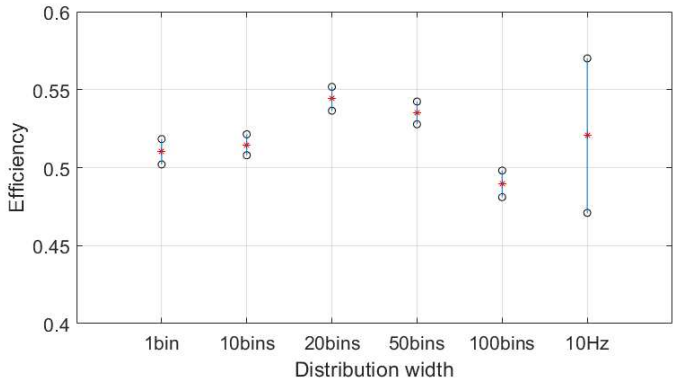

Figure 4.10: Error plot of the simulation described in Section 4.4.1, in the "low-density" regime. Differently from Fig. 4.9, efficiencies are combined together grouping for the different 12 injection frequency. Average efficiency η (stars) and standard deviation (bars) are shown as function of Δf_0.

whole procedure injecting the same signal alone in the data in order to get a direct estimate of the losses.

In Figure 4.11 the results of the simulation are shown. The plotted quantity is the ratio between the detection efficiency of signals in the clustered configuration and the efficiency of the same signals, when injected alone. This is done in order to compare efficiency variations at different frequencies and on signals with different amplitudes, which have different detection efficiencies. This efficiency ratio is plotted as function of the mean signal density. Colored areas span from minimum to maximum values of the mean ratio obtained from injections around different frequencies, in the range [100,400] Hz, in clean bands. The blue area represents the ratio for the whole ensemble of injected signals, whereas the green and red belts refer to the subsets of signals with h_0 respectively above and below O2 ULs. Looking at the different regimes, we recognize qualitatively different behaviors.

1) In the case of signals injected into a $\sim$ 0.06 Hz band (Figure 4.11, left plot), for signals with amplitude above O2 ULs, the efficiency loss ratio is of few percents at the most. After a minimum of ≈ 0.9 reached between $\rho_{sig} \approx 1-2$, the ratio grows up to 1. On the other side, for signals with amplitude below O2 ULs the efficiency ratio increases for growing signal densities, which means their detection efficiency increases - i.e. we recover more pixels belonging to those signals. As I will explain in the following, this effect is due to the superposition of signals in the same frequency bin. On the whole set of signals, the result is a global efficiency gain in the range $[1, 2.2]$, the highest reached at the highest signal densities. An analogous reinforcement effect is used in [172, 173], where the contributions of multiple sub-threshold CWs are combined to enhance their detection chances in the context of targeted searches. Consequently, in this configuration there is no overall efficiency loss and, moreover, also weak signals have a growing probability to be recovered. Since also stronger signals do not suffer a significant efficiency loss, the conclusion is that both detection efficiency and evaluation of ULs are not affected.

2) The case of signals injected into a $\sim$ 0.8 Hz wide band (Figure 4.11, right plot) corresponds to the most extreme situation depicted in [167]. In this case the behavior of the efficiency ratio changes significantly. First of all, the two distinct signal subsets have no opposite dynamics as they show both an efficiency loss as the signals density increases.

While the efficiency ratio of signals with amplitude below O2 ULs stops decreasing at a signal density $\rho_{sig} \approx 1$ (with a corresponding efficiency ratio of $\sim 0.8 \pm 0.05$), the efficiency ratio for the subset of signals with amplitude above the UL continues decreasing, reaching values around 0.6 for signal densities $\rho_{sig} \approx 2$. For the whole set of signals, values in the range 0.75 ± 0.05 are reached. Since the detection efficiency is directly related to the individual probability p_λ to select a peak if a signal is present, and given that the overall search sensitivity is proportional to the square root of that probability [122], the conclusion is that in the most extreme - and probably very unrealistic - cases the search procedure could lose up to $\sim 15\%$ of the "optimal" search sensitivity (i.e. that with no superposition of signals). As discussed in the following, a mean signal density of two is actually much larger than predicted in [167].

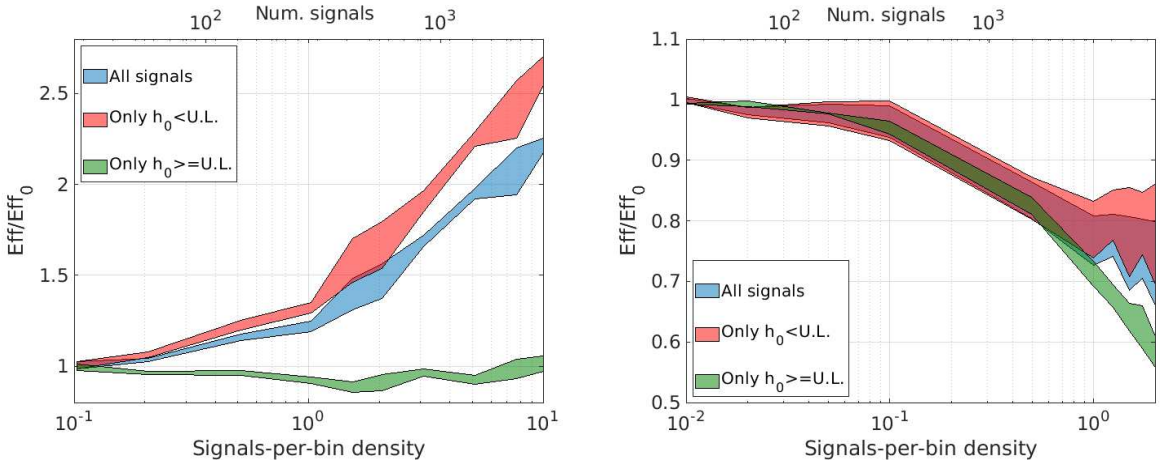

Figure 4.11: Injections in the "high-density" regime. Mean values of the ratio between detection efficiencies in the case of signals clustered together (Eff) and in the case of each of those signals taken alone (Eff_0), as function of the signals-per-bin density (bottom x axis) and number of injected signals (top x axis). The signals are injected around 170 Hz, 240 Hz, 338 Hz, 380 Hz: colored areas span from minimum to maximum values obtained at the different frequencies. The blue area shows the overall efficiency ratio for the whole signal ensemble, whereas green and red areas refer to signals that are respectively above and below O2 ULs. Left plot shows the result when signals are clustered in a wide 0.06 Hz frequency range. Right plot shows the result when signals are clustered in a wide 0.8 Hz frequency range. In both cases the same order of magnitude of signals has been injected, but in the right plot the wider frequency range leads to lower signal densities.

Both the described dynamics have a clear explanation in the way the AR spectral estimator works. When the signal density is such to produce a wide excess power in frequency, the answer of the AR estimator depends on how wide the bump is with respect to the AR memory τ_f defined in Section 4.2.1. The chosen value for AR memory is typically fixed for each frequency band. In the present case, in the frequency range [128-512] Hz, a memory $\tau_f = 0.02$ Hz was used. In case 1), the signal cluster covers a 0.06 Hz frequency range, which is the same order of τ_f. Consequently, AR estimate is not fast enough to adapt to the increased noise (plus signal) level. When $\rho_{sig} \geq 1$, every frequency bin has an expected occupation of 1 signal. After that, any added signal would superpose to signals already present in the same bin, thus increasing its power content. The result is that the signal power in all bins of interest increases with respect to the noise floor. If the AR estimation

is not fast enough to adapt, its level will result lower than the majority of those bins, so that also weaker signals get more detection chances. This explains the observed growing efficiency in case 1). On the other hand, in case 2) the signal cluster covers a wide 0.8 Hz frequency range, which is one order of magnitude bigger than τ_f. In this case, even if signals continue to accumulate in the same frequency bins at $\rho_{sig} \geq 1$ and their power content increases, the AR estimation is able to adapt to the changed level. Thus, weak signals remain below the AR level, while strong signals are weakened with respect to the previous noise level.

There are two important considerations to do. First, the loss happens when we have actually high numbers of detectable signals (i.e., above the upper limit), while it affect much less the estimation of ULs. Second, the efficiency loss is plotted as a function of the mean signal density. For instance, a density of two signals per bin, means that on average in *all* bins of the injection band (e.g., 0.8 Hz in 4.11, right plot) we have such density. Looking at the results of [167], in one of their "worst" situations - see [167] figure 40, left panel - where BH spins up to an unrealistically large value of 1 are considered, the signal density above the UL can reach values as large as 5 in few bins, while in the vast majority of bins is below 2 (and, actually, is zero in most bins). The corresponding average density is difficult to estimate, but it is quite likely well below 0.5. As a consequence, the sensitivity loss is likely of the order or smaller than 5%, as the impact on the AR estimation would be smaller. Anyway, these results suggest that in presence of signal clusters as large as the tested 0.8 Hz there would be worth to perform the search trying different values of AR memory τ_f.

4.6 Discussion

In the work presented in this chapter, mainly inspired by the claims of [167], I have studied in detail how the basic steps of the FH algorithm for CW searches could be affected by the presence of clusters of signals. Two regimes, of "low-density" (with up to ~ 0.1 signals per frequency bin) and "high-density" signals (with up to 10 signals per frequency bin), have been considered. In particular I have evaluated the impact of signal clusters in the estimation of the average spectrum, and on the construction of the PMs, finding them very robust. I have found that the procedure used to estimate the average spectrum, needed to normalize the FFTs and then to construct the PMs, is robust with respect to the presence of ensemble of signals and works even in the most extreme situations. The small signal peak amplitude loss is compensated by the fact that signals do have a different evolution in time (due to their position in the sky) and then through the proper Doppler correction each signal can be properly reconstructed. In addition to this, in the case of homogeneous high density of signals across a small frequency band, I have shown that when the signals are spread in a frequency interval smaller than ~ 0.1 Hz, the overall efficiency increases thanks to the presence of signal clusters, as the probability to select a peak at a given time is enhanced. When the signals are spread on a much larger frequency range of ~ 0.8 Hz, this results in an efficiency loss of up to $\sim 15\%$, when the mean signal density approaches a value of two, due to the impact the signals have in the AR estimation of the average power spectrum. On the other hand, the "worst" cases considered in [167] correspond to a mean signal density significantly smaller than two, so that the corresponding sensitivity loss is reduced to a few percent at the most. The conclusion is that the Frequency-Hough procedure is robust with respect to the presence of signal ensembles, with negligible losses even in extreme cases.

Chapter 5

Image filtering for long-lasting transients

The work presented in this chapter is focused on the search of long-lasting GWs from young NSs. This kind of signals, which includes those associated to r-mode emission or millisecond magnetars, has been introduced in Section 2.1.2. In particular, I focus on signals with duration of the order of 1000 seconds. The search strategies for this kind of signals are typically done using semi-coherent procedures which, as I have explained in Section 2.3, have a sensitivity lower than those based on matched filtering. However this sensitivity gap can be reduced thanks to the application of new techniques. Here, I present the development and application of a 2-dimensional filter, called *triangular filter*, to be used with numerical matrices, like monochromatic images or spectrograms, in order to increase the SNR of signals buried inside the noise. The chapter is organized as follows: in Section 5.1 I introduce the Generalized Frequency-Hough search method, describing the assumed signal model and the first steps procedure. In fact, in my work I have reproduced these first steps in order to generate the spectrograms that are the input of the triangular filter. In Section 5.2 I describe how the information on the shapes inside an image, in particular the inclinations of curves and lines, is stored in the 2D Fourier space. Since the information on inclinations of curves is stored in different regions in the Fourier space, I have chosen to implement the filter in the Fourier space. In Section 5.3 I define the triangular filter and characterize it by applying it on maps containing only white noise. In Section 5.4 I present a Monte Carlo simulation where I have reproduced the first steps of the Generalized Frequency-Hough procedure in order to estimate the sensitivity gain achievable with the filter.

5.1 The Generalized Frequency-Hough procedure

Since the possible processes that can take place in a newborn NS are various and are likely superimposed, we have not a full comprehension of its early-life phase. It is therefore difficult to make GW searches based on optimal matched filter strategies: on one side, we have not a solid basis to build a bank of waveform templates; on the other side, even if we had a reliable set of templates, the parameter space to be explored would be huge and would make such search computationally unfeasible. From this point of view, the problem is analogous to the one of persistent CWs.

A search procedure has been developed to deal with long-transient searches, called

Generalized Frequency-Hough (GFH). It is a semicoherent search that takes inspiration from the FH pipeline, developed for the all-sky searches of CWs from unknown sources and studied in depth in Chapter 4. The target signal, however, is strongly different. Moreover, the GFH pipeline assumes to know the sky location of the candidate signal source, e.g. through a GRB observation or a binary NS coalescence detection. The GFH pipeline is fully described in [174]. Here I recall its first steps since this is relevant for introducing my work.

5.1.1 A generic model for long duration gravitational waves

The signal model taken in consideration is a generic long-lived transient, as suggested in [175], with the GW frequency evolving following a power law with no fixed braking index n (already defined in Equation 2.17 in Section 2.1.1):

$$\dot{f} = -k\, f^n \tag{5.1}$$

where different values of n correspond to different mechanisms driving the frequency evolution and k is a constant, whose value depends on the specific emission mechanism and has to be measured by the search procedure. According to Section 2.1.2, the braking index would assume value $n = 5$ for magnetically-induced deformations or $n = 7$ for r-mode oscillations, but since electromagnetic emission is always present ($n = 3$), most likely its value will be somewhere in between. The time-frequency evolution of the signal is obtained just integrating Equation 5.1:

$$f_{\mathrm{gw}}(t) = f_0 \left[1 + k\,(n-1)\, f_0^{n-1}\,(t - t_0)\right]^{-\frac{1}{n-1}} = f_0 \left(1 + \frac{t - t_0}{\tau}\right)^{\frac{1}{1-n}} \tag{5.2}$$

where we have defined a spin-down timescale $\tau = \Omega_0^{1-n}/k\,(n-1)$ and labeled f_0 as the GW frequency at $t = t_0$. The signal amplitude is therefore

$$h_0(t) = h_0 \left(1 + \frac{t - t_0}{\tau}\right)^{\frac{2}{1-n}} \tag{5.3}$$

where h_0 is the initial amplitude of the signal, which can be related to the star's ellipticity ε or to the r-mode saturation amplitude α depending on the model, and the power factor 2 has to be changed to 3 when the emission mechanism is the r-mode. Note that, differently from standard CWs, the signal amplitude is time-varying. This is because the GW amplitude is proportional to f_{gw}^2 in the case of magnetically-induced deformations and to f_{gw}^3 in the case of r-modes and the GW frequency, differently from CWs, is expected to vary significantly.

5.1.2 The first steps of the search

The GFH analysis works with SFBD data for the first steps and on the BSD framework for the follow-up of signal candidates. For each detector, data are divided into short chunks with optimized coherence time. As explained in Section 4.2, the segment duration is chosen in order to have approximately monochromatic signals within the FFT resolution. The general criteria is that the variation of signal frequency, from the beginning to the end of the segment, is less than the frequency resolution

$$\left| f_{\mathrm{gw}}(t_0 + T_{\mathrm{fft}}) - f_{\mathrm{gw}}(t_0) \right| < \delta f = \frac{1}{T_{\mathrm{fft}}} \tag{5.4}$$

While in the first stage of the FH the Doppler effect dominates the frequency variation of CWs and is unknown, in the present case we assume that the source position is known through electromagnetic observations. In this case the Doppler can be corrected as a preliminary step of the analysis, the signal spin-down dominates the variation of the observed frequency. Thus, the criteria for choosing the optimal FFT length is

$$T_{\mathrm{fft}} < \frac{1}{\sqrt{|\dot{f}_0|}} \tag{5.5}$$

The SFDBs are built with multiple resolutions, with $T_{\mathrm{fft}} = 2 - 8\,\mathrm{s}$, which account for initial spin-down rates of $10^{-1} - 10^{-2}\mathrm{Hz/s}$. They cover the frequency range [50, 2000] Hz, considering the signal starting frequency f_0 in the range[500, 2000] Hz because of the conservation of the total angular momentum of the NS progenitor (typically binary NS merger or core-collapse SNe) [176]. The following part is analogue to the FH procedure: from each FFT, the power spectral density is evaluated and then whitened through an AR estimate. From the power spectra, the PM is built selecting only local maxima with whitened power above a fixed threshold. An example of PM with a simulated r-mode GW signal is shown in the top left plot of Figure 5.1. A GW signal like the long transient ones produces an excess of power along a time-frequency trajectory described by Equation 5.2, and consequently and excess of pixels in the PM. The next step consists in transforming the PM. Since the signal pattern is a power-law curve with unknown n, a nonlinear transformation is done on the PM frequencies in order to transform it in a straight line. A new variable x is introduced, defined as

$$x = \frac{1}{f^{n-1}} \quad ; \quad x_0 = \frac{1}{f_0^{n-1}} \tag{5.6}$$

which has physical dimensions of Hz^{1-n}. The time evolution of the signal 'x' parameter under this transformation is given by

$$x = x_0 + (n-1)\,k\,(t - t_0) \tag{5.7}$$

The transformation done in Equation 5.6 is repeated for different values of the braking index n. A grid of possible braking indexes n is constructed within the range $[2.5 - 7]$, with a step that is calculated requiring that the frequency variation stepping from a value of n to the next is within the frequency resolution [174]. If a signal with braking index n^* inside the grid is present, it is transformed in a straight line when the correction for that n^* is performed. This effect is shown in the top right plot of Figure 5.1. Then, the corrected PM is fed to the GFH transform which maps the peaks to the signal parameter space. The Hough map obtained is a 2D histogram on the signal parameters x_0, k: for each given x_0^*, k^* pair, it counts the number of pixels belonging to the time-frequency trajectory corresponding to that pair. GW candidates are selected in the different Hough maps created for the different values of n in the grid. A relevant difference with respect to the traditional FH procedure is that, because of the non-linear mapping, the noise in the transformed space is not uniform. In fact, the change of coordinates takes points that are equally spaced in frequency and concentrates them at higher frequencies, that is at lower x values, and spreads them out at lower frequencies, that is at high x values. This effect is well recognizable in the top right plot in Figure 5.1. The effect on the GFH map is to produce an higher number of noise counts at the lower x values. This is visible in the bottom left plot in Figure 5.1. Since candidate signals are selected comparing their number of counts with the number of

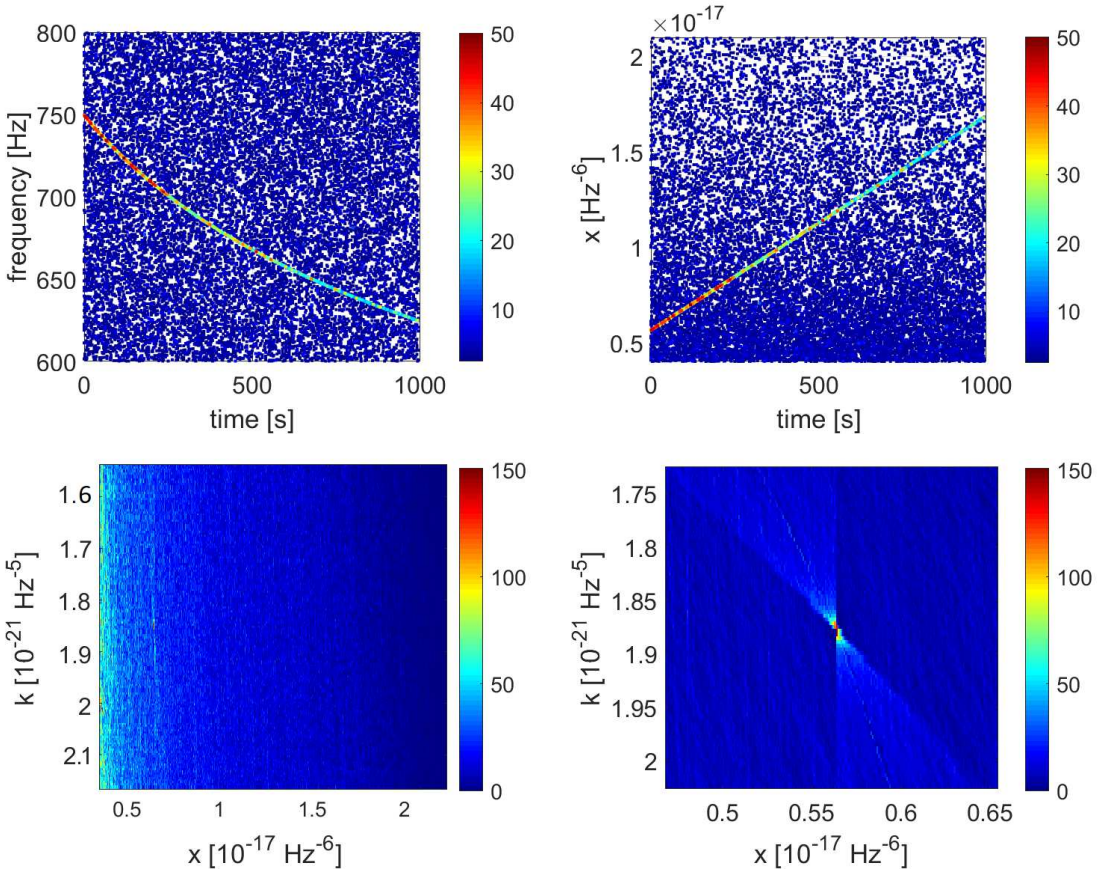

Figure 5.1: First stages of the GFH search pipeline. Top left plot shows a 1000-seconds PM where a long transient signal, with $f_0 = 750\,\mathrm{Hz}$, $\dot{f}_0 = -0.06\,\mathrm{Hz/s}$ and $n = 7$ has been injected. Top right plot shows the transformed PM, where the frequencies have been transformed following Equation 5.6. The signal after this transformation has become a straight line and the noise is no more uniformly distributed, with higher concentration at low values of x. Bottom left plot shows a large view of the Hough map computed from the transformed PM. The higher noise concentration a lower x values has produced higher noise counts. Bottom right plot shows a zoom of the Hough map on the square containing the signal parameters, corresponding to the highest counts. Note that, restricting to the square, the noise counts are approximately uniform.

noise counts, this non-uniformity would disfavour signals with lower x values. To overcome this problem the Hough map is divided in a number of squares determined by the number of candidates to be selected in each map. In each square, the two local candidates with the highest number count are selected. This practice has also the advantage to cover the parameter space as uniformly as possible. In the bottom right plot of Figure 5.1, a square of the Hough map obtained from the corrected PM (top right plot), containing the counts produced by the signal, is shown.

5.1.3 A way to enhance the search sensitivity

It is worth to underline that the steps presented above are crucial to determine the overall search sensitivity of the GFH procedure. If a GW signal is strong enough to be selected as a candidate from the Hough map and survive the coincidence veto between detectors, then it undergoes the follow-up described in [174]. Otherwise, there is no possibility to recover that signal in the subsequent steps. This search strategy results to be computationally feasible, but it loses about one order of magnitude in terms of sensitivity with respect to an ideal matched filter search. So, in principle there is room for enhancing the search sensitivity, thus increasing the maximum distance at which we can confidently detect a signal.

The method presented here introduces an intermediate step among the ones described in Section 5.1.2. When building the PM, the probability for a signal peak to be selected from a single spectrum depends only on its own power content and on the other adjacent frequencies. This process is done segment-by-segment, and the peaks selected from a FFT do not influence the selection in the next one. However, I have analyzed whitened spectrograms containing signals with borderline amplitudes, i.e. that produce a time-frequency pattern with whitened power oscillating around the selection threshold. I have found that in many cases those signals could be still recoverable. The reason is that signals with slightly sub-threshold power in the single power spectra can be reinforced if we correlate power spectra at adjacent times. In order to do this, we need to consider the whole spectrogram, instead of analyzing the spectra independently. The way to exploit the correlations between pixels is typical of image processing techniques, and I will end up building a two-dimensional image filter. Such filter will be implemented in the 2D Fourier domain.

5.2 How information is stored in 2D Fourier transform

Since the time-frequency pattern I want to extract is a simple regular monotonic decreasing curve, it is important to understand how the shape information is stored in the Fourier components of an image. Given an $\mathbb{R}^2$ space with coordinates $\vec{x} = (x, y)$ and a scalar function $f(\vec{x})$, the 2D Fourier transform and its inverse are defined as

$$\tilde{f}\,(u,v) = \mathcal{F}_2\left[f\,(x,y)\right] = \int_{\mathbb{R}^2} dxdy\, f\,(x,y)\; e^{-i\,2\pi\,(ux+vy)} \tag{5.8}$$

$$f\,(x,y) = \mathcal{F}_2^{-1}\left[\tilde{f}\,(u,v)\right] = \frac{1}{(2\pi)^2}\int_{\mathbb{R}^2} dudv\, \tilde{f}\,(u,v)\; e^{i\,2\pi\,(ux+vy)} \tag{5.9}$$

where the $\vec{u} = (u, v)$ are the reciprocal coordinates in the Fourier space. Since spectrograms are represented as scalar matrices, I focus only on monochromatic images. When passing from continuous to discrete space, there are some detail to pay attention to. Consider a scalar $M \times N$ matrix $F\,[j,k]$ with discrete indices $j = 1, ..., M$ and $k = 1, ..., N$. To make the

Fourier transform work, in analogy with the one-dimensional case, we consider this table infinitely replicated on a periodic table, so that

$$F[j \pm M, k] = F[j, k \pm N] = F[j \pm M, k \pm M] = F[j, k]$$

The 2D discrete Fourier transform of a matrix works as a sequence of 1D Fourier transforms - typically using the FFT algorithm - applied first on all the column vectors of the matrix then on all the raw vectors, or vice-versa. It is defined, together with its inverse, as

$$\tilde{F}[u, v] = \sum_{j=0}^{M-1} \sum_{k=0}^{N-1} F[j, k] \, e^{-i2\pi\left(\frac{uj}{M} + \frac{vk}{N}\right)} \tag{5.10}$$

$$F[j, k] = \frac{1}{MN} \sum_{u=0}^{M-1} \sum_{v=0}^{N-1} \tilde{F}[u, v] \, e^{i\,2\pi\left(\frac{uj}{M} + \frac{vk}{N}\right)} \tag{5.11}$$

Given the formal analogies with the 1D version, the 2D transform has the following symmetries:

1) If $F[j, k]$ is real, i.e. $F^*[j, k] = F[j, k]$, then $\tilde{F}^*[u, v] = \tilde{F}[-u, -v]$
2) If $F[j, k]$ is even, i.e. $F[-j, -k] = F[j, k]$, the transform is too: $\tilde{F}[-u, -v] = \tilde{F}[u, v]$
3) If $F[j, k]$ is odd, i.e. $F[-j, -k] = -F[j, k]$, the transform is too: $\tilde{F}[-u, -v] = -\tilde{F}[u, v]$
4) If $F[j, k]$ is real and even, the same the transform $F[u, v]$.
5) If $F[j, k]$ is real and odd, then $\tilde{F}[u, v]$ is purely immaginary and odd.

Regarding the operations that can be done, the 2D transform has the following properties:

- **Linearity**: given two arrays $F[j, k]$, $G[j, k]$ with the same dimensions $M \times N$, the transform of the linear combination of the two is the linear combination of the single transforms, with the same weights:

$$\mathcal{F}_2\{\alpha F[j, k] + \beta G[j, k]\} = \alpha \tilde{F}[u, v] + \beta \tilde{G}[u, v] \tag{5.12}$$

- **Scaling**: given an array $F[j, k]$ and its transform $\tilde{F}[u, v]$, by performing a contraction/dilation to the variables with two constants a, b, the transform will undergo an inverse effect:

$$\mathcal{F}_2\{F[a\,j, b\,k]\} = \frac{1}{|ab|} \tilde{F}\left[\frac{u}{a}, \frac{v}{b}\right] \tag{5.13}$$

- **Translations/Phase modulations**: given a matrix $F[j, k]$ and a couple of integers p, q, the translated array $F[j - p, k - q]$ transforms with a phase modulation:

$$\mathcal{F}_2\{F[j - p, k - q]\} = e^{-i\,2\pi\left(\frac{up}{M} + \frac{vq}{N}\right)} \tilde{F}[u, v] \tag{5.14}$$

  Inversely, applying to the array $F[j, k]$ a phase modulation through the couple p, q, that becomes a translation of the 2D transform:

$$\mathcal{F}_2\left\{e^{i\,2\pi\left(\frac{jp}{M} + \frac{kq}{N}\right)} F[j, k]\right\} = \tilde{F}[j - p, k - q] \tag{5.15}$$

  The straightforward consequence is that power spectra are invariant under translations.

- **Cross-correlation**: the cross-correlation between an array $F[j,k]$ and an array $G[p,q]$ gives in output an array $H[j,k]$ defined as:

$$H[j,k] = F[j,k] \star G[j,k] = \sum_{p,q} F[p,q]\, G[j+p, k+q] \tag{5.16}$$

  The Fourier transform of the resulting array is obtained through the multiplication of the Fourier transforms of the original arrays. Thus, the cross-correlation can be computed also as the inverse 2D transform

$$F[j,k] * G[j,k] = \mathcal{F}_2^{-1}\left\{\tilde{F}[u,v] \cdot \tilde{G}[u,v]\right\} \tag{5.17}$$

- **Parseval's identity**: it holds for any dimension and guarantees the Fourier series of a function is square-integrable. In discrete terms, for 2D matrices it states the identity:

$$\sum_{j=0}^{M-1}\sum_{k=0}^{N-1} |F[j,k]|^2 = \frac{1}{MN}\sum_{u=0}^{M-1}\sum_{v=0}^{N-1}\left|\tilde{F}[u,v]\right|^2 \tag{5.18}$$

  or, more generally,

$$\sum_{j=0}^{M-1}\sum_{k=0}^{N-1} F[j,k]\, G^*[j,k] = \frac{1}{MN}\sum_{u=0}^{M-1}\sum_{v=0}^{N-1} \tilde{F}[u,v]\, \tilde{G}^*[u,v] \tag{5.19}$$

The above properties provide all is needed to implement Fourier domain image filtering. The power spectrum is defined as in 1D by the square modulus of the transformed array

$$S_F[u,v] = \frac{\left|\tilde{F}[u,v]\right|^2}{M\,N} dx\, dy \tag{5.20}$$

where M, N are the array dimensions and dx, dy are the steps in the physical space.

The additional degree of freedom with respect to 1D arrays introduces new possibilities. In particular, we are interested in how straight and curve lines are transformed. In 1D, the continuous Fourier transform of two Dirac delta functions is a sinusoidal curve with period the inverse of half their separation:

$$\begin{aligned} f(t) &= \tfrac{1}{2}\delta(t-a) + \tfrac{1}{2}\delta(t+a) \\ \tilde{f}(\nu) &= \mathcal{F}_1[f(t)] = \cos(2\pi a \nu) \end{aligned} \tag{5.21}$$

In the same way, in 2D real space with coordinates $\vec{x}(x,y)$ we can take two delta functions symmetrically translated from the origin by a vector $\vec{x}_0(x_0,y_0)$. Its 2D continuous Fourier transform, with reciprocal coordinates $\vec{u}(u,v)$, is a sinusoidal function:

$$\begin{aligned} F(\vec{x}) &= \tfrac{1}{2}\delta(\vec{x}-\vec{x}_0) + \tfrac{1}{2}\delta(\vec{x}+\vec{x}_0) \\ \tilde{F}(\vec{u}) &= \mathcal{F}_2[F(\vec{x})] = \cos[2\pi(\vec{u}\cdot\vec{x}_0)] \end{aligned} \tag{5.22}$$

The top plots in Figure 5.2 show the two delta functions in the physical space and the 2D continuous Fourier transform corresponding to Equation 5.22. The first thing to note

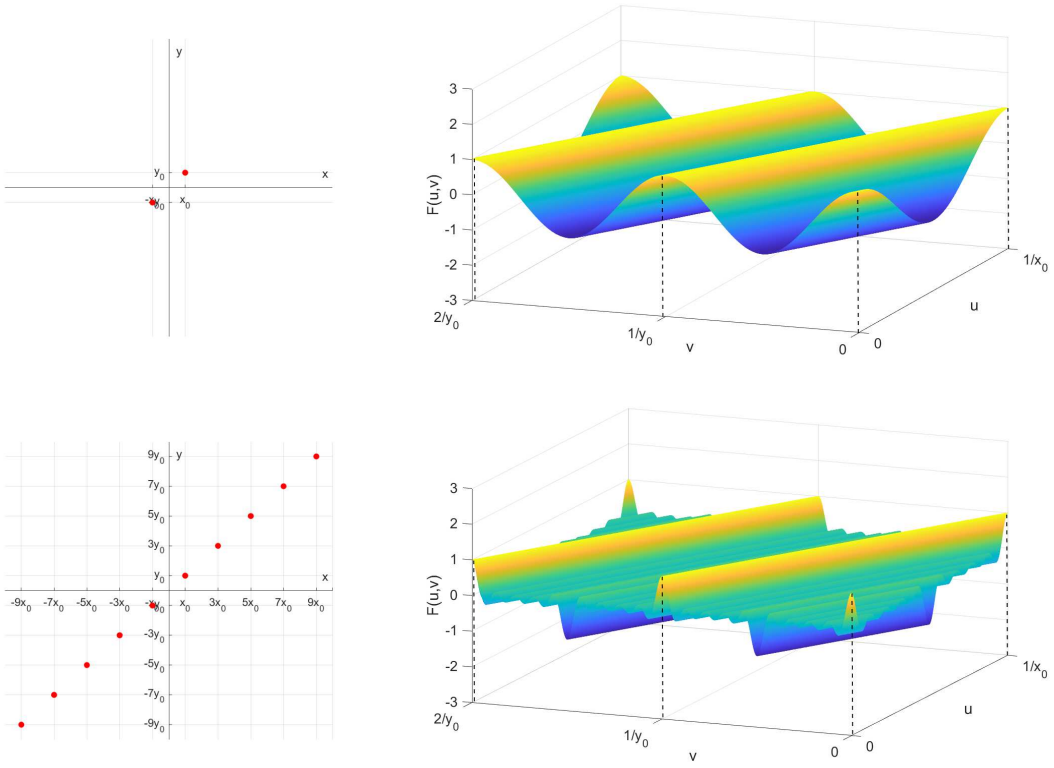

Figure 5.2: Examples of 2D continuous Fourier transform of a set of delta functions. The top right plot show the transform of a pair of delta functions (top left plot). The bottom right plot shows the transform of five pairs of delta functions (bottom left plot), placed with the same step and direction of the previous pair.

is how directions transform: while in the physical space the two delta are aligned on the slope y_0/x_0, the level lines of the transform have slope $-x_0/y_0$. For instance, the level lines $\tilde{F}(u,v) = 1$ are given by

$$\cos\left[2\pi\left(\vec{u}\cdot\vec{x}_0\right)\right] = 1 \quad \rightarrow \quad v = -\frac{x_0}{y_0}u + \frac{k}{y_0} \tag{5.23}$$

where k is an integer number. This is formally like an orthogonality relation, even if the two objects live in different spaces. Second, the wavelength of the sinusoidal function is the inverse of the separation between the delta functions. If we express the translation vector $\vec{x}_0$ in polar coordinates, with magnitude a and angle φ, the distance between the maxima is $1/a$:

$$\begin{aligned} x_0 &= a\,\cos\varphi \\ y_0 &= a\,\sin\varphi \end{aligned} \quad \rightarrow \quad \lambda = \frac{1}{\sqrt{x_0^2 + y_0^2}} = \frac{1}{a} \tag{5.24}$$

Third, if we add further pairs of delta functions with the same step and the same alignment, the effect on the Fourier transform is to add sinusoidal functions at odd multiples of the original frequency. Indicating with n the number of equally-spaced delta pairs, the total

function and its transform are given by

$$F(\vec{x}) = \frac{1}{2n} \sum_{K=0}^{n-1} \left[\delta\left(\vec{x} - \vec{x}_0\left(1+2k\right)\right) + \delta\left(\vec{x} + \vec{x}_0\left(1+2k\right)\right) \right] \tag{5.25}$$

$$\tilde{F}(\vec{u}) = \frac{1}{n} \sum_{k=0}^{n-1} \cos\left[2\pi\left(\vec{u}\cdot\vec{x}_0\right)\left(1+2k\right)\right] \tag{5.26}$$

The linear superposition of sinusoidal functions with same starting phase and odd-multiple frequencies generates a constructive interference on the points where $\vec{u}\cdot\vec{x}_0 = k/2$, and a destructive interference elsewhere. The bottom plot shows an example of this process, with five pairs of equally-spaced delta functions. The 2D Fourier transform has the same absolute maxima and minima than the transform in the top plot, but it is sharper around those maxima/minima. The more delta functions are added, the sharper the transform becomes around maxima/minima and the flatter becomes elsewhere. This trend is well visible in Figure 5.3. This effect is crucial, since lines in discrete space can be considered as a set of equally-spaced delta functions.

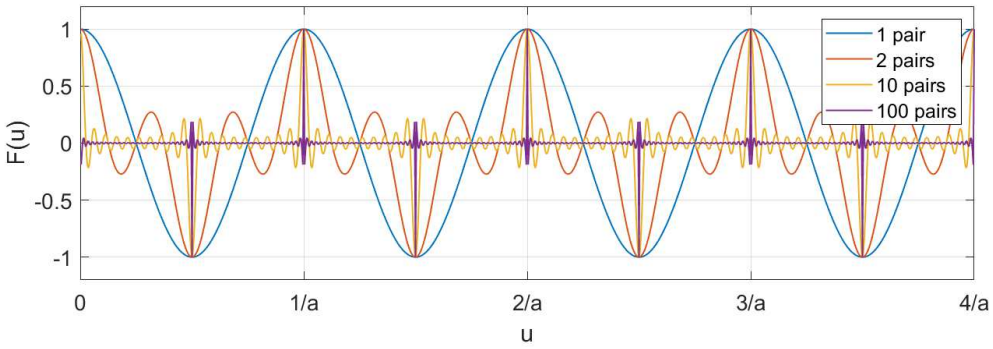

Figure 5.3: Realization of different transforms of $2n$ points with different number of pairs following Equation 5.26, showing only the u dimension. As n increases, the destructive interference between the sinusoidal curves becomes more effective, leaving the peaks with ever narrower periodicity $1/a$.

5.2.1 Discrete spectra of straight lines

When discrete and finite matrices are considered, some changes have to be taken into account with respect to the continuous $\mathbb{R}^2$ space. A slope m_{jk} in a $M \times N$ matrix is mapped in a m_{uv} slope in the reciprocal space with a correction factor that accounts for the uneven dimensions $M \neq N$. The relation to transform the slopes is given by

$$m_{\text{uv}} = -\frac{1}{m_{\text{jk}}}\left(\frac{N}{M}\right) \tag{5.27}$$

Considering again the example of the points in a plane, these will become single pixels in the discrete; however, while in $\mathbb{R}^2$ there is no limit to the number of points that can be added, in a $M \times N$ matrix this number is limited. Furthermore, by treating the space as a 2D torus, different behaviors will occur based on the mutual distance of the points. Starting

from just two points, two distances are associated with them: a direct one, identified by the joining line, and a complementary one, identified by crossing the border of the map and starting from the opposite extreme. If these distances are multiples of an integer divisor a of the dimensions of the map, the points identify two sites of a periodic lattice on the torus: in this case the pitch of this lattice, i.e. the minimum distance between two sites, determines the distance between the crests of the sinusoid in the transform. For example, if two points arranged horizontally, where the matrix has dimension M, identify a periodic lattice with pitch a such that $M = n_x\, a$, with $n_x \in \mathbb{N}$, then the 2D amplitude spectrum will be a sum of sinusoids on the conjugate variable v with crests spaced by $d = \frac{M}{a} = n_x$ in units of pixels. By adding further points on the empty sites of the lattice, once saturation is reached the situation corresponds to the limit of infinite points of the continuous case: the oscillations outside the peaks make destructive interference and only the isolated crests remain. If, on the other hand, the distances between the points do not comply with this condition, no periodic lattice is identified and the oscillations produced by the 2D FFT are irregular.

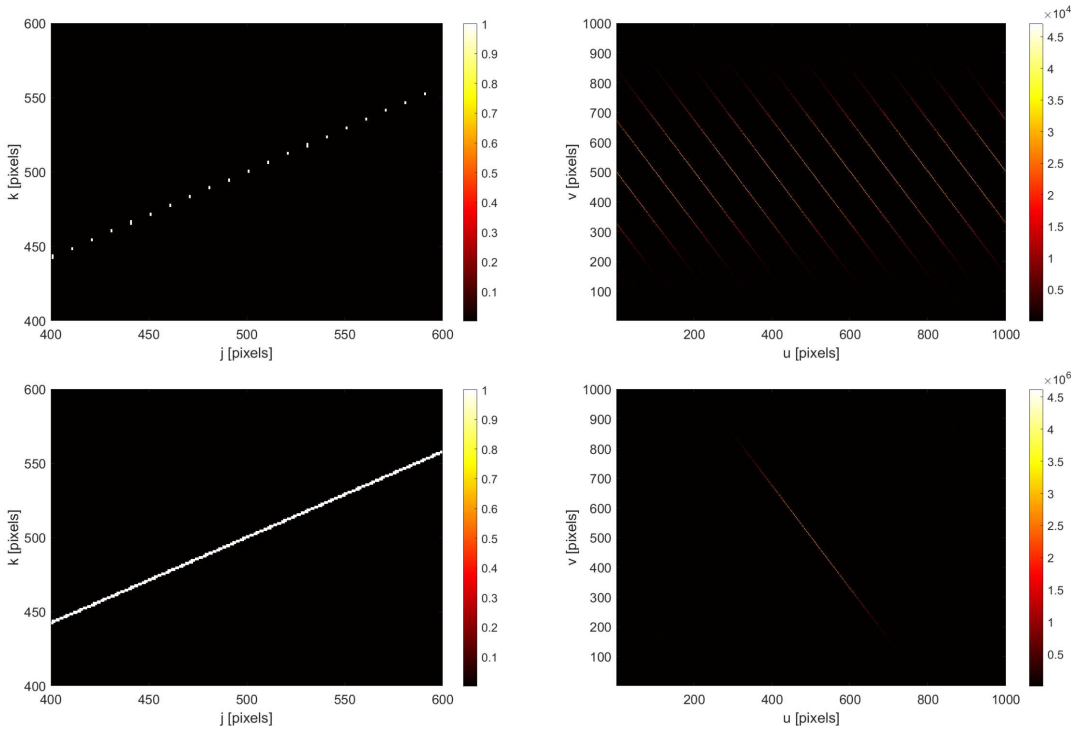

Figure 5.4: Top left plot: 1000×1000 empty image containing $n_x = 100$ dots aligned on a straight line with 30° inclination. Top right plot: power spectrum of the top left map. It results in a comb of modulated lines with inclination $-60°$ and distance $d = n_x\sqrt{3}/2$. Bottom left plot: 1000×1000 empty image containing a straight line made of $n_x = 1000$ dots aligned without holes, with 30° inclination. Bottom right plot: power spectrum of the bottom left map. The distance of the comb has become $d = 1000\sqrt{3}/2$, so it results in a single line with inclination $-60°$.

By arranging the points on an inclined straight line, things change: while still identifying a periodic lattice, this is incomplete, as the sequence of points, once it reaches the end of the matrix, should continue its path from the opposite end. We must then consider the sequence

of aligned points as the product between an infinitely extended sequence and a rectangular domain of the dimensions of the matrix, which produces an amplitude modulation on the transformed lines in Fourier space. Finally, when the maximum number of pixels has been reached, i.e. the pixels are adjacent, we have a straight line. In this situation the periodicity of the crests in the 2D transform coincides with the dimensions of the matrix: the lattice pitch identified corresponds to the entire length of the map, i.e. $a = 1$ and $n_x = M$. In practice, the effect is that all the crests superimpose on the same line. In the top plots in Figure 5.4 the power spectrum of a set of points aligned on a straight line in a 1000×1000 plane is shown. The points are spaced along the horizontal dimension by $a_x = 10$ pixels, therefore they are in number $n_x = M/a_x = 100$, and the straight line on which they lie is inclined by 30° with respect to the horizontal. The reticular step identified is $a = (2/\sqrt{3})a_x$, therefore in the transform we have straight lines inclined by $-60°$ with reciprocal distance $d = n_x\sqrt{3}/2$. It should also be noted that these straight lines are modulated in amplitude as expected. In the bottom plot in Figure 5.4 the spacing between the dots has been removed so that $a_x = 1$ and $n_x = M$. This situation corresponds to a straight line, with no holes. Therefore the distance between the straight lines in the 2D power spectrum is $d = M\sqrt{3}/2$, i.e. they are coincident. The consequence of this argument is crucial: *the information of a straight line in a monochromatic image is confined in a straight line in the 2D Fourier transform, with inclination given by Equation 5.27.*

5.2.2 Discrete spectra of curved lines

Once the working mechanism of 2D FFT on a domain containing a straight line is understood, it is easy to understand how the mechanism works when curved lines are present. In the 1D case, the information contained in the FFT modulus regards the presence of signals at a given frequency. Passing to 2D analysis, the same logic of a single dimension can obviously be applied to the two separate dimensions. On the other hand, the combined dimensions give information on the gradients that individuate patterns in the image. A curve can be approximated as a set of short, approximately linear segments, each one of them mapped in a straight line in the power spectrum. So, the modulus of the FFT of a curve contains the information concerning all the first derivatives present on it. The left plot in Figure 5.5 shows an image containing a simple curve with the typical shape of a long transient GW in a spectrogram. The map, with dimensions 1000×1000, is shown in the pixel scale without physical units to keep the explanation more general. The dashed cyan lines indicate the tangents to the curve at its extremes. All the intermediate points of the curve have first derivative between the slopes of the plotted tangents. The right plot in Figure 5.5 shows the 2D amplitude spectrum of the map in the left plot, rotated in order to put the (0,0) frequency at the center of the matrix. The information is concentrated in a triangular region symmetrical with respect to the center and whose amplitude, from the maximum reached in the centre, fades as it moves away towards the high frequencies. This region represents a proper beam of straight lines which correspond to the different inclinations assumed by all the tangents to the curve. Since the curve is a monotone decreasing function of time, it follows that the maximum and minimum slopes of the tangents are given by the inclinations at the extremes of the curve. The cyan dashed lines added in the plot indicate where the information on the two tangents at the extremes of the curve (the cyan dashed lines in the left plot) is located, according to Equation 5.27. They represent the boundaries of the region in the Fourier space where the information on the curve is concentrated. In particular, it can be noted that the more vertical side has an higher power: this

is because in the curve pattern the lower slopes are more recurrent than the higher ones, i.e. the density of the low slopes is greater. It should also be noted that since we are dealing with a monotonic decreasing curve, the modulus of its transform is located in the first and third quadrants of the Fourier map. A curve with a regularly increasing trend like chirp signals in time-frequency diagrams, on the contrary, would have the information stored in the second and fourth quadrant in the Fourier space.

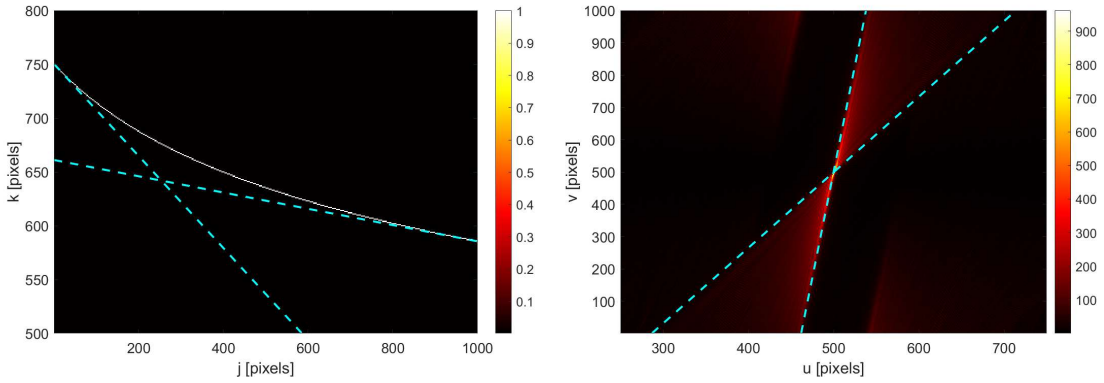

Figure 5.5: Left plot: 1000×1000 array containing a curve with the typical pattern of a long transient GW. The cyan dashed lines are the tangents to the curve at its extreme points. Right plot: amplitude spectrum of the array in the left plot. The cyan dashed lines indicate the tangents in the left plot transformed following Equation 5.27. Note that the majority of the information on the curve (red-coloured area) is confined between that two lines.

5.3 Triangular filter definition and characterization

Once the main mechanisms underlying the 2D Fourier transform of a numerical matrix have been clarified, it is possible to apply the filtering principles, typically used on 1D arrays, to 2D arrays. When implementing a specific filtering technique the main goal is to eliminate or reduce the noise in which a given signal is buried. An optimal technique is the Wiener filter, which applies a statistical approach [178]. The assumption of this filter is that the spectral characteristics of the signal and of the noise are known, and that the data can be decomposed in signal h[j,k] and noise n[j,k] components, $d[j,k] = h[j,k] + n[j,k]$, which is very reasonable. In the 2D physical domain the Wiener filter works as a matrix $w[j,k]$ that, applied in convolution to the data matrix $d[j,k]$, gives at output the signal estimate

$$\hat{h}[j,k] = w[j,k] * \{h[j,k] + n[j,k]\} \tag{5.28}$$

The condition which defines the Wiener filter is that the quadratic error between the output estimate and the signal is minimized, $E[(h - \hat{h})^2] = 0$. The solution is given, in the Fourier domain, by

$$\tilde{w}\,[j,k] = \frac{S_h\,[u,v]}{S_d\,[u,v]} = \frac{S_h\,[u,v]}{S_n\,[u,v] + S_h\,[u,v]} \tag{5.29}$$

According to the convolution theorem, the Wiener filter can be applied equivalently in the Fourier domain as follows

$$\hat{h}[j,k] = \mathcal{F}_2^{-1}\left\{\tilde{d}[u,v]\cdot\tilde{w}[u,v]\right\} = \mathcal{F}_2^{-1}\left\{\tilde{d}[u,v]\cdot\frac{S_h[u,v]}{S_d[u,v]}\right\} \tag{5.30}$$

In order to better estimate the output, we can use a smooth estimate of the noise power spectrum at the denominator of 5.29. Basically, the best filter to filter out the noise where a signal is buried is given by the power spectrum of that signal itself up to a normalization factor.

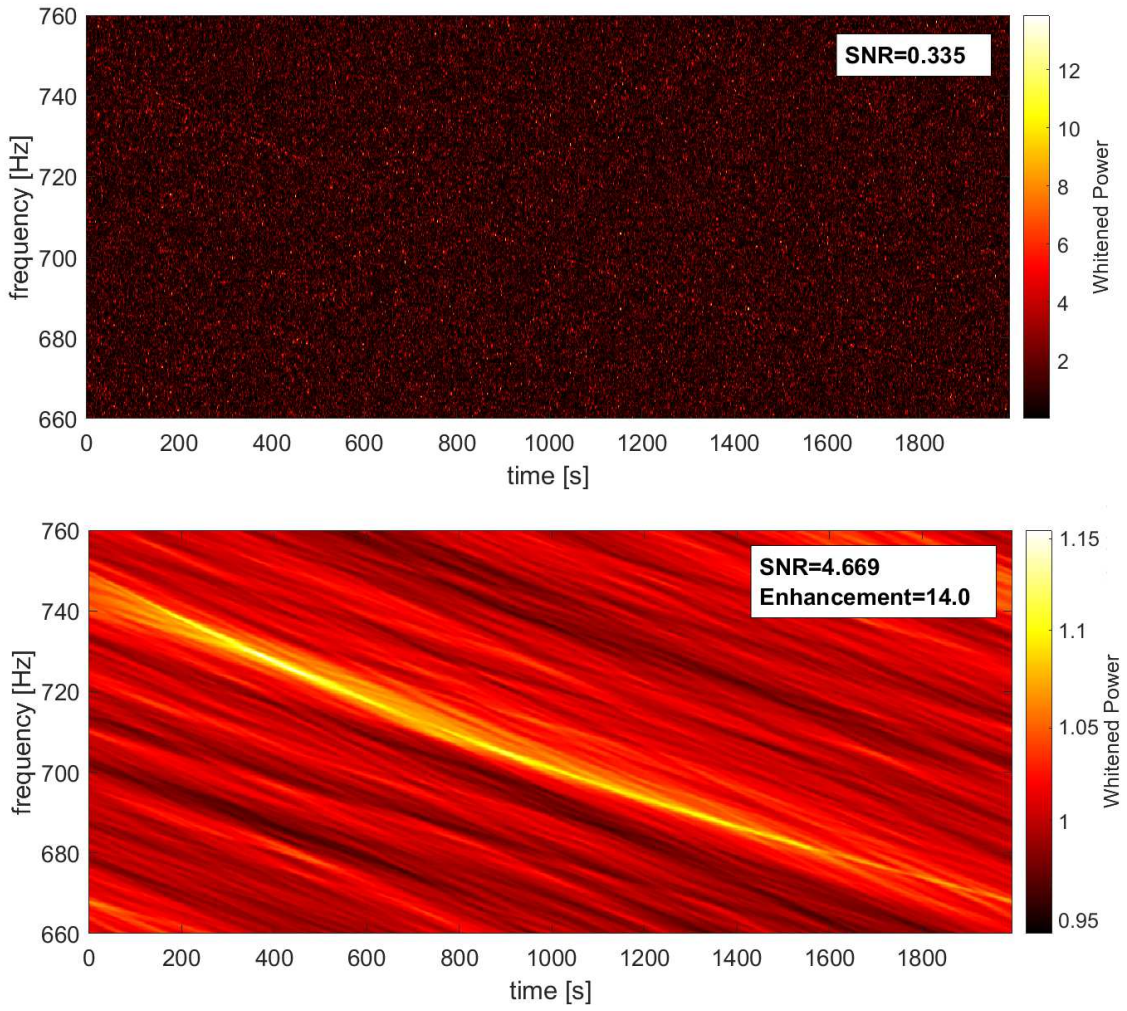

Figure 5.6: Top plot: spectrogram of simulated white noise with a simulated long transient GW, with parameters $f_0 = 750\,\text{Hz}$, $\dot{f}_0 = -0.06\,\text{Hz/s}$ and $n = 7$. The signal, barely visible, has an average SNR$\simeq 0.335$ with respect to the noise floor. Bottom plot: the same spectrogram after the application of the Wiener filter using the power spectrum of the simulated signal. The signal is strongly visible, with a SNR$\simeq 4.67$ which is enhanced by a factor 14 with respect to the original SNR.

In Figure 5.6 an example of the application of the Wiener filter is shown. In the top plot a spectrogram of simulated white noise containing a simulated long transient GW with

parameters $f_0 = 750\,\mathrm{Hz}$, $\dot{f}_0 = -0.06\,\mathrm{Hz/s}$ and $n = 7$ is shown. The signal amplitude is such to produce a time-frequency pattern barely visible. To quantify the signal power with respect to the noise I use an average SNR defined as

$$\bar{SNR} = \frac{\underset{in}{\mathrm{mean}}\left(f\left[j,k\right]\right) - \underset{out}{\mathrm{mean}}\left(f\left[j,k\right]\right)}{\underset{out}{\mathrm{std}}\left(f\left[j,k\right]\right)} \tag{5.31}$$

where the *in* and *out* labels indicate the subsets of points of the array that lay on the signal pattern and outside that pattern respectively, and the "mean" and "std" labels indicate the average and standard deviation operations respectively. In the top spectrogram the average SNR is $\bar{SNR}_0 \simeq 0.335$, meaning that the signal peaks are above the noise floor by 0.335 times the standard deviation of the noise. In the bottom plot of Figure 5.6 the spectrogram has been filtered with the Wiener filter built with the signal spectrogram. The SNR is significantly improved, by a factor ~ 14, up to $\bar{SNR}_w \simeq 4.67$, and has become well visible. So, the Wiener filter has the great power to bring out a given signal from the noise, increasing its SNR. However, this filtering technique has two problems. First, the Wiener filter lacks of generality: it works optimally if we have access to the time-frequency pattern of the signal, but in targeted searches we have no knowledge of the signal parameters. If we know the frequency evolution of the signal, we would not need to perform semi-coherent searches. Second, even if the filter strongly enhances the SNR of the signal, its fine time-frequency pattern is not well preserved. This is because the filter is not flat: as we have seen, the power is more concentrated in the region of the Fourier space corresponding to the lower slopes in the spectrogram. Moreover, the information in the 2D power spectrum is concentrated in the low frequencies, since the signal alone has a smooth time-frequency pattern in amplitude. Consequently the Wiener filter is also a low-pass filter. However, the low-frequency cut-off produces a coarse estimate of the signal pattern. This is a problem for semi-coherent searches like the GFH, since the time-frequency pattern of the signal needs to sum on a single pixel of the Hough map.

To overcome these problems I have developed a 2D filter which mimics the effect of a Wiener filter but preserving the generality of the search and the fine time-frequency pattern of the signal. I have called it *triangular filter* because of its shape in the 2D Fourier space. The triangular filter takes in input two numbers, m_1 and m_2, that represent the maximum and minimum inclinations of a curve inside an image. According to Equation 5.27 and to Figure 5.5, the information of the curve is contained inside the triangular area between the two straight lines in the Fourier space corresponding to the m_1, m_2 inclinations. The triangular filter is generated as a matrix with the same dimensions $M \times N$ of the image. It is a binary matrix in the Fourier space, where the pixels belonging to the area between the two straight lines are set to one, and the remaining others are set to zero. If we take $m_1 > m_2$ and label a generic inclination in the Fourier space as m_{uv}, the condition is given by

$$m_{\mathrm{uv}} \in \left[\frac{-1}{m_1}\frac{N}{M}\,,\ \frac{-1}{m_2}\frac{N}{M}\right] \tag{5.32}$$

There is room for an additional degree of freedom, which is a cut along the 'v' conjugate dimension. This parameter is an adimensional number in the range [0, 1] that represents the cut to be done along the v dimension, proportionally to the size of the filter, as shown in Figure 5.7. In the following, I will implicitly refer to this cut as to a "frequency cut".

The triangular filter acts on the noise distribution by removing the correlations between pixels with orientation outside the chosen range. It is important to be aware that this

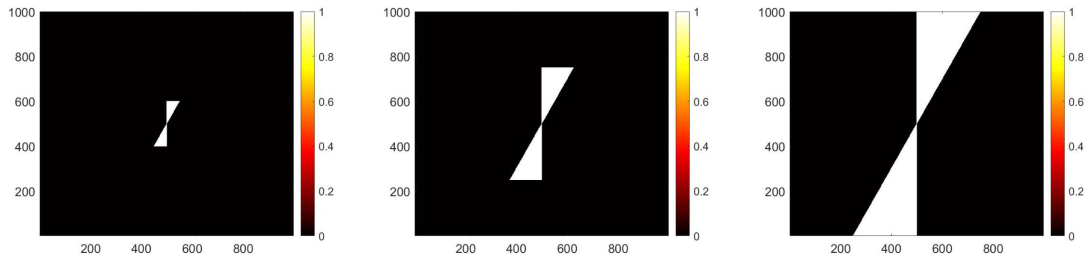

Figure 5.7: Examples of the triangular filter defined in the 2D Fourier space. The inclinations are set to filter curves with slopes between $-26°$ and $0°$. The left, middle and right plots show configurations with frequency cut set to 0.2, 0.5 and 1 respectively.

operation introduces some degree of correlation between the adjacent columns of the spectrogram. After the filtering, the noise has got some structure along the directions allowed by the filter, and this effect is more or less strong depending on the angle width of the filter. Moreover, its distribution is no more exponential as in the original spectrogram[1]. I have characterized the filter on 1000×1000 maps with simulated white noise, exponentially distributed with unit mean value, in different configurations:

1) Keeping the boundaries of the filter to a fixed width of $5°$, I have rotated the filter spanning from $0°$ to $90°$, with no frequency cut. At each rotation I have applied it to the noisy map and recorded mean value and standard deviation of the output map. These values are reported in the top plot in Figure 5.8 as function of the offset angle between the low boundary and the 'u' axis. As can be seen, the global distribution of the noise after the filter is almost independent on the chosen offset angle. There is a little bump around $45°$, corresponding to a $+5\%$ increase in the standard deviation, that is due to the rectangular geometry of the map: at these inclinations, the filter covers an higher number of pixels in the map. As it was expected, the triangular filter does not affect the global mean value of the map, so in the next tests I have focused only on the standard deviation.

2) I have progressively enlarged the angle width of the filter from $0°$ up to $180°$, keeping the cut at one (i.e. no frequency cut). For each different angle width I have applied the triangular filter and recorded the standard deviation of the noise at the output. The results are shown in the middle plot in Figure 5.8 as function of the angle width. The width of the noise distribution strongly depends on the width of the filter. The noise distribution also changes qualitatively: when the filter spans $180°$, it covers the whole map and practically there is no filtering, so the output noise is still exponentially distributed with unit standard deviation, corresponding to the horizontal red line in the plot. As the angle width decreases, the noise distribution distorts towards a chi-squared, progressively reducing the standard deviation.

3) I have changed the level of the frequency cut from 0.05 up to 1 keeping fixed the angular width of the filter and repeating the procedure for different angular widths. Also in this case, I have recorded the standard deviation of the output maps. In the bottom plot in Figure 5.8 I have reported the results for three angular widths,

[1] According to a preliminary study, it seems to follow a chi-squared distribution, but more investigations are needed.

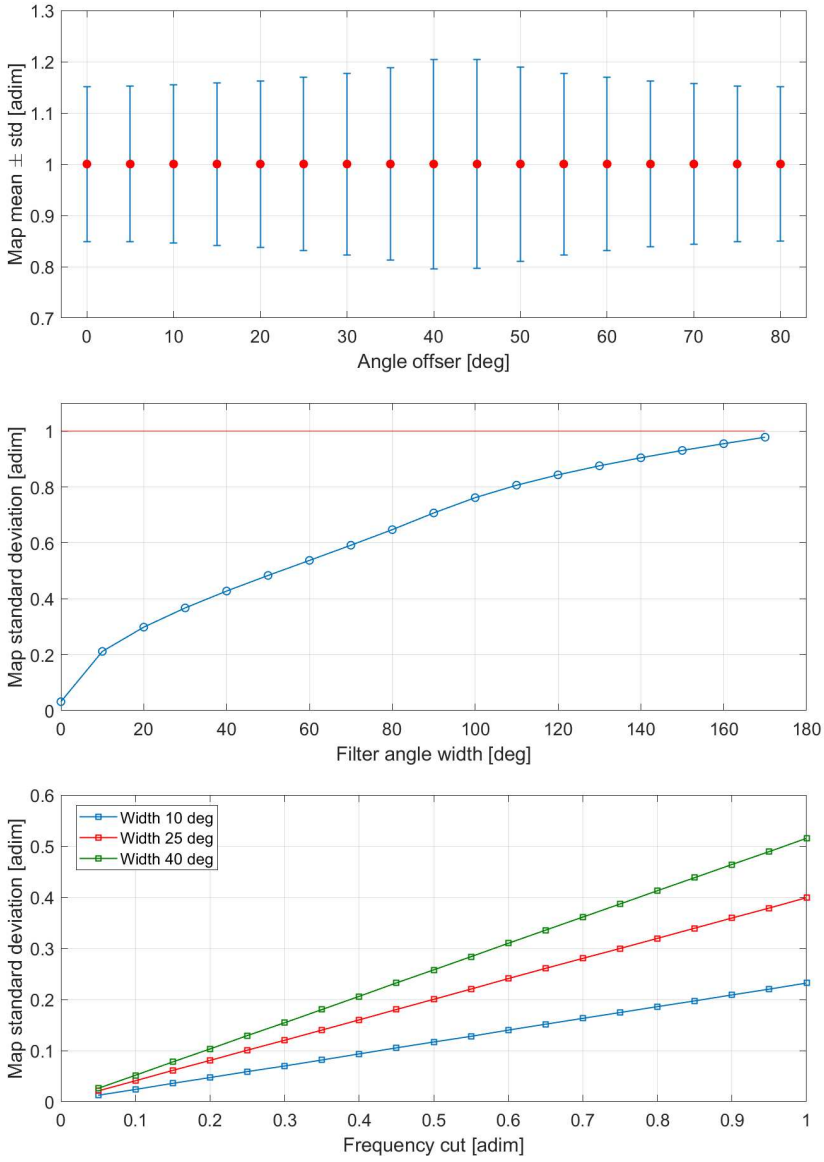

Figure 5.8: Results of the tests done to characterize the triangular filter, using a 1000×1000 map containing white Gaussian noise. The top plot shows error bars with mean value and the standard deviation of the output noise after the application the triangular filter with the same angular width of 5° but with different inclinations. The middle plot shows the standard deviation of the output noise after the application of the triangular filter with different choices of the angular width. The horizontal red line indicates the reference value for the unfiltered noise map. The bottom plot shows the standard deviation of the noise after the application of the triangular filter, at fixed values of the angular width, varying the frequency cut from 0.05 to 1. The blue, red and green lines represent the results with angular width of 10°, 25° and 46° respectively.

namely 10°, 25° and 40°. The trend of the standard deviation of the noise results to be linear with respect to the frequency cut. Note that the maximum values for each angular width, reached at cut=1, coincide with the values obtained for that width in the previous (middle) plot.

Even if it has been developed with the purpose of enhancing the sensitivity of long transient GW searches, the triangular filter could in principle be applied in various contexts, even far from the field of GW search. The characterization I have done allows to establish the optimal configuration of the filter depending on its use. In the present context, the purpose is the possible application as an intermediate step of the GFH procedure. The constraints related to the way the GFH works impose some specific choices on the filter configuration.

- **Frequency cut.** As I have showed in Section 5.1, the parameters of the GFH procedure are optimized in order to have the GW signal power concentrated in one single frequency bin in each FFT. The resolution of the grid in the braking index n, used to correct the PM, is optimized in order to transform the signal in a straight line when the right value of n is used. If all these parts work properly, the Hough transform concentrates all the counts belonging to the signal in the same pixel in the Hough map. For this reason, we do not want the triangular filter to coarsen the time-frequency pattern of the signal through a low-pass filter. Hence, *the frequency cut is set to 1.*

- **Limit inclinations.** Since the parameters of the signal are unknown, I set the the limits for the filter inclinations in the most general way. The frequency derivative of the signal is maximum in absolute value at the beginning and then progressively reduces according to 5.2. The limit for the final frequency derivative is set conservatively to zero. The other limit is given by the resolution chosen for the FFT. In fact, the SFDBs are constructed with multiple resolutions that correspond to different maxima frequency derivatives of the signal according to Equation 5.5. The most reasonable choice is to set the limit frequency derivative as coincident to the resolution limit of the spectrogram. So, the most general choise is

$$\dot{f}_1 = -\frac{1}{T_{\mathrm{fft}}^2} \quad ; \quad \dot{f}_2 = 0 \tag{5.33}$$

  The corresponding limits in geometric units, m_1 and m_2, are computed through the frequency and time resolution, $\delta f = 1/T_{\mathrm{fft}}$ and $\delta t = T_{\mathrm{fft}}/2$ respectively, of the spectrogram.

In Figure 5.9 an example of the application of the triangular filter to a spectrogram with simulated white noise and a simulated r-mode signal ($n = 7$) with parameters $f_0 = 750\,\mathrm{Hz}$, $\dot{f}_0 = -0.06\,\mathrm{Hz/s}$. For reference, in time domain the initial amplitude $h_0$of the signal has been set as 60-times weaker than the Gaussian noise amplitude. The spectrogram has been built using $T_{\mathrm{fft}} = 4\,\mathrm{s}$, so the triangular filter is set with $\dot{f}_1 = -0.0625\,\mathrm{Hz/s}$, $\dot{f}_2 = 0$ and a cut equal to 1. The output of the filter is shown in the bottom plot in Figure 5.9. The signal average SNR, starting from the original value $\bar{SNR}_0 \simeq 0.335$, is enhanced by a factor ~ 3.77 up to the value $\bar{SNR}_t \simeq 1.26$. The enhancement is clearly lower than the one achieved with the Wiener filter, but in this case the time-frequency pattern of the signal has been preserved and can be fed to the Hough transform. In the next section I show an application of the triangular filter to the first stages of the GFH procedure to get an estimate of the potential achievable improvement of the search sensitivity for long transient GWs.

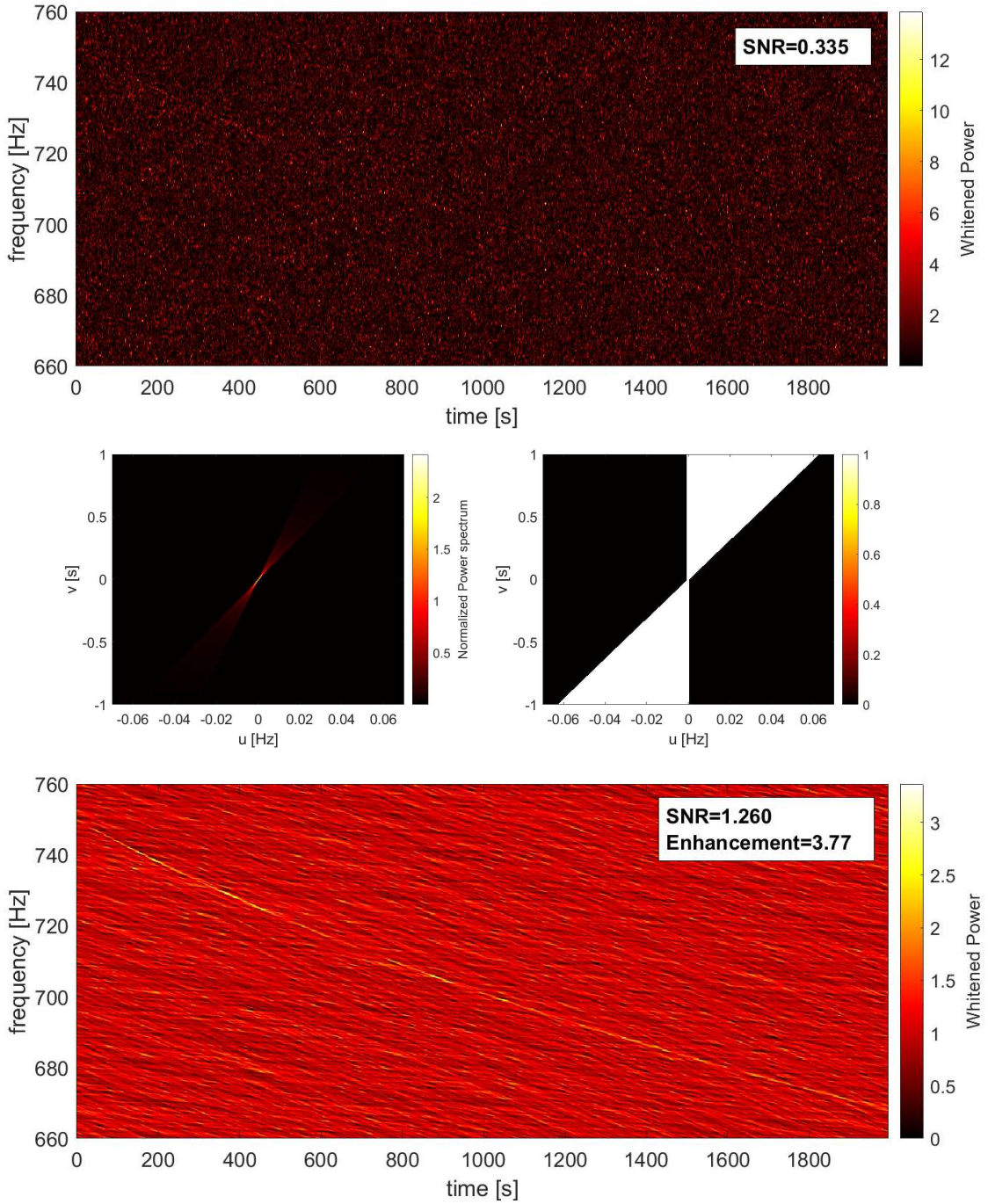

Figure 5.9: Top plot: spectrogram of simulated white noise with a simulated r-mode GW, with parameters $f_0 = 750\,\mathrm{Hz}$, $\dot{f}_0 = -0.06\,\mathrm{Hz/s}$ and $n = 7$. The signal, barely visible, has an average SNR$\simeq 0.335$ with respect to the noise floor. Middle plots: 2D power spectrum of the signal time-frequency pattern (left) and triangular filter applied to the spectrogram with parameters $\dot{f}_1 = -0.0625\,\mathrm{Hz/s}$, $\dot{f}_2 = 0$ and frequency cut equal to 1 (right). Bottom plot: the same spectrogram after the application of the triangular filter. The signal is well visible, with a SNR$\simeq 1.26$ enhanced by a factor ~ 3.77 with respect to the original SNR.

5.4 Sensitivity gain estimation

In the previous section I have shown that the application of the triangular filter to white noise can actually enhance the SNR of a long transient GW. However, the increased SNR does not translate directly in search sensitivity. As we have seen, the peaks selected in the PM are just counted by the Hough transform, but their power is not considered. The probability for a signal peak to be selected in the PM is proportional to its whitened power, so the application of the triangular filter has the effect of increasing the probability for signal peaks to be selected. Thus, the effectiveness of the filter can be measured looking at the total number of peaks counted in the Hough map.

I have repeated the first steps of the GFH procedure using public data from the LIGO Livingston detector during the O3 run, from GPS time 1253179440 s to 1253239440 s [179]. I have simulated a total of 1078 r-mode GW signals, with random parameters in the following ranges:

$n = 7$
$f_0 \in [700\ -\ 770]$ Hz
$k \in [3.9\ -\ 7.6] \cdot 10^{-22}\text{Hz}^{-5}$
$\tau \in [1\ -\ 2] \cdot 10^{3}\text{s}$
$h_0 \in \left[10^{-24}\ -\ 5 \cdot 10^{-23}\right]$

Table 5.1: Parameters used to simulate r-mode signals to be injected in LIGO Livingston O3 data to test the triangular filter.

I have injected these signals in time domain. For each injected signal I have repeated the SFDB construction using $T_{\text{fft}} = 4\,\text{s}$, but differently from the GFH procedure I have not built the PM for each single FFT. Instead, I have saved the whole spectrogram and applied the triangular filter. Then, I have repeated the procedure of peaks selection, non-linear correction of the PM and Hough transform for both the original and the filtered spectrogram. Note that in the case of the filtered spectrogram I have adapted the threshold for peaks selection in order to follow the new noise distribution, maintaining the same percentile of the old threshold for exponential noise. From the two obtained Hough maps, I have taken the number of counts from the point corresponding to the signal parameters and I have computed its critical ratio, i.e. the "standardized" counts with respect to the average counts due to the noise

$$CR = \frac{n_s - \bar{n}}{\sigma_n} \tag{5.34}$$

I have also registered the mismatch between the parameters of the pixel with the highest count, taken around the actual signal parameters, and the signal parameters themselves.

The results of the simulation are reported in Figure 5.10. In the top plot I show the number of counts associated to the pixel corresponding to the signal in the Hough map, before (blue curve) and after the filtering (green curve), as function of the signal initial amplitude h_0. The number of counts from the filtered maps increase by an average +55% with respect to the non-filtered maps, with maxima up to the +80%. However, in the bottom plot I show the critical ratio as function of h_0, both before (blue curve) and after the filtering (green curve). In this case the curve of the critical ratio for the filtered spectrograms has a different trend: when the signal amplitude is lower than $2 \cdot 10^{-23}$, the critical ratio is larger

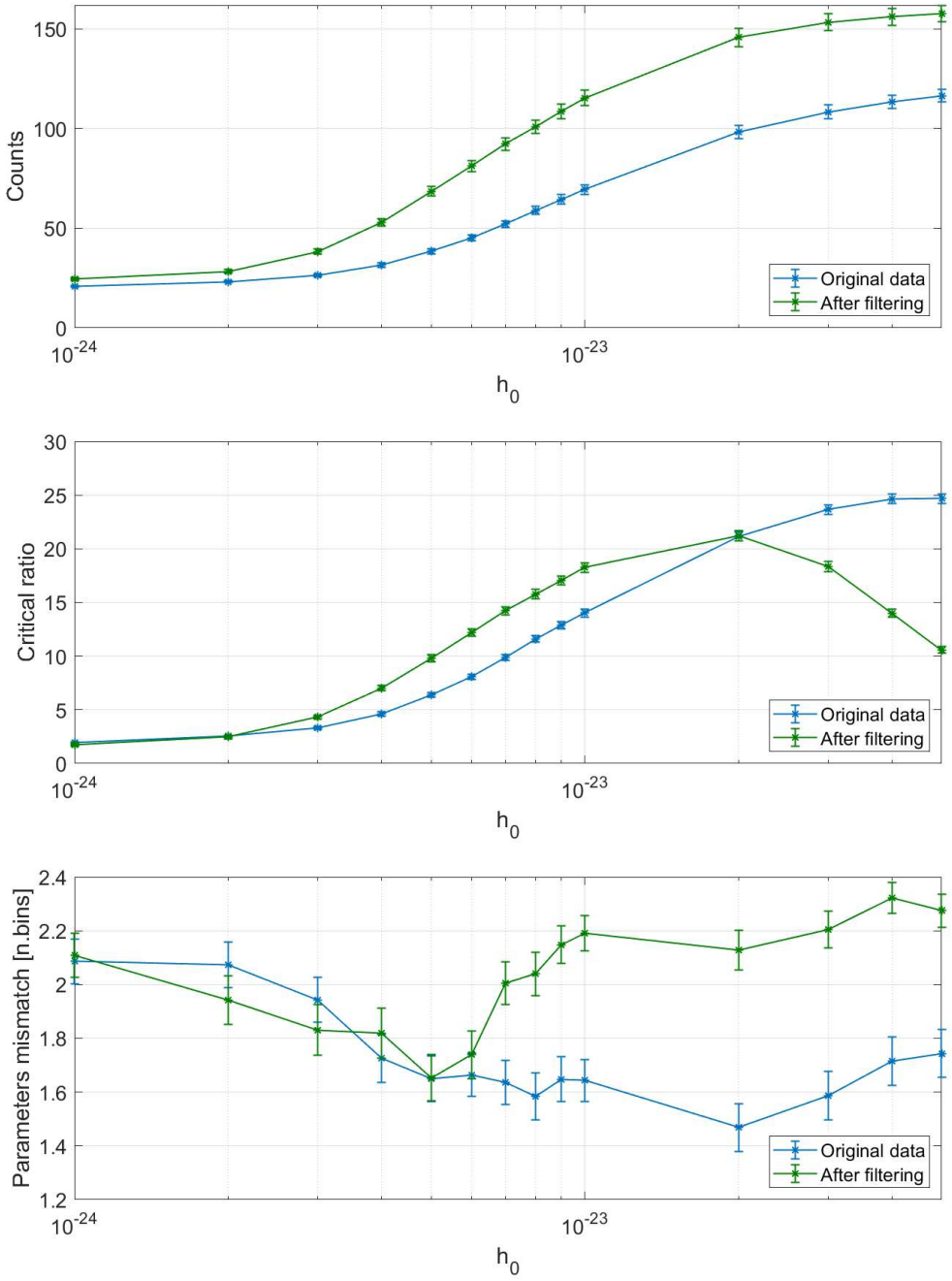

Figure 5.10: Results of the simulation described in Section 5.4. 1078 r-mode signals, with parameters reported in Table 5.1, have been added to O3 data of LIGO Livingston [179]. The blue lines represent the results from unfiltered spectrograms, the green lines represent the results from the same spectrograms after having applied the triangular filer. The top plot shows the number of counts associated to the signal pixel. The middle plot shows the critical ratio estimated from the previous counts using Equation 5.34. The bottom plot shows the parameters mismatch, i.e. the distance between the selected pixel and the signal parameters computed through Equation 5.35.

than that for the non-filtered case by about +30% on average, but for stronger signals the trend is inverted. The reason for this phenomenon is to be found in the filter mechanism. The triangular filter achieves the best performances when weak signals are buried in the noise. But when the signal amplitude grows, its power shows up from the spectrogram with SNR many times above the unit value. In this situation the noise surrounding the time-frequency pattern of the signal interferes with the triangular filter giving raise to spurious correlations and thus producing deformations on its path. This means that the triangular filter can be actually a good tool to enhance the search sensitivity for weak signals, but also that it has a negative impact when signals have high SNR. We can see a further confirmation of this explanation from the bottom plot. Here, I have reported the parameters mismatch estimation, i.e. the distance in the parameter space between the pixel with the highest count and the signal parameters, measured in terms of parameters resolution

$$d = \sqrt{\left(\frac{x_{0,\max} - x_{0,\mathrm{sig}}}{\delta x_0}\right)^2 + \left(\frac{k_{\max} - k_{\mathrm{sig}}}{\delta k}\right)^2} \tag{5.35}$$

The trend for unfiltered data (blue line) and filtered ones (green line), as function of the signal amplitude, shows that for $h_{\leq} 6 \cdot 10^{-24}$ the average mismatch is the same for both the data sets. After that value of h_o, parameter estimation is worse for the filtered data with respect to non-filtered data. This trend confirms that the triangular filter has a negative impact when the signal has an high SNR. However, this is not an issue since realistic signals are expected to be very weak.

In order to get an estimate of the potential gain in search sensitivity, we need to put a threshold to the estimated critical ratio to consider an outlier of the Hough map as a candidate to be further processed with a follow-up. I have set a nominal threshold to the critical ratio of $CR_{\mathrm{thr}} = 5$, which means that candidates are selected if their CR is $5\,\sigma$ above the noise floor. I have estimated the detection efficiency as the fraction of injected signals with CR above that threshold, for each value of h_0. In Figure 5.11 I have reported the curves of the detection efficiency as function of h_0, obtained from the analysis of the original spectrograms of the data (blue curve) and from the filtered spectrograms (green curve). The two efficiency curves are very similar, but the one representing the filtered data is shifted towards lower h_0 values by an average $\sim 2 \cdot 10^{-24}$. It can be seen that triangular filter can actually lower the threshold for the minimum detectable GW amplitude. For instance, in this example, from 77 injected signals with $h_0 = 4 \cdot 10^{-24}$, the 35% of them have surpassed the selection threshold, but after applying the triangular filter that fraction has grown up to the 85%. If we set a typical fiduciary efficiency level to $90 - 95\%$, this corresponds to an increase of +20% in the search sensitivity. I have done a preliminary presentation of this result in [180].

This result confirms the potentiality of the triangular filter to increase the sensitivity of long transient GW searches. However, the present work does not represent yet the implementation of a search procedure with the triangular filter. To implement the triangular filter as an intermediate step of a search procedure more work will be needed in order set the working point in relation with the changed noise distribution. A crucial aspect to be evaluated will be the impact of the filter on the production of noise artifacts, i.e. assess how the false alarm probability is influenced by the changes in the noise. The implementation of this filter will probably require a new tuning of the selection thresholds to optimize the equilibrium between the need to maximize the detection efficiency and minimize the false alarm probability. The implementation of a new, more sensitive search procedure will be

the object of a next work.

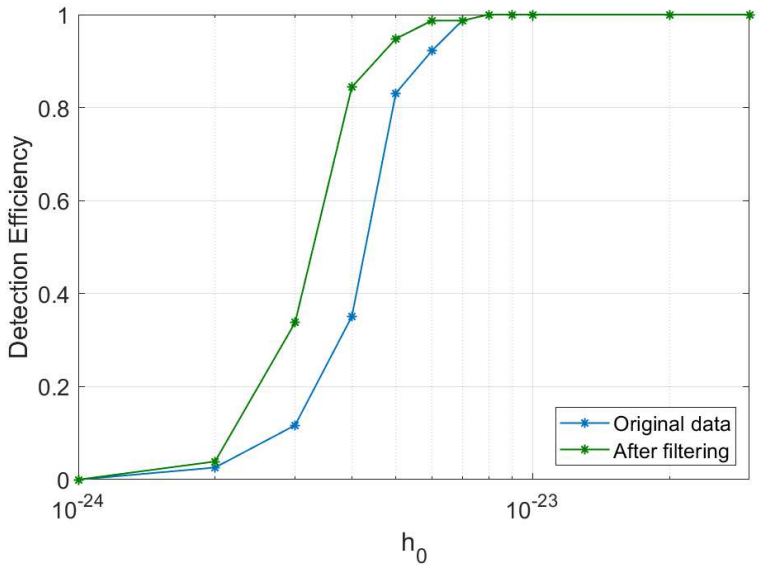

Figure 5.11: Detection efficiency curves as function of h_0, computed by putting a selection threshold of $CR_{\mathrm{thr}} = 5$ to the individual critical ratios associated to the simulated signals shown in Figure 5.10. The blue curve represents the detection efficiency for unfiltered spectrograms, while the green ones represent the spectrograms after the application of the triangular filter.

Chapter 6

All-sky searches exploiting the sidereal modulation

In this chapter I present the initial steps of a work which aims at developing a new all-sky search method, based on the so-called *sidereal filter*. This is a new filtering method for CW searches [181], which exploits the detector-induced sidereal modulation on signals of astrophysical origin. It can be either used for directed searches and as a follow-up scheme for candidates returned by all-sky searches. I have performed preliminary tests to use the sidereal filter as a first step to construct time-frequency maps and perform an all-sky search for CW signals. Although the work is still at an early stage, results show that all the components of the search work properly in sequence and the full chain is able to recover simulated signals. The chapter is organized as follows: in Section 6.1 I introduce the sidereal modulation of astrophysical signal, showing how it is related to the position of the sources and of the detector and explaining where the information on this modulation is stored. In Section 6.2 I present the procedure to extract the sidereal components from the detector data in order to produce time-frequency maps. In Section 6.3 I develop the tools to extract signals from the time-frequency maps and estimate their parameters. I also run the search on a limited parameter space, showing that the it is able to recover simulated signals present in the data.

6.1 Sidereal pattern of astrophysical signals

I have already shown in Section 2.3 that the two response functions of a detector, the antenna pattern functions, produce an amplitude modulation of the signal at the detector output. In fact the signal at the detector is given, according to Equation 2.31, by a combination of the two polarization weighted by the antenna pattern functions shown in Equation 2.35. These functions have a periodic dependence on the sidereal time. As a consequence, a monochromatic signal with angular frequency ω_0 and duration longer than a sidereal day ($T_\oplus \simeq 86164.09\,\mathrm{s}$) at the detector output is completely defined by its Fourier components at the angular frequencies ω_0, $\omega_0 \pm \Omega_\oplus$, $\omega_0 \pm 2\Omega_\oplus$, where $\Omega_\oplus = 2\pi f_\oplus \simeq 7.292 \cdot 10^{-5}\mathrm{rad/s}$. To better visualize this feature it is convenient to express the signal at the detector output with the so-called 5-vector formalism. The 5-vector formalism was introduced in [118] in the context of targeted searches, and is a very compact way to represent the CW signal.

The signal at the detector output is described in terms of five components as

$$h\left(t\right) = \mathrm{Re}\left\{H_0\, e^{i\,\omega_0 t} \sum_{k=-2}^{2} A_k\, e^{i\,k\,\Omega_\oplus t}\right\} \tag{6.1}$$

where the amplitude H_0 is related to the standard strain amplitude h_0 by a relation depending on the emission mechanism and A_k are the complex components of the signal 5-vector, whose explicit expression can be found in [118]. Here, it is important to underline that the 5-vector is fully determined by the localization and orientation of both the source and the detector. In the case of CWs from permanent deformations in NSs, we have

$$H_0 = h_0 \sqrt{\frac{1 + 6\cos^2\iota + \cos^4\iota}{4}} \tag{6.2}$$

If we take the time-dependent signal power at the detector, i.e. the squared modulus of the signal $P(t) = |h(t)|^2$, we find out that the power is fully described by its first five Fourier components as

$$P\left(t\right) = H_0^2\, \mathrm{Re}\left\{\sum_{r=0}^{4} c_r\, e^{i\,r\,\Omega_\oplus t}\right\} \tag{6.3}$$

where the coefficients c_r are related to the 5-vector components A_k as follows [118]

$$\begin{aligned}
c_0 &= \sum_{k=-2}^{2} |A_k|^2 \\
c_1 &= 2\mathrm{Re}\left[A_0 A_{-1}^* + A_1 A_0^* + A_{-1} A_{-2}^* + A_2 A_1^*\right] \\
c_2 &= 2\mathrm{Re}\left[A_0 A_{-2}^* + A_1 A_{-1}^* + A_2 A_0^*\right] \\
c_3 &= 2\mathrm{Re}\left[A_1 A_{-2}^* + A_2 A_{-1}^*\right] \\
c_4 &= 2\mathrm{Re}\left[A_2 A_{-2}^*\right]
\end{aligned}$$

where the asterisk denotes the complex conjugate. The sidereal pattern is periodic on the sidereal day, and is not explicitly dependent on the frequency. Once the detector is fixed, the sidereal pattern is determined only by the source location. In the left plot of Figure 6.1 a theoretical sidereal pattern, computed for a source located at the equatorial coordinates of the Vela pulsar $(\alpha, \delta) = (128.8365°, -45.1758°)$ and the Virgo detector, is shown (blue curve). There are a minimum and a maximum of the absorbed power, that occur periodically at each sidereal day. The red and green curves are the sidereal pattern obtained by shifting the source location by $\alpha + 20°$ and $\delta - 20°$ respectively. A change in declination changes the weights of the harmonics combination, whereas a change in right ascension determines a simple phase shift of the curve. In the right plot of Figure 6.1 the power spectra of the three curves is shown. According to Equation 6.3, the power is concentrated only in the first five harmonics. It is worth to note that the first five harmonics of the blue and red curves, which represent sources shifted along the right ascension, are coincident.

Looking at the sidereal patterns and their spectra, the crucial fact we want to exploit is that if a signal has an astrophysical origin, its power will be modulated with a sidereal pattern and its information will be stored only in the first five harmonics. All the other harmonics of the spectrum are not related to astrophysical signals, and in the case of the simulated pattern in Figure 6.1 their value is due to the intrinsic numerical noise for double-precision data. At the detector output, the CW signal is added to the detector noise, which

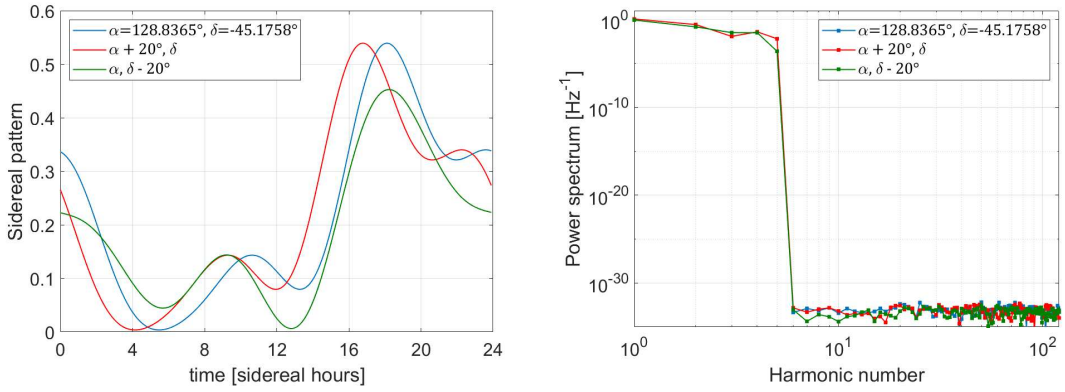

Figure 6.1: Left plot: sidereal pattern for three sources with different sky positions with respect to the Virgo detector. The blue curve represents a source located at $(\alpha, \delta) = (128.8365°, -45.1758°)$, which is the position of the Vela pulsar, the red and green represent sources translated by $+20°$ in right ascension and $-20°$ in declination respectively. Right plot: power spectral density of the sidereal pattern curves shown in the left plot, as function of the harmonic number. The information is fully contained in the first five harmonics. The values for other harmonics are due to numerical noise.

is not affected by sidereal modulation. *The basic idea is therefore to use the feature of the sidereal pattern as a filter to discriminate between astrophysical signals and noise artifacts.* By extracting the first five harmonics from the power spectrum, we are actually filtering the power componens that are related to the astrophysical origin of a signal. In the next Section I will explain how this *sidereal filter* is implemented.

6.2 Implementation of the sidereal filter

In order to extract the sidereal pattern from the detector data, some processing is necessary. Starting from the BSD data framework [170], data covering frequency sub-bands of 1-Hz and the whole run duration $T_{\rm obs}$ are extracted. Each extracted sub-band can be processed independently. Let us focus on a given sub-band $x(t)$, which covers a frequency interval $[f_k,\ f_k + 1\,\text{Hz}]$. We take the Fourier transform of the series, $\tilde{x}(f)$, and divide it into N_f interlaced sub-intervals $\tilde{x}_i(f)$, with $i = 1, ...N_f$. Each sub-interval has a width Δf, centered at a frequency f_i and interlaced with the next one by a factor $R = N_f(\Delta f/1\,\text{Hz})$.

The choice of the sub-interval width Δf is crucial for the sensitivity of the whole search. From one side, there is the need to keep it large enough to contain the whole signal. Since the signal power is split in five peaks with frequency separation $f_\oplus$, this width cannot be smaller than $5\,f_\oplus$, but we have to take into account also that the signal moves in frequency. On the other side, there is the need to keep as less noise as possible, which tends to overwhelm the signal modulation. I have found a reasonable compromise by setting $\Delta f = 20\,f_\oplus$ and interlacing the sub-intervals by one fourth, i.e. taking $R = 4$. This means that each 1-Hz band is divided in $N = 17233$ sub-intervals. For each sub-interval, its inverse Fourier transform $x_i(t)$ is taken and it is then divided in shorter time segments $x_{i,j}(t)$. A scheme of the procedure is shown in Figure 6.2. The choice of the segment duration is another crucial part. It cannot be as short as a sidereal day because we need to observe more than one period of the sidereal pattern, but if it is too long we would likely lose the signal as

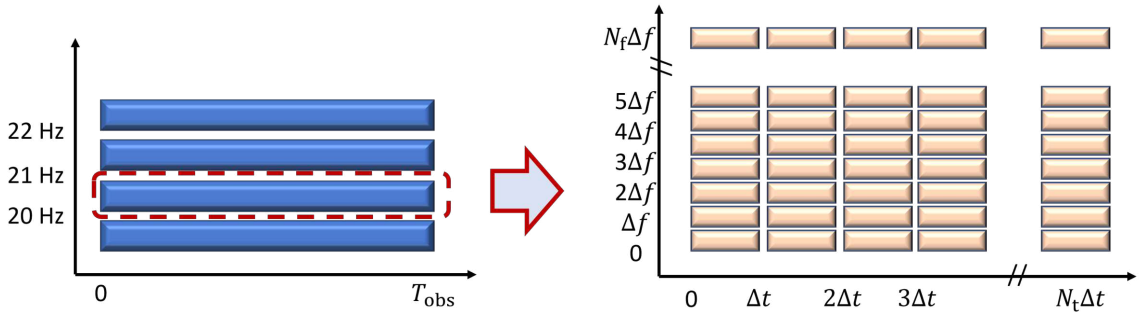

Figure 6.2: Schematic representation of the data pre-processing. The blocks on the left represent the detector output data divided in 1-Hz sub-bands covering the whole observing run $T_{\rm obs}$. Each block is processed as shown in the right side: it is divided in N_f sub-intervals Δf wide and interlaced by a factor R (in this scheme an $R = 1$ is used, to make it easily readable), and each sub-interval is divided in N_t segments with duration Δt.

its frequency variation can exceed the frequency interval Δf. The reasonable choice I have adopted for the application I am going to describe consists in segments one sidereal week long, $\Delta t = 7\,T_\oplus$, so one sub-interval is divided in $N_t = T_{\rm obs}/\Delta t$ segments. This choice could be changed after future tests when the full procedure will be completed.

We have then a set of $N_f \times N_t$ time series $x_{i,j}(t)$, each one covering a $[f_i, f_i + \Delta f]$ frequency range and a $[t_j, t_j + \Delta t]$ time range, and that globally cover 1 Hz of data over the whole observing time. Then, their power $P_{i,j}(t) = |x_{i,j}(t)|^2$ is evaluated. In order to estimate the sidereal pattern, $S_{p;i,j}(t)$, the estimated power is folded over one sidereal day $T_\oplus$. The quantity $S_{p;i,j}(t)$ should describe the power impinging on the detector as a function of the sidereal time, however it is distorted by the presence of gaps in the data. In practice, the time segments where the duty cycle, i.e. the percentage of science mode data, is lower are disfavoured with respect to other time segments. To get a non-distorted estimation of the sidereal pattern, the quantity $S_{p;i,j}(t)$ is averaged over a number K (e.g. $K = 10$) of time intervals $\delta t = T_\oplus/K$ in which the sidereal day is divided and weighted by the percentage of science-mode data in each interval:

$$\langle S_{p;i,j}\,(t)\rangle = \sum_{k=1}^{K} \frac{S_{p;i,j}\,(t)}{w_i\,(k)}\bigg|_{t\in[t_k,\,t_k+\delta t]} \tag{6.4}$$

where the function $w_i(k)$ is the fraction of the time covered by the segment in the i-th sub-interval in the time interval $(t_k,\, t_k + \delta t)$.

From the square modulus of the Fourier transform of the non-distorted estimation we get the sidereal power spectrum estimation

$$\tilde{S}_{i,j;\,m} = \left|\mathrm{FFT}\left(\langle S_{p;i,j}\,(t)\rangle\right)\right|^2 \tag{6.5}$$

where the integer index m indicates the sidereal frequency harmonic component. In Figure 6.3 I show a detail of the estimated sidereal amplitude spectra (i.e. the square root of the power spectral density) in the frequency band [108, 109] Hz over a sidereal week during the O2 run of the LIGO Livingston detector[158], starting at GPS time 1182729618 s. I have cut from the plot the fundamental $m = 0$ harmonic, since by definition of the FFT algorithm it gives the data total power and is generally dominated by the noise, distorting

the color scale of the plot. The spectra are zoomed around the frequency of a specific hardware injection, called pulsar3, which simulates a CW signal with frequency of about 108.85 Hz[1]. The estimated sidereal spectrum of the detector noise, visible at frequencies different from the hardware injection, is not flat as one might assume. Instead, it shows a slight excess of power at the lower harmonics, from harmonic number 20 downwards. This non-uniformity originates from the fact that in an Earth-based detector the noise is often modulated by night-day effects linked both to human activity and to oscillations of air pressure, temperature and so on. Consequently, the astrophysical harmonics of the power spectrum have to emerge from that noise floor. The excess of power at the first five harmonics, at the frequency of the hardware injection, is well visible.

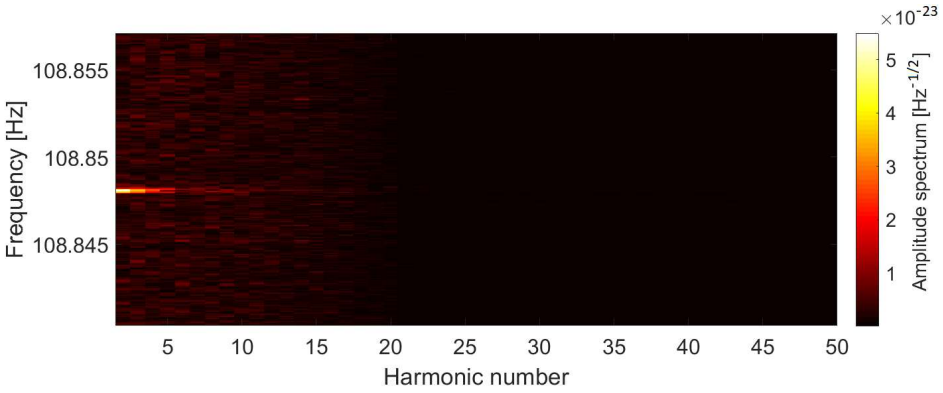

Figure 6.3: Detail of the estimated sidereal amplitude spectra in the frequency band [108, 109] Hz from a sidereal week during the O2 run [158], starting at GPS time 1182729618 s, from LIGO Livingston detector. The spectra are zoomed around the frequency of a specific hardware injection called pulsar3.

In Figure 6.4 two different sidereal pattern estimates from the data set shown in Figure 6.3 are reported, one (the blue curve) at the frequency of the hardware injection pulsar3, 108.848 Hz, and one (the red curve) from a 108.847 Hz. The sidereal modulation (left plot) of the segment containing the signal is clearly visible with respect to the pure noise. The absorbed power has a maximum corresponding to the expected sidereal hour, given the source right ascension. In the right plot the corresponding sidereal spectra are shown. The first thing to note is that the fundamental harmonic is dominated by the noise, therefore it cannot be used to estimate the sidereal power. Harmonics from the first to the fourth contain the power related to the astrophysical origin of the signal, and in the example they are significantly stronger than the pure noise ones. The remaining harmonics are related to noise and the power in the two curves is comparable. This distinct contribution of signal and noise is at the base of the sidereal filter. Starting from the sidereal power spectrum $\tilde{S}_{i,j;\,m}$ of a data segment $x_{i,j}(t)$, we can define three quantities. The first one is the total power, corresponding just to the $m = 0$ harmonic

$$P_{0;\,i,j} = \tilde{S}_{i,j;\,m=0} \tag{6.6}$$

The second one is the signal power, defined as the sum of the sidereal harmonics from the

[1]Hardware injections are generated by directly displacing the mirrors through an actuator [182].

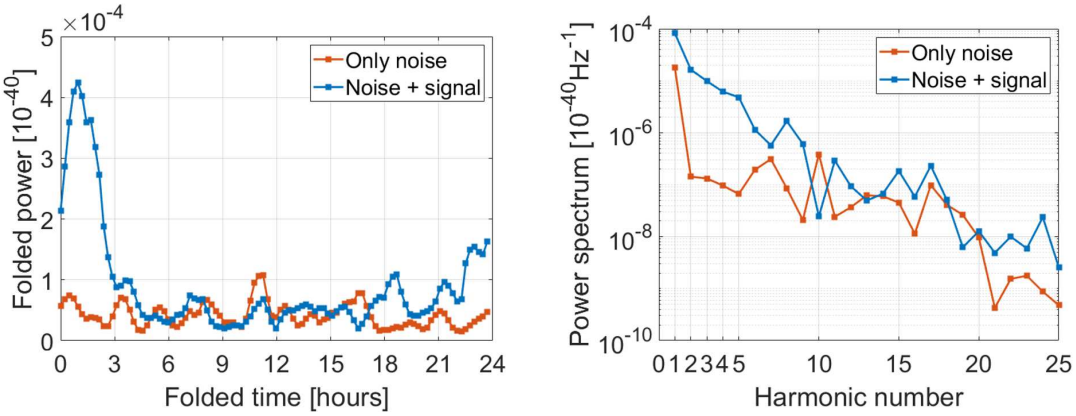

Figure 6.4: Estimated sidereal pattern (left plot) and sidereal power spectrum (right plot) of two data segments of one sidereal week starting from GPS=1182729618 s. The blue curve corresponds to the frequency bin around 108.848 Hz containing the hardware injection pulsar3, while the red curve is taken at a close frequency.

first to the fourth:

$$P_{s;\,i,j} = \sum_{m=1}^{4} \tilde{S}_{i,j;\,m} \tag{6.7}$$

Last, the third one is the noise power, defined as the sum of the harmonics of order greater than four:

$$P_{n;\,i,j} = \frac{1}{M-4} \sum_{m=5}^{M} \tilde{S}_{i,j;\,m} \tag{6.8}$$

At the end of the processing, the information from each segment, labeled with indices $(i,\, j)$ and covering a frequency range $[f_i,\, f_i + \Delta f]$ and a time range $[t_j,\, t_j + \Delta t]$, is condensed in just three scalar numbers, namely $P_{0;\,i,j}$, $P_{s;\,i,j}$ and $P_{n;\,i,j}$. One possibility is to construct a statistics based only on the absolute signal power. This choice provides the higher signal-to-noise ratio (SNR), but is not so robust with respect to strong noise disturbances. In fact, a strong noise line would distribute a higher power across all harmonics, including the first four. To get a more robust statistics a reasonable choice is to consider the ratio between the signal power and the total power, P_s/P_0, or between the signal power and the noise power, P_s/P_n. The former produces a more regular statistics but inevitably loses some SNR, since part of the signal power is included in the denominator. The latter should avoid SNR losses but produces a more noisy statistics.

Once the statistics is chosen, each data segment is represented by just one number and the information of a 1-Hz data block over the whole observing time is condensed into a $N_t \times N_f$ matrix. In the example in Figure 6.5 I have reported the detail of the sidereal map built over the [108, 109] Hz data block of LIGO Livingston detector during O2. The plot is zoomed around the frequency of the hardware injection pulsar3, which is well visible with the characteristic annual Doppler modulation. The quantity plotted in this example is the signal-to-total power ratio P_s/P_0. Each single pixel in the map represents the synthesis of the processing done on a one-sidereal-week time segment. In the next Section I show the further steps I have done towards the development of an all-sky search method.

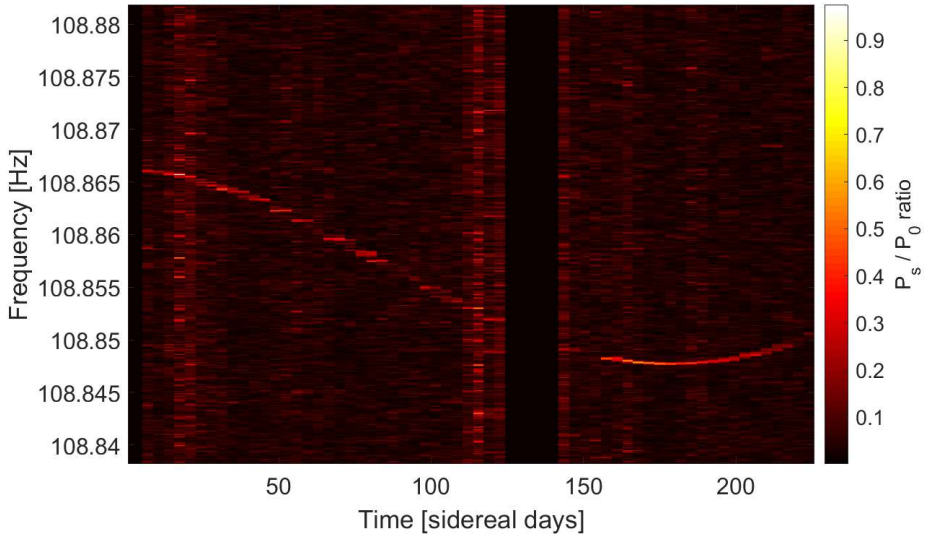

Figure 6.5: Detail of a sidereal map obtained from a [108, 109] Hz data block of LIGO Livingston detector during O2, zoomed on the frequency of the hardware injection pulsar3. The quantity plotted in color scale is the ratio between the signal power P_s and the total power P_0.

6.3 First steps for a fully incoherent all-sky search

Sidereal maps like the one shown in Figure 6.5 are the basis on which I have implemented a procedure to detect the signal time-frequency pattern. Similarly to the FH procedure discussed in Chapter 4, the steps to be done are the correction of the Doppler effect and a transformation of the map to recover the signal parameters. However, there are many differences.

First of all, I have not used the phase information at all. From the beginning, taking the power of the time segments, the resulting quantities are independent on the signal phase. Semicoherent methods increase their sensitivity with the segment duration as $T_{\rm fft}^{1/4}$ [122], but the more the segment duration increases, the more the resolution of the search increases. Analyses based on longer segment duration are more subject to possible deviations of the signal from the expected models, with a resulting sensitivity loss that could cancel the advantage of longer segments. In the sidereal filter framework, time resolution and frequency resolution are related in the sense that the frequency resolution must be tuned to take into account the frequency shift of the signal within the time resolution, but are not inversely proportional. A semicoherent search with a time resolution of a sidereal week would have a frequency resolution of $\sim 1.65 \cdot 10^{-6}$Hz. The sidereal filter, instead, works with $\delta f = 5\, f_\oplus \simeq 5.8 \cdot 10^{-5}$Hz, so any deviation of the signal from models within that frequency range does not impact the sensitivity.

Second, I don't need to select a sparse subset of the sidereal maps, since their dimensions are negligible with respect to the SFDB and PM used in the FH procedure. Here, the computational load is more focused on the pre-processing phase, which can be done progressively during the observing run, as the detector output data are produced.

Third, the processed data segments have duration of a sidereal week. During this time,

the Earth has completed $\sim$ 7 rotations around its axis. Therefore, the daily rotational Doppler effect is averaged and does not influence the time-frequency signal pattern. The Doppler correction must be done only for the annual Doppler.

Doppler correction

The correction of the Doppler effect is done by shifting the frequency of the individual pixels of the sidereal map. The shift in frequency due to the annual orbit, according to [122], is more easily described in ecliptic coordinates (β, λ) and is given by

$$f(t) \simeq f_0 \left[1 + \frac{\Omega_{\rm orb} R_{\rm orb}}{c} \cos\beta \sin\left(\Omega_{\rm orb} t - \lambda\right)\right] \tag{6.9}$$

where $R_{\rm orb}$ is the radius of the Earth's orbit and $\Omega_{\rm orb}$ is the orbital period. For a given sky position of the source, the amount of the shift for a frequency bin is obtained by inverting Equation 6.9. For the explicit estimate of the shift, the Earth barycentric velocity with respect to the mean equator and equinox is computed, using a version of the Ron & Vondrak trigonometric series [183]. The Doppler correction is repeated for a grid of points in the sky. The needed resolution of that grid is determined by the frequency resolution. A given frequency f_0 would be shifted, at most, by a quantity $f_0(\Omega_{\rm orb} R_{\rm orb})/c$, so the maximum shift in terms of number of frequency bins is given by

$$N_D = \frac{f_0}{\delta f} \frac{\Omega_{\rm orb} R_{\rm orb}}{c} \tag{6.10}$$

where the value of N_D is rounded to an integer. By imposing that the frequency shift corresponding to a variation in λ or β correspond to one frequency bin, the sky resolution in ecliptic coordinates is given by [122]

$$\delta\lambda = \frac{1}{N_D \cos\beta} \quad ; \quad \delta\beta = \frac{1}{N_D \sin\beta} \tag{6.11}$$

The corresponding sky grid is built by means of the algorithm described in [122].

Radon transform

The Doppler correction is performed covering the whole discrete sky grid. Each correction produces a sidereal map where the frequencies have been shifted in a different way. If a map contains a CW signal with sky position matching the one used for the correction, that signal has become a straight line. The top plot in Figure 6.6 shows an example: the sidereal map already shown in Figure 6.5 has been corrected for the Doppler effect by the sky position of the hardware injection pulsar3, and the signal has become a straight line.

In order to recover the signal parameters I have implemented a Radon transform. The Radon transform is an integral transform that in the original formulation maps a two-dimensional function onto its integral projections. Its use for shape detection dates back to 1965 [184][2]. The Radon transform is formally equivalent to the Hough transform, but in the practical implementation the latter results optimized for sparse data input. In my

[2]In the publication, the authors describe a technique that is essentially a Radon transform, even if its name was not recognized.

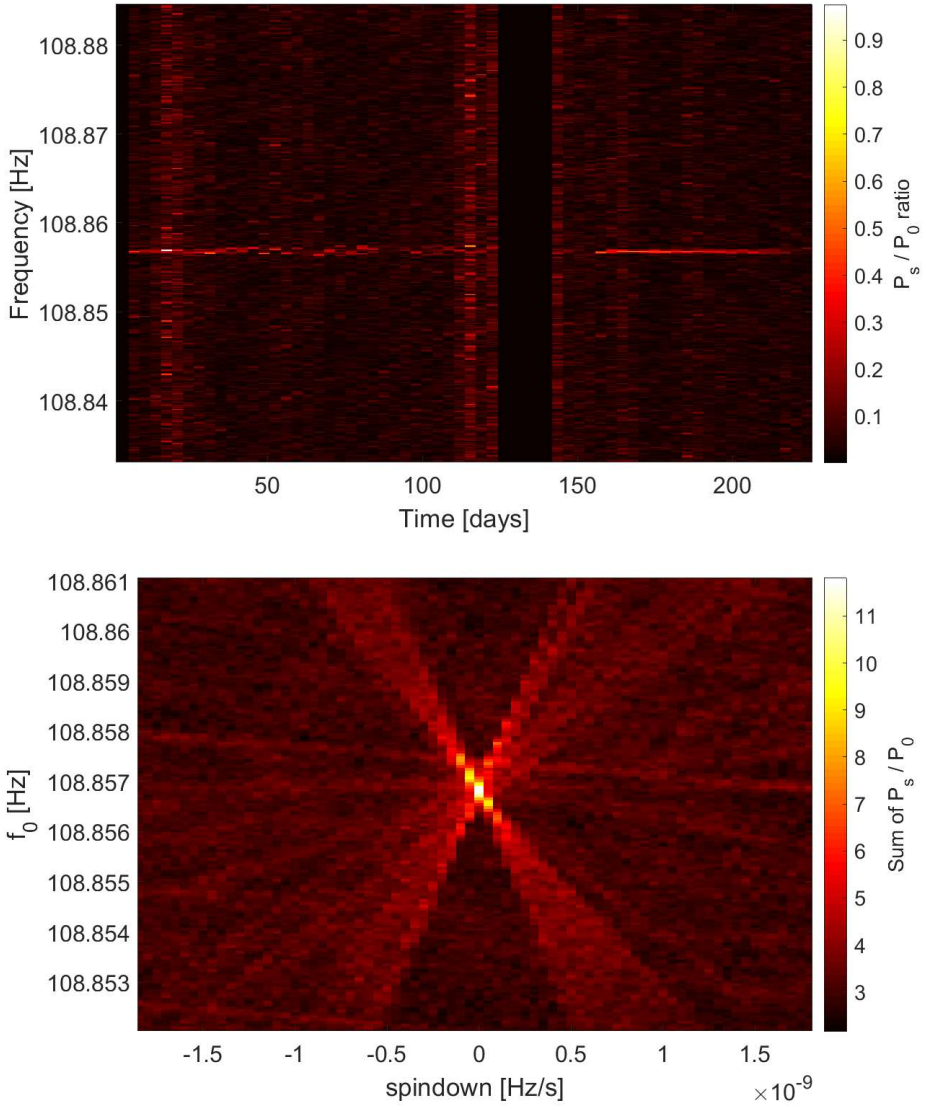

Figure 6.6: Top plot: sidereal map from LIGO Livingston O2 data between 108 Hz and 109 Hz, already shown in Figure 6.5, where the Doppler effect has been corrected for the sky position of the hardware injection pulsar3. Bottom plot: Radon transform of the sidereal map in the top plot, as function of the source frequency and first-order spindown.

implementation, I have parameterized the function to be searched using the 1st-order Taylor series for the frequency evolution, already presented in Section 2.3

$$f\left(t\right) = f_0 + \dot{f}_0\left(t - t_0\right) \tag{6.12}$$

By labeling with $I(t, f)$ the sidereal map given as input, the Radon transform $\mathcal{R}$ returns a map in the parameter space $(f_0, \dot{f}_0)$ given by

$$\mathcal{R}\left\{I\right\}\left(f_0, \dot{f}_0\right) = \int I\left(t, f\right)\delta\left[f - \dot{f}_0\left(t - t_0\right) - f_0\right] dt\, df \tag{6.13}$$

where $\delta(\cdot)$ is the delta function. The frequency resolution used for the Radon map coincides with the one, δf, of the sidereal maps. The resolution in spin-down is given by the minimum detectable frequency shift, δf, over the whole observing time:

$$\delta f_0 = \delta f \quad ; \quad \delta \dot{f}_0 = \frac{\delta f}{T_{\mathrm{obs}}} \tag{6.14}$$

An example of the output of the Radon transform is given in the bottom plot in Figure 6.6. The plot shows a detail of the Radon transform applied to the Doppler-corrected sidereal map in the top plot in the same Figure. The content of each pixel in the radon map represents the sum of the pixels in the sidereal map aligned on the line described by its $(f_0, \dot{f}_0)$ coordinates. The maximum of the sum in the example corresponds to the physical parameters that describe the pulsar3, at the beginning of the O2 run.

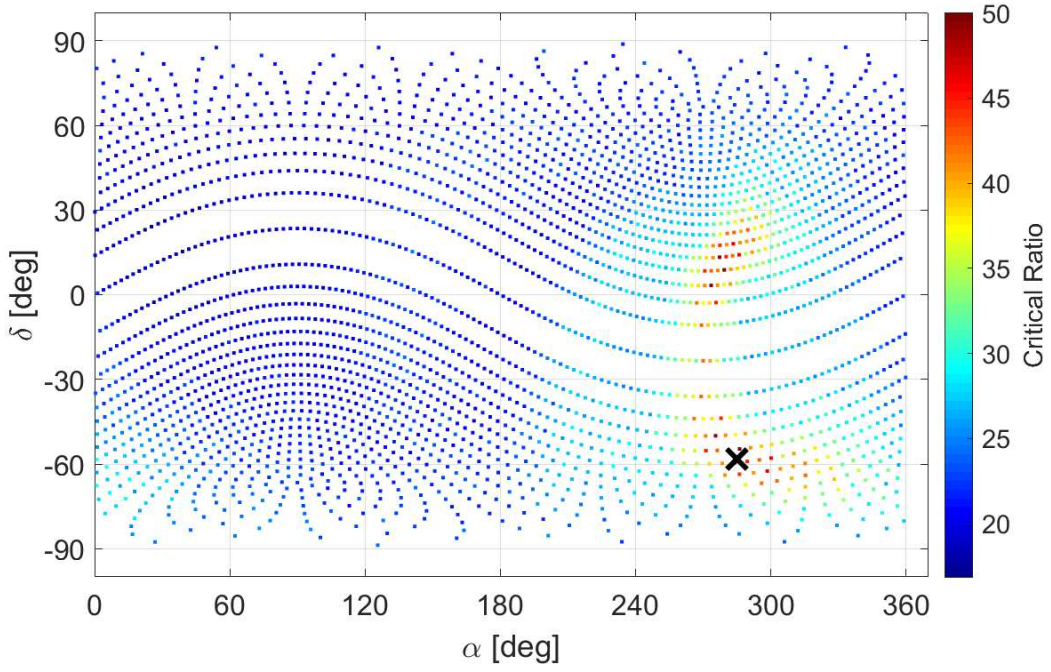

Figure 6.7: Sky map showing the measured CR values of the most significant candidates selected selected in each point of the sky grid in the frequency band [31.0, 31.5] Hz. The black "X" marker indicates the position of the hardware injection pulsar11, with parameters $f_0 \simeq 31.424\,\mathrm{Hz}$, $\dot{f}_0 \simeq -5.07 \cdot 10^{-13}$, corresponding to the maximum CR found.

Candidate selection

From each output of the Radon transform, the two most significant candidates are selected. The significance is evaluated by defining a *critical ratio* as

$$CR = \frac{s - \mu_s}{\sigma_s} \tag{6.15}$$

where s is the measured value of a pixel in the Radon map, μ_s is the mean value of all the pixels in the Radon map and σ_s is their standard deviation.

Figure 6.7 shows a sky map representing the CR of the most significant candidate selected for each point in the sky grid, in the frequency band [31.0, 31.5] Hz. In that band an hardware injection, called pulsar11, with parameters $f_0 \simeq 31.424\,\text{Hz}$, $\dot{f}_0 \simeq -5.07 \cdot 10^{-13}$ at GPS=1130529362 s and sky location $\alpha \simeq 285.1°$, $\delta \simeq -58.3°$. Its location is marked by a black "X" in the sky map, which actually coincides with the maximum CR recovered at that frequency, confirming the consistency of the procedure.

Even if the search loop is still not optimized and many steps are rough at the moment, I have performed a full search loop on the data from LIGO Livingston detector during the O2 run [158]. To save computational resources, I have run the search in the frequency range $[20, 1000]$ Hz and covering the range of spin-down $[-1,\ 1] \times 10^{-9}$ Hz/s, with resolution $\delta f = 5\, f_\oplus \simeq 5.8 \cdot 10^{-5}$Hz and $\delta \dot{f}_0 = 0.5 \cdot 10^{-10}$Hz/s. The recovered hardware injections are reported in Table 6.1. Four hardware injections, namely pulsar4, pulsar7, pulsar13 and pulsar14, have not been found because their frequencies were out of the searched range. Other three injections, namely pulsar6, pulsar8 and pulsar12, have not been found because their spin-down values were out of the searched range.

H.I. name	CR	f_0 [Hz]	$\dot{f}_0$ [Hz/s]
pulsar1	36.2	848.9551	$-3 \cdot 10^{-10}$
pulsar2	35.7	575.1638	0
pulsar3	60.2	108.8568	0
pulsar5	60.5	52.8091	0
pulsar9	31.1	763.8476	$-0.5 \cdot 10^{-10}$
pulsar10	28.2	26.3380	$-1 \cdot 10^{-10}$
pulsar11	37.0	31.4256	0

Table 6.1: Recovered hardware injections after performing an all sky loop over the $[20, 1000]$ Hz frequency range and covering the range of spin-down $[-1,\ 1] \times 10^{-9}$ Hz/s. The first column indicates the name of the hardware injection, the second column the measured critical ratio, the third and fourth columns show the inferred frequency and spin-down parameters.

6.4 Discussion and open points

The steps presented in this chapter represents the first part of the work to build a new all-sky search method. Starting from frequency band-sampled data divided in blocks covering 1 Hz and the whole observing time, I have built a bank of short interlaced segments with

duration a sidereal week and covering a frequency width $\Delta f = 5\, f_{\oplus}$. On each segment I have estimated the sidereal pattern by folding on one sidereal day and weighting to compensate for holes in the data. After computing the sidereal power spectrum, I have extracted the total power, the signal power and the noise power to construct a detection statistics and build time-frequency sidereal maps. The sidereal maps are then shifted in frequency to compensate the annual Doppler effect, for each point of a discrete sky grid, and fed as input at the Radon transform, which maps the data from the time-frequency plane to the parameter space $(f_0, \dot{f}_0)$. Candidate signals are then selected from the Radon map according to a critical-ratio statistics.

At this stage of the work, all the components of the procedure have been developed, tested and operated in sequence. However, a big amount of work is still missing in order to have a full, working search pipeline. I have tuned many fundamental quantities, like the frequency and time resolution of the base time segments, the width of the time intervals to produce a non-distorted estimate of the sidereal pattern, the resolution of the sky grid for the Doppler correction and the resolution of the Radon map, in a reasonable way. However, to make a robust tuning of all that quantities I will need to run the full search adjusting that quantities in order to maximise the final detection statistics. I am evaluating the possibility to implement a rough Doppler pre-correction to the data before starting the procedure, in order to keep the signals frequencies inside the segments for a longer time. I will have to implement the checks and follow-up procedure to be done on the candidate signals selected from the Radon maps. Finally, a further work will be needed in order to characterize the sensitivity of the procedure and compare it with other existing methods for all-sky searches. All these missing items will be the completed in a future work.

Conclusions

This PhD thesis has been fully devoted to the search for continuous gravitational waves, with the purpose of enhancing their sensitivity and thus increasing the chances of a first detection. Such a detection would have a huge impact on the gravitational-wave physics field, with important implications for fundamental physics, nuclear-matter physics and testing theories beyond the standard model. My effort has been devoted both to the data-analysis and instrumental science, as they all contribute to increase the detection chances.

The noise hunting work done at the Virgo site, described in Chapter 3, was focused on technical noises generated by HVAC, vacuum systems and the external environment. I have identified noise sources from the water pumps in the terminal buildings, from vacuum dry pumps and air handling units in the central building and from the external gas pipelines. In all the reported cases a combination of sniffing campaigns and analysis of measurements has been necessary to correctly identify the sources. The analysis tool I have developed to visualize the spatial propagation of seismic noise has proved to be very effective for quickly locating noise sources, and is currently used by other components of the noise hunting team. In the majority of the identified noise sources we have been able to perform mitigation actions that have been very effective.

On the data analysis side, one of the topic I have studied is the possible impact of several continuous-wave signals, which are clustered together in the same frequency band, on the Frequency-Hough procedure. The study, reported in Chapter 4, was motivated by recent new scenarios that predict the emission of continuous waves by ultra-light boson condensates around rotating black holes. It has been predicted that many superposing signals from galactic black holes would be unresolvable and produce some confusion noise. I have found that the first steps of the search, namely the spectral autoregressive estimation, the construction of the peakmap and the selection of candidates from histograms of Doppler-corrected peakmaps as function of the frequency, are robust with respect to the presence of clusters of signals. I have found that moderate signal clusters, i.e. with frequency width less than 0.1 Hz, do not impact the search sensitivity. Larger clusters can cause a $\sim 5\%$ sensitivity loss when they reach densities of the order of thousands of signals confined in a $\sim 0.8\,\mathrm{Hz}$ wide band. However, this would likely represent an unrealistic situation. In the most realistic scenarios predicted by simulations, the sensitivity loss is negligible. I have individuated the cause in the way the autoregressive estimation follows the changing noise floor, i.e. the so-called memory. I indicate a possible solution in running the autoregressive estimate with different memory resolutions, in order to adapt to different configurations. These results are very relevant also in view of future detectors like Einstein Telescope or LISA, for which the problem of signal clusters will be more relevant.

A further topic of my Thesis has been the development of a two-dimensional filter, so-called triangular filter, to enhance the signal-to-noise ratio of fast-evolving signals, with the frequency changing by several Hertz over few hours or days, in whitened spectrograms. The

considered signals have typical duration of $\sim 10^3$ seconds and are emitted by newly-born neutron stars, endowed with a very strong inner magnetic field or when unstable oscillation modes of the star are excited.

In Chapter 5 I have introduced the two dimensional Fourier transform, and I have shown how the information on curves in a monochromatic image is stored in the Fourier transform of the image itself. I have exploited that information to develop the triangular filter, which works in the Fourier domain and reinforces the pattern of signals against the noise. I have characterized the effect of the filter on white noise and I have performed a Monte Carlo simulation to estimate its potential impact on the searches, finding that a $\sim 20\%$ sensitivity gain is achievable.

In Chapter 6 I have presented the first steps of a wide work to develop a new procedure for all-sky continuous-wave searches, exploiting the sidereal modulation that the detector imprints to astrophysical signals. I have developed and tested the components of the new method and I have verified that the full chain works properly. In particular, performing a search on a limited parameter space I was able to recover the hardware injections that are present in the detector output data. Some further work will be needed to complete, characterize and test the full search method.

At the moment, the start of the next O4 observing run by the LIGO-Virgo-KAGRA collaboration is scheduled for the end of May 2023. During the shutdown period the detectors have been subject to numerous upgrades which will lead to an improvement in sensitivity across the entire frequency spectrum. Further strong improvements will be implemented also for the subsequent O5 run, and a study to exploit the full potentiality of the existing infrastructures is on the way. A strong synergy between instrumental science and the development of more efficient and sensitive methods is the best way to maximize the chances of a forthcoming discovery.

Bibliography

[1] Einstein, A., & Rosen, N. (1937). On gravitational waves. *Journal of the Franklin Institute*, **223(1)**, 43-54.

[2] Pirani, F. A. (1956). On the physical significance of the Riemann tensor. *Acta Physica Polonica*, **15**, 389-405.

[3] Weber, J. (1960). Detection and generation of gravitational waves. *Physical Review*, **117(1)**, 306.

[4] Gerstenshtein, M. E., & Pustovoit, V. I. (1963). On the detection of low frequency gravitational waves. *Soviet Physics-JETP*, **16(2)**, 433-435.

[5] Weiss, R., & Muehlner, D. (1972). Electronically coupled broadband gravitational antenna. *Quarterly Progress Report, Research Laboratory of Electronics, MIT*, **105**, p. 54.

[6] Ferrari, V., Gualtieri, L., & Pani, P. (2020). General Relativity and Its Applications: Black Holes, Compact Stars and Gravitational Waves. *CRC Press*.

[7] Maggiore, M. (2007). Gravitational waves: Volume 1: Theory and experiments. *OUP Oxford*.

[8] Abbott, B. P., *et al.*, LIGO Scientific Collaboration and Virgo Collaboration (2019). GWTC-1: a gravitational-wave transient catalog of compact binary mergers observed by LIGO and Virgo during the first and second observing runs. *Physical Review X*, **9(3)**, 031040.

[9] Abbott, R., *et al.*, LIGO Scientific Collaboration and Virgo Collaboration (2021). GWTC-2: compact binary coalescences observed by LIGO and Virgo during the first half of the third observing run. *Physical Review X*, **11(2)**, 021053.

[10] Abbott, R., *et al.*, LIGO Scientific Collaboration and Virgo Collaboration (2021). Gwtc-2.1: Deep extended catalog of compact binary coalescences observed by ligo and virgo during the first half of the third observing run. *arXiv preprint* arXiv:**2108.01045** (Submitted to PRD).

[11] Abbott, R., *et al.*, LIGO Scientific Collaboration, Virgo Collaboration and KAGRA collaboration (2021). GWTC-3: compact binary coalescences observed by LIGO and Virgo during the second part of the third observing run. *arXiv preprint* arXiv:**2111.03606** (Submitted to PRX).

[12] Blanchet, L., Faye, G., Iyer, B. R., & Joguet, B. (2002). Gravitational-wave inspiral of compact binary systems to 7/2 post-Newtonian order. *Physical Review D*, **65(6)**, 061501.

[13] Blanchet, L., Buonanno, A., & Faye, G. (2006). Higher-order spin effects in the dynamics of compact binaries. II. Radiation field. *Physical Review D*, **74(10)**, 104034.

[14] Pretorius, F. (2005). Numerical relativity using a generalized harmonic decomposition. *Classical and Quantum Gravity*, **22(2)**, 425.

[15] Kokkotas, K. D., & Schmidt, B. G. (1999). Quasi-normal modes of stars and black holes. *Living Reviews in Relativity*, **2(1)**, 1-72.

[16] Abbott, B. P., *et al.*, LIGO Scientific Collaboration and Virgo Collaboration (2020). A guide to LIGO–Virgo detector noise and extraction of transient gravitational-wave signals. *Classical and Quantum Gravity*, **37(5)**, 055002.

[17] Usman, S. A., *et al.*(2016). The PyCBC search for gravitational waves from compact binary coalescence. *Classical and Quantum Gravity*, **33(21)**, 215004.

[18] Cannon, K., *et al.*(2021). GstLAL: A software framework for gravitational wave discovery. *SoftwareX*, **14**, 100680.

[19] Adams, T., *et al.*(2016). Low-latency analysis pipeline for compact binary coalescences in the advanced gravitational wave detector era. *Classical and Quantum Gravity*, **33(17)**, 175012.

[20] Turatto, M. (2003). Classification of supernovae. Supernovae and Gamma-Ray Bursters (pp. 21-36). Springer, Berlin, Heidelberg. Turatto, M. (2003). Classification of Supernovae. *In: Weiler, K.W. (eds) Supernovae and Gamma-Ray Bursters. Lecture Notes in Physics*, **vol 598**, pp. 21-36. Springer, Berlin, Heidelberg.

[21] Maggiore, M. (2007). Gravitational waves: Volume 2: Astrophysics and cosmology. *OUP Oxford*.

[22] Ott, C. D. (2009). The gravitational-wave signature of core-collapse supernovae. *Classical and Quantum Gravity*, **26(6)**, 063001.

[23] Abbott, R., *et al.*, LIGO Scientific Collaboration, Virgo Collaboration and KAGRA collaboration (2021). All-sky search for short gravitational-wave bursts in the third Advanced LIGO and Advanced Virgo run. *Physical Review D*, **104(12)**, 122004.

[24] Klimenko, S., Yakushin, I., Mercer, A., & Mitselmakher, G. (2008). A coherent method for detection of gravitational wave bursts. *Classical and Quantum Gravity*, **25(11)**, 114029.

[25] Klimenko, S., Vedovato, G., Drago, M., *et al.*(2016). Method for detection and reconstruction of gravitational wave transients with networks of advanced detectors. *Physical Review D*, **93(4)**, 042004.

[26] Abbott, B. P., *et al.*, LIGO Scientific Collaboration and Virgo Collaboration (2017). All-sky search for short gravitational-wave bursts in the first Advanced LIGO run. *Physical Review D*, **95(4)**, 042003.

[27] Abbott, B. P., *et al.*, LIGO Scientific Collaboration and Virgo Collaboration (2019). All-sky search for short gravitational-wave bursts in the second Advanced LIGO and Advanced Virgo run. *Physical Review D*, **100(2)**, 024017.

[28] Regimbau, T. (2011). The astrophysical gravitational wave stochastic background. *Research in Astronomy and Astrophysics*, **11(4)**, 369.

[29] Maggiore, M. (2000). Gravitational wave experiments and early universe cosmology. *Physics Reports*, **331(6)**, 283-367.

[30] Ain, A., Suresh, J., & Mitra, S. (2018). Very fast stochastic gravitational wave background map making using folded data. *Physical Review D*, **98(2)**, 024001.

[31] Abbott, R., *et al.*, LIGO Scientific Collaboration, Virgo Collaboration and KAGRA collaboration (2021). Upper limits on the isotropic gravitational-wave background from Advanced LIGO and Advanced Virgo's third observing run. *Physical Review D*, **104(2)**, 022004.

[32] Abbott, R., *et al.*, LIGO Scientific Collaboration, Virgo Collaboration and KAGRA collaboration (2021). Constraints on cosmic strings using data from the third Advanced LIGO–Virgo observing run. *Physical review letters*, **126(24)**, 241102.

[33] Abbott, R., *et al.*, LIGO Scientific Collaboration, Virgo Collaboration and KAGRA collaboration (2021). Search for anisotropic gravitational-wave backgrounds using data from Advanced LIGO and Advanced Virgo's first three observing runs. *Physical Review D*, **104(2)**, 022005.

[34] Abbott, R., *et al.*, LIGO Scientific Collaboration, Virgo Collaboration and KAGRA collaboration (2022). All-sky, all-frequency directional search for persistent gravitational waves from Advanced LIGO's and Advanced Virgo's first three observing runs. *Physical Review D*, **105(12)**, 122001.

[35] Ni, W. T., & Zimmermann, M. (1978). Inertial and gravitational effects in the proper reference frame of an accelerated, rotating observer. *Physical Review D*, **17(6)**, 1473.

[36] Michelson, A. A., & Morley, E. (1887). On the relative motion of the Earth and the luminiferous aether. *American Journal of Science*, **34(203)**, 333-345.

[37] Caron, B., *et al.*, Virgo Collaboration (1997). The virgo interferometer. *Classical and Quantum Gravity*, **14(6)**, 1461.

[38] Abbott, B. P., *et al.*, LIGO Scientific Collaboration (2009). LIGO: the laser interferometer gravitational-wave observatory. *Reports on Progress in Physics*, **72(7)**, 076901.

[39] Accadia, T., *et al.*, Virgo Collaboration (2012). Virgo: a laser interferometer to detect gravitational waves. *Journal of Instrumentation*, **7(03)**, P03012.

[40] Acernese, F., *et al.*, Virgo Collaboration (2022). Calibration of advanced Virgo and reconstruction of the detector strain h (t) during the observing run O3. *Classical and Quantum Gravity*, **39(4)**, 045006.

[41] Caves, C. M. (1981). Quantum-mechanical noise in an interferometer. *Physical Review D*, **23(8)**, 1693.

[42] Caves, C. M. (1980). Quantum-mechanical radiation-pressure fluctuations in an interferometer. *Physical Review Letters*, **45(2)**, 75.

[43] Saulson, P. R. (1994). Fundamentals of interferometric gravitational wave detectors. *World Scientific*, Chapter 8.

[44] Saulson, P. R. (1984). Terrestrial gravitational noise on a gravitational wave antenna. *Physical Review D*, **30(4)**, 732.

[45] Acernese, F., *et al.*(2010). Measurements of Superattenuator seismic isolation by Virgo interferometer. *Astroparticle Physics*, **33(3)**, 182-189.

[46] Callen, H. B., & Greene, R. F. (1952). On a theorem of irreversible thermodynamics. *Physical Review*, **86(5)**, 702.

[47] Greene, R. F., & Callen, H. B. (1952). On a theorem of irreversible thermodynamics. II. *Physical Review*, **88(6)**, 1387.

[48] Saulson, P. R. (1990). Thermal noise in mechanical experiments. *Physical Review D*, **42(8)**, 2437.

[49] Harms, J. (2015). Terrestrial gravity fluctuations. *Living reviews in relativity*, **18**, 1-150.

[50] Beccaria, M., *et al.*(1998). Relevance of Newtonian seismic noise for the VIRGO interferometer sensitivity. *Classical and Quantum Gravity*, **15(11)**, 3339.

[51] Acernese, F. A., *et al.*, Virgo Collaboration (2014). Advanced Virgo: a second-generation interferometric gravitational wave detector. *Classical and Quantum Gravity*, **32(2)**, 024001.

[52] Aasi, J., *et al.*, LIGO Scientific Collaboration (2015). Advanced ligo. *Classical and quantum gravity*, **32(7)**, 074001.

[53] Grote, H., *et al.*(2004). Dual recycling for GEO 600. *Classical and Quantum Gravity*, **21(5)**, S473.

[54] Buonanno, A., & Chen, Y. (2001). Quantum noise in second generation, signal-recycled laser interferometric gravitational-wave detectors. *Physical Review D*, **64(4)**, 042006.

[55] Abbott, B. P., , *et al.*, LIGO Scientific Collaboration and Virgo Collaboration (2016). Observation of gravitational waves from a binary black hole merger. *Physical review letters*, **116(6)**, 061102.

[56] Abbott, B. P., *et al.*, LIGO Scientific Collaboration and Virgo Collaboration (2016). Binary black hole mergers in the first advanced LIGO observing run. *Physical Review X*, **6(4)**, 041015.

[57] Abbott, B. P., *et al.*, LIGO Scientific Collaboration and Virgo Collaboration (2017). GW170814: a three-detector observation of gravitational waves from a binary black hole coalescence. *Physical review letters*, **119(14)**, 141101.

[58] Abbott, B. P., *et al.*, LIGO Scientific Collaboration and Virgo Collaboration (2017). GW170817: observation of gravitational waves from a binary neutron star inspiral. *Physical review letters*, **119(16)**, 161101.

[59] Abbott, B. P., *et al.*, LIGO Scientific Collaboration and Virgo Collaboration (2017). Multi-messenger observations of a binary neutron star merger. *The Astrophysical Journal Letters*, **848**, L12.

[60] Abbott, B. P., *et al.*, LIGO Scientific Collaboration and Virgo Collaboration (2020). GW190425: Observation of a compact binary coalescence with total mass $\sim 3.4 M_{\odot}$. *The Astrophysical journal letters*, **892(1)**, L3.

[61] Abbott, R., *et al.*, LIGO Scientific Collaboration and Virgo Collaboration (2020). GW190412: Observation of a binary-black-hole coalescence with asymmetric masses. *Physical Review D*, **102(4)**, 043015.

[62] Abbott, R., *et al.*, LIGO Scientific Collaboration and Virgo Collaboration (2020). GW190814: gravitational waves from the coalescence of a 23 solar mass black hole with a 2.6 solar mass compact object. *The Astrophysical Journal Letters*, **896(2)**, L44.

[63] Abbott, R., *et al.*, LIGO Scientific Collaboration and Virgo Collaboration (2020). GW190521: a binary black hole merger with a total mass of $150 M_{\odot}$. *Physical review letters*, **125(10)**, 101102.

[64] Abbott, R., *et al.*, LIGO Scientific Collaboration, Virgo Collaboration and KAGRA collaboration (2021). Observation of gravitational waves from two neutron star–black hole coalescences. *The Astrophysical journal letters*, **915(1)**, L5.

[65] Abbott, R., *et al.*, LIGO Scientific Collaboration and Virgo Collaboration (2021). Tests of general relativity with binary black holes from the second LIGO-Virgo gravitational-wave transient catalog. *Physical review D*, **103(12)**, 122002.

[66] Abbott, R., *et al.*, LIGO Scientific Collaboration, Virgo Collaboration and KAGRA collaboration (2021). Tests of General Relativity with GWTC-3. *arXiv preprint* arXiv:**2112.06861**. (Submitted to PRD)

[67] Astone, P., *et al.*(2001). Search for periodic gravitational wave sources with the Explorer detector. *Physical Review D*, **65(2)**, 022001.

[68] Astone, P., *et al.*(2003). All-sky upper limit for gravitational radiation from spinning neutron stars. *Classical and Quantum Gravity*, **20(17)**, S665.

[69] Yakovlev, D. G., Haensel, P., Baym, G., & Pethick, C. (2013). Lev Landau and the concept of neutron stars. *Physics-Uspekhi*, **56(3)**, 289.

[70] Baade, W., & Zwicky, F. (1934). Remarks on super-novae and cosmic rays. *Physical Review*, **46(1)**, 76.

[71] Oppenheimer, J. R., & Volkoff, G. M. (1939). On massive neutron cores. *Physical Review*, **55(4)**, 374.

[72] Hewish, A., Bell, S. J., Pilkington, J. D., Scott, P. F., & Collins, R. A. (2013). 74. Observation of a Rapidly Pulsating Radio Source. *Nature*, **217**, 709–713.

[73] Gold, T. (1968). Rotating neutron stars as the origin of the pulsating radio sources. *Nature*, **218**, 731–732.

[74] Cerda-Duran, P., & Elias-Rosa, N. (2018). Neutron stars formation and core collapse supernovae. In *The Physics and Astrophysics of Neutron Stars* **(pp. 1-56)**. Springer, Cham.
Public arXiv chapter: `https://doi.org/10.48550/arXiv.1806.07267`

[75] Shapiro, S. L., & Teukolsky, S. A. (1983). Black holes, white dwarfs, and neutron stars: The physics of compact objects. *John Wiley & Sons*.

[76] Lattimer, J. M., & Prakash, M. (2001). Neutron star structure and the equation of state. *The Astrophysical Journal*, **550(1)**, 426.

[77] Miller, M. C., *et al.*(2021). The radius of PSR J0740+ 6620 from NICER and XMM-Newton data. *The Astrophysical Journal Letters*, **918(2)**, L28.

[78] Raaijmakers, G., *et al.*(2021). Constraints on the dense matter equation of state and neutron star properties from NICER's mass–radius estimate of PSR J0740+6620 and multimessenger observations. *The Astrophysical Journal Letters*, **918(2)**, L29.

[79] Riley, T. E., *et al.*(2019). A NICER view of PSR J0030+ 0451: Millisecond pulsar parameter estimation. The Astrophysical Journal Letters, 887(1), L21.

[80] Buschauer, R., & Benford, G. (1976). General theory of coherent curvature radiation. *Monthly Notices of the Royal Astronomical Society*, **177(1)**, 109-136.

[81] Riles, K. (2022). Searches for Continuous-Wave Gravitational Radiation. *arXiv preprint* arXiv:**2206.06447** (Submitted to LRR).

[82] Manchester, R. N., Hobbs, G. B., Teoh, A., & Hobbs, M. (2005). The Australia telescope national facility pulsar catalogue. *The Astronomical Journal*, **129(4)**, 1993. Repository URL: `https://www.atnf.csiro.au/research/pulsar/psrcat/`

[83] Mösta, P., Ott, C. D., Radice, D., Roberts, L. F., Schnetter, E., & Haas, R. (2015). A large-scale dynamo and magnetoturbulence in rapidly rotating core-collapse supernovae. *Nature*, **528(7582)**, 376-379.

[84] Treves, A., Turolla, R., Zane, S., & Colpi, M. (2000). Isolated neutron stars: accretors and coolers. *Publications of the Astronomical Society of the Pacific*, **112(769)**, 297.

[85] Owen, B. J. (2005). Maximum elastic deformations of compact stars with exotic equations of state. *Physical Review Letters*, **95(21)**, 211101.

[86] Bildsten, L. (1998). Gravitational radiation and rotation of accreting neutron stars. *The Astrophysical Journal*, **501(1)**, L89.

[87] Chandrasekhar, S., & Fermi, E. (1953). Problems of gravitational stability in the presence of a magnetic field. *Astrophysical Journal*, **118**, 116.

[88] Haskell, B., Samuelsson, L., Glampedakis, K., & Andersson, N. (2008). Modelling magnetically deformed neutron stars. *Monthly Notices of the Royal Astronomical Society*, **385(1)**, 531-542.

[89] Glampedakis, K., & Gualtieri, L. (2018). Gravitational waves from single neutron stars: an advanced detector era survey. *The Physics and Astrophysics of Neutron Stars*, **673-736**. Public arXiv chapter: `https://doi.org/10.48550/arXiv.1709.07049`

[90] Haskell, B., Jones, D. I., & Andersson, N. (2006). Mountains on neutron stars: accreted versus non-accreted crusts. *Monthly Notices of the Royal Astronomical Society*, **373(4)**, 1423-1439.

[91] Andersson, N., & Kokkotas, K. D. (2001). The r-mode instability in rotating neutron stars. *International Journal of Modern Physics D*, **10(04)**, 381-441.

[92] Lasky, P. D. (2015). Gravitational waves from neutron stars: a review. *Publications of the Astronomical Society of Australia*, **32**, e034.

[93] Owen, B. J. (2010). How to adapt broad-band gravitational-wave searches for r-modes. *Physical Review D*, **82(10)**, 104002.

[94] Owen, B. J., Lindblom, L., Cutler, C., Schutz, B. F., Vecchio, A., & Andersson, N. (1998). Gravitational waves from hot young rapidly rotating neutron stars. *Physical Review D*, **58(8)**, 084020.

[95] Abbott, R., *et al.*, LIGO Scientific Collaboration, Virgo Collaboration and KAGRA collaboration (2021). Constraints from LIGO O3 Data on Gravitational-wave Emission Due to R-modes in the Glitching Pulsar PSR J0537–6910. *The Astrophysical Journal*, **922(1)**, 71.

[96] Kouveliotou, C., *et al.*(1987). SMM hard X-ray observations of the soft gamma-ray repeater 1806-20. *The Astrophysical Journal*, **322**, L21-L25.

[97] Mereghetti, S., & Stella, L. (1995). The very low mass X-ray binary pulsars: A new class of sources?. *The Astrophysical Journal*, **442**, L17-L20.

[98] Dall'Osso, S., & Stella, L. (2022). Millisecond Magnetars. In *Millisecond Pulsars* **(pp. 245-280)**. Springer, Cham.
Public arXiv chapter: `https://doi.org/10.48550/arXiv.2103.10878`

[99] Zhong, S. Q., & Dai, Z. G. (2020). Magnetars from neutron star–white dwarf mergers: application to fast radio bursts. *The Astrophysical Journal*, **893(1)**, 9.

[100] Lasky, P. D., Leris, C., Rowlinson, A., & Glampedakis, K. (2017). The braking index of millisecond magnetars. *The Astrophysical Journal Letters*, **843(1)**, L1.

[101] Sarin, N., Lasky, P. D., & Ashton, G. (2020). Interpreting the X-ray afterglows of gamma-ray bursts with radiative losses and millisecond magnetars. *Monthly Notices of the Royal Astronomical Society*, **499(4)**, 5986-5992.

[102] Dall'Osso, S., Shore, S. N., & Stella, L. (2009). Early evolution of newly born magnetars with a strong toroidal field. *Monthly Notices of the Royal Astronomical Society*, **398(4)**, 1869-1885.

[103] Stella, L., Dall'Osso, S., Israel, G., & Vecchio, A. (2005). Gravitational radiation from newborn magnetars in the virgo cluster. *The Astrophysical Journal*, **634(2)**, L165.

[104] Essig, R., *et al.*(2013). Dark sectors and new, light, weakly-coupled particles. *arXiv preprint* arXiv:**1311.0029**.

[105] Arvanitaki, A., Dimopoulos, S., Dubovsky, S., Kaloper, N., & March-Russell, J. (2010). String axiverse. *Physical Review D*, **81(12)**, 123530.

[106] Marsh, D. J. (2016). Axion cosmology. *Physics Reports*, **643**, 1-79.

[107] Brito, R., Cardoso, V., & Pani, P. (2020). Superradiance. *Springer International Publishing*.

[108] Penrose, R. (2002). Gravitational collapse: the role of general relativity. *General Relativity and Gravitation*, **34(7)**, 1141-1165.

[109] Brito, R., Ghosh, S., Barausse, E., Berti, E., Cardoso, V., Dvorkin, I., Klein, A., & Pani, P. (2017). Gravitational wave searches for ultralight bosons with LIGO and LISA. *Physical Review D*, **96(6)**, 064050.

[110] Palomba, C., *et al.*(2019). Direct constraints on the ultralight boson mass from searches of continuous gravitational waves. *Physical review letters*, **123(17)**, 171101.

[111] Baryakhtar, M., Galanis, M., Lasenby, R., & Simon, O. (2021). Black hole superradiance of self-interacting scalar fields. *Physical Review D*, **103(9)**, 095019.

[112] Abbott, R., *et al.*, LIGO Scientific Collaboration, Virgo Collaboration and KAGRA collaboration (2022). All-sky search for gravitational wave emission from scalar boson clouds around spinning black holes in LIGO O3 data. *Physical Review D*, **105(10)**, 102001.

[113] Taylor, J. H. (1992). Pulsar timing and relativistic gravity. *Philosophical Transactions of the Royal Society of London*. Series A: Physical and Engineering Sciences, **341(1660)**, 117-134.

[114] Jaranowski, P., Krolak, A., & Schutz, B. F. (1998). Data analysis of gravitational-wave signals from spinning neutron stars: The signal and its detection. *Physical Review D*, **58(6)**, 063001.

[115] Abbott, R., *et al.*, LIGO Scientific Collaboration, Virgo Collaboration and KAGRA collaboration (2022). Searches for gravitational waves from known pulsars at two harmonics in the second and third LIGO-Virgo observing runs. *The Astrophysical Journal*, **935**, 1

[116] Mastrogiovanni, S., *et al.*(2017). An improved algorithm for narrow-band searches of continuous gravitational waves. *Classical and Quantum Gravity*, **34(13)**, 135007.

[117] Dupuis, R. J., & Woan, G. (2005). Bayesian estimation of pulsar parameters from gravitational wave data. *Physical Review D*, **72(10)**, 102002.

[118] Astone, P., D'Antonio, S., Frasca, S., & Palomba, C. (2010). A method for detection of known sources of continuous gravitational wave signals in non-stationary data. *Classical and Quantum Gravity*, **27(19)**, 194016.

[119] Astone, P., Colla, A., D'Antonio, S., Frasca, S., & Palomba, C. (2012). Coherent search of continuous gravitational wave signals: extension of the 5-vectors method to a network of detectors. In *Journal of Physics: Conference Series*, (**363(1)**, 012038. IOP Publishing.

[120] Jaranowski, P., & Królak, A. (2010). Searching for gravitational waves from known pulsars using the and statistics. *Classical and Quantum Gravity*, **27(19)**, 194015.

[121] Brady, P. R., Creighton, T., Cutler, C., & Schutz, B. F. (1998). Searching for periodic sources with LIGO. *Physical Review D*, **57(4)**, 2101.

[122] Astone, P., Colla, A., D'Antonio, S., Frasca, S., & Palomba, C. (2014). Method for all-sky searches of continuous gravitational wave signals using the frequency-Hough transform. *Physical Review D*, **90(4)**, 042002.

[123] Krishnan, B., Sintes, A. M., Papa, M. A., Schutz, B. F., Frasca, S., & Palomba, C. (2004). Hough transform search for continuous gravitational waves. *Physical Review D*, **70(8)**, 082001.

[124] Aasi, J., *et al.*(2014). Implementation of an F-statistic all-sky search for continuous gravitational waves in Virgo VSR1 data. *Classical and quantum gravity*, **31(16)**, 165014.

[125] Bayley, J., Messenger, C., & Woan, G. (2019). Generalized application of the Viterbi algorithm to searches for continuous gravitational-wave signals. *Physical Review D*, **100(2)**, 023006.

[126] Abbott, B. P., *et al.*(2016). Results of the deepest all-sky survey for continuous gravitational waves on LIGO S6 data running on the Einstein@ Home volunteer distributed computing project. *Physical Review D*, **94(10)**, 102002.

[127] Walsh, S., *et al.*(2016). Comparison of methods for the detection of gravitational waves from unknown neutron stars. *Physical Review D*, **94(12)**, 124010.

[128] Abbott, R., *et al.*, LIGO Scientific Collaboration, Virgo Collaboration and KAGRA collaboration (2022). All-sky search for continuous gravitational waves from isolated neutron stars using Advanced LIGO and Advanced Virgo O3 data. *Physical Review D*, **106(10)**, 102008.

[129] Abbott, R., *et al.*, LIGO Scientific Collaboration, Virgo Collaboration and KAGRA collaboration (2022). Search for continuous gravitational wave emission from the Milky Way center in O3 LIGO-Virgo data. *Physical Review D*, **106**, 042003.

[130] Abbott, R., *et al.*, LIGO Scientific Collaboration, Virgo Collaboration and KAGRA collaboration (2022). Search for gravitational waves from Scorpius X-1 with a hidden Markov model in O3 LIGO data. *Physical Review D*, **106**, 062002.

[131] Davis, D., *et al.*, LIGO Scientific Collaboration (2021). LIGO detector characterization in the second and third observing runs. *Classical and Quantum Gravity*, **38(13)**, 135014.

[132] Acernese, F., *et al.*, Virgo Collaboration (2022). Virgo detector characterization and data quality during the O3 run. *arXiv preprint*, arXiv:**2205.01555** (Submitted to CQG).

[133] Abbott, B. P., *et al.*, LIGO Scientific Collaboration and Virgo Collaboration (2018). Effects of data quality vetoes on a search for compact binary coalescences in Advanced LIGO's first observing run. *Classical and Quantum Gravity*, **35(6)**, 065010.

[134] Covas, P. B., *et al.*, LIGO Scientific Collaboration and Virgo Collaboration (2018). Identification and mitigation of narrow spectral artifacts that degrade searches for persistent gravitational waves in the first two observing runs of Advanced LIGO. *Physical Review D*, **97(8)**, 082002.

[135] Cirone, A., *et al.*(2018). Magnetic coupling to the Advanced Virgo payloads and its impact on the low frequency sensitivity. *Review of Scientific Instruments*, **89(11)**, 114501.

[136] Acernese, F., *et al.*, Virgo Collaboration (2022). The Virgo O3 run and the impact of the environment. *Classical and quantum gravity*, **39**, 235009.

[137] Fiori, I., Effler, A., Nguyen, P., Paoletti, F., Schofield, R. M., & Tringali, M. C. (2021). Environmental Noise in Gravitational-Wave Interferometers. In *Handbook of Gravitational Wave Astronomy* (pp. **1-72**). Springer, Singapore.

[138] The OpenStreetMap contributors 2022 OpenStreetMap `https://openstreetmap.org/`.

[139] De Rosa, R., Fiori, I. (2019). Advanced Virgo ENV probe maps (fast and slow sensors). *Virgo Technical Documentation System (TDS)*, `https://tds.virgo-gw.eu/ql/?c=13976`

[140] Fiori, I., *et al.*(2020). The hunt for environmental noise in virgo during the third observing run. *Galaxies*, **8(4)**, 82.

[141] Paoletti, F., Fiori, I., Ciardelli, Fabozzi, C., D'Andrea, Paoli, A., Romboli (2019) Global HVAC Switch-OFF. *Virgo Logbook*, report: `https://logbook.virgo-gw.eu/virgo/?r=45683`.

[142] Accadia, T., *et al.*, Virgo Collaboration (2012). The NoEMi (noise frequency event miner) framework. In *Journal of Physics: Conference Series*,**363(1)**, 012037. IOP Publishing.

[143] Tringali, M.C, Soldani, D., Fiori, I., Paoletti, F., Passaquieti, R., Ruggi, P. (2020) WEB, NEB, MCB: HVAC switch-off test. *Virgo Logbook*, report: `https://logbook.virgo-gw.eu/virgo/?r=49997`.

[144] Pierini, L., Fiori, I., Tringali, M.C., Paoletti, F., Soldani, D. (2021) Slow-down and switch test on WEB hot water pumps. *Virgo Logbook*, report: `https://logbook.virgo-gw.eu/virgo/?r=52167`.

[145] Pierini, L. (2021) Comment to Slow-down and switch test on WEB hot water pumps. *Virgo Logbook*, report: `https://logbook.virgo-gw.eu/virgo/?r=52193`.

[146] Fiori, I., Tringali, M.C., Passaquieti, R., Soldani, D., Paoletti, F., Nenci, F. (2021) NEB water pumps tests. *Virgo Logbook*, report: `https://logbook.virgo-gw.eu/virgo/?r=52531`.

[147] Soldani, D. (2021) Tuesday maintenance: Valve and anti-vibration joint at WEB - new expansion vessel for NEB boiler. *Virgo Logbook*, report: `https://logbook.virgo-gw.eu/virgo/?r=53385`.

[148] Fiori, I., Paoletti, F., Passaquieti, R., Tringali, M.C., Soldani, D. (2021) WEB cold water pipe noise mitigation. *Virgo Logbook*, report: `https://logbook.virgo-gw.eu/virgo/?r=53584`.

[149] Pierini, L., Fiori, I., Tringali, M.C. (2022) Investigation on 18.74 Hz line noise in DET area and temporary sensor installation. *Virgo Logbook*, report: `https://logbook.virgo-gw.eu/virgo/?r=55963`.

[150] Fiori, I., Pasqualetti, A., Pierini, L. (2022) Comment to Investigation on 18.74 Hz line noise in DET area and temporary sensor installation. *Virgo Logbook*, report: `https://logbook.virgo-gw.eu/virgo/?r=56111`.

[151] Pierini, L., Tringali, M.C., Fiori, I. (2022) Installation of temporary accelerometer on CEB remoted dry pump. *Virgo Logbook*, report: `https://logbook.virgo-gw.eu/virgo/?r=55248` and comment: `https://logbook.virgo-gw.eu/virgo/?r=55332`.

[152] Pierini, L., Fiori, I., Tringali, M.C. (2022) Comment to Installation of temporary accelerometer on CEB remoted dry pump. *Virgo Logbook*, report: `https://logbook.virgo-gw.eu/virgo/?r=55975`.

[153] Paoletti, F., Montanari, B., Fiori, I., Tringali, M.C., Fabozzi, C. (2021) Comment to Damage to external magnetometers and weather station due to lightning. *Virgo Logbook*, report: `https://logbook.virgo-gw.eu/virgo/?r=53979`.

[154] Thrane, E., Christensen, N., & Schofield, R. M. (2013). Correlated magnetic noise in global networks of gravitational-wave detectors: observations and implications. *Physical Review D*, **87(12)**, 123009.

[155] Janssens, K., *et al.*(2023). Correlated 1–1000 Hz magnetic field fluctuations from lightning over Earth-scale distances and their impact on gravitational wave searches. *Physical Review D*, **107(2)**, 022004.

[156] Paoletti, F. (2022) Comment to Damage to external magnetometers and weather station due to lightning. *Virgo Logbook*, report: `https://logbook.virgo-gw.eu/virgo/?r=54216`.

[157] Paoletti, F., Fiori, I., Tringali, M.C., Raymond, J.L., Pierini, L. (2022) Comment to Damage to external magnetometers and weather station due to lightning. *Virgo Logbook*, report: `https://logbook.virgo-gw.eu/virgo/?r=55542`.

[158] Abbott, R., *et al.*(2021). Open data from the first and second observing runs of Advanced LIGO and Advanced Virgo. *SoftwareX*, **13**, 100658.

[159] Pierini, L., Astone, P., Palomba, C., *et al.*(2022). Impact of signal clusters in wide-band searches for continuous gravitational waves. *Physical Review D*, **106(4)**, 042009.

[160] Palomba, C., *et al.*(2019). Direct constraints on the ultralight boson mass from searches of continuous gravitational waves. *Physical review letters*, **123(17)**, 171101.

[161] D'Antonio, S., *et al.*(2018). Semicoherent analysis method to search for continuous gravitational waves emitted by ultralight boson clouds around spinning black holes. *Physical Review D*, **98(10)**, 103017.

[162] Arvanitaki, A., & Dubovsky, S. (2011). Exploring the string axiverse with precision black hole physics. *Physical Review D*, **83(4)**, 044026.

[163] Reitze, D., *et al.*(2019). Cosmic explorer: the US contribution to gravitational-wave astronomy beyond LIGO. *White paper, arXiv preprint* arXiv:**1907.04833**.

[164] Maggiore, M., *et al.*(2020). Science case for the Einstein telescope. *Journal of Cosmology and Astroparticle Physics*, **2020(03)**, 050.

[165] La Rana, A. (2022). EUROGRAV 1986–1989: the first attempts for a European Interferometric Gravitational Wave Observatory. *The European Physical Journal H*, **47(1)**, 1-32.

[166] Babak, S., *et al.*(2017). Science with the space-based interferometer LISA. V. Extreme mass-ratio inspirals. *Physical Review D, 95(10)*, 103012.

[167] Zhu, S. J., Baryakhtar, M., Papa, M. A., Tsuna, D., Kawanaka, N., & Eggenstein, H. B. (2020). Characterizing the continuous gravitational-wave signal from boson clouds around Galactic isolated black holes. *Physical Review D*, **102(6)**, 063020.

[168] Abbott, B. P., *et al.*, LIGO Scientific Collaboration and Virgo Collaboration (2019). All-sky search for continuous gravitational waves from isolated neutron stars using Advanced LIGO O2 data. *Physical Review D*, **100(2)**, 024004.

[169] La Rosa, I., Astone, P., D'antonio, S., Frasca, S., Leaci, P., Miller, A. L., Palomba, C., Piccinni, O.J., Pierini, L., & Regimbau, T. (2021). Continuous Gravitational-Wave Data Analysis with General Purpose Computing on Graphic Processing Units. *Universe*, **7(7)**, 218.

[170] Piccinni, O. J., *et al.*(2018). A new data analysis framework for the search of continuous gravitational wave signals. *Classical and Quantum Gravity*, **36(1)**, 015008.

[171] Astone, P., Frasca, S., & Palomba, C. (2005). The short FFT database and the peak map for the hierarchical search of periodic sources. *Classical and Quantum Gravity*, **22(18)**, S1197.

[172] D'Onofrio, L., De Rosa, R., Errico, L., Palomba, C., Sequino, V., & Trozzo, L. (2022). 5n-vector ensemble method for detecting gravitational waves from known pulsars. *Physical Review D*, **105(6)**, 063012.

[173] Bennett, M. F., Melatos, A., Delaigle, A., & Hall, P. (2013). REANALYSIS OF STATISTIC GRAVITATIONAL-WAVE SEARCHES WITH THE HIGHER CRITICISM STATISTIC. *The Astrophysical Journal*, **766(2)**, 99.

[174] Miller, A., Astone, P., *et al.*(2018). Method to search for long duration gravitational wave transients from isolated neutron stars using the generalized frequency-Hough transform. *Physical Review D*, **98(10)**, 102004.

[175] Lasky, P. D., Sarin, N., Sammut, L. (2017). Long-duration waveform models for millisecond magnetars born in binary neutron star mergers. *Technical Repory LIGO-T1700408*, `https://dcc.ligo.org/LIGO-T1700408/public`.

[176] Abbott, B. P., *et al.*, LIGO Scientific Collaboration and Virgo Collaboration (2019). Search for gravitational waves from a long-lived remnant of the binary neutron star merger GW170817. *The Astrophysical Journal*, **875(2)**, 160.

[177] Gonzalez, R. C., & Woods, R. E. (1992). Digital Image Processing, 4th edition. Pearson Publisher.

[178] Papoulis, A., & Unnikrishna Pillai, S. (2002). Probability, random variables and stochastic processes.

[179] Abbott, R., *et al.*, LIGO Scientific Collaboration, Virgo Collaboration and KAGRA collaboration (2023). Open data from the third observing run of LIGO, Virgo, KAGRA and GEO. *arXiv preprint*, arXiv:**2302.03676** (Submitted to ApJSS).

[180] Pierini, L. (2022). Improving agnostic searches of Gravitational Waves from Neutron Star instabilities using image filtering. *Proceedings of the International Astronomical Union*, **16(S363)**, 352-353.

[181] D'Antonio, S., *et al.*(2021). Sidereal filtering: A novel robust method to search for continuous gravitational waves. *Physical Review D*, **103(6)**, 063030.

[182] Biwer, C., *et al.*(2017). Validating gravitational-wave detections: The Advanced LIGO hardware injection system. *Physical Review D*, **95(6)**, 062002.

[183] Ron, C., & Vondrak, J. (1986). Expansion of annual aberration into trigonometric series. *Bulletin of the Astronomical Institutes of Czechoslovakia*, **37**, 96-103.

[184] Bazin, M. J., & Benoit, J. W. (1965). Off-line global approach to pattern recognition for bubble chamber pictures. *IEEE Transactions on Nuclear Science*, **12(4)**, 291-293.

[185] van Ginkel, M., Hendriks, C. L., & van Vliet, L. J. (2004). A short introduction to the Radon and Hough transforms and how they relate to each other. *Delft University of Technology*. Url repository: `https://www.cb.uu.se/~cris/Documents/Ginkel2004.pdf`.